UNIVERSITAT POLITÈCNICA DE CATALUNYA

DOCTORAL THESIS

Controlling interactions in quantum materials: from a microscopic description to quantum simulation

Author:
Sergi JULIÀ-FARRÉ

Supervisor:
Prof. Dr. Maciej LEWENSTEIN
Co-Supervisor:
Dr. Alexandre DAUPHIN

A thesis submitted in fulfillment of the requirements for the degree of Doctor of Philosophy

in the

Quantum Optics Theory Group
at
Institut de Ciències Fotòniques (ICFO)

Barcelona, May 2022

Abstract

The last decades have witnessed impressive technical advances in all the fields of quantum science, including solid-state systems or atomic, molecular, and optical physics, allowing one to control materials at the microscopic scale with a high degree of precision. This development opens the road for the investigation of complex many-body phenomena in quantum materials, which cannot be easily inferred from the behavior of their individual constituents. Indeed, interactions in quantum many-body systems can lead to richer physics compared to the noninteracting case, as they are deeply connected with spontaneous symmetry breaking, quantum correlations, i.e., entanglement, and some collective behaviors.

On the one hand, in some cases, the motivation to study such interacting systems is the possibility to synthesize them in the lab, such as for instance with cold atoms in optical lattices. The latter platform can be used as a *quantum simulator* of systems that were regarded just as toy models in the last century, as it is the case of *topological insulators*: materials characterized by a global topological invariant leading to protected surface modes. While so far experiments have concentrated their efforts on engineering noninteracting topological insulators, state-of-the art techniques can also be used to study the role of interactions in these systems. In this context, the first goal of this thesis is to investigate novel effects in interaction-induced topological insulators. In the one-dimensional case, we reveal the topological nature of *fermionic chains* with frustrated interactions, which could be realized with dipolar quantum gases. For the two-dimensional case, we focus on *topological Mott insulators*, for which we propose an experimental scheme based on Rydberg-dressed atoms. Furthermore, we show that these systems can exhibit rich spatial features intertwined with their topological protection, owing to the interacting nature of the phase.

On the other hand, there are some paradigmatic cases, as in *high-T_c superconductors*, where exotic experimental results clearly point towards the need of finding a microscopic model in a many-body interacting framework. In the particular case of high-T_c superconductors, their complex composition and unknown exact form of intrinsic interactions make it challenging to characterize their rich phase diagram: such materials not only host a high-T_c superconducting phase, but also other exotic phases, such as the strange metal or *pseudogap* phases. In this regard, the second goal of this thesis is to gain physical insight of the pseudogap phase of cuprate high-T_c superconductors. To this aim, we numerically study the effect of interactions between electrons and bond phonons within a particular Hamiltonian modeling of the system. We show that, by properly accounting for the subtle interplay between electron-electron and electron-phonon interactions, one can indeed numerically reproduce the main experimental features of the pseudogap phase.

Finally, the study of collective interaction-induced effects is also needed to analyze the quantum advantage theoretically claimed for some systems. In particular, many-body interactions and entanglement are sometimes regarded as a resource for *quantum thermodynamic machines*: devices that perform tasks related to refrigeration, heat-to-work conversion, or energy storage. On this basis, the third goal of this thesis is to study fundamental bounds imposed by quantum mechanics to collective charging effects in systems for energy storage, called *quantum batteries*.

Resum

Les últimes dècades han presenciat grans avenços tècnics en tots els camps de la física quàntica, com en física de l'estat sòlid, o en física atòmica, molecular i òptica, els quals han permès controlar materials a escala microscòpica amb alta precisió. Aquests avenços obren la porta a l'estudi de fenòmens complexos de diverses partícules en materials quàntics, els quals no poden ser explicats de manera simple a partir del comportament individual de cadascuna d'aquestes partícules. En aquest sentit, les interaccions en sistemes quàntics de vàries partícules poden donar lloc a una física més rica en comparació amb el cas sense interaccions, ja que aquestes estan profundament connectades amb la ruptura espontània de simetria, correlacions quàntiques com l'entrellaçament, i alguns fenòmens col·lectius.

Per una banda, una de les motivacions per estudiar aquests sistemes amb interaccions ve donada per la possibilitat de sintetitzar-los al laboratori, per exemple amb àtoms freds en xarxes òptiques. Aquesta plataforma pot ser emprada com a simulador quàntic de sistemes que al llarg del segle passat eren considerats models purament teòrics, com és el cas dels aïllants topològics: materials caracteritzats per un invariant global topològic, el qual dona lloc a estats de superfície protegits. Tot i que de moment els experiments s'han enfocat a simular aïllants topològics sense interaccions, aquestes també es poden estudiar experimentalment amb les tècniques més avançades. En aquest context, el primer objectiu d'aquesta tesi és investigar nous fenòmens en aïllants topològics generats a través d'interaccions. En una dimensió, descobrim la naturalesa topològica de cadenes d'electrons amb interaccions frustrades, que podrien ser simulades amb gasos dipolars. En dues dimensions, ens centrem en l'estudi d'aïllants topològics de tipus Mott, pels quals proposem una implementació experimental basada en àtoms de Rydberg parcialment excitats, i mostrem que, degut a les interaccions inherents a aquest tipus de fases, aquestes poden presentar propietats espacials interessants entrellaçades amb la topologia.

Per altra banda, hi ha alguns casos paradigmàtics, com el dels superconductors a altes temperatures, en què per explicar resultats experimentals exòtics és necessari trobar un model microscòpic en un marc de diverses partícules amb interaccions. En el cas particular dels superconductors a altes temperatures, la seva composició complexa i el desconeixement de la forma de les interaccions internes fan difícil caracteritzar el seu diagrama de fases: més enllà de la fase superconductora, aquests materials també presenten altres fases interessants com la del metall estrany o la fase de *pseudogap*. En aquest cas, el segon objectiu d'aquesta tesi és entendre millor la física de la fase de *pseudogap* dels *cuprates*, una família de de materials superconductors a altes temperatures. Amb aquesta finalitat, estudiem numèricament l'efecte d'interaccions electró-fonó, dins d'una modelització Hamiltoniana del sistema. Mostrem que, quan és té en compte la interrelació entre interaccions electró-fonó i electró-electró de manera adequada, es poden reproduir de forma numèrica les principals propietats experimentals de la fase de *pseudogap*.

Finalment, l'estudi d'efectes col·lectius causats per interaccions també és necessari per analitzar els avantatges quàntics que s'han predit de manera teòrica en alguns sistemes. En concret, les interaccions entre diverses partícules i l'entrellaçament quàntic són considerats com a recursos per les màquines termodinàmiques quàntiques: dispositius que s'encarreguen de realitzar tasques com refrigerar, convertir calor en treball, o emmagatzemar energia. En aquesta direcció, el tercer objectiu d'aquesta tesi és estudiar els límits fonamentals imposats per la mecànica quàntica als efectes col·lectius de càrrega en sistemes emprats per emmagatzemar energia, les bateries quàntiques.

Resumen

Las últimas décadas han presenciado grandes avances técnicos en todos los campos de la física cuántica, como en física del estado sólido, o en física atómica, molecular y óptica, que han permitido controlar materiales a escala microscópica con alta precisión. Estos avances abren la puerta al estudio de fenómenos complejos de diversas partículas en materiales cuánticos, que no pueden ser explicados de manera simple a partir del comportamiento individual de cada una de estas partículas. En este sentido, las interacciones en sistemas cuánticos de varias partículas pueden dar lugar a una física más rica en comparación con el caso sin interacciones, puesto que éstas están profundamente conectadas con la ruptura espontánea de simetría, correlaciones cuánticas como el entrelazamiento, y algunos fenómenos colectivos.

Por un lado, una de las motivaciones para estudiar estos sistemas con interacciones viene dada por la posibilidad de sintetizarlos en el laboratorio, por ejemplo con átomos fríos en redes ópticas. Esta plataforma puede utilizarse como simulador cuántico de sistemas considerados como modelos puramente teóricos en el siglo pasado, como los aislantes topológicos: materiales caracterizados por un invariante global topológico, que da lugar a estados de superficie protegidos. Aunque por el momento los experimentos se han enfocado a simular aislantes topológicos sin interacciones, éstas también pueden estudiarse experimentalmente con las técnicas más avanzadas. En ese contexto, el primer objetivo de esta tesis es investigar nuevos fenómenos en aislantes topológicos generados a través de interacciones. En una dimensión, descubrimos la naturaleza topológica de cadenas de electrones con interacciones frustradas, que podrían ser simuladas con gases dipolares. En dos dimensiones, nos centramos en el estudio de aislantes topológicos de tipo Mott, por los que proponemos una implementación con átomos de Rydberg parcialmente excitados, mostrando que, debido a las interacciones inherentes a este tipo de fases, éstas pueden presentar propiedades espaciales interesantes entrelazadas con la topología.

Por otro lado, existen algunos casos paradigmáticos, como el de los superconductores a altas temperaturas, en los que para explicar resultados experimentales exóticos es necesario encontrar un modelo microscópico en un marco de diversas partículas con interacciones. En los superconductores a altas temperaturas, su composición compleja y el desconocimiento de la forma de las interacciones internas hacen difícil caracterizar su diagrama de fases: más allá de la fase superconductora, estos materiales presentan también otras fases interesantes como la del metal extraño o la fase de *pseudogap*. En este caso, el segundo objetivo de esta tesis es entender mejor la física de la fase de *pseudogap* de los *cuprates*, una familia de superconductores a altas temperaturas. Para ello, estudiamos numéricamente el efecto de interacciones electrón-fonón, dentro de una modelización Hamiltoniana del sistema. Mostramos que, teniendo en cuenta de forma adecuada la interrelación entre interacciones electrón-fonón y electrón-electrón, podemos reproducir numéricamente las principales propiedades experimentales de la fase de *pseudogap*.

Por último, el estudio de efectos colectivos causados por interacciones también es necesario para analizar las ventajas cuánticas que se han predicho de forma teórica en algunos sistemas. En concreto, las interacciones entre diversas partículas y el entrelazamiento cuántico son considerados como recursos por las máquinas termodinámicas cuánticas: dispositivos que se encargan de realizar tareas como refrigerar, convertir calor en trabajo, o almacenar energía. En esta dirección, el tercer objetivo de esta tesis es estudiar los límites fundamentales impuestos por la mecánica cuántica a efectos colectivos de carga en sistemas empleados para almacenar energía, las baterías cuánticas.

List of publications

This thesis is based on the peer-reviewed and preprint articles listed below.

Peer-reviewed

1. S. Julià-Farré, T. Salamon, A. Riera, M. N. Bera, and M. Lewenstein. Bounds on the capacity and power of quantum batteries. Phys. Rev. Research 2, 023113 (2020) [1]. Chapter 9.

2. S. Julià-Farré, A. Dauphin, R. W. Chhajlany, P. T. Grochowski, S. Wall, M. Lewenstein, and P. R. Grzybowski. Nanoscale phase separation and pseudogap in the hole-doped cuprates from fluctuating Cu-O-Cu bonds. Phys. Rev. B 101, 125107 (2020) [2]. Chapter 8.

3. S. Julià-Farré, M. Müller, M. Lewenstein, and A. Dauphin. Self-trapped Polarons and Topological Defects in a Topological Mott Insulator. Phys. Rev. Lett. 125, 240601 (2020) [3] (Highlighted as an editor's suggestion). Chapter 6.

Preprints

4. S. Julià-Farré, D. González-Cuadra, A. Patscheider, M. J. Mark, F. Ferlaino, M. Lewenstein, L. Barbiero, and A. Dauphin. Revealing the topological nature of the bond order wave in a strongly correlated quantum system. arXiv:2112.08785 (2021) [4]. Chapter 4.

5. L. Cardarelli, S. Julià-Farré, M. Lewenstein, A. Dauphin, and M. Müller. Accessing the topological Mott insulator in cold atom quantum simulators with realistic Rydberg dressing. arXiv:2203.14818 (2022) [5]. Chapter 5.

6. S. Julià-Farré et al., *in preparation (2022)*. Chapter 7.

Other works of the author not included in this thesis

7. M. L. Bera, S. Julià-Farré, M. Lewenstein, and M. N. Bera. Quantum Heat Engines with Carnot Efficiency at Maximum Power. Phys. Rev. Research 4, 013157 (2022) [6].

Code availability

The codes for the numerical studies of Refs. [3] and [5] are openly available in the online repository [7].

Acknowledgements

After these amazing four years at ICFO I have an immense feeling of gratitude towards many people. First of all, I would like to thank Maciej for giving me the opportunity to become part of the QOT family. Thank you for always helping me to stay positive, and for encouraging me to explore so many different fields, which has allowed me to learn from very diverse people. Among all of them, I would like to specially thank my co-supervisor Alex, who has become a really good friend, and also give him credit for the design of the thesis cover. Gracias por todas las horas dedicadas a explicarme los conceptos físicos más profundos, o en revisar los errores más simples en los códigos. Y, sobretodo, gracias por explicar esta gran cantidad de conocimento que tienes de la manera más cercana, paciente y humilde possible.

I would also like to express my gratitude to all the other collaborators, which have also contributed to a great part of this thesis. Thank you Tymek, Manab, Arnau, Ravi, Przemek, Piotr, and Simon, for the immense number of things I learnt from each of you during the first two years of this adventure. In the last years, there has been a nice interplay between local and nonlocal scientific interactions. On this regard, thanks to Dani and Luca, for helping me to deal with frustration, by means of DMRG, and to Markus, Lorenzo, Francesca, Manfred, and Alexander, from whom despite the distance I learnt, among other things, many valuable implementation aspects, which are strongly reflected in the experimental proposals of this thesis.

These four years would have not been the same without Albert, Gorka, Christos, Mohit, Joana, Borja, Niccolò, and all the other QOT members, who have filled all the days at ICFO with funny and happy memories. Beyond them, I would also like to thank all the other ICFOnians, who also contributed to such a wonderful experience, with a special mention to the ICFO football group and the ICFO futbolín gang.

I would also like to take the chance to thank my former professors, whose enthusiasm for teaching motivated me to keep learning things. In this regard, I feel very grateful to Oriol and his group in Innsbruck, from which I got a scientific and personal treasure. Gràcies també a tots els professors de la UAB, els quals recordo amb gran afecte. També em sento molt agraït a tots els professors d'anteriors etapes, com l'Assumpta, per aportar-me una gran motivació per les matemàtiques, i al Javier i el Toni, que em van apropar a la física per primer cop, i que, tot i que malauradament ja no hi siguin, m'agradaria que també es sentissin aquesta tesi com a seva.

També m'agradaria donar les gràcies a tots els que heu tingut la paciència d'estar sempre al meu costat durant aquests anys i els anteriors, en els bons i els mals moments. Gràcies a tots els amics de la universitat; la Claudia, el César, el Marcel i el Marc, pels Hey there Delilahs, i per seguir sent un constant suport malgrat la distància. Gràcies també als meus amics de Terrassa; el López, el Mou, el Dami, l'Álvaro, l'Ivan i el Mati, per ajudar-me tant a desconectar i passar-m'ho bé sempre que ho he necessitat durant aquests últims anys. Gràcies a tota la meva família, i en particular al tiet Pepe, que durant tants anys ha tingut el millor laboratori de llum del món a la Rasa. A la meva àvia Josepa, gràcies per guardar-me tantes revistes de ciència, i a la meva altra àvia Rosa que, tot i ja no ser-hi, sempre em recordes que cal que sempre estiguem contents. Gràcies també en especial a tu, Meri, per ser una font inesgotable d'energia i alegria que m'ha ajudat moltíssim a arribar fins al final d'aquest viatge. I, per últim, vull donar les gràcies a les tres persones que porten tota una vida fent-me costat. Gràcies pare i mare, per haver-m'ho donat tot i més, i gràcies, Pol, per ser-hi sempre que t'he necessitat, i per ajudar-me a revisar el manuscrit d'aquesta tesi.

This thesis would not have been possible without the financial support from ERC AdG NOQIA; Agencia Estatal de Investigación (R&D project CEX2019-000910-S, funded by MCIN/ AEI/10.13039/501100011033, Plan National FIDEUA PID2019-106901GB-I00, FPI (reference code BES-2017-082118), QUANTERA MAQS PCI2019-111828-2, Proyectos de I+D+I "Retos Colaboración" QUSPIN RTC2019-007196-7); Fundació Cellex; Fundació Mir-Puig; Generalitat de Catalunya through the European Social Fund FEDER and CERCA program (AGAUR Grant No. 2017 SGR 134, QuantumCAT U16-011424, co-funded by ERDF Operational Program of Catalonia 2014-2020); EU Horizon 2020 FET-OPEN OPTOlogic (Grant No. 899794); National Science Centre, Poland (Symfonia Grant No. 2016/20/W/ST4/00314); European Union's Horizon 2020 research and innovation programme under the Marie-Skłodowska-Curie grant agreement No. 101029393 (STREDCH) and No. 847648 ("La Caixa" Junior Leaders fellowships ID100010434: LCF/BQ/PI19/11690013, LCF/BQ/PI20/11760031, LCF/BQ/PR20/11770012, LCF/BQ/PR21/11840013).

Contents

List of Abbreviations

AMO	**A**tomic, **M**olecular, and **O**ptic
IQHE	**I**nteger **Q**uantum **H**all **E**ffect
SSB	**S**pontaneous **S**ymmetry **B**reaking
SSH	**S**u, **S**crieffer, and **H**eeger
BCS	**B**ardeen, **C**ooper, and **S**chrieffer
HF	**H**artree **F**ock
DMRG	**D**ensity **M**atrix **R**enormalization **G**roup
iDMRG	**I**nfinite **D**ensity **M**atrix **R**enormalization **G**roup
MPS	**M**atrix **P**roduct **S**tate
iMPS	**I**nfinite **M**atrix **P**roduct **S**tate
BOW	**B**ond **O**rder **W**ave
TMI	**T**opological **M**ott **I**nsulator
TKNN	**T**houless, **K**ohmoto, **N**ightingale, and den **N**ijs
QAH	**Q**uantum **A**nomalous **H**all
SPT phases	**S**ymmetry-**P**rotected **T**opological phases
NN	**N**earest **N**eighbors
NNN	**N**ext **N**earest **N**eighbors
CDW	**C**harge **D**ensity **W**ave
ES	**E**ntanglement **S**pectrum
FBM	**F**luctuating **B**ond **M**odel
ARPES	**A**ngle-**R**esolved **P**hotoemission **S**pectroscopy
STM	**S**canning **T**unneling **M**icroscope
RI	**R**esidual **I**nteractions
GHZ	**G**reenberger, **H**orne, and **Z**eilinger
LMG	**L**ipkin, **M**eshkov, and **G**lick

To my family, and to Pluja and Goofy, the other animals.

Introduction

Motivation

Quantum mechanics was born at the very beginning of the last century with the breakthrough ideas of Planck and Einstein to explain, respectively, the black-body radiation [8] and the photoelectric effect [9]. Despite initial controversies arising from some counterintuitive aspects of its postulates, the quantum theory became a well-established physical theory by the end of the 1920 decade. The improvement in our fundamental understanding of Nature at the microscopic scale had also practical applications, and the last century witnessed the appearance of the first technologies described with quantum mechanics. This fruitful technological period, known as the *first quantum revolution*, led to the invention of the transistor and the laser [10–12], whose impact in modern societies can be hardly overestimated.

In the last decades of the last century, and specially since the beginning of the 21st century, there have been exciting technological advances in all the experimental fields of quantum science, leading to a *second quantum revolution* [13]. In this era, in which we are immersed nowadays, not only we are able to correctly describe the microscopic scale with quantum laws, but we can also actively control it for technological purposes. The latter include applications in quantum metrology [14], quantum sensing [15], quantum simulation [16, 17] and computation [18], and quantum communication [19], which require to address the microscopic scale with an unprecedented precision. Examples of such degree of control of quantum matter can be seen, for instance, in solid-state physics. In this field, the manufacturing of one-atom thick materials such as graphene [20], or the use of light to control the properties of this and other materials are already a reality [21, 22].

Another paradigmatic example can be found in the field of atomic, molecular, and optical (AMO) physics. There, the technical advances in optical and mechanical elements have given rise to well-established experimental techniques for atomic cooling [23, 24], allowing one to reach the lowest temperatures of the Universe in the lab [25, 26], and for trapping and manipulating single-atoms with a high degree of control and isolation [27], leading to highly precise atomic clocks [28, 29]. The study of collective quantum phenomena in AMO physics has also been a focus of interest in the last decades [30–33], boosted by the possibility to realize in the lab long standing theoretical predictions. An exemplary case is the Bose-Einstein condensation [34–36], proposed in the 1920s by these two authors, and whose experimental realization [37, 38] in 1995 is one of the milestones of the AMO physics community.

The possibility to isolate ultracold many-body systems of atoms or molecules, interacting with light in a controlled way, as in the Bose-Einstein condensate, allows one to use them as quantum simulators, as envisioned by Feynman in the 1980s [39]. Quantum simulators [16, 17, 40–43] are quantum systems that mimic the behavior of a more complex solid-state material, that could not be simulated with a classical computer, in a very controlled environment. For the quantum simulation purpose, the atoms can be trapped in one, two, or three dimensions by means of optical

lattices, in order to simulate the crystalline arrangement of electrons in real materials. Interestingly, despite the obvious differences between the two systems (e.g., in atomic and electron masses), in many cases the Hamiltonian description of both systems is very similar. Hence, the quantum simulator can be used to gain insights about the underlying physical model, as it allows one to tune its parameters and perform measurements with high precision. In this spirit, there are great advances in the simulation of very diverse phenomena with cold atoms in optical lattices, such as Fermi-Hubbard models [31, 44, 45] relevant for high-T_c superconductors [46, 47], or lattice gauge theory models [48, 49] appearing in high-energy physics. Moreover, quantum simulators can also be used to synthesize novel quantum systems in addition to Bose-Einstein condensates, such as topological phases of matter [50, 51], or quantum thermodynamic machines [52].

Motivated by the experimental possibility to access such a wide variety of physical phenomena in many different solid-state and quantum simulation platforms, in this thesis we theoretically address several open questions related to three main topics: topological insulators, high-T_c superconductors, and quantum thermodynamics. As described below, such fundamental problems are highly intertwined with the practical applications of the second quantum revolution, as they need to be answered to understand novel behaviors observed in materials, or to propose new ones.

Topological insulators. The first topic is related to topological phases of matter, exotic many-body states characterized by global properties that are robust against local perturbations [51, 53]. This field started with the experimental discovery of the integer quantum Hall effect (IQHE) [54] in 1980, and its explanation in terms of a global topological invariant only a few years later [55]. Notice that the latter is in stark contrast with the traditional classification of phases of matter given by the Landau-Ginzburg-Wilson paradigm [56, 57], in which different phases are characterized instead by local order parameters arising from a spontaneous symmetry breaking (SSB) process. Moreover, the topologically protected properties of these materials are also interesting from an applied perspective, as they can be used in quantum metrology [58]. The global topological nature of the IQHE fueled the search of new topological states, such as the quantum spin Hall effect, first predicted [59] in graphene. The experimental realization of the quantum spin Hall effect [60] in semiconductor quantum wells, following its theoretical prediction [61], was one of the experimental landmarks of the past decades, as it represented the first experimental evidence of a topological insulator [51]: a bulk insulating system characterized by a global topological invariant, with topologically protected surface currents. A few years later, in 2010, a general theoretical classification of topological insulators was partially achieved, for noninteracting systems, with the introduction of the periodic table of topological insulators and superconductors [62–64]. Ever since, there has been a growing interest in finding other topological systems that escape this general classification, such as topological Weyl semimetals [65], recently observed in several solid-state compounds [66, 67], or light-induced topological phases [21, 68, 69].

In the last decade, the use of quantum simulators has been also very prolific to realize several of the theoretically proposed models of topological insulators [50, 70]. For instance, cold atoms in optical lattices have been used to simulate the static Su-Schrieffer-Heeger (SSH) model [71, 72] using an optical superlattice, or the Harper-Hofstadter [73–77] and Haldane [78–80] models by means of artificial gauge fields [81, 82] or synthetic dimensions [83]. Furthermore, Floquet topological insulators [84] have been engineered in photonic platforms via periodic driving [85,

86]. The versatility of cold atoms, in particular, provides yet another route to address timely open questions that go beyond the standard classification of these systems. The latter include the study of the interplay between topological protection and many-body interactions [87], which can be highly tuned in cold atom ensembles.

In this context, in this thesis we investigate novel interaction-induced topological insulators in one- and two-dimensional models. To this aim, we employ both analytical methods, as well as a numerical toolbox including mean-field approximations and state-of-the art tensor network methods, to simulate interacting models, characterize their topology, and put in evidence which are the differences of these systems compared to their noninteracting counterparts. In the spirit of quantum simulation, we also propose experimental setups, based on cold atoms in optical lattices, to realize each of the interacting models under consideration, and discuss prospects for the experimental detection of their topological properties.

High-T_c superconductors. The second topic of this thesis focuses on high-T_c superconductors [46, 47], that represents in itself a subfield of quantum mechanics, with both practical and fundamental applications. This area of research started in 1986 with the experiment of Ref. [88], which showed that the superconducting phase of a ceramic material of the cuprates family persisted until a critical temperature (T_c) of 35 K. Notice that the usual superconductivity, that is, the phenomenon of a vanishing electrical resistivity, was known since its experimental discovery in 1911 [89], but was limited to metals at extremely low temperatures close to the absolute zero. In this sense, the potential ability of high-T_c superconductors to conduct electric currents without losses at high temperatures makes them very valuable for the technological development of modern societies. To this aim, there is a quest in material science for room temperature superconductors, with exciting findings at high pressures [90–93]. From a more fundamental perspective, while the physical mechanism for normal superconductivity at low temperatures is well captured with the Bardeen-Cooper-Schrieffer (BCS) theory [94], it is not yet clear which is the physical mechanism that allows this phase to persist at high temperatures in some materials [46, 47]. The latter represents one of the most interdisciplinary and active experimental areas of research, in which state-of-the-art techniques are being used to gain physical insight about the high-T_c superconductivity of several systems. These include the use of light to excite lattice phonons and induce transient high-T_c superconductivity [22, 95–98], recent experiments on two-dimensional twisted-bilayer graphene [99, 100], or the use of the previously discussed cold atom quantum simulators to simulate the Fermi-Hubbard Hamiltonian [44, 101]. Such Hamiltonian model of interacting electrons on a lattice is thought to capture many of the properties of high-T_c superconductors, and it is currently the subject of many analytical and numerical studies. These studies focus on solving variants of this model in some limits and within some approximations, to understand which basic ingredients need to be incorporated on it for faithfully describing the complex phase diagram of high-T_c superconductors [46, 47], which apart from the superconducting phase also exhibits two other intriguing phases: the strange metal and the pseudogap phase.

In this thesis, we consider the effect of adding bond phonons in a Fermi-Hubbard model describing the cuprate family of high-T_c superconducting materials. More specifically, we study the relevance of such phonon degrees of freedom to explain some of the experimentally observed features in the pseudogap phase of these materials. Our numerical analysis is based on hybrid techniques combining both mean-field and exact diagonalization methods.

Quantum thermodynamics. Finally, the third topic of this thesis is quantum thermodynamics [102], a relatively young field born during this second quantum revolution, aimed at generalizing classical thermodynamics to the peculiarities of the microscopic quantum world. This challenging task has led to very interdisciplinary fundamental studies, including the quantum formulation of the thermodynamic laws [103, 104], the introduction of quantum fluctuation-dissipation theorems [105–109], the formulation of quantum thermodynamics from a quantum information perspective [110, 111], or the study of thermalization in closed quantum systems [112], initially motivated by its observation in isolated cold atom many-body ensembles [113–116]. From a practical perspective, quantum thermodynamics is also expected to be relevant in the miniaturization process of several devices. In this context, there has been a renewed interest during the last decades in the study of quantum thermodynamic machines [102], which were initially proposed around 1960 for quantum optical systems [117, 118], culminating with the recent experimental realization of a single-ion quantum heat engine [52]. Beyond the single-particle devices, several theoretical studies have also started to investigate the possibility to boost the performance of such thermodynamic machines by means of collective quantum effects [119–126] in many-body systems.

In this thesis, we focus on the study of quantum batteries, that is, quantum devices for energy storage and delivery, for which it is believed that many-body quantum entanglement can lead to a quantum advantage. First, we take a quantum geometrical approach to analyze the relation between entanglement and charging power in quantum batteries from a general point of view. Second, we use analytical and exact diagonalization methods to analyze particular models of quantum batteries.

Contents

This thesis is divided in three parts. Part I contains the first three preliminary Chapters 1-3, that review some physical concepts and numerical tools that will be recurrent through this thesis. Part II is devoted to the first topic of the thesis, topological phases of matter, with a focus on the study of interaction-induced topological insulators in one (Chapter 4) and two (Chapters 5-7) dimensions, and their simulation with cold atoms in optical lattices. Part III includes the study of microscopic models to explain many-body quantum phenomena, relevant to the two other topics of the thesis; the high-T_c superconductors, studied in Chapter 8, focusing on the pseudogap phase of these materials, and quantum thermodynamics, the topic of Chapter 9, in which we investigate collective effects in quantum batteries. Below we summarize the contents of each of the chapters of the thesis.

Part I

In Chapter 1, we discuss three different variational methods that are used through this thesis as a toolbox to describe strongly-correlated quantum systems. These are the Hartree-Fock (HF) method for fermionic Gaussian states, the configuration-interaction method, and the density matrix renormalization group (DMRG) using a matrix product state (MPS) representation of the quantum state.

In Chapter 2, we discuss the notion of topology in physics by giving an historical overview of the most important topological phases of matter and its classification.

We also discuss two paradigmatic physical models realizing a topological phase in one and two dimensions.

In Chapter 3, we review some basic aspects of cold atoms experiments, including the use of optical lattices, the control over many-body Hamiltonian terms, and techniques for state manipulation and detection of these systems.

Part II

In Chapter 4, we study a one-dimensional fermionic chain in which frustrated interactions induce a topological phase, the bond order wave (BOW) phase. We characterize the topology of the system and propose the realization of the physical model with dipolar magnetic atoms loaded in an optical lattice. This chapter is based on the original work of Ref. [4].

In Chapter 5, we start by reviewing the appearance of the two-dimensional topological Mott insulator (TMI), induced by fermionic interactions that spontaneously break time-reversal symmetry. In particular, we focus on the appearance of this phase in a two-dimensional checkerboard lattice of interacting spinless fermions at the mean-field level, by means of a HF decoupling of the interactions. We then present an in-depth analysis of the realization of the model with Rydberg-dressed atoms in an optical lattice. This chapter is based on the original work of Ref. [5].

In Chapter 6, we show that the TMI can exhibit rich spatial features intertwined with the topological nature of the system, owing to the interaction-induced origin of this phase. In particular, we show the appearance of self-trapped polarons and domain wall solutions separating bulks with opposite topological invariants. The latter exotic many-body states are the ground state of the model when considering particle numbers incommensurate with the number of lattice unit cells. This chapter is based on the original work of Ref. [3].

In Chapter 7, we analyze the TMI in a cylinder geometry, which allows us to treat the system beyond the mean-field approximation with the DMRG algorithm in its MPS formulation. We confirm the mean-field results of the previous chapters, and we also generalize well-established methods to compute the topological invariant of an MPS to situations in which the system exhibits domains with opposite topological invariants. Furthermore, we use the MPS representation to discuss prospects for preparing the topological phase of the model and measure its topological invariant.

Part III

In Chapter 8, we study an electron-phonon model used to describe the two-dimensional CuO_2 planes of cuprate high-T_c superconductors. In particular, we focus on the pseudogap phase of this model, from which the superconducting phase arises when lowering the temperature. We first show that the pseudogap phase proposed for the original model is unstable towards phase separation. Then, we show that, by including minimal electronic correlations to the model, one can recover many of the pseudogap features observed in experiment. This chapter is based on the original work of Ref. [2].

In Chapter 9, we study the fundamental limitations that quantum mechanics imposes to the charging power of quantum systems acting as quantum batteries. We introduce a novel bound on the power of a quantum battery that allows one to quantify the role of quantum entanglement in a charging process. In the light of this newly introduced bound, we analyze several models proposed in the literature for a quantum-enhanced power (the so-called quantum speedup), and some other novel

models that could also be considered for the realization of a quantum battery. This chapter is based on the original work of Ref. [1].

Part I

Preliminaries

Chapter 1

Variational methods for strongly-correlated quantum systems

The development of efficient classical algorithms to compute the equilibrium state of a quantum many-body system is one of the biggest challenges of modern physics. The problem can be defined by introducing a quantum many-body Hamiltonian

$$\hat{H} = \hat{H}_0 + \hat{H}_{\text{int}}, \tag{1.1}$$

where $\hat{H}_0$ is a Hamiltonian describing the noninteracting dynamics of L individual constituents[1], which are typically quantum spins, fermions, or bosons, and $\hat{H}_{\text{int}}$ contains many-body interactions between them.

Usually, one assumes that $\hat{H}_0$ is easy to solve and its eigenstates and eigenenergies are known. The goal is then to find the many-body eigenstates and eigenenergies of the total Hamiltonian satisfying

$$\hat{H} \left|E_i\right\rangle = E_i \left|E_i\right\rangle, \tag{1.2}$$

or, in most of the cases, only the ground state $\left|g\right\rangle$ satisfying

$$\hat{H} \left|g\right\rangle = E_g \left|g\right\rangle, \quad E_g = \min_i(E_i), \tag{1.3}$$

which allows one to compute physically relevant expectation values of many-body operators $\hat{O}$ at zero temperature

$$\left\langle \hat{O} \right\rangle_g = \left\langle g\right| \hat{O} \left|g\right\rangle. \tag{1.4}$$

For moderate system sizes such exact approach is feasible, and there are efficient methods, such as the Lanczos algorithm [127], to find the low energy states of Hamiltonians with a sparse matrix structure (e.g., those containing only short-range interactions). This exact approach is useful to benchmark the accuracy of approximated methods in small systems, as in Chapter 8 of this thesis.

However, the fundamental difficulty lies in the exponential increase of the Hilbert space $\mathcal{H}$ of $\hat{H}$ with the number of particles L, which prevents the exact diagonalization approach for large system sizes in classical computers. In these cases, one can still use variational methods that impose numerical constraints to the coefficients of the many-body quantum wavefunction, such that the dimension of the resulting effective Hilbert space $\mathcal{H}_r$ does not scale exponentially with the system size. The latter

[1] Notice that throughout this thesis we only consider discrete systems.

allows one to find a variational ground state $|\tilde{g}\rangle$ satisfying

$$\langle\tilde{g}|\,\hat{H}\,|\tilde{g}\rangle = \min_{\mathcal{H}_r} \langle\Psi|\,\hat{H}\,|\Psi\rangle\,, \tag{1.5}$$

and gives an upper bound to the ground state energy of the system $\langle\tilde{g}|\,\hat{H}\,|\tilde{g}\rangle \geq E_g$.

In this first preliminary chapter, we outline some of the most common variational methods, which will be used through this thesis in a wide variety of contexts. In Section 1.1, we discuss the set of fermionic Gaussian states and its relevance for solving interacting fermionic problems in mean-field approximation after a HF decoupling. In Section 1.2, we review the configuration-interaction method, which can be used to improve the HF method by including further quantum fluctuations. Finally, Section 1.3 is devoted to the use of tensor networks as variational ansatzes for many-body fermionic ground states. In particular, we focus on the use of the MPS representation and the DMRG algorithm.

1.1 Fermionic Gaussian states and mean-field methods

The set of fermionic Gaussian states [128] is one of the most used variational subspaces when dealing with many-body fermionic problems. To define them, let us consider the second quantized fermionic creation (anhiliation) operators $\hat{c}_i^\dagger$ ($\hat{c}_i$) of L independent fermionic modes i. The latter satisfy the fermionic anticommutation rules $\{\hat{c}_i, \hat{c}_j^\dagger\} = \delta_{ij}$ and $\{\hat{c}_i, \hat{c}_i\} = 0$. Fermionic Gaussian states are those states which are fully specified by the expectation value of their two-body correlators, i.e., the expectation values $\langle\hat{c}_i^\dagger\hat{c}_j\rangle$ and $\langle\hat{c}_i^\dagger\hat{c}_j^\dagger\rangle$ for all $i, j \in (1, \ldots, L)$.

These states are of big importance in physics, as they are the ground state of any fermionic Hamiltonian involving only quadratic terms in the creation and annihilation operators [128]. For more general situations, in which they can only be used as a variational ansatz, they can also capture many interacting phenomena. For instance, they are used in the BCS theory [94] of superconductivity to capture the pairing mechanism and compute the superconducting gap, and they can qualitatively reproduce complex magnetic orders in the doped two-dimensional Fermi-Hubbard model [129].

The intuitive reason why fermionic Gaussian states are also a good approximation to these interacting systems is the fact that, in many situations, complex interacting fermionic Hamiltonians can be brought to a quadratic form by means of some mean-field approximation for the interaction terms. In particular, here we will review the widely used HF mean-field decoupling. Before arriving to that, let us first show how to find the fermionic Gaussian state corresponding to the ground state of a quadratic fermionic Hamiltonian.

1.1.1 Quadratic fermionic Hamiltonians

Here we consider fermionic lattice Hamiltonians involving only quadratic terms in fermionic operators [128, 130], which have the form

$$\hat{H} = \sum_{i=1}^{L} \beta_i \hat{c}_i^\dagger \hat{c}_i + \sum_{ij} t_{ij} \hat{c}_i^\dagger \hat{c}_j. \tag{1.6}$$

Notice that, we do not include the pairing terms $\hat{c}_i^\dagger\hat{c}_j^\dagger$ and $\hat{c}_i\hat{c}_j$, which do not conserve the fermionic particle number, as they will not appear through this thesis. Such

Hamiltonian can be written in a compact form

$$\hat{H} = \Psi^\dagger M \Psi, \tag{1.7}$$

where $\Psi \equiv (\hat{c}_1,\ \hat{c}_2,\ \ldots, \hat{c}_{L-1},\ \hat{c}_L)^T$ is a column vector containing all the fermionic anhiliation operators, and M is an $L \times L$ hermitian matrix which encodes the Hamiltonian. Now, we introduce an $L \times L$ unitary matrix U and insert it in Eq. (1.7)

$$\hat{H} = \Psi^\dagger U^\dagger U M U^\dagger U \Psi. \tag{1.8}$$

The many-body problem can then be solved by choosing the unitary matrix U that brings M into a diagonal form, i.e., $UMU^\dagger = D$ with $D_{ij} = \varepsilon_i \delta_{ij}$. Importantly, the transformation U preserves the fermionic anticommutation relations, such that we can define a new set of fermionic operators $\Phi \equiv (\hat{f}_1,\ \hat{f}_2,\ \ldots, \hat{f}_{L-1},\ \hat{f}_L)^T = U\Psi$. The latter is called a fermionic Bogoliubov transformation. The Hamiltonian in terms of these transformed fermionic modes, usually known as the Bogoliubov modes, has the simple form

$$\hat{H} = \Phi^\dagger D \Phi = \sum_{i=1}^{L} \varepsilon_i \hat{f}_i^\dagger \hat{f}_i, \tag{1.9}$$

and the quantum many-body problem is reduced to a collection of independent fermionic particles. Notice that the diagonalization here involves a matrix scaling linearly with the system size and not exponentially, as in the general case. Moreover, in systems with translational invariance, an extra Fourier transformation can be applied to the fermionic modes to bring the M matrix into a block form, which facilitates even more the diagonalization.

Finally, in the equilibrium state at temperature T, the occupation number of the Bogoliubov modes is given by the Fermi distribution

$$\left\langle \hat{f}_i^\dagger \hat{f}_j \right\rangle = \delta_{ij} f(\varepsilon_i, \mu, T) = \frac{\delta_{ij}}{1 + \exp[(\varepsilon_i - \mu)/k_B T]}, \tag{1.10}$$

where μ is the chemical potential that is used to fix the total particle number through the condition $\sum_i f(\varepsilon_i, \mu, T) = N$.

The many-problem is then already solved, as the equilibirum states of quadratic fermionic Hamiltonians are Gaussian fermionic states [128], and are thus fully specified by such two-operator correlators. Furthermore, notice that any expectation value in the original fermionic modes can be computed using Eq. (1.10) together with the Bogoliubov transformation U.

1.1.2 Hartree-Fock decoupling

While the Bogoliubov transformation is a powerful analytical tool to solve quadratic fermionic Hamiltonians, typical fermionic systems contain interactions involving four fermionic operators. For instance, in this thesis we will mostly work with repulsive density-density interactions giving rise to Hamiltonians of the form

$$\hat{H} = \sum_{i=1}^{L} \beta_i \hat{n}_i + \sum_{ij} (t_{ij} \hat{c}_i^\dagger \hat{c}_j + v_{ij} \hat{n}_i \hat{n}_j), \tag{1.11}$$

where $\hat{n}_i \equiv \hat{c}_i^\dagger \hat{c}_i$ is the fermion number operator at site i. In this case, the quartic term in fermionic operators does not allow to express the Hamiltonian in the form of

Eq. (1.7). One common approach is to perform the following mean-field decoupling of such term

$$\hat{n}_i\hat{n}_j \simeq \bar{n}_i\hat{n}_j + \bar{n}_j\hat{n}_i - \bar{n}_i\bar{n}_j - \xi_{ij}\hat{c}_j^\dagger\hat{c}_i - \xi_{ij}^*\hat{c}_i^\dagger\hat{c}_j + \left|\xi_{ij}\right|^2, \tag{1.12}$$

where $\xi_{ij} \equiv \langle\hat{c}_i^\dagger\hat{c}_j\rangle$ and $\bar{n}_i \equiv \langle\hat{n}_i\rangle$ are the expectation values in the equilibrium fermionic state. Within this approximation, know as the HF method [130], the Hamiltonian of the system is brought to a quadratic form, the HF Hamiltonian

$$\hat{H}_{\mathrm{HF}}(\bar{n},\xi) = \sum_{i=1}^{L}[\beta_i + \sum_j (v_{ij}\bar{n}_j)]\hat{n}_i + \sum_{ij}\left[(t_{ij} - v_{ij}\xi_{ij}^*)\hat{c}_i^\dagger\hat{c}_j + v_{ij}(\left|\xi_{ij}\right|^2 - \bar{n}_i\bar{n}_j)\right], \tag{1.13}$$

which can be easily diagonalized following the procedure described above. While the HF ansatz retains some quantum fluctuations, it represents an approximation to the true ground state within the subspace of fermionic Gaussian states, and its accuracy needs to be considered in every particular case. Furthermore, notice that $\hat{H}_{\mathrm{HF}}(\bar{n},\xi)$ depends on the expectation values at equilibrium, which have to be found with a self-consistent loop. That is, one starts from an ansatz for the HF values $\bar{n}_i^0$ and ξ_{ij}^0, and finds the fermionic state at filling n and temperature T of the corresponding initial HF Hamiltonian. From this equilibrium state, one computes the new HF values $\bar{n}_i^1$ and ξ_{ij}^1 and performs the loop again until self-consistency of the HF values is achieved. Notice that the final HF solution corresponds to a noninteracting system of fermions, with effectively renormalized Hamiltonian parameters due to the presence of interactions.

Despite the apparent simplicity of the HF method, it is worth mentioning some subtleties of its practical numerical implementation. First, one typically imposes some constrains to reduce the number of HF parameters. For instance, usually one assumes translational invariance within a given unit cell, known as the restricted Hartree-Fock (RHF) method, in contrast to the more general unrestricted Hartree-Fock (UHF) method [131, 132]. Alternatively, one might be interested in states which spontaneously break certain symmetries of the Hamiltonian. In this latter case it is crucial to start with a HF ansatz that already breaks such symmetries. Second, in order to avoid oscillating pseudo solutions of the algorithm, sometimes there is the need of a progressive update of the HF parameters

$$\langle\cdot\rangle_{i+1} = (1-\eta)\langle\cdot\rangle_i + \eta\langle\cdot\rangle_i^{\mathrm{new}}. \tag{1.14}$$

Here $\langle\cdot\rangle_i$ represents some HF parameter at the ith iteration, and $\langle\cdot\rangle_i^{\mathrm{new}}$ its new value after performing one iteration step. The update parameter η lies in the interval $(0,1]$. Third, the algorithm can lead to a metastable solution, and it is therefore very important to compare the Free energies of different converged solutions. The latter can be expressed as

$$F_{\mathrm{HF}} = \sum_i \left\{ \frac{\mu}{1+\exp\left(\frac{\epsilon_i-\mu}{k_{\mathrm{B}}T}\right)} - k_{\mathrm{B}}T\ln\left[\exp\left(-\frac{\epsilon_i-\mu}{k_{\mathrm{B}}T}\right)+1\right]\right\} + C, \tag{1.15}$$

where ϵ_i are the single-particle HF energies and C is the scalar term appearing from the HF decoupling in Eq. (1.12). A final remark is that, for concreteness, in this section we introduced the self-consistent loop for the HF Hamiltonian of spinless fermions of Eq. (1.11), which is used in Chapters 5-6. However, such procedure can be easily extended to the spinful case, or to determine the equilibrium state of

any quadratic fermionic Hamiltonian $H^q(\vec{x})$ that depends on some set of dynamical variables $\vec{x}$, related to another classical or quantum system easy to solve, such as the semi-classical phonons described in Chapter 8.

1.2 Configuration-interaction method

The configuration-interaction method is widely used in quantum chemistry [133] to improve HF energy calculations of electronic orbitals. The basic idea is to hybridize low-energy HF solutions in order to lower the HF ground state energy. The latter procedure can also be used in fermionic lattice systems [134–136] to improve the HF solution obtained with the self-consistency loop described above. For instance, when working with particle numbers which are incommensurate with the number of unit cells of a lattice, one typically encounters a huge number of degenerate localized solutions which spontaneously break translational invariance, and which depend on the initial conditions for the HF parameters. Notice that there is no guarantee that such states are orthogonal, which means that by superposing them one could obtain a translational invariant state with lower energy than the HF solution, due to the fact that further quantum fluctuations would be taken into account in the superposition.

More specifically, one first obtains a set $\{|\Psi_j(N)\rangle\}$ of degenerate HF solutions with a fixed number of particles N. In the many-body basis, each of the solutions is given by the Slater determinant (SD) of the occupied single-particle HF states. Then, one uses the variational ansatz

$$|\chi(N)\rangle = \sum_j \alpha_j |\Psi_j(N)\rangle , \tag{1.16}$$

to minimize the energy of the system. Notice again that the many-body wavefunctions $\{|\Psi_j(N)\rangle\}$ are not orthogonal. The overlap matrix between two SDs is given by [137]

$$S_{ij} \equiv \langle \Psi_i | \Psi_j \rangle = \begin{vmatrix} \langle \psi_1^i | \psi_1^j \rangle & \dots & \langle \psi_1^i | \psi_N^j \rangle \\ \vdots & \ddots & \vdots \\ \langle \psi_N^i | \psi_1^j \rangle & \dots & \langle \psi_N^i | \psi_N^j \rangle \end{vmatrix} , \tag{1.17}$$

where $|\psi_k^i\rangle$ is the k-th single-particle state of the i-th HF solution. The biggest numerical cost of the configuration-interaction method is to compute the matrix elements $H_{ij} = \langle \Psi_i | H | \Psi_j \rangle$ of the Hamiltonian (1.11). We first split it in the kinetic (hopping) term T and the interaction term V:

$$H = T + V . \tag{1.18}$$

The matrix elements corresponding to T, which are quadratic in fermionic operators, are then given by

$$T_{ij} = \begin{vmatrix} \langle \psi_1^i | T | \psi_1^j \rangle & \dots & \langle \psi_1^i | \psi_N^j \rangle \\ \vdots & \ddots & \vdots \\ \langle \psi_N^i | T | \psi_1^j \rangle & \dots & \langle \psi_N^i | \psi_N^j \rangle \end{vmatrix} + \dots + \begin{vmatrix} \langle \psi_1^i | \psi_1^j \rangle & \dots & \langle \psi_1^i | T | \psi_N^j \rangle \\ \vdots & \ddots & \vdots \\ \langle \psi_N^i \psi_1^j \rangle & \dots & \langle \psi_N^i | T | \psi_N^j \rangle \end{vmatrix} . \tag{1.19}$$

On the other hand, V contains two-body terms of the form $\hat{n}_k\hat{n}_l$, whose matrix elements read

$$\langle\Psi_i|\, n_k n_l \,|\Psi_j\rangle = \begin{vmatrix} \langle\psi_1^i|\, n_k \,|\psi_1^j\rangle & \langle\psi_1^i|\, n_l \,|\psi_2^j\rangle & \dots & \langle\psi_1^i|\psi_N^j\rangle \\ \vdots & \ddots & \dots & \vdots \\ \langle\psi_N^i|\, n_k \,|\psi_1^j\rangle & \langle\psi_N^i|\, n_l \,|\psi_1^j\rangle & \dots & \langle\psi_N^i|\psi_N^j\rangle \end{vmatrix} + \text{permutations.} \tag{1.20}$$

Once H is computed, it has to be diagonalized, taking into account that we are working in a non-orthogonal basis. That is, we want to find the energies ε and eigenvectors $\vec{\alpha}$ satisfying

$$(H - \varepsilon S)\vec{\alpha} = 0 \tag{1.21}$$

To find the energies of the system in this non-orthogonal basis we proceed as follows:

1. Diagonalize S, as $\sigma = D^\dagger S D$. Notice that $\sigma \geq 0$ due to the fact that S is an overlap matrix. A zero eigenvalue indicates that one of the Φ_j is a linear combination of the others, and should be removed from the set.
2. Construct $A_{ij} = D_{ij}/\sqrt{\sigma}$. This means that $A^\dagger S A = I$.
3. By defining $A\vec{\alpha} \equiv \vec{c}$, and $\tilde{H} \equiv A^\dagger H A$, the eigenvalue problem has the standard form $(\tilde{H} - \varepsilon)\vec{c} = 0$.

1.3 Tensor Networks

Tensor network approaches [138] are one of the most fruitful numerical techniques to study correlated quantum systems. The main idea is to find an efficient numerical representation of the quantum wave function by taking advantage of the entanglement structure of physical quantum states, and construct efficient numerical algorithms to find such states (e.g, the ground state) within this representation. The success of these techniques lies in the fact that they can capture high order quantum correlations which are absent in the HF ansatz or other mean-field approaches, the limitations imposed by the system size are not as dramatic as in exact diagonalization, and they lack fermionic sign problems typical of quantum Monte Carlo techniques.

In Chapters 4 and 7 of this thesis we focus on the DMRG method introduced by White [139] to find the ground state of several strongly-correlated fermionic models, in one and two dimensions, in the modern representation MPS [140, 141]. In particular, we have used its implementation in the TENPY [142] library in PYTHON, and in the ITENSOR library in C++ [143]. While there are currently extensive reviews in the literature [141], below we outline both the MPS representation and DMRG algorithm, emphasizing those aspects which are of particular interest for this thesis.

Matrix product states and operators

Let us first consider one-dimensional discrete systems of L sites for which the local Hilbert space associated to each site n is d-dimensional and is represented by the

set of orthogonal states $\{|i_n\rangle\}$, with $i = 1, \ldots, d$. The general wavefunction for this system reads

$$|\Psi\rangle = \sum_{i_1,\ldots,i_L=1}^{d} c_{i_1,\ldots,i_L} |i_1, \ldots, i_L\rangle , \tag{1.22}$$

and one needs d^L independent complex coefficients $c_{i_1,\ldots,i_L}$ (up to the normalization constraint) to describe the wave function.

Alternatively, in the MPS representation [140, 144] one writes the wavefunction as

$$|\Psi\rangle = \sum_{i_1,\ldots,i_L=1}^{d} M^{i_1} \ldots M^{i_L} |i_1, \ldots, i_L\rangle , \tag{1.23}$$

where M^{i_n} are $\chi \times \chi$ tensors except for the first (last) sites, in which its dimension is $1 \times \chi$ ($\chi \times 1$). The number χ is called the bond dimension of the MPS and controls the size of the subspace spanned within this representation, whose number of independent coefficients scales as $\mathcal{O}(Ld\chi^2)$.

Importantly, by writing the global wave function through local building blocks (the tensors M^{i_n}), one can control the amount of entanglement in the MPS hierarchically. In particular, the entanglement entropy of a segment of length l depends only on the bond dimension $S(l) \sim \mathcal{O}(\chi)$ [141, 145]. For D spatial dimensions the entanglement entropy for a subregion with linear dimension l of a generic quantum state scales as $S(l) \sim \mathcal{O}(l^D)$ (volume law) [146]. However, it is well known that for gapped ground states of local Hamiltonians the scaling is $S(l) \sim \mathcal{O}(l^{D-1})$ (area law) [145]. In the one-dimensional case, this gives a scaling of the entanglement entropy independent of the segment size l, meaning that for open boundary conditions an MPS with a fixed bond dimension χ can faithfully represent such ground states [147, 148]. Furthermore, the required χ can be reduced in practice by exploiting Hamiltonian symmetries, e.g., particle number conservation, which can be incorporated in the MPS representation [142, 143, 149–152].

Finally, one also needs to express quantum operators, e.g., the Hamiltonian, as matrix product operators, which have the form [153]

$$\hat{H} = \sum_{i_1,\ldots,i_L,i'_1,\ldots,i'_L=1}^{d} W^{i_1,i'_1} \ldots W^{i_L,i'_L} |i_1, \ldots, i_L\rangle \langle i'_1, \ldots, i'_L| . \tag{1.24}$$

It is worth noticing that for most one-dimensional Hamiltonians that are a sum of local terms, the matrix product operator representation is exact for small matrix dimensions of the W^{i_n,i'_n} tensors [148].

A final remark is that in this thesis we focus on fermionic systems exhibiting nonlocal anticommutation rules, which might seem incompatible with the local nature of the MPS representation. However, notice that fermionic chains can be mapped to spin chains through the Jordan-Wigner transformation [154, 155], and local or quasi-local operators in the fermionic chain retain its character in the spin representation.

1.3.1 Density matrix renormalization group

The ground state search within the MPS subspace can be cast into an optimization problem where one is interested in finding the extremum of

$$\langle\Psi| \hat{H} |\Psi\rangle - \lambda \langle\Psi|\Psi\rangle \tag{1.25}$$

in the presence of the Lagrange multiplier λ that ensures the normalization of the MPS. While this is a highly nonlinear problem in the space of all the M^{i_n} tensors representing the MPS, in the DMRG method [139, 141] one performs local optimization sweeps of the MPS from left to right and vice versa, allowing to find the global ground state of the system efficiently. At each step, only one M^{i_n} is optimized, leading to a linear optimization problem that can be efficiently solved by means of standard techniques such as the Lanczos algorithm. As in many other variational approaches, such as the HF method outlined above, when applying the DMRG method there are severeal numerical tricks to avoid getting stucked in local minima, such as choosing an appropriate initial MPS, or including noise terms in the Hamiltonian in the first sweeps of the algorithm. To ensure the convergence of the algorithm it is also crucial to check the evolution of the ground state energy, entropy, and local order parameters, as a function of the bond dimension χ. Another useful quantity to estimate the level of accuracy of the MPS in the DMRG procedure is the truncation error E_{trunc}, which is defined as the weight of the states discarded by truncating the MPS at a bond dimension χ.

Finally, so far we have focused on finite systems with open boundary conditions, but the MPS and the DMRG algorithm also provide a route to access the thermodynamic limit of the bulk by assuming translational invariance of a certain unit cell of M^{i_n} tensors. In this case, the infinite-size variant of the DMRG method (iDMRG) [141] starts with a small system size of the MPS and at each optimization step grows the MPS by one unit cell. A fixed point is achieved when the inserted unit cell does not vary with the iteration step, and this is taken as the unit cell of the infinite MPS (iMPS) in the thermodynamic limit, from which all the relevant quantities can be extracted.

1.3.2 Two-dimensional algorithm

Despite the one-dimensional nature of the sweep-based optimization, the DMRG method has been shown to be also useful for state-of-the-art numerical studies of complex two-dimensional systems in ladder or cylinder geometries with a finite width [156]. For instance, spin models exhibiting topological order [157], or Hubbard models in the context of high-Tc superconductors [158, 159], chiral spin liquids [160], and topological Mott insulators [161–163].

In this case, the two-dimensional lattice is mapped to a one-dimensional chain in a snake-like folding, and the standard DMRG algorithm is applied [156]. Such folding implies that short-range Hamiltonian terms in the two-dimensional lattice become long-range in the one-dimensional chain, leading to Hamiltonians with larger matrix product operator dimensions. Furthermore, the two-dimensional case lacks an area law independent of the system size as in the one-dimensional case, and the bond dimension needed to accurately describe such systems with MPS scales exponentially with respect to the ladder and cylinders widths. Still, the two-dimensional DMRG allows one to access widths of the order of $\gtrsim 10$ sites [156] in long cylinders and ladders with many more sites in total than in any exact diagonalization simulation, and it lacks the sign problem of quantum Monte Carlo techniques.

Chapter 2

Topological phases of matter

The complexity of our surrounding world manifests itself in the wide variety of phases observed in Nature, which can be as diverse as, for instance, an Ising ferromagnet [164–169] or a Bose-Einstein condensate [170, 171]. From a physical perspective, it is thus crucial to establish a general framework that allows one to distinguish and classify this plethora of phases. In this context, the Landau-Ginzburg-Wilson theory of phase transitions [56, 57] represents one of the most fruitful approaches both in the classical and quantum regimes. According to this paradigm, the classification of phases of matter is based on the symmetries that they break, which in turn lead to the presence of local order parameters characteristic of each phase. The two examples mentioned above fall within this paradigm: the Ising ferromagnet is characterized by the spontaneous breaking of the $\mathbb{Z}_2$ spin discrete rotational symmetry and the presence of a local net magnetization, while in a Bose-Einstein condensate there is a spontaneous breaking of the $U(1)$ symmetry, and the order parameter is given by the value of the real-space wavefunction.

Topological phases of matter [51, 64] are exotic states that escape this classification based on broken symmetries and local order parameters, and are instead characterized by a global order parameter, the topological invariant. In mathematics, topological invariants characterize those global properties that are robust against smooth deformations of a manifold, the typical example being the number of holes of an object. In this preliminary chapter, we show that such topological invariants also appear in the description of several physical systems, and can be used to classify them beyond the Landau-Ginzburg-Wilson paradigm. We start with an historical review of topological phases of matter. In Section 2.1, we explain the discovery of the IQHE in 1980. Then, in Section 2.2 we describe the modern classification of topological phases, and in Section 2.3 we give an outline of recently discovered systems that escape such modern classification. In Section 2.4, we come to two paradigmatic models of noninteracting topological insulators, to provide with background for the more complex interacting models considered in this thesis.

2.1 Integer quantum Hall effect

The IQHE is arguably one of the most relevant physical discoveries of the last century. In 1980, Von Klitzing and coauthors discovered that, when a two-dimensional system of electrons at low temperature is subjected to a strong perpendicular magnetic field, the measured transverse conductivity (Hall conductivity) exhibits plateaus as a function of the applied magnetic field that take quantized values [54]

$$\sigma_{\mathrm{H}} = \frac{e^2}{h}\nu, \qquad (\nu \in \mathbb{Z}), \tag{2.1}$$

independently of local perturbations such as disorder or material imperfections. This universality and robustness of the quantized Hall conductivity was theoretically explained only two years after its experimental discovery by Thouless, Kohmoto, Nightingale, and den Nijs (TKNN) [55], who wrote the Hall conductivity in terms of the Berry phase, i.e., the local curvature of the electronic Bloch bands

$$\sigma_{\mathrm{H}} = \frac{e^2}{h} \sum_{n \leq N} \frac{i}{2\pi} \int_{\mathrm{BZ}} d^2\mathbf{k} \left(\left\langle \partial_{k_x} u_n(\mathbf{k}) \middle| \partial_{k_y} u_n(\mathbf{k}) \right\rangle - \left\langle \partial_{k_y} u_n(\mathbf{k}) \middle| \partial_{k_x} u_n(\mathbf{k}) \right\rangle \right), \tag{2.2}$$

where $|u_n(\mathbf{k})\rangle$ is the Bloch band corresponding to the n-th Landau level, and the sum is performed over the N filled Landau levels. The quantization of the Hall conductivity comes from the fact that, when integrated over the Brillouin zone, the Berry curvature of each filled band is equal to the Chern number ν_n of that band, a topological invariant which is quantized to integer values [55]. Therefore, the integer appearing in the expression (2.1) for the Hall conductivity is the total Chern number of the N populated bands in the presence of an energy gap at the Fermi energy

$$\nu \equiv \sum_{n \leq N} \nu_n. \tag{2.3}$$

Being a sum of topological invariants, ν does not change with smooth deformations of the bands caused by disorder or imperfections, as long as the gap remains open, which explains the robustness of the observed quantization in the Hall conductivity. According to the TKNN formula in Eq. (2.3), the transition between the phase with $\sigma_{\mathrm{H}}(\nu)$ and $\sigma_{\mathrm{H}}(\nu+1)$ occurs at the critical value of the magnetic field where the lowest unoccupied Landau level falls below the chemical potential and gets occupied. Notice that this is in stark contrast with the conventional Landau-Ginzburg-Wilson theory of phase transitions, based on SSB and local order parameters [56, 57].

2.2 Periodic table of topological insulators

The IQHE and its topological origin, explained in terms of the TKNN formula, opened the field of topological phases of matter, which has been very active ever since. In 1988, Haldane [78] showed that the fundamental origin of the IQHE is not the presence of an external magnetic field, but rather the breaking of time-reversal symmetry, giving rise to the notion of a quantum anomalous Hall (QAH) effect. The Haldane model, outlined in Section 2.4.2, represented the first instance of a topological Chern insulator, which have been later generalized to systems with other broken symmetries, or even without any broken symmetry, such as the quantum spin Hall effect [59].

A major step towards a general classification of this plethora of topological phases of matter was achieved with the introduction of the periodic table of topological insulators and superconductors [62–64], shown in Table 2.1. This table contains all the possible topological phases of gapped Hamiltonians of d-dimensional systems in the absence of interactions, in terms of their behavior under time-reversal (T), particle-hole (C) and chiral (S) symmetries. That is, each nonzero entry of the table corresponds to the existence of a nontrivial topological phase and gives the nature of the topological invariant. As an example, the QAH effect exhibited by the Haldane model belongs to the class A, which does not require any symmetry, and is characterized by a $\mathbb{Z}$ topological invariant, the Chern number.

TABLE 2.1: Periodic table of topological insulators and superconductors [63].

class \ d	T	C	S	0	1	2	3	4	5	6	7
A	0	0	0	$\mathbb{Z}$	0	$\mathbb{Z}$	0	$\mathbb{Z}$	0	$\mathbb{Z}$	0
AIII	0	0	1	0	$\mathbb{Z}$	0	$\mathbb{Z}$	0	$\mathbb{Z}$	0	$\mathbb{Z}$
AI	+	0	0	$\mathbb{Z}$	0	0	0	$2\mathbb{Z}$	0	$\mathbb{Z}_2$	$\mathbb{Z}_2$
BDI	+	+	1	$\mathbb{Z}_2$	$\mathbb{Z}$	0	0	0	$2\mathbb{Z}$	0	$\mathbb{Z}_2$
D	0	+	0	$\mathbb{Z}_2$	$\mathbb{Z}_2$	$\mathbb{Z}$	0	0	0	$2\mathbb{Z}$	0
DIII	-	+	1	0	$\mathbb{Z}_2$	$\mathbb{Z}_2$	$\mathbb{Z}$	0	0	0	$2\mathbb{Z}$
AII	-	0	0	$2\mathbb{Z}$	0	$\mathbb{Z}_2$	$\mathbb{Z}_2$	$\mathbb{Z}$	0	0	0
CII	-	-	1	0	$2\mathbb{Z}$	0	$\mathbb{Z}_2$	$\mathbb{Z}_2$	$\mathbb{Z}$	0	0
C	0	-	0	0	0	$2\mathbb{Z}$	0	$\mathbb{Z}_2$	$\mathbb{Z}_2$	$\mathbb{Z}$	0
CI	+	-	1	0	0	0	$2\mathbb{Z}$	0	$\mathbb{Z}_2$	$\mathbb{Z}_2$	$\mathbb{Z}$

2.2.1 Bulk-edge correspondence

In many cases, the topological invariant, which is a bulk property, is related to the presence of edge modes localized at the boundaries of the topological system. This is known as the bulk-edge correspondence [53, 172], and leads to the notion of topologically protected surface states. They appear due to the change of the topological invariant at the interface between the topological bulk and the vacuum (or any other trivial insulator), which implies a local gap closing signalled by the appearance of such exponentially localized states inside the insulating gap.

2.3 Topological insulators beyond the periodic table

Notwithstanding the importance of the periodic table, there are many topological phases which escape this classification. For instance, there exist crystalline topological insulators [173] with spatial symmetries not included in Table 2.1, such as reflection symmetry, or Weyl semimetals [65], which exhibit topological properties despite its metallic nature. Furthermore, it has been shown that, in the presence of many-body interactions that preserve the protecting symmetries, some of the topological classes of Table 2.1 can be continuously connected to trivial ones without closing the gap [174]. This leads to the more general concept of symmetry-protected topological (SPT) phases [175–177], which are the ones that cannot be connected to trivial ones without a gap closing, even when including symmetry-preserving interactions, and thus go beyond the single-particle notion of topological protection. Even more surprisingly, there are some situations in which interactions generate the nontrivial topology through a SSB process [87]. The latter is the case for the BOW phase studied in Chapter 4, and the TMI considered in Chapters 5-7. In what follows, we review the main properties of their noninteracting counterparts in Table 2.1: the static SSH model (class BDI) and the Haldane model (class A).

2.4 Paradigmatic topological insulators

2.4.1 Su-Schrieffer-Heeger model

The static SSH model is one of the most paradigmatic models exhibiting a one-dimensional SPT phase belonging to the class BDI in Table 2.1. The original SSH Hamiltonian was introduced in the seminal work by these three authors [71] to

describe an organic compound, the polyacetylene chain, which exhibits an spontaneous dimerization due to the Peierls instability [178]. According to the Peierls instability, any equally spaced one-dimensional chain of fermions is unstable towards dimerization caused by lattice distortions (phonons) that open a gap in the fermionic band at half filling. This dimerization occurs through a SSB of the translational symmetry of the lattice, which undergoes a transition from a full translational invariance to a two-site unit cell translational invariance, while preserving the bond inversion and chiral (sublattice) symmetries. For each of the two spontaneous dimerizations at half filling (see Fig. 2.1), the fermionic system can be effectively described by the static version of the SSH Hamiltonian:

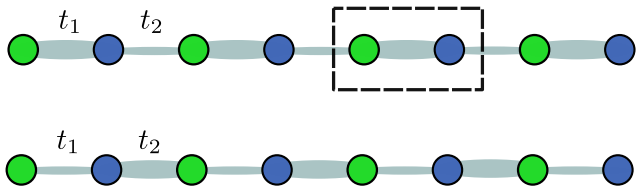

FIGURE 2.1: Sketch of the SSH model with alternate t_1 and t_2 hopping strengths. Here thick (thin) lines correspond to strong (weak) bonds.

$$\hat{H}_{\text{SSH}} = t_1 \sum_{i \text{ even}} (\hat{c}_i^\dagger \hat{c}_{i+1} + \text{H.c.}) + t_2 \sum_{i \text{ odd}} (\hat{c}_i^\dagger \hat{c}_{i+1} + \text{H.c.}), \tag{2.4}$$

where we consider $t_1, t_2 \geq 0$. Furthermore, we consider that in total there is an even number of sites L, and we label the i-th bond as the one connecting sites $(i, i+1)$, being $i = 0$ the first bond of the chain. As shown in Fig. 2.1, the system has a two-site unit cell, which we define in such a way that the intra-cell bonds are of type t_1. Notice that from Fig. 2.1 it is easy to see that the system is symmetric under the reflection with respect to the central bond. As discussed below, the regime with $t_1 > t_2$ corresponds to the trivial SSH chain, while for $t_1 < t_2$ the system realizes a SPT phase. Under periodic boundary conditions, the system exhibits two bands given by the eigenvalues of the k-space Hamiltonian matrix $H(\mathbf{k}) = \vec{h}(\mathbf{k}) \cdot \vec{\sigma}$ with

$$h_x = t_1 + t_2 \cos k, \;\; h_y = t_2 \sin k, \;\; h_z = 0, \tag{2.5}$$

and $\vec{\sigma}$ being the vector of Pauli matrices. Here the off-diagonal nature of the single-particle Hamiltonian in k-space reflects the chiral symmetry of the system:

$$\Gamma \vec{h}(k) \cdot \vec{\sigma} \Gamma^{-1} = -\vec{h}(k) \cdot \vec{\sigma}, \;\; \Gamma^2 = \mathbb{1}, \tag{2.6}$$

which is satisfied for the choice $\Gamma = \sigma_z$. The resulting single-particle band structure, depicted in Fig. 2.2(a), shows an insulating gap at half filling for $t_1 \neq t_2$. Due to full translational invariance under periodic boundary conditions, the two regimes are related by a simple single-site translation and thus there is no physical difference between them.

The situation changes under open boundary conditions, as shown in Figs. 2.2(b)-(c). For $t_1 < t_2$, there are zero-energy single-particle states inside the gap, which are exponentially localized at the borders. On the contrary, the regime with $t_1 > t_2$ does not exhibit nontrivial edge physics. While the presence of such localized states seems obvious in the limiting case $t_1 = 0$, as the end sites are completely decoupled from the rest of the bulk, these are in fact topological states that appear for any

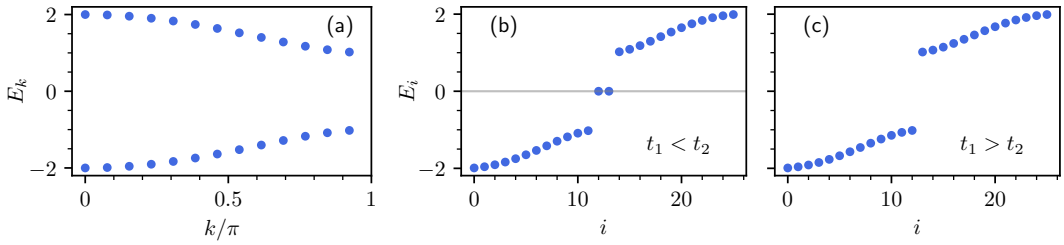

FIGURE 2.2: Band structure of the SSH model for (a) periodic boundary conditions, and (b)-(c) open boundary conditions for the two possible regimes of the model.

value $t_1 < t_2$ and are protected against perturbations that do not close the gap and preserve the chiral symmetry.

Winding number and the Zak phase

By virtue of the bulk-edge correspondence of SPT phases, the robustness of the zero-energy modes can be inferred by directly computing the winding number of the bulk, a well-defined topological invariant for such chiral-symmetric one-dimensional fermionic system. Being a bulk property, the winding number can be computed from the bulk band structure as

$$\nu = \frac{1}{2\pi}\int_{BZ} dk[\vec{n}(k)\times\partial_k\vec{n}(k)]_z \in \mathbb{Z},\ \vec{n}(k) \equiv \frac{\vec{h}(k)}{\left\|\vec{h}(k)\right\|}, \tag{2.7}$$

and takes the value $\nu = 1$ in the topological regime ($t_1 < t_2$) and $\nu = 0$ in the trivial one ($t_1 > t_2$). Moreover, notice that ν counts the number of edge states (per edge) in the case of open boundary conditions. Therefore, ν and the associated topologically protected edge states are robust against perturbations that respect the chiral symmetry and do not close the gap.

Finally, while the winding number is not restricted to the values 0 and 1, it is worth mentioning that for chiral-symmetric systems there is indeed a $\mathbb{Z}_2$ topological invariant, the Zak phase [179]

$$\phi_{\text{Zak}} = i\int_{\text{BZ}} \langle e_{k,-}|\,\partial_k\,|e_{k,-}\rangle\,, \tag{2.8}$$

where $|e_{k,-}\rangle$ represents the lower occupied band. The Zak phase is related to the winding number by $\phi_{\text{Zak}}/\pi = \nu(\text{mod}2)$ and it is in general much easier to compute. For instance, while Eq. (2.7) is gauge dependent, there are efficient gauge-invariant methods to compute $\mathbb{Z}_2$ invariants, such as the Wilson loop technique [180, 181].

2.4.2 Haldane model

In 1988, a few years after the discovery of the IQHE, Haldane proposed a two-dimensional lattice model [78] exhibiting a quantized Hall conductivity in the absence of a magnetic field, i.e., without Landau levels. He showed that the magnetic field is not the key ingredient to realize a quantum Hall effect, but rather breaking the time-reversal symmetry, leading to the notion of a QAH effect at zero magnetic field. The Haldane model, depicted in Fig. 2.3(a), consists of an hexagonal latttice of spinless fermions with real nearest-neighbor (NN) hopping amplitudes t_1, and complex next-nearest-neighbor (NNN) hopping amplitudes $t_2 e^{i\phi}$. These complex terms

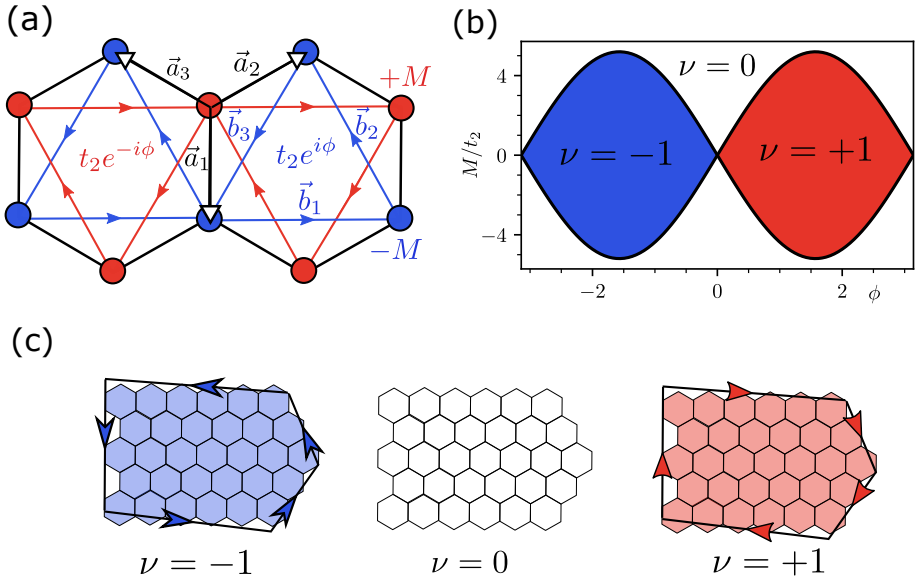

FIGURE 2.3: (a) Sketch of the Haldane model on the hexagonal lattice. (b) Phase diagram showing the value of the Chern number in the $\phi - M$ plane. (c) Sketch of the edge physics in the Haldane model with open boundary conditions. For nontrivial values of the Chern number $\nu = \pm 1$ the system exhibits topologically protected edge currents whose chirality is given by the sign of ν. Such states are absent in the trivial case $\nu = 0$.

break explicitly the time-reversal symmetry without inducing a net magnetic flux per unit cell, as the fluxes in the two sublattices have opposite signs. Moreover, the lattice is subject to a staggered on-site potential M with opposite sign on the red and blue sublattices. In k-space, the system is described by the single-particle Hamiltonian $H(\mathbf{k}) = \vec{h}(\mathbf{k}) \cdot \vec{\sigma}$ with

$$\begin{aligned} h_0 &= 2t_2 \cos\phi \sum_i \cos(\mathbf{k} \cdot \mathbf{b}_i), \\ h_x &= t_1 \sum_i \cos(\mathbf{k} \cdot \mathbf{a}_i), \\ h_y &= -t_1 \sum_i \sin(\mathbf{k} \cdot \mathbf{a}_i), \\ h_z &= M + 2t_2 \sin\phi \sum_i \sin(\mathbf{k} \cdot \mathbf{b}_i). \end{aligned} \tag{2.9}$$

At $M = 0$, the breaking of time-reversal symmetry induced by any complex $t_2 e^{i\phi}$ opens a topological gap at half filling, and the energy spectrum is split into a lower and upper band. On the contrary, for dominant M the charge imbalance between the red and blue sublattices opens a trivial gap.

Chern number

The Haldane model belongs to the class A of the periodic table, and its $\mathbb{Z}$ topological invariant is the Chern number of the lowest band $\left|u^0_{\mathbf{k}}\right\rangle$

$$\nu = \frac{1}{2\pi \mathrm{i}} \int_{\mathrm{BZ}} d^2\mathbf{k} \left(\left\langle \partial_{k_x} u^0_{\mathbf{k}} \middle| \partial_{k_y} u^0_{\mathbf{k}} \right\rangle - \left\langle \partial_{k_y} u^0_{\mathbf{k}} \middle| \partial_{k_x} u^0_{\mathbf{k}} \right\rangle \right). \tag{2.10}$$

This invariant changes in a topological transition occurring at the critical value

$$|M/t_2| = 3\sqrt{3}\sin\phi. \tag{2.11}$$

and it is accompanied with the closing of the single-particle gap. The resulting phase diagram in terms of the value of the Chern number is shown in Fig. 2.3(b).

For open boundary conditions, the bulk-edge correspondence leads to topologically protected surface modes at the borders where the quantized Chern number of the insulating bulk changes to a trivial value in vacuum. As depicted in Fig. 2.3(c), such modes lead to quantized edge currents, similar to the IQHE effect.

Chapter 3

Cold atoms in optical lattices for quantum simulators

Cold atoms [33] represent one of the most versatile toolboxs for the quantum simulation of complex quantum systems [39]. Compared to other platforms [16], these systems offer a high degree of isolation and tunability over the model parameters, in addition to very precise measurement techniques. Moreover, the use of optical lattices [30, 182] provides a natural framework to simulate the behavior of electrons in crystalline solid-state materials [33, 40, 183]. Despite the apparent difference in several physical scales between these two systems[2], cold atoms can mimic the behavior of solid-state materials when cooled down below their Fermi temperature. For this purpose, the initially hot atoms can be highly isolated and cooled down [23, 24] to nK temperatures by using Doppler and evaporative cooling techniques in the presence of an harmonic trap, in order to bring the system into the quantum regime. The latter has been achieved for a wide variety of alkali-metal fermionic, as well as bosonic, atomic isotope species (see e.g., the seminals experiments of Refs. [37, 38, 185]). Once the ultracold regime is reached, the atoms can be subsequently addressed with external fields, in order to control their position, motion, and interactions [33, 40].

In this preliminary chapter, we start by reviewing [33, 40] how optical fields can be used to trap neutral atoms in lattice geometries. Then, we sketch the computation of the tight-binding Hamiltonian that describes particles hopping and interacting in such lattice systems, emphasizing how the different Hamiltonian terms can be controlled in an experiment. Finally, we discuss several of the most used state-of-the art techniques [184] to locally control and measure the properties of these systems.

3.1 Trapping of neutral atoms in an optical lattice

In order to describe the interaction between a free atom and a classical laser field $\boldsymbol{E} = E(\boldsymbol{r})e^{-i\omega t}\boldsymbol{e}_l$, let us consider, for simplicity, a two-level atom, with internal ground and excited states $|g\rangle$ and $|e\rangle$, respectively, and whose free dynamics are described by the free Hamiltonian

$$\hat{H}_{\text{atom}} = \hat{\boldsymbol{p}}^2/2m + \hbar\omega_{\text{atom}} |e\rangle \langle e| , \tag{3.1}$$

[2]Electrons have a mass of 10^{-30}kg, much lighter than those of atoms 10^{-25}kg. The lattice spacing in solid-state systems is typically of the order $\sim$ 0.5nm, while in optical lattices it is $\sim$ 500nm. The tunneling/kinetic energy scale in solids is of the order of 10^4K, which sets the Fermi temperature much higher than typical temperatures in solid-state experiments $\sim$ 1K. In contrast, the tunneling in cold atoms is of the order of 100nK, requiring very low temperatures to enter the quantum regime [184].

where $\hat{\boldsymbol{p}}$ denotes the canonical momentum of the atom with mass m, the excited state is separated from the ground state by an energy $\hbar\omega_{\text{atom}}$, and we assumed that the ground-state energy is zero.

The interaction Hamiltonian with the external field is given by the dipole interaction

$$\hat{H}_{\text{dipole}} = -\hat{\boldsymbol{\mu}} \cdot \boldsymbol{E} + \text{H.c.}, \tag{3.2}$$

where $\hat{\boldsymbol{\mu}}$ is the atomic dipole operator that only has off-diagonal elements, i.e., $\langle e| \hat{\boldsymbol{\mu}} |e\rangle = \langle g| \hat{\boldsymbol{\mu}} |g\rangle = 0$.

For a large detuning between atomic and laser frequencies, i.e., $\Delta_{\text{latt}} \equiv \omega_{\text{atom}} - \omega \gg |\hat{\boldsymbol{\mu}} \cdot \boldsymbol{E}|/\hbar$, the laser does not induce atomic transitions to the excited state, but leads to a position-dependent AC-Stark shift of the ground-state energy, proportional to the square of the electric field, and inversely proportional to the detuning. That is, the effective Hamiltonian for the atomic ground state reads

$$\hat{H}^{g}_{\text{atom}} = \hat{\boldsymbol{p}}^2/2m + V_{\text{latt}}(\boldsymbol{r}), \tag{3.3}$$

with $V_{\text{latt}}(\boldsymbol{r}) = -|E(\boldsymbol{r})|^2(\langle e| \hat{\boldsymbol{\mu}} \cdot \boldsymbol{e}_l |g\rangle)^2/\Delta_{\text{latt}}$. Therefore, $V_{\text{latt}}(\boldsymbol{r})$ represents an optical potential that can be used to trap the atom at the minimum of the laser intensity $|E(\boldsymbol{r})|^2$ for a red-detuned laser ($\Delta_{\text{latt}} > 0$), or at the intensity maximum for a blue-detuned laser ($\Delta_{\text{latt}} < 0$). In particular, by using counter-propagating laser beams with orthogonal polarizations in each of the three spatial dimensions, one can achieve standing waves that form a periodic potential

$$V_{\text{latt}}(\boldsymbol{r}) = V_x \cos^2(k_x \hat{r}_x) + V_y \cos^2(k_y \hat{r}_y) + V_z \cos^2(k_z \hat{r}_z), \tag{3.4}$$

which corresponds to a square cubic lattice with lattice spacings $a_i = \pi/k_i$, and lattice depths V_i, in each spatial direction. For simplicity, hereafter we assume the isotropic case $V_i = V_0$, and $k_i = k$. The deepness of the lattice is given by the ratio V_0/E_r, where E_r is the single photon recoil energy $E_r = \hbar^2 k^2/2m$. Typically, $V_{\text{latt}}(\boldsymbol{r})$ also contains an harmonic confinement term needed to prevent the atoms from leaving the optical lattice. Alternatively, one can also engineer infinite-potential hard walls at the edges of the optical lattice with recently developed digital mirror device techniques [186, 187].

For a periodic potential $V_{\text{latt}}(\boldsymbol{r})$, such as the one of Eq. (3.4), and under the approximation of an infinite lattice, the single-particle atomic eigenstates of the Hamiltonian (3.3) are given by Bloch states $\psi_{n,\boldsymbol{q}}(\boldsymbol{r}) = e^{i\boldsymbol{q}\cdot\boldsymbol{r}} u_n(\boldsymbol{r})$, where $\boldsymbol{q}$ belongs to the first Brillouin zone of the reciprocal lattice, $u_n(\boldsymbol{r})$ has the same spatial periodicity of $V(\boldsymbol{r})_{\text{latt}}$, and n is the band index. For deep lattices satisfying $V_0 \gg E_r$, the band structure is flat, with vibrational states localized at each lattice site with an energy gap $\hbar\omega_0 = 2E_r\sqrt{V_0/E_r}$. In this case, it is convenient to describe the single-particle atomic states in terms of Wannier functions $w_{n,i}(\boldsymbol{r})$, which are obtained from a Fourier transformation of the Bloch states over the discrete lattice sites $\boldsymbol{R}_i$:

$$\psi_{n,\boldsymbol{q}}(\boldsymbol{r}) = \sum_i w_{n,i}(\boldsymbol{r}) e^{i\boldsymbol{q}\cdot\boldsymbol{R}_i}. \tag{3.5}$$

3.2 Control over many-body Hamiltonian terms

In the presence of the optical lattice, the second-quantized many-body Hamiltonian for fermionic or bosonic particles can be written in the general form

$$\hat{H} = \hat{H}_0 + \hat{H}_{\text{int}} = \int \mathrm{d}^3 r \hat{\Psi}^\dagger(\boldsymbol{r}) \left[-\frac{\hbar^2 \nabla^2}{2m} + V_{\text{latt}}(\boldsymbol{r}) \right] \hat{\Psi}(\boldsymbol{r}) + \\ + \int \mathrm{d}^3 r \mathrm{d}^3 r' \hat{\Psi}^\dagger(\boldsymbol{r}) \hat{\Psi}^\dagger(\boldsymbol{r}') V_{\text{int}}(\boldsymbol{r} - \boldsymbol{r}') \hat{\Psi}(\boldsymbol{r}) \hat{\Psi}(\boldsymbol{r}'), \tag{3.6}$$

where $\hat{\Psi}(\boldsymbol{r})$ are the fermionic or bosonic annihilation operators at an arbitrary point of space $\boldsymbol{r}$, and V_{int} parametrizes a general two-body interaction. In what follows, we outline the derivation of a tight-binding version of $\hat{H}$ for deep optical lattices.

3.2.1 Hopping amplitudes and on-site light potentials

The Wannier functions, introduced in Eq. (3.5), can be used to express the general second-quantized operators in terms of the creation operators (fermionic or bosonic) for Wannier states $\hat{b}_{n,i}$, which have a discrete lattice index:

$$\hat{\Psi}(\boldsymbol{r}) = \sum_{n,i} w_{n,i}(\boldsymbol{r} - \boldsymbol{R}_i) \hat{b}_{n,i}. \tag{3.7}$$

For low temperatures compared to the lattice depth, i.e., $k_{\text{B}} T \ll \hbar \omega_0$, only the lowest lattice band is populated, and the above expression simplifies to

$$\hat{\Psi}(\boldsymbol{r}) \simeq \sum_i w_i(\boldsymbol{r} - \boldsymbol{R}_i) \hat{b}_i, \tag{3.8}$$

where we have defined $w_i \equiv w_{0,i}$, and $\hat{b}_i \equiv \hat{b}_{0,i}$. By inserting Eq. (3.8) into $\hat{H}_0$ in Eq. (3.6), such term takes the form

$$\hat{H}_0 = \sum_{i,j} t_{ij} \hat{b}_i^\dagger \hat{b}_j - \sum_i \mu_i \hat{n}_i, \tag{3.9}$$

with $\hat{n}_i \equiv \hat{b}_i^\dagger \hat{b}_i$, and where we have defined the hopping amplitude as

$$t_{ij} = \int \mathrm{d}^3 r w_i^*(\boldsymbol{r} - \boldsymbol{R}_i) \left[-\frac{\hbar^2 \nabla^2}{2m} + V_{\text{latt}}(\boldsymbol{r}) \right] w_j(\boldsymbol{r} - \boldsymbol{R}_j), \tag{3.10}$$

and the on-site potential as

$$\mu_i = \int \mathrm{d}^3 r V_{\text{latt}}(\boldsymbol{r}) w_i(\boldsymbol{r} - \boldsymbol{R}_i). \tag{3.11}$$

Notice that Eq. (3.9) describes the hopping processes within the lowest band of localized single-particle orbitals. The latter are possible for large but finite lattice depths, such that the Wannier orbitals are not fully localized at each lattice site, but rather overlap with the Wannier functions of neighboring sites. By adjusting the lattice depth, one can therefore tune the values of t_{ij}, which also depend on the atomic mass m and the lattice spacing a_{latt}. Nevertheless, one usually assumes that the overlap is only finite for NN sites. Moreover, while the parameters t_{ij} and μ_i are typically regarded as site-independent, under the assumption of spatially homogeneous optical lattice fields, there are situations in which one is interested in having disordered or staggered on-site potentials and hopping amplitudes (e.g., to realize the dimerized static SSH model discussed in Chapter 2). To this aim, one can use interference

patterns between several optical beams, in order to create optical superlattices, or optical lattices with a quasi-periodic structure.

Before discussing many-body interactions in such tight-binding systems, it is also worth to remark that current techniques based on lattice tilting and Raman-assisted tunneling [83], or periodic modulations of the lattice in time (Floquet driving) [82], can be used to effectively modify the hopping amplitudes by introducing complex phases $t_{ij} \to e^{i\phi} t_{ij}$. Such schemes can be used, for instance, to create artificial magnetic fluxes or gauge fields [80, 188], and give rise to very exotic phases already at the single-particle level, such as in the Haldane model, discussed in Section 2.4.2.

3.2.2 Interactions in cold atoms

The interactions described by $\hat{H}_{\text{int}}$ in Eq. (3.6) are typically split into short- and long-range contrubtions, i.e., $\hat{H}_{\text{int}} = \hat{H}_{\text{int,s}} + \hat{H}_{\text{int,l}}$ [33, 40]. On the one hand, short-ranged interactions between neutral atoms, usually described by the van der Waals potential $C_6/|\boldsymbol{r} - \boldsymbol{r}'|^6$, can be approximated by a contact potential of the form

$$V_{\text{int,s}}(\boldsymbol{r} - \boldsymbol{r}') \simeq \frac{2\pi\hbar a_s}{m} \delta(\boldsymbol{r} - \boldsymbol{r}'). \tag{3.12}$$

in the ultracold limit, where the interaction is dominated by the s-wave scattering channel with scattering length a_s. For the atomic species used in experiment, such regime corresponds to the sub-mK temperatures achieved in a typical experimental setup. In the case of bosonic atoms, inserting Eq. (3.12) into the expression of $\hat{H}_{\text{int}}$ in Eq. (3.6) yields

$$\hat{H}_{\text{int,s}} = U \sum_i \hat{n}_i(\hat{n}_i - 1), \tag{3.13}$$

with

$$U = \frac{2\pi\hbar a_s}{m} \int \mathrm{d}^3 r |w_i(\boldsymbol{r} - \boldsymbol{R}_i)|^4. \tag{3.14}$$

Notice that, due to the Pauli exclusion principle, such s-wave contact interactions are not present for fermionic atoms. In this case, however, one can still engineer similar contact interactions between different fermionic states $\uparrow$ and $\downarrow$, which can represent internal atomic states or two different fermionic species, leading to an on-site interaction between them of the form

$$\hat{H}^{\uparrow\downarrow}_{\text{int,s}} = U_{\uparrow\downarrow} \sum_i \hat{n}_{i,\uparrow} \hat{n}_{i,\downarrow}, \tag{3.15}$$

where $U_{\uparrow\downarrow}$ can be expressed as in Eq. (3.14) provided that the Wannier functions and masses of both fermionic states are the same.

One remarkable and generic feature of contact interactions is that their scattering length a_s can be highly tuned via magnetic or optical Feshbach resonances [33, 189, 190], allowing for a high control over the strength and even the sign of the contact interactions U and $U_{\uparrow\downarrow}$.

On the other hand, long-range interactions are also present in polar molecules, magnetic atoms, or neutral atoms excited to Rydberg states with a large electric dipole moment. In these cases, the long-range potential $V_{\text{int,l}}(\boldsymbol{r} - \boldsymbol{r}')$ can be directly inserted in the expression of $\hat{H}_{\text{int}}$ from Eq. (3.6), leading to a Hamiltonian of the form

$$\hat{H}_{\text{int,l}} = \sum_{i \neq j} V_{ij} \hat{n}_i \hat{n}_j, \tag{3.16}$$

where we have neglected on-site potential terms proportional to $\hat{n}_i$. Several strategies can be used to tune long-range interactions. For instance, highly anisotropic interactions can be engineered via the magnetic (electric) dipole-dipole interactions of magnetic atoms (polar molecules), and control over the values of V_{ij} at different distances can be achieved via Rydberg-dressing.

3.3 Experimental tools for state manipulation and detection

The cold atom quantum simulation toolbox not only offers the possibility to tune Hamiltonian terms, but also enjoys well-established techniques to control and diagnose the quantum many-body state. In this section, we outline some of the most important ones [33, 184].

3.3.1 Time-of-flight measurements

Time-of-flight techniques [33] are among the most common tools for measuring the momentum distribution of the trapped atoms. They are based on turning off the optical lattice and measuring the atomic density distribution $n(\boldsymbol{r})$ after a fixed time t, via standard absorption images at several positions $\boldsymbol{r}$. Assuming that the atoms propagate ballistically after they are released, i.e., $\boldsymbol{r}(t) \propto \boldsymbol{k}t$, the real-space density distribution $n(\boldsymbol{r}, \boldsymbol{t})$ allows one to infer the momentum (quasi-momentum) distribution of the particles for a sudden (adiabatic) release of the lattice potential, as was done, respectively, in the pioneering experiments of Ref. [191] and Ref. [192]. It is also worth to mention that, although time-of-flight techniques mainly probe single-particle properties of the quantum state, they can also be used to study the effect on interactions, which cause deviations from the ballistic behavior that can be detected in the density-density correlations noise [33].

3.3.2 Quantum gas microscope

The use of highly precise quantum gas microscopes [193, 194] allows for in situ measurements and addressing of the atoms with a remarkable single-site resolution, allowing for a wide range of applications. In first place, this technique allows to perform snapshots of complex many-body systems, providing access to several spatial correlations of interest to diagnose bosonic and fermionic Mott transitions [186, 195–197], particle-hole [198] and anti-ferromagnetic properties [44, 199–201], or even nonlocal string order correlators [198, 202]. Moreover, notice that the possibility to address single atoms is a powerful tool for state-preparation protocols.

The main idea of a quantum gas microscope [193, 194] is to use a high-aperture optical device with a high resolution, which allows one to collect fluorescence images of individual lattice sites. As fluorescence is caused by the scattering of photons by the atoms, the optical molasses used to generate the fluorescence light are typically also used for laser cooling the atoms, i.e., to prevent a fast heating of the system caused by the photon-induced recoil. Beyond the fluorescence atomic detection, one can also use tightly focused off-resonant beams to induce light-shifts of the atomic levels with single-site resolution [194]. The latter can be subsequently used to address particular level transitions with a less-focused pulse in resonance with the light-shifted levels, to induce flipping between internal atomic states. Moreover, while the pioneering quantum gas microscopes [193, 194] where limited to parity projected measurements, which detected the number of atoms per site modulo two due to pair losses, current techniques allow for spin-selective and atom-number

measurements [199, 203, 204] by spatially separating the different components before fluorescence imaging.

Finally, notice also that the recent realization of a quantum gas magnifier [205] allows one to achieve even higher resolution than with the quantum gas microscope, and to extend high resolution detection and addressing methods to 3D geometries.

3.3.3 Measurement of topological invariants

Several techniques can be used to measure global topological invariants, introduced in Chapter 2, in cold atom experiments. Here we discuss some of the most used schemes, without pretending to provide an exhaustive list of all the available methods.

In one dimension, the topological Zak phase of chiral-symmetric systems, such as the SSH model discussed in Section 2.4.1, has been experimentally evaluated via Ramsey interferometry measurements of a single particle undergoing Bloch oscillations in a topological band [72]. In addition, the nonlocal string correlations accessible with the quantum gas microscope can also be used to characterize the topological nature of interacting topological insulators in one dimension [198, 202], as further discussed in Chapter 4.

In the two-dimensional case, the close relation between the topological Chern number, introduced in Section 2.4.2, and the quantized Hall response, allows one to determine this topological invariant through cold atom transport measurements [206, 207], as in the IQHE. Following this scheme, the Chern number has been measured in the experimental realization of the Harper-Hofstadter Hamiltonian of Ref. [75] by measuring the transverse displacement experienced by the center-of-mass of the atomic cloud when subjected to an external perpendicular electric force. Apart from transport measurements, it has been shown that the Chern number can also be obtained by comparing the frequency-integrated depletion rates of a cold atom lattice subjected to two different circular drives with orthogonal polarizations [208]. Such quantized spectroscopic response, denoted quantized circular dichroism, has allowed to measure the Chern number of the Haldane model, discussed in Section 2.4.2, in the experiment of Ref. [209]. Finally, it is also interesting to note that the Chern number can be obtained in far-from-equilibrium scenarios from the dynamical linking number of momentum-space trajectories, as proposed in Ref. [210], and experimentally implemented in Ref. [211] to measure the Chern number of a Chern insulator after a sudden quench from a trivial one.

Part II

Interaction-induced topological phases for cold atom quantum simulators

Chapter 4

Revealing the topological nature of the bond order wave

The static SSH model introduced in Section 2.4.1 has been recently realized in several atomic and photonic quantum simulators [72, 212, 213], paving the road towards the study of more complex SPT phases in one-dimension. For instance, as these experiments focused on noninteracting topological properties, there are still many open questions regarding the interplay between strong correlations and topology. A paradigmatic example is the Haldane phase [214], an interacting SPT phase characteristic of antiferromagnetic spin-1 chains that has been recently realized in a cold atom quantum simulator [215]. For the case of the static SSH model, there are also several works focusing on the role of electronic interactions [216–220] and also on the bosonic version of the model (the bosonic SSH model), which has been also recently realized in a cold atom quantum simulator [221].

Even more, recent theoretical studies have shown that interacting atomic mixtures [222–224] or atoms in an optical cavity [225, 226] could mimic the original SSH model, where the nontrivial topology is acquired due to the electron-phonon coupling via a spontaneous Peierls mechanism. The motivation is to recover the richer physics exhibited by the original model, such as the bulk ground state degeneracy and the associated topological bulk excitations in the form of solitons interpolating between these two degenerate configurations. To this aim, the idea behind these works is to substitute the phononic degrees of freedom by quantum spins [222–224] or light modes [225, 226] at the bonds of a fermionic or bosonic chain.

In this chapter, based on Ref. [4], we show that these physics can be realized even in the absence of such extra quantum degrees of freedom by using solely fermionic interactions. We do so by analysing the BOW phase arising from frustration between competing interactions in many spinless [227–229] and spinful [230–239] fermionic chains. These works were able to numerically establish the presence of a spontaneously dimerized fermionic phase, i.e., the BOW phase, in finite regions of the phase diagram comprised between two charge density wave (CDW) insulating orders in the spinless case, or between a CDW insulator and a conventional Mott insulator (MI) in the spinful case. For concreteness, we base our analysis on the BOW phase exhibited by the one-dimensional extended Fermi-Hubbard model of spinful fermions, motivated by the fact that it could be simulated with dipolar gases in optical lattices. While its insulating nature and effective dimerization have been very carefully characterized, here we establish its connection with SPT phases by showing that one of its two degenerate ground states exhibits a nontrivial topology.

This chapter is organized as follows. Before discussing the interaction-induced BOW phase, in Section 4.1 we revisit the spinful version of the static SSH model,

in order to show which numerical techniques can be used to characterize the topology in the interacting spinful case within an MPS representation of the ground state. In particular, when the external dimerization favors the topological sector, the MPS ground state found with the iDMRG method exhibits a degenerate entanglement spectrum (ES) and finite string order correlators, which are characteristic of SPT phases. Section 4.2 is devoted to the study of the extended Hubbard model in the absence of any static dimerization. We complement previous numerical studies of this model in finite systems [232–236, 238] by studying the appearance of the BOW phase in this model with the iDMRG method. The latter allows us to find an exact twofold bulk degeneracy in this phase. We show that one of these two ground states is topological, as it exhibits the same degeneracy of the ES and finite string-order correlators of the topological spinful SSH model. Furthermore, we show that, in a finite-size system, the topological sector of the BOW can be stabilized by means of a suitable local pinning. In this case, the *bulk-edge* correspondence of SPT phases translates into the presence of gapless spin edge modes that were not observed in previous finite-size studies. Exemplary to the rich phenomenology of the system, we find that further spin bulk excitations create solitonic structures interpolating between the topological and trivial sectors of the BOW. Finally, in Section 4.3, we discuss an experimental scheme to realize the BOW phase with magnetic dipolar atoms in an optical lattice.

4.1 Spinful Su-Schrieffer-Heeger model

The spinful SSH model considers two interacting spin species described by the dimerized extended Hubbard Hamiltonian

$$\begin{aligned}\hat{H}_{\mathrm{SSH}_2} = t_1 \sum_{i\,\mathrm{even},\sigma} (\hat{c}^\dagger_{i,\sigma}\hat{c}_{i+1,\sigma} + \mathrm{H.c.}) + t_2 \sum_{i\,\mathrm{odd},\sigma} (\hat{c}^\dagger_{i,\sigma}\hat{c}_{i+1,\sigma} + \mathrm{H.c.}) + \\ + U\sum_i \hat{n}_{i,\uparrow},\hat{n}_{i,\downarrow} + V\sum_{ij}\hat{n}_i\hat{n}_j,\end{aligned} \tag{4.1}$$

where $\sigma = \uparrow,\downarrow$ labels the two spin species, $\hat{n}_i \equiv \hat{n}_{i,\uparrow} + \hat{n}_{i,\downarrow}$, and $U, V > 0$. Unless specified, we consider the ground-state sector with zero total magnetization $\hat{S}_z \equiv \sum_i(\hat{n}_{i,\uparrow} - \hat{n}_{i,\downarrow})/2 = 0$. Notice also that, in the spinful case, both charge and spin degrees of freedom have to be considered. More precisely, we refer to a gapped charge or spin sector when the system has to pay a finite energy for adding/removing an up-down pair, or flipping a single fermion, respectively. Furthermore, notice that despite the presence of interactions, the Hamiltonian (4.1) preserves the chiral symmetry $\Sigma\hat{H}_{\mathrm{SSH}_2}\Sigma = \hat{H}_{\mathrm{SSH}_2}$, which in this interacting case is given by the invariance under the chiral operator

$$\Sigma = \prod_{i=0}^{L-1}(\hat{c}^\dagger_{i,\uparrow} + (-1)^i\hat{c}_{i,\uparrow})(\hat{c}^\dagger_{i,\downarrow} + (-1)^i\hat{c}_{i,\downarrow}), \tag{4.2}$$

that generalizes the chiral invariance of noninteracting systems given by Eq. (2.6). In the noninteracting limit $U, V = 0$ the spinful system consists simply of two copies of the spinless SSH discussed in Section 2.4.1. That is, at half filling the system is insulating with finite charge and spin gaps, and for $t_1 < t_2$ and open boundary conditions there are four topological edge states (one for each spin species and edge). Interestingly, while the winding number takes the value $\nu = \nu_\downarrow + \nu_\uparrow = 2$, the Zak

phase takes a trivial value $\phi_{\text{Zak}} = 0$ due to its $\mathbb{Z}_2$ character. The lack of $\mathbb{Z}_2$ character in the spinful topological invariant makes it difficult to determine in the general interacting case, as its computation via Green's functions generally requires to compute real-time dynamics of the ground state [216, 218, 219]. Such studies have shown that the winding number $\nu = 2$ is robust against arbitrary U values, and finite V values below a critical value, for which the system develops a trivial CDW insulator.

Alternatively, interacting SPT phases can also be characterized by means of their ES properties and the presence of finite nonlocal string-order correlators, which can be easily accessed in DMRG studies, as we discuss below.

4.1.1 Entanglement spectrum

The degeneracy of the ES represents a powerful alternative to characterize the topology of one-dimensional systems when the winding number is difficult to compute, as it has been shown that phases with the same ES degeneracy and symmetries can be connected adiabatically and are thus topologically equivalent. Moreover, the ES can be easily accessed when working with an MPS representation of the ground state [176, 240]. The ES is defined for a bipartite cut of the fermionic chain, that allows for a Schmidt decomposition of the ground state:

$$|\Psi_g\rangle = \sum_i \lambda_i |\Psi_i\rangle_{\text{L}} |\Psi_i\rangle_{\text{R}}, \tag{4.3}$$

where $|\Psi_i\rangle_{\text{L}}$ ($|\Psi_i\rangle_{\text{R}}$) are states belonging to the left (right) segment of the bipartition. The ES is given by $\varepsilon_\lambda = -2\log(\lambda_i)$, where λ_i are the Schmidt values for the bipartite cut. The bipartite cut introduces a virtual edge in the system, and the entanglement degeneracy encodes the information about the associated degenerate manifold. Thus, notice that the location of the bipartite cut is important. Here we performed it between two sites connected by an odd bond in the iMPS, such that after the cut these end sites are dangling sites isolated from the rest of their half-chain bulks in the topological case $t_1 = 0$. In Figure 4.1 we show the lowest levels

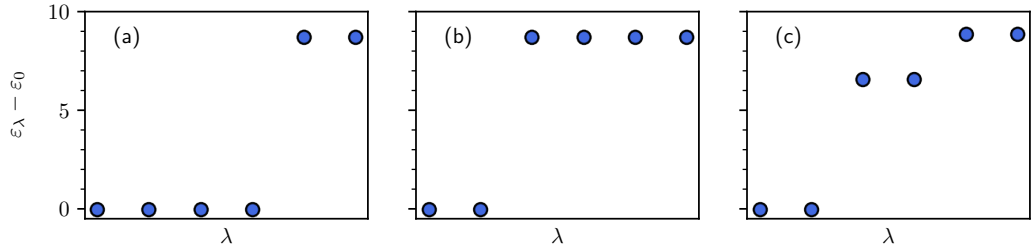

FIGURE 4.1: Lowest energy levels of the ES in the spinful SSH model for $(t_1, t_2) = (0.1, 1.9)$. (a) Noninteracting case with $U = V = 0$. (b) Interacting case with $U = 0.5t$ and $V = 0$. (c) Interacting case with $U = 0$ and $V = 0.5t$.

of the ES in the fully dimerized topological regime ($t_1 = 0$) for three different values of interactions (U, V) [218, 241]. In the noninteracting case, the ES is fourfold degenerate, in agreement with the value of the winding number $\nu = 2$: there is one single-particle state per spin at each edge, and the fact that there is no Pauli exclusion principle between $\uparrow$ and $\downarrow$ species leads to a fourfold degenerate edge manifold $|\uparrow\rangle, |\downarrow\rangle, |\uparrow\downarrow\rangle, |0\rangle$. However, for finite-interactions there is a sharp transition of these single-particle edge states into correlated ones, and the fourfold degeneracy is reduced twofold. This is discussed in detail in Refs. [216, 218], where it is shown that

even though the bulk winding number is the same for the noninteracting and interacting systems, the noninteracting case has an extra symmetry which is broken for any finite interactions, and is the responsible of the reduction of the ES degeneracy. For instance, in the large U limit, and under the global half-filling constraint, there is a large energy penalty for the edge states $|\uparrow\downarrow\rangle$, $|0\rangle$, but there is still a twofold topological degeneracy in the ground state.

4.1.2 Nonlocal string order correlators

For one-dimensional interacting systems, the presence of a SPT phase is also signalled by a nonvanishing value of a nonlocal string order parameter [242–244] that can be measured in ultracold atomic systems with a quantum gas microscope [44, 198, 202, 245]. In particular, the topological nature of SSH-like chains is captured by the long-range order of the following string correlator [246–248]:

$$\mathcal{O}^{\nu}_{\text{odd}}(|i-j|) = \left| 4\langle \hat{S}^{\nu}_{2i+1} \exp\left[i\pi \sum_{k=2i+2}^{2j-1} \hat{S}^{\nu}_{k} \right] \hat{S}^{\nu}_{2j} \rangle \right|, \tag{4.4}$$

where $\nu = s, c$ denotes the spin and charge sectors. Due to the fully gapped nature of the spinful SSH ground state, the string correlator (4.4) can be calculated both in the spin sector, where $\hat{S}^{s}_{i} = \frac{1}{2}(\hat{n}_{i,\uparrow} - \hat{n}_{i,\downarrow})$ and in the charge sector, where $\hat{S}^{c}_{i} = \frac{1}{2}(\hat{n}_{i} - 1)$. A proper scaling of these quantities allows one to infer the limit of $\mathcal{O}^{\nu}_{\text{odd}} \equiv \lim_{|i-j|\to\infty} \mathcal{O}^{\nu}_{\text{odd}}(|i-j|)$: $\mathcal{O}^{s}_{\text{odd}}$ and $\mathcal{O}^{c}_{\text{odd}}$ are finite for the gapped topological spin and charge sectors and vanish for the topologically trivial phase. Figure 4.2 shows this behavior for for three different values of interactions (U, V). An impor-

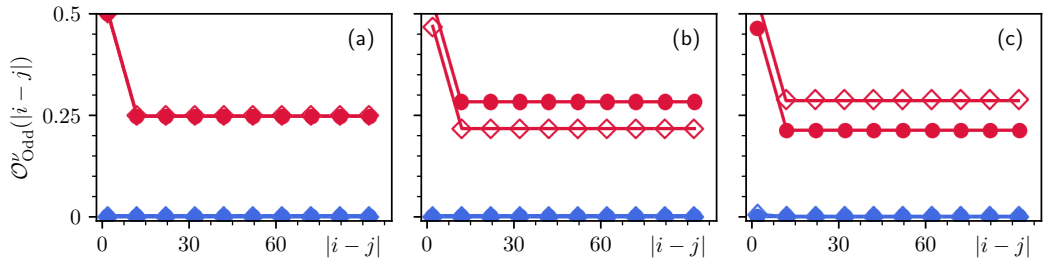

FIGURE 4.2: String order correlators in the spinful SSH model for $(t_1, t_2) = (0.1, 1.9)$. Red (blue) colors are used for the odd (even) string order correlators, and full circles (empty squares) are used for the spin (charge) sectors. (a) Noninteracting case with $U = V = 0$. (b) Interacting case with $U = 0.5t$ and $V = 0$. (c) Interacting case with $U = 0$ and $V = 0.5t$.

tant observation here is that, as in the ES, where the choice of the bipartite cut was crucial for a proper analysis of the topology, since the two bulk ground states are identical up to a translation of one site, the even string order

$$\mathcal{O}^{\nu}_{\text{even}}(|i-j|) = \left| 4\langle \hat{S}^{\nu}_{2i} \exp\left[i\pi \sum_{k=2i+1}^{2j} \hat{S}^{\nu}_{k} \right] \hat{S}^{\nu}_{2j+1} \rangle \right| \tag{4.5}$$

has the opposite property: it is finite in the trivial sector and vanishing in the topological one.

4.2 Bond order wave of the extended Fermi-Hubbard model

In this section we show that the interacting extended Fermi-Hubbard model can exhibit the same topological properties as the spinful SSH model, with the difference that in the latter model there is a fixed static staggerization in the hopping giving rise to the nontrivial topology, while in the former topology is acquired via the same fermionic interactions, which mimic the effect of lattice phonons to induce a dimerization spontaneously.

The extended Fermi-Hubbard model describes a chain of length L where N spinful fermions, labeled by $\sigma = \uparrow, \downarrow$, interact through contact and NN repulsion. The Hamiltonian modeling such system reads

$$\hat{H} = -t \sum_{\langle ij \rangle, \sigma} (\hat{c}^{\dagger}_{i,\sigma} \hat{c}_{j,\sigma} + \text{H.c.}) + U \sum_{i=0}^{L-1} \hat{n}_{i,\uparrow} \hat{n}_{i,\downarrow} + V \sum_{\langle ij \rangle} \hat{n}_i \hat{n}_j, \tag{4.6}$$

where t parametrizes the NN hopping, U accounts for the on-site Hubbard interaction, and V describes the repulsion between fermions in NN sites. Here we restrict our investigation to the case where both N and the total magnetization $\hat{S}_z \equiv \sum_i (\hat{n}_{i,\uparrow} - \hat{n}_{i,\downarrow})/2$ are conserved and, unless specified, we consider the half-filled case with $N = L$ and $\hat{S}_z = 0$.

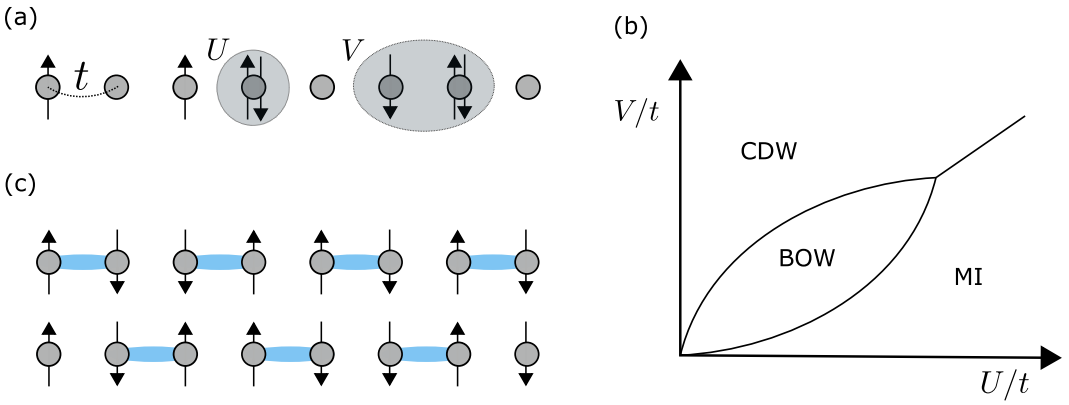

FIGURE 4.3: (a) Extended Fermi-Hubbard model. (b) Phase diagram in the $U - V$ plane. The BOW phase appears for moderate interactions at the transition point between the MI and the CDW phases. (c) Sketch of the spontaneous dimerization in the BOW phase, with bonds corresponding to a large $|\hat{B}_i|$ depicted in blue. The upper chain corresponds to the trivial case, while the lower chain is topologically nontrivial.

4.2.1 Half-filling phase diagram

The phase diagram of the system at half filling is well known [238], and exhibits three different phases, as shown schematically in Fig. 4.3(b). When U dominates the system is a MI with a finite charge gap and short range antiferromagnetic order. Alternatively, for large V the system is a fully gapped CDW insulator, characterized by an effective antiferromagnetic order, with alternating empty and doubly occupied sites. In the strongly interacting limit $U, V \gg t$ there is a direct transition between these two phases at $U = 2V$. However, when V and U compete and are comparable to the hopping amplitude t, frustration effects induce a third phase, the fully gapped BOW [230–239]. Such a phase is characterized by a uniform distribution of particles, as in MIs, accompanied by a spontaneous dimerization that leads to a

staggered expectation value of the bond operator $\hat{B}_i = \frac{1}{2}\sum_\sigma(\hat{c}^\dagger_{i,\sigma}\hat{c}_{i+1,\sigma} + \text{H.c.})$ captured by $\Delta B_i \equiv \langle \hat{B}_i - \hat{B}_{i+1}\rangle$. Here we complement the previous analyses in finite

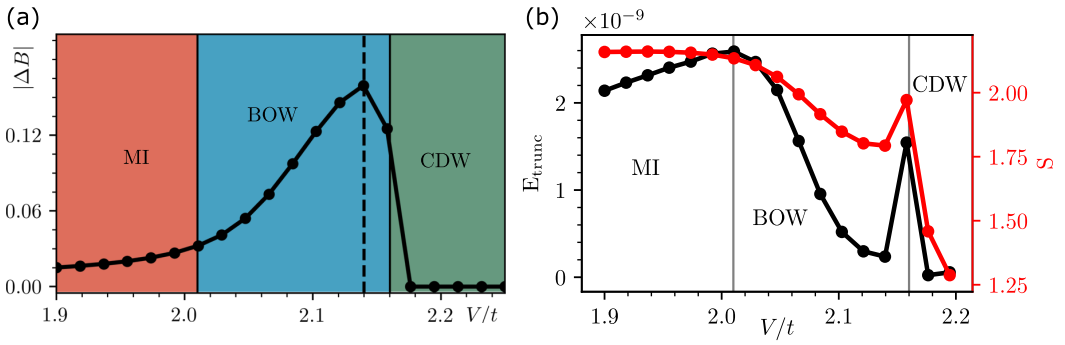

FIGURE 4.4: (a) $|\Delta B|$ at fixed $U = 4t$ and different values of V/t. We use the iDMRG algorithm with a two-site unit cell and a large bond dimension $\chi = 3000$. The dashed line $V/t \simeq 2.14$ corresponds to the maximum value of ΔB. (b) Evolution of the truncation error E_{trunc} and entanglement entropy S of the iDMRG ground state for a fixed $U/t = 4$ as a function of V/t. Here the iDMRG is iterated until a system size $L = 20\,000$.

systems by performing iDMRG calculations [142] where boundaries do not play any role, thus allowing one to study only the properties of the bulk of the system. Figure 4.4(a) shows $|\Delta B| \equiv |\Delta B_{L/2}|$ as a function of V for $U = 4t$: while the BOW-CDW transition can be accurately determined at $V_{\text{BOW-CDW}} \simeq 2.16t$, the Berezinskii-Kosterlitz-Thouless nature of the MI-BOW transition, with an exponentially slow gap opening, leads to a divergence in the correlation length close to the transition point, which makes a precise calculation of such point challenging. However, the MI-BOW transition point can be estimated precisely by studying the lack of convergence of the iDMRG algorithm at a large bond dimension and system size. The latter can be analyzed with the behavior of both the entanglement entropy and the truncation error in the iDMRG ground state, as shown in Fig. 4.4(b). When entering the BOW phase, there is a change in the monotony of the truncation error of the iDMRG ground state. This is also accompanied by a reduction of the entanglement entropy, which indicates a reduction of the correlation length. From the results of this Fig. 4.4(b), we thus estimate $V_{\text{MI-BOW}} \simeq 2.01t$, in agreement with the finite-size estimates $V_{\text{MI-BOW}} \simeq 1.88 - 2.08$ of Refs. [233, 234, 238, 249].

Our iDMRG calculations allow one to identify an exact bulk degeneracy between the two BOW ground states. Such equivalent bulk solutions correspond to the two bulk sectors of the spontaneously symmetry-broken BOW with $\pm|\Delta B|$ [Fig. 4.4(b)]. Notice that these two degenerate ground states correspond to two effective lattice dimerizations, which are reminiscent of the two possible static dimerizations in the spinful SSH model. Indeed, the behavior of the parity operators in the BOW phase [243] is the same as in the spinful SSH model with on-site repulsion [220], and the BOW phase also exhibits the chiral symmetry Σ given by Eq. (4.2). In what follows, by characterizing the topology of the BOW in the bulk, we confirm that the system realizes a SPT phase protected by chiral symmetry.

4.2.2 Bulk topology

In Section 4.1 we have seen that the topology of interacting SSH chains can be efficiently characterized by means of the ES and nonlocal string correlators. In Figure 4.5 we provide this analysis for the two BOW ground states of the extended Fermi-Hubbard Hamiltonian of Eq. (4.6). On the one hand, Figure 4.5(a) shows the

spin and charge string order correlators. We see that the asymptotic values $\mathcal{O}^{s}_{\text{odd}}$ and $\mathcal{O}^{c}_{\text{odd}}$ are finite for the gapped topological spin and charge sectors and vanish for the topologically trivial phase. On the other hand, Figure 4.5(b) shows the ES for the two degenerate iDMRG ground states of the BOW: the BOW is either a trivial phase with a lack of even degeneracy of the ES or a topological phase with an even degenerate spectrum, as in the spinful SSH model [218, 220, 241, 250]. Thus, our bulk analysis reveals that the BOW phase of the extended Fermi-Hubbard model has a topological sector with the same properties as the topological regime of the spinful SSH model with finite interactions.

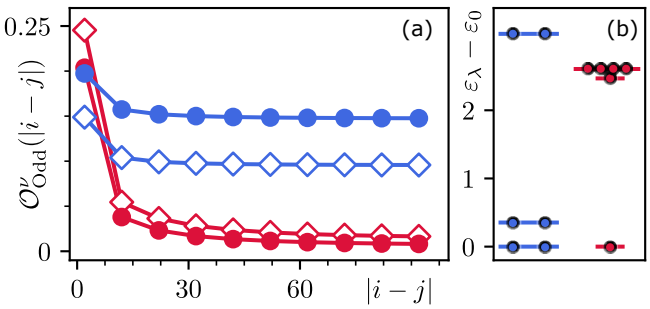

FIGURE 4.5: Topological properties of the BOW at half filling for $U = 4t$ and $V = 2.14t$ obtained with iDMRG. Red (blue) colors are used for the trivial (topological) sectors. (a) Long-range behavior of the odd string order parameters. Full circles (empty squares) are used for the spin (charge) strings. (b) Values of the ES.

4.2.3 Topological correlated edges states

For a finite-size system, border effects break the degeneracy of the two ground states and the topological dimerized pattern turns out to be an excited state for open boundary conditions: in the bulk, the fermions always tunnel to the left/right site with an effective hopping strength $t(1 \pm |\Delta B|)$ but, at the edge of the chain, the system is forced to select the most favorable hopping configuration, namely the one given by $t(1 + |\Delta B_0|)$. Therefore, previous finite DMRG studies of Eq. (4.6) only focused on the state related to the trivial topology. We now show how such a BOW phase can be stabilized in the presence of edges with finite DMRG. In order to select a given dimerization, we use a local pinning field that fixes the bond pattern at the borders of the chain. We use the pinning Hamiltonian

$$H_p = 2\delta \left(\sum_{j<j_0} (-1)^j \hat{B}_j + \sum_{j \geq L-j_0} (-1)^j \hat{B}_j \right) + V(\hat{n}_0 + \hat{n}_{L-1}), \tag{4.7}$$

where δ is the strength of the pinning applied to the first and last j_0 bonds of the chain. For our calculations, we set $j_0 = 2$ (H_p only acts on the two first and last bonds) and $|\delta| = 0.5t$. For $\delta > 0$ ($\delta < 0$) the topological (trivial) BOW is favored. The V boundary term prevents the accumulation of unwanted charges at the edges caused by the sharp boundary conditions of the interaction term. In an experiment, a similar term would be present due to the fact that even though the edge sites would not be allowed to tunel outside of the chain they would still feel the interaction with surrounding atoms.

Figures 4.6(a)-(b) show the two staggered bond patterns obtained by varying the sign of the pinning field, that correspond to the trivial and topological BOW phase,

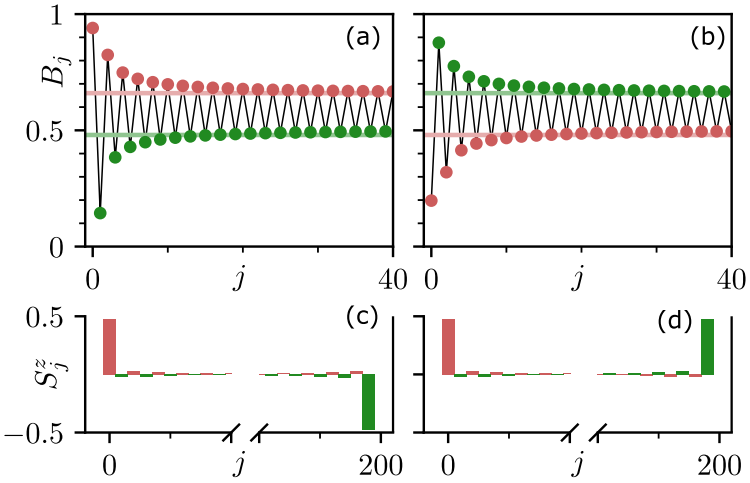

FIGURE 4.6: Finite DMRG results at half filling for $U = 4t$, $V = 2.14t$, $L = 200$, and $\chi_{\max} = 1200$. Red (green) points are used for the even (odd) bonds or sites. (a)-(b) Expectation value of the bond operator in the BOW phase exhibiting the trivial (a) and topological (b) staggered patterns. Only the first sites on the left part of the chain are shown, as the bond profile is symmetric with respect to its center. Solid lines represent the iDMRG value with $\chi_{\max} = 3000$. (c)-(d) Local polarization of two degenerate topological solutions corresponding to the bond staggerization of (b) for $S_z = 0$ (c) and $S_z = +1$ (d).

respectively. Figure 4.6(c) shows the spin polarized edge states only appearing in the topological sector. As these edge states couple weakly with the bulk, we can approximate the reduced density matrix of the edges by the product state wave function $|\Psi\rangle_{\text{edges}} = |\cdot\rangle_L |\cdot\rangle_R$, where $|\cdot\rangle_{L(R)}$ represents the quantum state of the first (last) site of the chain. Let us now discuss the degeneracy of such edge state manifold. In the $\hat{S}_z = 0$ sector, the system has two degenerate topological ground states corresponding to $|\downarrow\rangle_L |\uparrow\rangle_R$ and $|\uparrow\rangle_L |\downarrow\rangle_R$ [the latter shown in Fig. 4.6(c)], in accordance with the twofold degeneracy of the ES. Furthermore, as shown in Figs. 4.6(d), these two ground states also have gapless edge spin excitations: the spin sector $S_z = \pm 1$ exhibits degenerate ground states of the form $|\uparrow\rangle_L |\uparrow\rangle_R$ or $|\downarrow\rangle_L |\downarrow\rangle_R$, respectively. Therefore, the edge state manifold for a finite-size system, including both the $S_z = 0$ and $S_z = \pm 1$ sectors, is fourfold degenerate.

Let us now compare this degeneracy with the the previously discussed spinful SSH model including the Hubbard interaction U [216–220, 241, 250, 251]. In the limiting case $U = 0$, the SSH topological ground state exhibits a sixfold degeneracy composed by the states

$$|\uparrow\rangle_L |\downarrow\rangle_R , |\downarrow\rangle_L |\uparrow\rangle_R , |\uparrow\downarrow\rangle_L |0\rangle_R , |0\rangle_L |\uparrow\downarrow\rangle_R \tag{4.8}$$

in the $S_z = 0$ sector, and $|\uparrow\rangle_L |\uparrow\rangle_R , |\downarrow\rangle_L |\downarrow\rangle_R$ for $S_z = \pm 1$. However, a finite U results in an energy penalty for the states $|\uparrow\downarrow\rangle_L |0\rangle_R , |0\rangle_L |\uparrow\downarrow\rangle_R$, which become gapped. Hence, the interaction-induced BOW phase exhibits the same edge state manifold as a static dimerized model with on-site interaction U.

4.2.4 Solitonic topological defects

Another interesting aspect of the BOW in a finite chain is related to the interplay between SSB and topology when bulk excited states are considered. In noninteracting topological insulators with static dimerizations, such as the SSH model, the excited

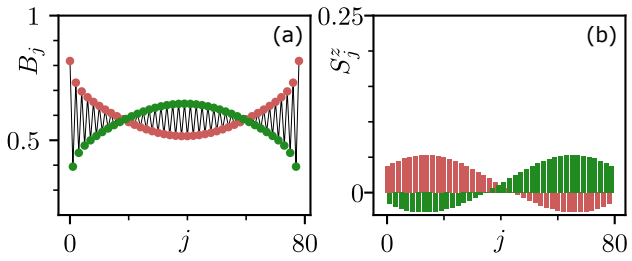

FIGURE 4.7: Finite DMRG results for $U = 4t$, $V = 2.14t$, $L = 80$, and $\chi_{\max} = 1200$, with $S_z = +1$. (a) Solitonic profile in the bond order. (b) Local magnetization profile exhibiting a delocalized spin excitation.

bulk states are described as gapped modes carrying charge or spin on top of a background with a fixed sector of the dimerization. In contrast, here the dimerization is spontaneously induced via interactions, allowing for solitonic excitations interpolating between the two possible dimerization patterns. We note that, although topological defects also appear when a fermionic or bosonic chain couples to other degrees of freedom [71, 252, 253], here we observe them for single species through the frustration-induced SSB mechanism. We focus on bulk spin excitations of the topological BOW at half filling obtained by flipping a single spin. These are the low energy excitations of the system, as adding particles to the half-filled state has a much larger energetic cost due to the presence of strong U and V repulsions, i.e., the charge gap is significantly larger than the spin one [238].

Importantly, such spin excitations also represent a route to obtain the topological sector of the BOW in a finite chain without relying on a pinning mechanism at the borders. This is what is shown in Fig. 4.7(a), where one can observe the first bulk spin excitation ($S_z = +1$) in the trivial BOW phase. We observe the solitonic domain walls interpolating between the trivial dimerization (left and right borders) to the topological one (central region). Notice that, as shown in Fig. 4.7(b), this corresponds to a delocalized soliton picture and thus this static solution is expected to be mobile; the DMRG solution corresponds to the minimum of a soliton band in the spin sector. The latter is reminiscent of a Peierl's mechanism with quantum phonons, but in the present case the solitons are generated by the same fermionic interactions.

4.3 Experimental proposal with ultracold dipolar gases

In this section, we discuss the simulation of the Hamiltonian (4.6) using a spin-mixture in a dipolar Fermi gas of highly magnetic atoms in an optical lattice. In Section 4.3.1, we provide the lattice and atomic parameters to access the BOW regime, and list the main state-of-the-art techniques needed to prepare and detect the phase. In Section 4.3.2, we analyze the effect of Hamiltonian terms appearing in the experimental model and not present in Eq. (4.6).

4.3.1 Experimental scheme with fermionic Erbium

For our proposal we focus on lattice-confined fermionic Erbium (Er)[254] in a rectangular 3D lattice with lattice spacings and lattice depths given by

$$\begin{aligned}(\Delta x, \Delta y, \Delta z) &= (266, 266, 532)\text{nm}, \\ (E_x, E_y, E_z) &= (19, 40, 80)E_{\text{rec}},\end{aligned} \tag{4.9}$$

were E_{rec} is the photon recoil energy. The states $|\uparrow\rangle$ and $|\downarrow\rangle$ can be mapped into the two lowest Er Zeeman states, with magnetic moments $m_F^{\uparrow} = -19/2$ and $m_F^{\downarrow} = -17/2$, respectively.

For the experimental values of U, V, and t we first calculate the 3D Wannier functions of the lowest band for the given cubic lattice $\phi(r) = \phi^x(x)\phi^y(y)\phi^z(z)$ and then evaluate the following terms numerically (i and j denote neighboring lattice sites along x):

$$U = \frac{4\pi\hbar a_s}{m}\int dr|\phi_i(r)|^4 + \int drdr'|\phi_i(r)|^2 V_{\text{DDI}}(r,r',\Theta)|\phi_i(r')|^2 \tag{4.10}$$

$$V_{\sigma\sigma'} = \int drdr'|\phi_i(r)|^2 V_{\text{DDI}}^{\sigma\sigma'}(r,r',\Theta)|\phi_j(r')|^2 \tag{4.11}$$

$$t = -\int dr\phi_i^*(r)(-\frac{\hbar^2\nabla^2}{2m} + V_{\text{latt}}(r))\phi_j(r) \tag{4.12}$$

using

$$V_{\text{DDI}}^{\sigma\sigma'}(r,r',\Theta) = \frac{\mu_B^2\mu_0 m_F^{\sigma} m_F^{\sigma'}}{4\pi}\frac{1-3\cos^2(\Theta_{r-r'})}{|r-r'|^3}, \tag{4.13}$$

and where $V(r)_{\text{latt}}$ is the optical lattice trapping potential. The numerical integration is done on a grid with 23x23x45 points on the full volume of a unit cell of the lattice centered on a lattice site for the dipolar part of U, while for $V_{\sigma\sigma'}$ and t a grid of 33x17x33 on the volume of two neighboring unit cells is used. The singularity is simply omitted, leading to a slight underestimation of the integral on the few percent level. Notice also that the NN dipolar term $V_{\sigma\sigma'}$ has a small spin-dependence in this setup, as discussed in more detail below, in Section 4.3.2.

For the lattice spacings and depths of Eqs. (4.9), the computed tunneling rate reads $t_x = 12.5$ Hz, much larger than those computed in the other lattice directions, i.e., $(t_y, t_z) = (0.5, 0.001)$Hz, realizing the required effective one-dimensional chains.

Furthermore, for the above lattice parameters and a scattering length of $a_s = 20a_0$ between $|\uparrow\rangle$ and $|\downarrow\rangle$, we indeed calculate $U = 55$Hz and $V_{\uparrow\downarrow} = 28$Hz. Thus, we find that the BOW phase, i.e. $U/t \sim 4$ and $V/t \gtrsim 2$, can be realized in the experiment with realistic parameters that allow to match these conditions.

Apart from allowing for a high tunability of the Hamiltonian parameters, magnetic atoms lend themselves very well to all the Hamiltonian manipulation and engineering techniques developed with alkali atoms, which can be used to prepare and detect the BOW phase. This includes preparation of MI states, spin manipulation, high-resolution imaging, and local control made accessible via microscopic techniques [255]. In addition, the rich atomic spectrum, distinctive of lanthanides [256], allows for new types of ultrafast control of the spin dynamics via optical manipulation based e.g. on clock-type optical transitions [257, 258].

4.3.2 Dipolar Hamiltonian corrections

From the experimental perspective, it is also important to take into account that the Hamiltonian will unavoidably contain higher order terms which are not included in Eq. (4.6), such as dipolar interactions beyond NN [239], density-induced tunneling [259], or the above mentioned spin-dependent dipolar terms. However, such terms do not destabilize the BOW phase, as discussed below.

Density-induced tunneling

In the experimental setup, one expects a small density-induced tunneling [259]

$$\hat{H}_{\delta t} = -\delta t \sum_{\langle ij\rangle,\sigma} (\hat{c}^{\dagger}_{i,\sigma}\hat{c}_{j,\sigma}(\hat{n}_{i,\bar{\sigma}} + \hat{n}_{j,,\bar{\sigma}}) + \text{H.c.}) \tag{4.14}$$

with

$$\delta t = -\frac{4\pi\hbar a_s}{m}\int dr|\phi_i(r)|^2\phi_i^*(r)\phi_j(r) - \int drdr'|\phi_i(r)|^2 V_{\text{DDI}}(r,r',\Theta)\phi_i^*(r')\phi_j(r'). \tag{4.15}$$

This term is however of the order $\delta t/t \sim 10^{-2}$ in our case, and being so small it is only expected to slightly renormalize the bare hopping strength.

Longer-range dipolar interactions

In this thesis, we have not considered dipolar interactions beyond NN, as they decay as $1/r^3$. Nevertheless, the full dipolar repulsive potential has been shown to stabilize the BOW in a larger window of interactions [239].

Spin-dependent dipolar interactions

Here we provide numerical evidence that the BOW and its topological properties survive if the V term is substituted by a spin-dependent dipolar interaction of the form

$$\hat{H}_{V_{\sigma\sigma'}} = \sum_{\langle ij\rangle,\sigma\sigma'} V_{\sigma\sigma'}\hat{n}_{i,\sigma}\hat{n}_{j,\sigma'} \tag{4.16}$$

with a moderate asymmetry between up and down species. From Eqs.(4.11)-(4.13), the difference in magnetic moment between up and down states leads to $V_{\uparrow\uparrow} = 0.9V_{\uparrow\downarrow}$, and $V_{\downarrow\downarrow} = 1.1V_{\uparrow\downarrow}$.

For this analysis we focus on the parameters $U/t = 4$, $V_{\uparrow\downarrow}/t = 2.14$. The iDMRG simulation of the resulting Hamiltonian at half filling leads to two degenerate ground states with $\Delta B = \pm 0.157$, in agreement with the spin-independent case shown in Fig. 4.4(a). The odd string order correlators for these two degenerate bulk ground states are shown in Fig. 4.8(a), and are in agreement with the spin-independent case of Fig. 4.5(a). The ES are also shown in Fig. 4.8(b) and one can observe that the the one of the topological sector exhibits the same degeneracy as in the spin-independent case of Fig. 4.5(b). The only appreciable difference is that the breaking of the spin symmetry lifts the degeneracy of some excited entanglement energies in the trivial ground state.

For studying the preservation of topological edge states we take a finite chain with $L = 30$. A first observation is that the topological edge state manifold of the Hamiltonian (4.6) presented a degeneracy between the $S_z = 0, \pm 1$ sectors. With the spin-dependent repulsive potential that we are considering such a degeneracy is clearly broken, as the $S_z = +(-)1$ sector will pay more (less) energy penalty compared to the $S_z = 0$ sector due to the fact that we are considering $V_{\downarrow\downarrow} < V_{\uparrow\downarrow} < V_{\uparrow\uparrow}$. Nevertheless, one still expects a twofold degeneracy within the $S_z = 0$ sector because the spin-dependent potential does not break the inversion and chiral symmetries protecting the topological phase. This is indeed what is shown in Fig.4.9, where we show the three lowest energy states of the topological sector of the BOW with $S_z = 0$. One observes the presence of correlated edge states (signalled by a large

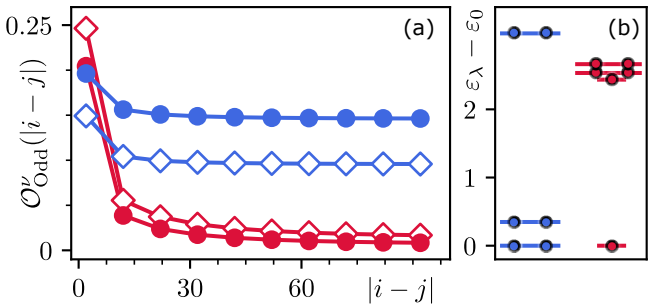

FIGURE 4.8: Topological properties of the BOW at half filling for $U = 4t$ and $V_{\uparrow\downarrow} = 2.14t$, $V_{\uparrow\uparrow} = 0.9V_{\uparrow\downarrow}$, and $V_{\downarrow\downarrow} = 1.1V_{\uparrow\downarrow}$ obtained with iDMRG. Red (blue) colors are used for the trivial (topological) sectors. (a) Long-range behavior of the odd string order parameters. Full circles (empty squares) are used for the spin (charge) strings. (b) ES.

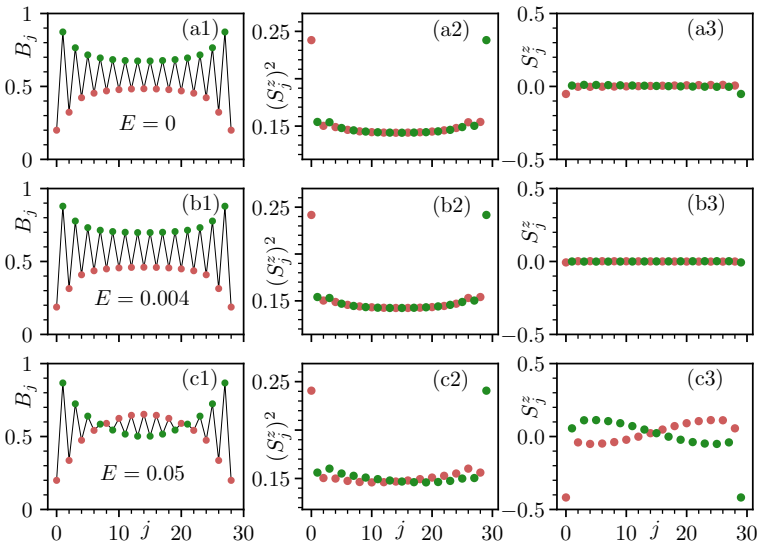

FIGURE 4.9: Real-space properties of the BOW at half filling for $U = 4t$ and $V_{\uparrow\downarrow} = 2.14t$, $V_{\uparrow\uparrow} = 0.9V_{\uparrow\downarrow}$, and $V_{\downarrow\downarrow} = 1.1V_{\uparrow\downarrow}$ obtained with finite DMRG and $L = 30$. The three rows (a),(b), and (c) correspond to the ground state and first two excited states, respectively. (a1)-(b1)-(c1) Bond order. (a2)-(b2)-(c2) Local spin-spin correlations. (a3)-(b3)-(c3) Local spin polarization.

value of S_z^2) in the two lowest states, which are almost degenerate. The third state corresponds to a hybridization of the edge states of the $S_z = -1$ sector (which minimize the energy within the edge-state manifold) and a delocalized spin excitation in the bulk carrying $S_z = +1$ such that globally $S_z = 0$. An important observation is that, for a given amount of asymmetry in $V_{\sigma\sigma'}$, this third state would become the ground state of the system below a critical value of the spin gap in the bulk. Such spin gap remains finite in the thermodynamic limit but diminishes as the system size is increased. The latter leads to a constrain to the maximum system size that one could use in an experiment given by the amount of spin asymmetry in the repulsive potential.

4.4 Summary

In this chapter, we have characterized the topological character of the BOW phase appearing in the extended Fermi-Hubbard model. We have started by giving an

overview of the interacting spinful SSH model, to show that the topological nature of dimerized fermionic chains can be captured by means of the ES degeneracy and string order correlators, even in the presence of strong correlations. We have then used this toolbox to characterize the bulk topology of the BOW ground state, which wa have obtained with the iDMRG method. We have furthermore showed that, for finite systems, the topological sector of the BOW phase is an excited state due to edge effects caused by the open boundary conditions. In this regard, we discussed strategies to stabilize the topological sector via a local edge pinning. Finally, we have proposed a realistic experimental scheme with dipolar gases in optical lattices to realize such interaction-induced topological phase. The methods proposed in this chapter are general and can be generalized to BOW phases in other strongly correlated systems.

Chapter 5

Topological Mott insulators with Rydberg atoms

Despite their complexity and their topological properties, two-dimensional Chern insulators can be understood in terms of noninteracting electronic bands, i.e., at the single-particle level, as for example for the Haldane model outlined in Section 2.4.2. The quantum simulation of such topological bands typically relies on the generation of artificial gauge fields through Floquet engineering [75, 76, 79, 209] or synthetic dimensions [77, 80, 83], that break time-reversal symmetry explicitly at the single-particle Hamiltonian level.

Nevertheless, the role of interactions in Chern insulators has attracted a great interest in the last years [87]. In the case of spinless fermions, the exact diagonalization study in Ref. [260] considered for the first time the effect of NN Coulomb interactions in the Haldane model, showing that interactions destroyed the Chern insulator by inducing a trivial charge ordered phase. Instead of destroying the topological phase, there are also other situations in which the inclusion of electronic interactions lead to fractional values of the Chern number [261], in analogy with the well-known fractional quantum Hall effect [262]. More strikingly, Chern insulators could also be induced directly from interactions in a time-reversal SSB process. The resulting state, discovered a decade ago in a mean-field analysis, is usually referred as a TMI [263][3]. The quantum simulation of these interacting phases is timely, and Rydberg-dressed atoms in optical lattices represent an ideal candidate to realize them [265], as will be discussed in detail in this chapter for a concrete model.

In the original proposal of a TMI, Raghu et al. [263] considered a system of spinless fermions in the honeycomb lattice at half filling, for which the noninteracting band structure is topologically trivial and exhibits a linear band touching, i.e., Dirac cones. The authors showed that, in mean-field approximation, the inclusion of repulsive interactions opens a topological gap, leading therefore to an interaction-induced topological phase that they called a TMI. However, subsequent exact diagonalization and DMRG studies of Dirac semimetals, including the one of the initial proposal, showed that, beyond the mean-field approximation, the topological gap vanishes or it is too small to be detected numerically, and interactions favor trivial charge ordered phases with lower energy than the TMI phase [266–272] instead.

[3] As discussed below, the topological Mott insulators considered in this thesis are a particular instance of an interaction-induced quantum anomalous Hall phase, and throughout this thesis we will use both nomenclatures to refer to this phase. However, notice that while the name topological Mott insulator is widely used in the literature for the same phase that we consider here, there are also some works [264] in which the name topological Mott insulator is restricted only to phases exhibiting an interaction-induced quantum anomalous Hall phase in the limit of strong interactions, in analogy with the usual Mott insulator obtained in the standard Fermi-Hubbard model.

More recently, researchers have numerically identified several models hosting stable TMI phases beyond the mean-field approximation with a robust topological gap present already at moderate system sizes. In these models, the stability of the TMI phase seems to arise from the quadratic band touching nature of the noninteracting fermionic band, as is for example the case for the kagome lattice at $1/3$ filling [273, 274], or the checkerboard lattice at $1/2$ filling [161–163, 273] considered here.

In this chapter, we show that the TMI could be realised in optical lattices of Rydberg-dressed atoms with available techniques. In Section 5.1, we review the appearance of the TMI in a checkerboard lattice of spinless fermions described by a two-dimensional extended Fermi-Hubbard model with up to NNN repulsive interactions. In particular, we show that, in HF approximation, the zero-temperature half-filled ground state is an interaction-induced QAH phase for certain ratios of the interactions. In Section 5.2, we present a scheme based on Rydberg-dressed atoms for the quantum simulation of the model in state-of-the-art setups. Importantly, this scheme unavoidably contains interactions beyond NNN. In Section 5.3, we analyze the stability of the TMI when considering this longer-range nature of the Rydberg-dressed potential, and also the effect of finite temperatures. We conclude in Section 5.4, where we discuss for which set of experimental parameters the TMI could be prepared and detected.

5.1 Topological Mott insulator in the checkerboard lattice

Our starting point for studying the TMI is a Hamiltonian of spinless fermions on a checkerboard lattice with periodic boundary conditions, depicted in Fig. 5.1(a),

$$\hat{H} = \hat{H}_0 + \hat{H}_{\text{int}}, \tag{5.1}$$

where $\hat{H}_0$ is the quadratic part and $\hat{H}_{\text{int}}$ contains the interactions. On the one hand, the quadratic part of the fermionic Hamiltonian [161–163, 273] reads ($\hbar = 1$)

$$\begin{aligned}\hat{H}_0 = &- t\sum_{\langle ij\rangle}(\hat{c}^\dagger_{i,A}\hat{c}_{j,B} + \text{H.c.}) + \\ &+ \sum_i \sum_{\substack{\alpha=A,B \\ \nu=x,y}} (J^\alpha_\nu \hat{c}^\dagger_{i,\alpha}\hat{c}_{i+2\nu,\alpha} + \text{H.c.}) - \mu\sum_i \hat{n}_i,\end{aligned} \tag{5.2}$$

where t stands for the NN hopping amplitude between sites A and B, J^α_ν is the NNN hopping amplitude, with $\nu = x, y$ and $\alpha = A, B$, and μ is the chemical potential that controls the total number of particles N in the lattice with $L = L_x \times L_y$ two-site unit cells. We also set $t = 1$, and $J^A_x = J^B_y = +0.5$ and $J^A_y = J^B_x = -0.5$, which generates a π flux on each sublattice. Such Hamiltonian has two bands with a quadratic band touching at half filling. On the other hand, for the interactions, we consider a general Hamiltonian with interactions of the density-density type, that reads

$$\hat{H}_{\text{int}} = \sum_{m\leq M}\sum_{\langle ij\rangle_m} V_m \hat{n}_i\hat{n}_j. \tag{5.3}$$

Here the second sum is performed over the m-th order neighbors $\langle ij\rangle_m$ of the checkerboard lattice, e.g., $\langle ij\rangle_1$ corresponds to NN terms. The isotropic repulsive interaction between m-th neighbours is then parametrized by the potential $V_m > 0$.

As will be discussed in Section 5.2, the Hamiltonian (5.3) with interactions up to $M = 4$ faithfully describes the repulsive interactions experienced by Rydberg-dressed atoms in an optical checkerboard lattice. For the sake of clarity, we first review some known results for the $M = 2$ case to understand the appearance of an interaction-induced topological phase.

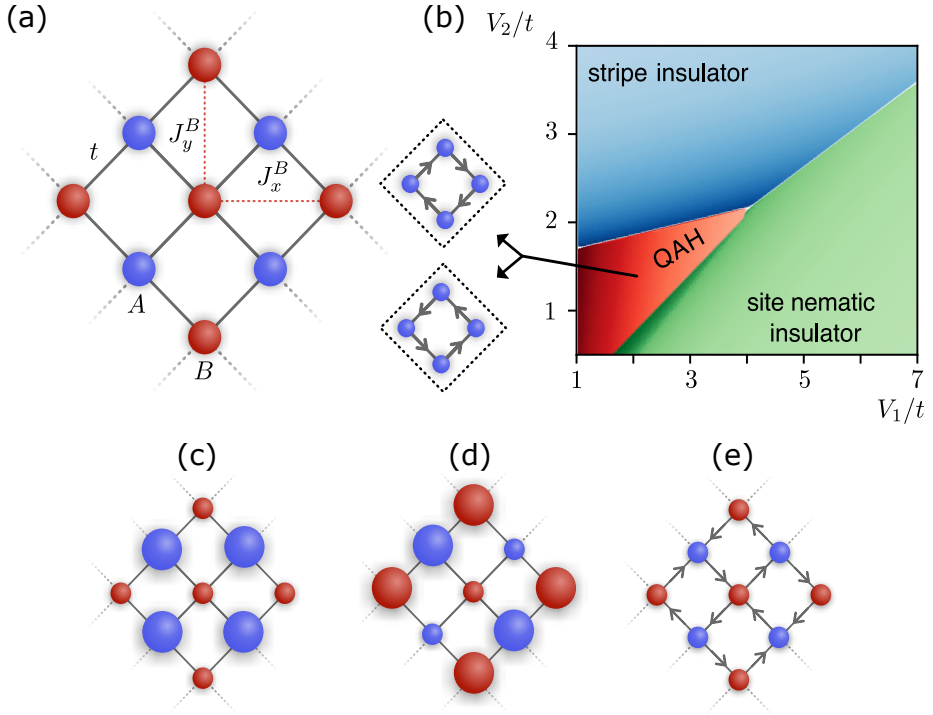

FIGURE 5.1: (a) The system is described by a Hamiltonian of spinless fermions $\hat{H}$ on a checkerboard lattice, which has NN and NNN hoppings and interactions. (b) Mean-field phase diagram of the system at half filling in terms of the NN (V_1) and NNN (V_2) interactions. For the QAH phase, the two degenerate SSB solutions are explicitly shown. (c)-(e) Sketch of the three phases appearing in the phase diagram. Larger circles indicate an enhanced value of the local charge in these sites, leading to a site-nematic charge order (c) or a stripe charge order (d). In the QAH phase (e) the charge is distributed uniformly, but the time reversal symmetry is broken due to the appearance of a current loop order in the NN bonds.

5.1.1 Half-filling interacting phases

The TMI phase is captured already at the mean-field level, as can be seen in Fig. 5.1(b), which shows the half-filling phase diagram of $\hat{H}$ at zero temperature [161, 162]. By means of a standard HF decoupling, the repulsive interactions V_1 and V_2 are approximated as

$$\begin{aligned}\hat{n}_i\hat{n}_j \simeq &- \xi_{ij}\hat{c}_j^\dagger\hat{c}_i - \xi_{ij}^*\hat{c}_i^\dagger\hat{c}_j + |\xi_{ij}|^2 + \\ &+ \bar{n}_i\hat{n}_j + \bar{n}_j\hat{n}_i - \bar{n}_i\bar{n}_j,\end{aligned} \tag{5.4}$$

with $\xi_{ij} \equiv \langle\hat{c}_i^\dagger\hat{c}_j\rangle$ and $\bar{n}_i \equiv \langle\hat{n}_i\rangle$. The HF values ξ_{ij} and $\bar{n}_i$ are found by solving iteratively the resulting self-consistent quadratic Hamiltonian, as discussed in Section 1.1. In the semiclassical limit $t \to 0$, the phase diagram hosts two insulating

phases which spontaneously break the lattice translational symmetry, as can be seen in Figs. 5.1(c)-(d). The state resulting from the SSB is determined by the competition between V_1 and V_2. As a consequence of the repulsive density-density interactions there is an energy cost of V_1 on pairs of particles occupying NN sites, and of V_2 for NNN. For dominant V_1 the ground state is a site-nematic insulator characterized by a strong charge imbalance $\rho_n \equiv \bar{n}_{\mathrm{A}} - \bar{n}_{\mathrm{B}}$ between the two sublattices [Fig. 5.1(c)]. Alternatively, for dominant V_2, the energy penalty of NNN pairs favors states with stripe density order, characterized by a finite value of the stripe density imbalance $\rho_s \equiv \bar{n}_{\mathrm{S}_1} - \bar{n}_{\mathrm{S}_2}$ between, e.g., the stripes of Fig. 5.1(d). As shown in Fig. 5.1(b), the transition between these two charge orders happens along the line $V_2 = V_1/2$ for strong interactions. However, when the kinetic energy becomes comparable to the interactions, the quantum fluctuations lead to a frustration between the two competing charge orders close to the phase transition. In this scenario of charge homogeneity (translational symmetry), the ground state can still be insulating due to the appearance of a current loop order across NN, which spontaneously breaks time-reversal symmetry [see Fig. 5.1(e)]. The local order parameter is defined as the staggered sum of currents in a closed loop of NN bonds

$$\xi_{\mathrm{QAH}} \equiv \frac{1}{4} \sum_{<ij>\in l} \epsilon_{ij} \operatorname{Im} \xi_{ij}, \tag{5.5}$$

where $\epsilon_{ij} = +1$ if the bond $i \to j$ follows the arrow convention of Fig. 5.1(e), and $\epsilon_{ij} = -1$ otherwise. This phase is known as TMI or interaction-induced quantum QAH phase, as each of its two symmetry-breaking ground states with opposite current chiralities is characterized by a global topological invariant, the Chern number.

The Chern number of the QAH phase can be computed by considering the two-band Hamiltonian that results from assuming a two-site unit cell (notice that this ansatz is valid inside the QAH and nematic phases, but does not capture the stripe order, which requires the four-site unit cell). Such two-band Hamiltonian reads

$$H(\mathbf{k}) = h_0(\mathbf{k})\sigma_0 + \vec{h}(\mathbf{k}) \cdot \vec{\sigma}, \tag{5.6}$$

with

$$\begin{aligned} h_0 &= 2(V_1 + V_2)n - \sum_{\mu\in(x,y)} T_\mu \cos(2k_\mu), \\ h_x &= -2(V_1 - V_2)\rho_n - \sum_{\mu\in(x,y)} \Delta_\mu \cos(2k_\mu), \\ h_y &= -4\left[t + V_1 \mathrm{Re}(\xi_{BA})\right] \cos(k_x) \cos(k_y), \\ h_z &= -4V_1 \mathrm{Im}(\xi_{BA}) \sin(k_x) \sin(k_y), \end{aligned} \tag{5.7}$$

and the definitions

$$\begin{aligned} T_\mu &= J_\mu^A + J_\mu^B + V_2(\xi_{A\mu} + \xi_{B\mu}), \\ \Delta_\mu &= J_\mu^A - J_\mu^B + V_2(\xi_{A\mu} - \xi_{B\mu}), \\ n &= \bar{n}_A + \bar{n}_B. \end{aligned} \tag{5.8}$$

In the QAH phase, the self-consistent HF equations lead to a vanishing site-nematic order $\rho = 0$ and a finite $\mathrm{Im}(\xi_{BA})$, which breaks time-reversal symmetry and opens a single-particle insulating gap

$$\Delta_{\mathrm{QAH}} = 8V_1 \mathrm{Im}(\xi_{BA}) = 8V_1 \xi_{\mathrm{QAH}}. \tag{5.9}$$

The time-reversal SSB HF Hamiltonian of Eq. (5.6) is reminiscent of the noninteracting Haldane model in the hexagonal lattice described in Section 2.4.2, with the difference that here the time-reversal SSB is encoded in the HF parameters rather than in any static parameter of the Hamiltonian. In accordance, the Chern number of the lower band, computed as

$$\nu = \frac{\pi}{2L} \sum_k \vec{n}_k \cdot \left(\frac{\partial \vec{n}_k}{\partial k_x} \times \frac{\partial \vec{n}_k}{\partial k_y} \right), \tag{5.10}$$

with $\vec{n}_{\mathbf{k}} = \vec{h}(\mathbf{k}) / \left\| \vec{h}(\mathbf{k}) \right\|$, can take the values $\nu = \pm 1$ in the QAH phase. In contrast, the Chern number takes the trivial value $\nu = 0$ in the two other gapped phases with charge orders. Notice that the two possible values of ν in the QAH phase account for the twofold ground-state degeneracy in the interaction-induced QAH phase, i.e., the current loops can flow in two opposite directions, and the system reaches one of the two symmetry-breaking sectors through a time-reversal SSB mechanism [see Fig. 5.1(b)]. This is the main difference of this model with respect to the Haldane model, where the value of the Chern number is fixed by the external field ϕ.

Before concluding this section, it is worth comparing our HF results at half filling with previous works. The study [273] suggested, for the first time, the existence of a stable TMI in the checkerboard geometry in the V_1-only model based on renormalization group and HF analyses. The QAH of the V_1-only model was confirmed by subsequent exact diagonalization and DMRG studies [161, 163]. One drawback of the V_1-only model is that the topological gap opens exponentially small as V_1 increases, and closes for $V_1 \gtrsim t$, so the QAH order is typically very small and difficult to detect numerically. The advantage of including a V_2 term is that it allows to obtain a larger QAH current loop order, as the phase is also present at larger values of the interactions due to the frustration of the charge orders, ultimately leading to an enhanced insulating gap Δ_{QAH}. In this line, the study [162] considered the same $V_1 - V_2$ model as here with the DMRG and the power-expanded Gibbs potential techniques, obtaining a phase diagram in qualitative agreement with the one shown in Fig. 5.1(b).

5.2 Implementation with Rydberg-dressed atoms in optical lattices

Here we focus on the quantum simulation of the TMI with Rdyberg atoms loaded in an optical lattice. Rydberg states [275] represent one of the most fruitful cold atom platform to simulate quantum systems, owing to their long-lived nature and strong long-range interactions leading to the paradigmatic Rydberg blockade effect [276]. Furthermore, individually controlled Rydberg atoms in optical tweezers [277] have emerged as a powerful platform for quantum computation [278–283], and for the simulation of quantum spin models [153, 221, 284–287], culminating with the recent observations of 2D spin liquid phases [157, 288].

While the strong interactions in Rydberg arrays are typically well captured by spin Hamiltonians, in which kinetic terms accounting for the itinerant nature of the particles can effectively be neglected, the simulation of the TMI requires interactions of the same order of tunneling (kinetic) terms. This can be achieved in other platforms that also feature long-range interactions, such as dipolar quantum gases [289–294] or polar molecules [295, 296], and in the presence of an optical lattice this allows one to simulate extended Hubbard Hamiltonians with both nonlocal interactions

and tunneling terms [254, 297–301]. Rydberg dressing [302–305] has emerged as a powerful alternative in this context. In this scheme, instead of exciting the atoms resonantly to a highly excited Rydberg state, in which the energy scale of the strong dipole-dipole interactions dominates over the itinerant dynamics, the atomic gas in the ground state is instead coupled off-resonantly to the Rydberg state, thereby admixing a reduced amount of Rydberg character to the electronic ground state. Compared to other techniques, Rydberg dressing offers the possibility to tune the strength and shape of interactions, which can be highly adjusted by a proper choice of the atomic and laser parameters of the underlying dressing protocol. Such degree of control has allowed to generate Bell spin pairs in optical tweezers [306], to engineer long-range [307–309] or even distance-selective [310] interactions in Ising Hamiltonians, and to realize extended Fermi-Hubbard Hamiltonians [311] with interaction strengths and kinetic terms of the same order of magnitude. The latter has led to the observation of quench dynamics of a Fermi gas with long-range interactions [311], paving the way for the simulation of other novel phases of quantum matter resulting from the interplay between nonlocal interactions and the kinetic energy.

In this section, we discuss in detail the form of the interaction Hamiltonian derived for cold Rydberg-dressed gases, which has the form of $\hat{H}_{\text{int}}$ [Eq.(5.3)]. Before, we discuss how a checkerboard lattice with a π-flux can be realized to achieve a free Hamiltonian of the form of $\hat{H}_0$ [Eq.(5.2)]. Remarkably, the demonstration of all essential elements has been reported in currently available experimental setups for the parameters of our concern.

5.2.1 Free Hamiltonian

The TMI has been numerically identified in various lattices with a quadratic band touching, including the kagome [163, 274], or the checkerboard lattice [161–163]. In this thesis we are interested in this latter case, where the checkerboard lattice is obtained from a square lattice geometry by introducing a sublattice-dependent π-flux on NNN plaquettes [Eq. (5.2)].

On the one hand, the design of a wide variety of optical lattice geometries, including the square lattice, has been demonstrated experimentally [312, 313] and can be realized by properly adjusting the interference pattern of the standing laser beams.

On the other hand, the injection of an artificial flux on NNN plaquettes of the square lattice leads to a checkerboard lattice with a quadratic band touching, which can be resolved via band mapping techniques, already used to certify the presence of Dirac points in a free Fermi gas on a tunable honeycomb lattice [313]. The flux insertion has been demonstrated experimentally in cold gases quantum simulators [50, 81, 82] and requires control over the magnitude, sign and complex phase of the hopping amplitude t. The dynamics of cold gases in lattices, a tight-binding system, occurs via hopping between nearest-neighbours and, marginally, next-to-nearest-neighbours. Coherent control of the hopping amplitude can be attained with several methods. Periodic perturbations of the optical lattice (Floquet techniques) [314] make it possible to reduce, suppress and eventually change the sign of the tunnelling amplitude [315]. Combining a strong lattice tilting with assisted tunnelling allows to exert selective control on hopping events.

The tilting inhibits the tunnelling by introducing inter-site energy barriers larger than the hopping amplitude. Then, one can activate again the hopping in a selective manner and controlling the hopping amplitude, using e.g. lattice amplitude modulation [316] or Raman-assisted tunnelling [81].

In particular, Raman-assisted tunnelling allows one to engineer hopping terms with complex amplitudes $e^{i2\pi\phi_{jk}}\hat{c}_k^\dagger\hat{c}_j$, which can result in finite effective magnetic fluxes on closed paths [82]. The engineering of artificial fluxes was a crucial step for the experimental simulation of static Abelian gauge fields [76, 188]. The method can be readily adapted to the π-flux case $\phi = 1/2$ discussed in this paper, which induces the quadratic band touching present in the checkerboard lattice. It is worth stressing that the π-flux does not break explicitly the time-reversal symmetry, as opposed to generic finite fluxes $\phi \neq 1/2$. As discussed in this thesis, the SSB in TMIs occurs by effect of the interactions.

5.2.2 Interaction Hamiltonian

Here we consider a scheme based on effective interactions between Rydberg-dressed atoms. Rydberg states are atomic electronically excited states with a large principal quantum number [277, 317–319].

The laser-driven (single- or two-photon) transition that couples the electronic ground state or low-energy state $|g\rangle$, and an excited Rydberg state $|r\rangle$ [319], in rotating-wave approximation and in the co-rotating frame, is described by the single-particle Hamiltonian

$$\hat{H}_c = (\Omega_R |r\rangle \langle g| + \text{H.c.}) + \Delta |r\rangle \langle r| , \tag{5.11}$$

with effective two-photon Rabi frequency Ω_R and detuning Δ. In this work, we consider the repulsive two-body van der Waals interactions experienced between two atoms in the same Rydberg state $|r\rangle$, described by the van der Waals potential $U_{vdW}(r) = C_6/r^6$, where r is the inter-atomic distance and C_6 depends on the Rydberg state [318, 319]. The van der Waals interaction between Rydberg atoms is long-ranged and strong at short distances; as an example, $U_{vdW}(r_1) = 90$ MHz for the 28P Rydberg state of ^{6}Li at $r_1 = 752$ nm [311]. A characteristic effect of the strong Rydberg potential at short distances is the dipole blockade: the laser excitation to the Rydberg state of multiple atoms within a certain exclusion volume is inhibited, as the strong interaction shifts the energy level of a state with multiple Rydberg atoms by more than the line width [318]. The Rydberg blockade has been observed in numerous experiments (see e.g. [320, 321]) and lies at the heart of Rydberg-based analog quantum simulation, e.g. of quantum spin models [277]. Also, the implementation of a CNOT gate based on the blockade was demonstrated [278, 279], which represents the basis for potential applications in quantum computations, under rapid development in recent years [282, 283, 322].

The strong interaction within the blockade radius can also be advantageously used in a Rydberg-dressing scheme [265] for the quantum simulation of extended Hubbard-type models. In the limit of far off-resonant laser coupling, i.e., for small values of the parameter $\beta = \Omega_R/\Delta \ll 1$, the transitions between $|g\rangle$ and $|r\rangle$ are energetically suppressed.

The laser induces a weak hybridization of the electronic ground state with the Rydberg state; the strong van der Waals interaction occurring in the marginal Rydberg component of the admixture results in a finite and attenuated spatial-dependent potential [318].

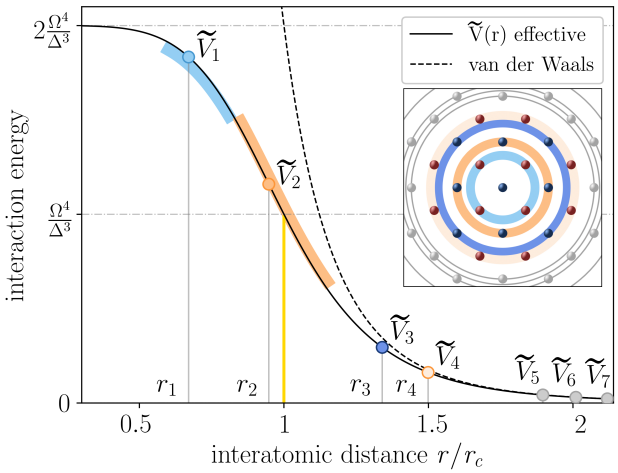

FIGURE 5.2: Interactions between Rydberg-dressed atoms in a lattice. The continuous curve shows the effective interaction potential $\tilde{V}(r)$ from Eq. (5.12), between two Rydberg-dressed atoms. At large inter-particle distances, $\tilde{V}(r)$ decays as $\beta^4 r^{-6}$, consistently with the repulsive van der Waals interaction (dashed line) in the doubly-excited component of the two-atom dressed state. The colored slabs show the ranges of $\tilde{V}_1$ and $\tilde{V}_2$ for which a topological QAH phase emerges. The inset shows an excerpt of the lattice, illustrating the succession of inter-site distances r_i.

The ground-state energy of a laser-dressed two-atom system can be obtained as a power series of the perturbation parameter β using e.g. van Vleck's perturbation theory [265, 323]. The spatial-dependent correction to the unperturbed electronic ground-state energy up to fourth order in β reads:

$$\tilde{V}(r) = 2\beta^4\Delta\left[\frac{1}{2\Delta/U_{vdW}(r)+1}\right]. \tag{5.12}$$

Here we have not included the interaction-independent single-particle shift $2(\Omega^2/\Delta)[1-(\Omega/\Delta)^2]$, which can be compensated. By defining a critical length

$$r_c^6 = C_6/(2\Delta) \tag{5.13}$$

at the full width at half maximum of $\tilde{V}(r)$, the inter-site density-density effective interaction for discrete distances r_m can be written as

$$\tilde{V}_m = 2\beta^4\Delta\left[\frac{1}{1+(r_m/r_c)^6}\right]. \tag{5.14}$$

Notice that in the presence of an optical lattice this leads to an interaction Hamiltonian of the form of $\hat{H}_{\text{int}}$ [Eq.(5.3)] in second quantization. We plot $\tilde{V}_i$ in Fig. 5.2, for the r_m discrete distances between i-th order neighbors in the checkerboard lattice under consideration, with $\{r_{m\leq 5}/r_1\} = \{1, \sqrt{2}, 2, \sqrt{5}, 2\sqrt{2}\}$.

At large distances, the interaction takes the form

$$\tilde{V}_{r_m \gg r_c} \sim \beta^4 U_{vdW}(r_m), \tag{5.15}$$

that is, we observe a suppression of the bare interaction $U_{vdW}(r_m)$ by a factor β^4, which indicates the small probability to find the dressed two-atom system in a doubly excited Rydberg state. This is crucial for the TMI, as it allows to have reduced

Rydberg interactions comparable to the hopping energy scale. The plateau at short distances can be readily inferred from Eq. (5.14)

$$\tilde{V}_{r_m \ll r_c} \sim 2\beta^4 \Delta. \tag{5.16}$$

Interestingly, both the value of the plateau as well as the location of r_c can be controlled with the Rabi frequency Ω_R and the detuning Δ. In Section 5.4, we show how these parameters can be adequately tuned to adjust $\tilde{V}_m$ and access QAH states of matter in a quantum simulation.

However, it should be emphasized at this point that the effective interaction potential $\tilde{V}_i$ is a particular case of the interaction Hamiltonian (5.3), i.e., $\tilde{V}_m$ is a constrained parametrization of the more general V_m. For instance, note that fixing $\tilde{V}_1$ and $\tilde{V}_2$, or any other pair of $\tilde{V}_i$, uniquely determines the value of the remaining $\tilde{V}_i$. We also remark that the ratio between two interaction amplitudes $\tilde{V}_i/\tilde{V}_j$, with $i < j$, is a monotonically increasing function of r_c/r_1, with a lower bound set by $\tilde{V}_i/\tilde{V}_j = (d_i/d_j)^6$ in the limit $r_c/r_1 \to 0$. In particular, $\tilde{V}_2/\tilde{V}_1$ has a lower bound of $1/8$. The other limit $r_c/r_1 \to \infty$ corresponds to an unphysical regime where Eq. (5.14) is no longer valid, as all long-distance $\tilde{V}_i$ would be comparable in magnitude to $\tilde{V}_1$.

In order to avoid this unphysical regime and, as we are interested in studying how the physical properties of the model in Eq. (5.1) with $M = 2$ change when we include a finite number of sub-leading long-distance interaction terms, we limit our investigation to a regime in which a truncation of the effective Rydberg potential to $\tilde{V}_4$ represents a meaningful approximation of the entire effective potential, including the tail. To this aim, we impose the condition $\tilde{V}_1 > 10\tilde{V}_5$, corresponding to $r_c/r_1 > 2$.

5.3 Phase diagram of Rydberg-dressed atoms

In this section, we present an extended numerical analysis of the Hamiltonian (5.1) in the presence of long-range interactions beyond NNN, motivated by the shape of the effective Rydberg potential in Eq. (5.14). Then, in the prospect of a quantum simulation, we examine the robustness of the QAH phase against thermal fluctuations with the finite-temperature HF method.

5.3.1 Zero temperature

Here we consider the Hamiltonian describing Rydberg-dressed atoms

$$\hat{H}_{\mathrm{R}} = \hat{H}_0 + \sum_{m=1}^{4} \sum_{\langle ij \rangle_m} \tilde{V}_m \hat{n}_i \hat{n}_j, \tag{5.17}$$

where we emphasize that $\tilde{V}_m$ are constrained by Eq. (5.14) and the truncation condition $\tilde{V}_1 > 10\tilde{V}_5$. This Hamiltonian includes a finite $\tilde{V}_3$ term which promotes a different charge order (see Fig. 5.3) than the nematic and stripe orders favored by $\tilde{V}_1$ and $\tilde{V}_2$. It also contains a finite $\tilde{V}_4$ term, which favors the site-nematic order generated by $\tilde{V}_1$. Notwithstanding, since both $\tilde{V}_3$ and $\tilde{V}_4$ are subleading terms, we expect the appearance of the QAH for $\hat{H}_{\mathrm{R}}$ also.

This is indeed what we observe in the phase diagram of $\hat{H}_{\mathrm{R}}$, shown in Fig. 5.4, for which we have used restricted HF method in the eight-site unit cell of Fig. 5.3, to account for the HF decouplings of $\tilde{V}_3$ and $\tilde{V}_4$ terms.

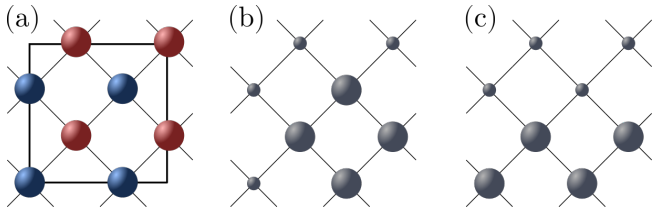

FIGURE 5.3: Lattice unit cell for numerical analysis in mean-field approximation (a). The V_3 interaction favors two types of charge order: squares (b) and zig-zag (c).

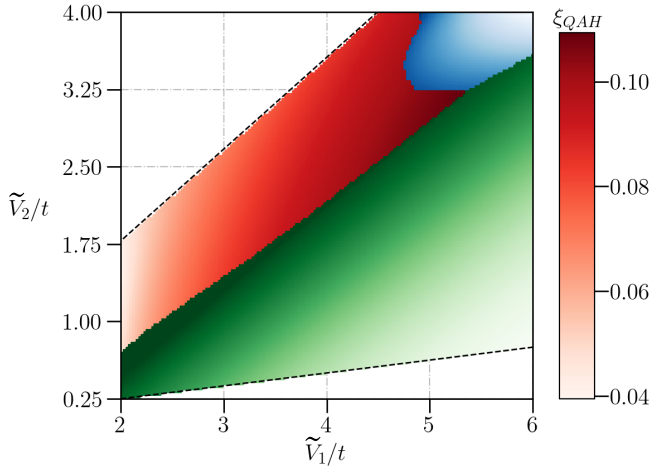

FIGURE 5.4: Ground-state phase diagram for effective Rydberg interactions at $T = 0$. We retrieve the three insulating phases observed in the $M = 2$ case and shown in Fig. 5.1(b): site-nematic in green, stripe in blue, and topological QAH phase in red. The diagram is bounded below by the largest ratio $\tilde{V}_1/\tilde{V}_2 = 8$ attainable within the Rydberg-dressed potential and above by the truncation condition $\tilde{V}_1 > 10\tilde{V}_5$.

The site-nematic phase prevails in large part of the phase diagram, owing to the predominance of $\tilde{V}_1$ over the other interactions. A QAH phase emerges as $\tilde{V}_2/\tilde{V}_1$ increases. We observe that the QAH region in the phase diagram is considerably larger than that of the $M = 2$ model, in Fig. 5.1(b), as effect of the frustration introduced by the competition between multiple charge orders. The topological order parameter ξ_{QAH} assumes larger values at larger $\tilde{V}_1$ and $\tilde{V}_2$, as indicated by the darker red color.

5.3.2 Finite temperature

We here study the stability of the QAH phase with respect to temperature by means of the finite-temperature HF method, where the occupations of the HF single-particle states with energies E_i are given by the Fermi-Dirac distribution

$$f(E_i) = \frac{1}{1 + e^{(E_i - \mu)/(k_B T)}}. \tag{5.18}$$

Figure 5.5(a) presents the energy band gap E_{gap} along the cut in the phase diagram indicated by the yellow line in the inset. The gap refers to the HF single-particle band structure, at half-filling and for different temperatures. While the traditional notion of topology is typically defined at zero temperature, one can still

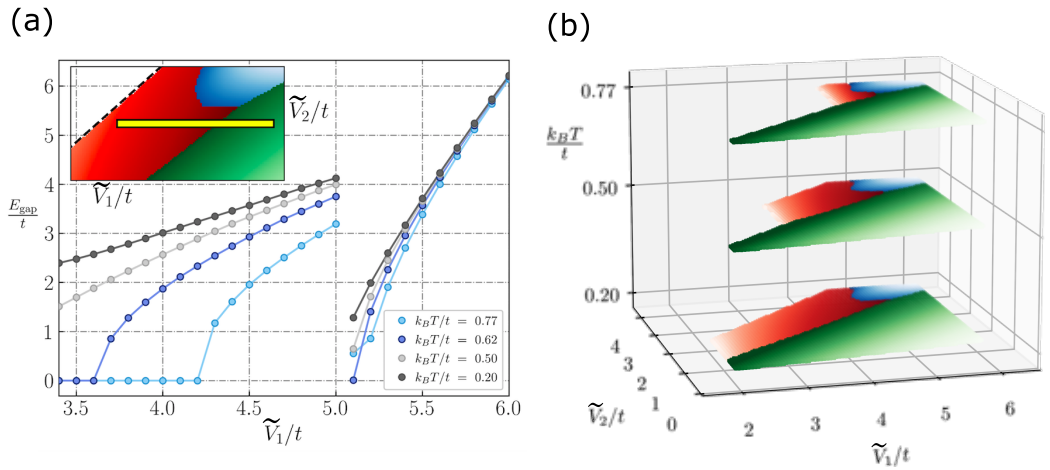

FIGURE 5.5: Finite temperature analysis of the QAH phase with Rydberg atoms. (a) Gap in the energy band structure at finite temperatures, for effective Rydberg interactions with $\tilde{V}_2 = 3$, corresponding to the yellow cut in the inset (clip of the phase diagram in Fig. 5.4). (b) Mean-field phase diagrams at finite temperature. Darker red indicates stronger topological order (see Fig. 5.4). All phases are robust against thermal excitations up to $k_BT/t \simeq 0.2$. Higher temperatures progressively break the topological phase. No QAH phase is observed above $k_BT/t \simeq 1$. For a realistic value of the hopping $t/\hbar = 1.7$ kHz [311], the temperatures in the z-axis correspond to $T \in \{16,\ 40,\ 63\}$ nK.

use the notion of a topological invariant at finite temperature for the density matrix [324], provided that the thermal energy scale k_BT is lower than this insulating gap $E_{\rm gap}$.

As a first remark, we note that the zero-temperature gap $E_{\rm gap}(T = 0)$, not shown, is indistinguishable from the gap at $k_BT/t = 0.2$. The sharp discontinuity at $\tilde{V}_1 \simeq 5t$ pins the phase transition between the QAH and the site-nematic phase. This jump in the value of the gap, in agreement with the first order nature of the transition, can be understood from the fact that this quantity is correlated with the value of the order parameter of the respective phase: when approaching the transition from the QAH side, both the current loop order as well as the gap are enhanced, whereas when approaching it from the site-nematic phase the charge order as well as the gap vanish. With regards to the QAH phase, the gap $E_{\rm gap}$ is of the order of the hopping rate t in most of the QAH region, taking the maximum value of about $4t$ around $\tilde{V}_1 = 5t$, $\tilde{V}_2 = 3t$. From the zero temperature gap analysis, one would estimate that the topological QAH phase is robust for temperatures up to a few t/k_B. However, given the interacting nature of the HF band structure, a finite temperature calculation of the gap is required in order to establish the critical temperature of the QAH phase. As shown in Fig. 5.5(a), the gap decreases nonlinearly with increasing temperature, affecting most rapidly states with smaller gap at $T = 0$. Ultimately, we can roughly estimate a critical temperature for the appearance of the QAH phase of about $T_c = t/k_B$, well below the temperature $T \simeq 4t/k_B$ suggested by the gap structure at $T = 0$. Using $t = 1.7$ kHz, a value on the scale of current experimental realizations [311], we obtain a critical temperature of $T_c = 82$ nK around $V_1 = 5t$ and $V_2 = 3t$.

It is also worth visualizing the effect of temperature without restricting to a point or a line of the phase diagram. To this end, in Figure 5.5(b), we show the whole phase diagram of $\hat{H}_{\rm R}$ at three different finite temperatures.

The QAH phase emerges from the competition between kinetic energy and the frustrated charge order driven by the interaction. As such, it results to be most fragile against thermal fluctuations. As the temperature increases, the valence-conduction gap of all insulating phases is progressively reduced, with a major impact on the QAH phase. The QAH gap closes first in the region of lower $\tilde{V}_1$ and $\tilde{V}_2$, where the zero-temperature current loop is smaller, leading to a gapless semi-metallic phase.

5.4 Experimental parameters analysis

In this section we study the relevant experimental parameter regimes to simulate the model of Eq. (5.17) with Rydberg-dressed atoms [302–305] in an optical lattice. Notice that this dressing technique has been already widely used in several recent experiments [306–311], which have succeeded in engineering tunable long-range interactions in two-dimensional systems. Of particular interest for the simulation of the TMI phase is the experiment of Ref. [311], which has allowed for the observation of a long coherence time in a two-dimensional Fermi lattice gas, in the presence of tunnelling and inducing strong nonlocal interactions [311]. Such system paves the way towards the quantum simulation of other Fermi-Hubbard Hamiltonians with long-range interactions, including models with topological properties.

Motivated by this prospect, we investigate and identify parametric regions for which a similar experimental system would well approximate the model of (5.17) and allow one to reach the interaction-induced topological phase. To begin the analysis, we consider the coherence time as a crucial figure of merit in the context of many-body quantum simulations. In a Rydberg-dressed cold gas, coherence is affected by spontaneous decay of atoms from the Rydberg state, which limits the time scale up to which the effective Hamiltonian (5.17) faithfully describes the system; the time scale is given, in a simple single-particle picture, by the effective Rydberg decay rate

$$\Gamma_{\text{eff}} = \left(\frac{\Omega}{\Delta}\right)^2 \Gamma_0, \tag{5.19}$$

where Γ_0 is the bare decay rate of the Rydberg state. Thus, Γ_{eff} sets a lower limit for both the hopping and the interaction rates, namely that $t, \tilde{V}_i > \Gamma_{\text{eff}}$.

We now show that the experimental conditions allowing one to engineer and observe the topological phase can be attained by a suitable choice of atomic and laser system parameters. The choice of the atomic species and the target Rydberg state determines the van der Waals interaction strength C_6, the bare decay rate Γ_0, the wavelength of the optical lattice a_{latt} at which the species can be trapped, and the upper bound to the tunneling amplitude t [4]. The remaining free parameters are the detuning Δ and the Rabi frequency Ω, which can be tuned by means of external laser fields.

We envision the quantum simulation being based on a light atomic species in order to favour the itinerant character of the TMI phase, hence we consider the fermionic isotope ^{6}Li of Lithium. This species can be trapped in optical lattices of wavelength $a_{\text{latt}} = 752$ nm and is accompanied by a fast tunneling which we assume to be $t \simeq 3$ kHz. A repulsive and isotropic van der Waals interaction can be found between atoms in $|nS\rangle$ Rydberg states, for which the series of C_6 values can be calculated using the library from Ref. [325]. Here we consider a Rydberg coefficient $C_6 \simeq 100$ MHz a_{latt}^6, which can be attained for principal quantum numbers roughly

[4] Notice that the tunneling t can be further fine-tuned by changing the lattice depth

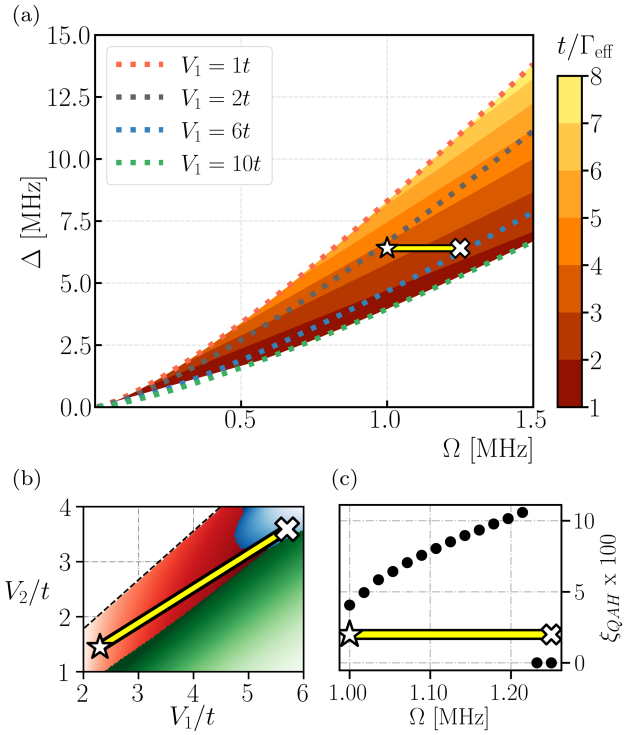

FIGURE 5.6: Laser parameters giving access to the QAH phase. Relevant parameters are fixed to plausible values for this type of experiments: $1/\Gamma_0 = 30$ μs, $C_6 = 100$ MHz $a_{\rm latt}^6$, $t = 3$ kHz. (a) Figure of merit $t/\Gamma_{\rm eff}$ in the $\Delta - \Omega$ plane. The dotted curves have constant $\tilde{V}_1/t$. The QAH phase emerges for $2 \leq \tilde{V}_1 \leq 6$ and $\tilde{V}_2/\tilde{V}_1 \in \{0.9, 0.5\}$. In this region, the hopping is always larger than the effective Rydberg time decay. A possible trajectory to cross the QAH phase is indicated by the oriented yellow line, at $\Delta = 6$ MHz, corresponding to $\tilde{V}_2/\tilde{V}_1 = 0.62$. (b) A clip of Fig. 5.4, where we indicate the oriented yellow line. (c) Amplitude of the QAH order parameter along the oriented line.

above $n = 33$. For these states, the radiative lifetime is estimated to be approximately $1/\Gamma_0 \simeq 30$ μs [326]. We fix the parameters mentioned so far and leave out Ω and Δ as independent variables.

Figure 5.6(a) shows the figure of merit $t/\Gamma_{\rm eff}$, i.e., the ratio between the tunneling rate and the effective Rydberg decay rate, as a function of the free parameters Ω and Δ, as given by Eq. (5.19). An important remark here is that, for each point in Fig. 5.6(a), the values of the interactions $\tilde{V}_i$ are determined by the rest of the fixed experimental parameters discussed above. In particular, we only show $t/\Gamma_{\rm eff}$ in the region comprised between the equipotential lines $\tilde{V}_1 = t$ and $\tilde{V}_1 = 10t$ that can be obtained from the condition

$$\frac{\tilde{V}_1}{t} = \frac{2\Omega^4}{t\Delta^3}\left(1 + 2a_{\rm latt}^6\Delta/C_6\right). \tag{5.20}$$

Notice that for this range of interaction strengths, relevant for the simulation of the TMI phase, the hopping rate is always larger than the decay rate, i.e., $t/\Gamma_{\rm eff} > 1$. Therefore, the system is expected to experience sufficiently long coherent dynamics before spontaneous decays begin.

We now discuss a specific region of Δ and Ω that allows one to reach the TMI phase. In particular, we consider the yellow line at a fixed $\Delta = 6$ MHz in Fig. 5.6(a), which corresponds to fixing the ratio $\tilde{V}_1/\tilde{V}_2 = 0.62$, as can be inferred from Eqs. (5.13)-(5.14). The interaction parameters spanned by this yellow line are mapped into the

phase diagram of Rydberg-dressed atoms in Fig. 5.6(b). The current loop order parameter ζ_{QAH} along this cut is also shown in Fig. 5.6(c): within this parametric span one can access the topological phase.

As an example, we can choose to pin $\tilde{V}_1 = 4t$ in this yellow line, which corresponds to $\tilde{V}_2 = 2.5t$, $\tilde{V}_3 = 0.63t, \tilde{V}_4 = 0.34t$; this specific set of $\tilde{V}_i$ is illustrated by the circles shown in Fig. 5.2. For this example, we obtain a large current loop order $\zeta_{\mathrm{QAH}} \sim 0.08$, a moderate decay rate leading to $t/\Gamma_{\mathrm{eff}} \sim 4$, and the ground state is relatively robust to thermal fluctuations with a critical temperature of $k_{\mathrm{B}}T \sim 50$ nK, obtained from the finite-temperature gap analysis of Fig. 5.5(a).

As a conclusive note, we remark that the observation of collective phenomena in the quantum simulation set-up considered here critically hinges on the validity of Eq. (5.19) to describe the decay rate of macroscopic metastable Rydberg-dressed states. Previous experiments have observed a rather larger decay rate, scaling with the number of particles. This phenomenon is modelled as a blackbody-driven collective resonant decay from the dressed state, an avalanche mechanism triggered by the first individual atom decay that drives the entire system out of its simulation task. The suppression of this avalanche mechanism will be crucial in order to scale the system size and was to a good extent achieved by the authors of Ref. [311].

5.5 Summary

In this chapter, we have investigated a TMI model and addressed the question regarding its quantum simulation with state-of-the art experimental methods. More precisely, we have considered a Fermi-Hubbard Hamiltonian on a checkerboard lattice with inter-site density-density interactions, a model which is known in the literature to host a QAH phase in the $V_1 - V_2$ case, i.e. when featuring interactions up to NNN [3, 161–163]. After a review of the $V_1 - V_2$ model in HF approximation, we have discussed a possible implementation of a similar model with Rydberg-dressed atoms in an optical lattice, motivated by the technological progress reached in the field of optically trapped cold Rydberg atoms [277], as highlighted by recent experiments [311]. As this realistic model typically contains interaction terms beyond the V_2 NNN interaction, we have also used the HF method to unveil the impact of longer-range interactions. Interestingly, we have observed that the Rydberg-dressed model Hamiltonian hosts a larger QAH phase in the ground-state phase diagram, as compared to the $V_1 - V_2$ model, which constitutes an encouraging result for the purpose of quantum simulating the model. We have furthermore performed a finite-temperature HF analysis of the QAH phase, which has revealed that temperatures below 100 nK are needed to observe the phase. Finally, we have discussed concrete sets of atomic and laser parameters allowing to access the QAH phase in an experiment, based on our numerical studies, and the modelling of the tight-binding interacting Hamiltonian describing Rydberg-dressed atoms in a checkerboard optical lattice.

Chapter 6

Self-trapped polarons and topological defects in a topological Mott insulator

The possibility to quantum simulate a TMI with Rydberg-dressed atoms, as discussed in Chapter 5, provides a route to investigate an interaction-induced Chern insulator. Interaction-induced topological insulators are quite different from externally induced topological phases [87]. On the one hand, the addition or removal of particles in the insulating state cannot be described within a rigid band picture, as the added or removed particles strongly interact with the rest of the system. On the other hand, the most important difference is arguably the ground-state degeneracy. In the case of externally induced Chern insulators, the bulk ground state is non degenerate, whereas the ground state of the TMI is twofold degenerate. That is, the SSB nature of the phase leads to two degenerate ground states characterized by opposite-valued Chern numbers. Interestingly, these two exotic properties of the TMI, not present in its noninteracting counterparts (e.g., the Haldane model of Section 2.4.2), naturally lead to many scenarios in which the system also breaks spontaneously the translational symmetry of the half-filled state.

Notice that such solutions breaking translational invariance are common in insulating magnetic systems, such as in the antiferromagnetic phase of many Fermi-Hubbard models [327, 328]. There, the addition of particles to the insulating state typically results in the breaking of an interacting band picture and the creation of localized polaron solutions. Moreover, for a large number of added or removed particles, these form spatial structures separating the two degenerate antiferromagnetic configurations, i.e., the well-known phenomenon of magnetic domain walls.

In this chapter, we show that similar solutions are also present in the TMI, and that they exhibit novel properties due to the presence of a topological invariant characterizing each of the two degenerate ground states. We focus on its appearance at the HF level when working with incommensurate fillings around half filling. That is, we study solutions of the hamiltonian $\hat{H}$ of Eq. (5.1) of the previous Chapter 5 with a particle number

$$N = L + \delta, \tag{6.1}$$

where δ is the number of added particles from half filling.

This chapter, based on Ref.[3], is organized as follows. Before presenting the numerical results at finite dopings, in Section 6.1 we introduce the Local Chern number, a quasi-local topological invariant needed to characterize spatially inhomogeneous TMIs. In Sections 6.2-6.3 we present, respectively, the main results concerning the appearance of self-trapped polarons and domain walls in a doped TMI. For simplicity, there we neglect the full Rydberg potential described in Section 5.2, and fix the

value of the interactions to $V_1/t = 2.5$ and $V_2/t = 1.5$, which corresponds to a point deep in the topological Mott insulating phase in the simplified $V_1 - V_2$ model. The effect of Rydberg interactions is left for Section 6.4, where we also discuss the fate of these inhomogeneous solutions at finite temperature.

6.1 Local Chern number

The analysis of Chern Insulators breaking translational invariance might seem complicated from the point of view that the Chern number is usually defined for a translationally invariant bulk, i.e., it is computed from the Bloch band structure. In the presence of local disorder, the use of twisted boundary conditions provides a route to define a Bloch band structure and compute the Chern number, but still under the assumption that the hole system is described by a unique topological invariant.

The Local Chern number $\mathcal{C}$, introduced by Bianco and Resta [329, 330], provides a powerful tool in this context, as it allows to compute the Chern number in finite regions of a system. The latter is useful to compute the Chern number in the presence of disorder, for nonperiodic structures such as quasicrystals, or to study changes of this topological invariant inside the bulk of a system. The value of $\mathcal{C}$ is quantized to the same value as the Chern number for a finite but sufficiently large subregion, and a nonzero value indicates the presence of topologically protected chiral states at the edges of the bulk in which $\mathcal{C}$ is computed. For completeness, we briefly outline the computation of this quantity. First, we define the projectors onto the occupied and unoccupied single-particle states of the UHF Hamiltonian

$$P = \sum_{i \in \text{occ}} |\Phi_i\rangle \langle \Phi_i| , \qquad \hat{Q} = \mathbb{1} - \hat{P}. \tag{6.2}$$

We also define the operators

$$\hat{\boldsymbol{r}}_P = \hat{P}\hat{\boldsymbol{r}}\hat{Q} = (\hat{x}_P, \hat{y}_P), \qquad \hat{\boldsymbol{r}}_Q = \hat{Q}\hat{\boldsymbol{r}}\hat{P} = (\hat{x}_Q, \hat{y}_Q). \tag{6.3}$$

These operators are quasi-local, in the sense that $\langle i| \hat{r}_{P,Q} |j\rangle \sim \exp\{(-\kappa_{P,Q}\|i-j\|)\}$. Now, we define the local Chern marker as

$$\mathfrak{C}(i) = -4\pi \text{Im}\left[\sum_j \langle i| \hat{x}_Q |j\rangle \langle j| \hat{y}_P |i\rangle\right] \tag{6.4}$$

with

$$\langle i| \hat{x}_Q |j\rangle = \sum_l Q(i,l) x_l P(l,j), \ \langle j| \hat{y}_P |i\rangle = \sum_l P(j,l) y_l Q(l,i). \tag{6.5}$$

Finally, to compute the Chern number $\mathcal{C}$, one has to perform the spatial average of the local Chern marker of (6.4).

$$\mathcal{C} = \frac{1}{A_{\text{disk}}} \sum_{i \in \text{disk}} \mathfrak{C}(i), \tag{6.6}$$

where the disk is the set of points inside a circle of a certain radius, considered to lie inside the bulk of the lattice, where edge effects do not play a role, and A_{disk} is the area of this disk. In this work, we always set the radius to $r = a/\sqrt{2}$, where a is the distance between NN.

6.2 Self-trapped polarons

We now focus on the TMI at low particle doping δ, starting for the case of one extra particle ($\delta = 1$). We first study the translational invariant solution with the RHF method and a four-site unit cell ansatz. The resulting single-particle states around half-filling are shown as diamonds in Fig. 6.1(a); the self-consistent band structure exhibits only a slight deformation of the bands due to interactions and, indeed, we observe the occupation of a single-particle state above the gap. This result corresponds to a noninteracting rigid band picture, e.g., the δ added particles populate the half-filling upper band in the absence of edges (periodic boundary conditions). The energetic cost of this addition takes the value of the insulating gap, and the system looses its insulating character. Notice that this is the same behavior that one would observe for $\delta = 1$ in the Haldane model outlined in Section 2.4.2. However,

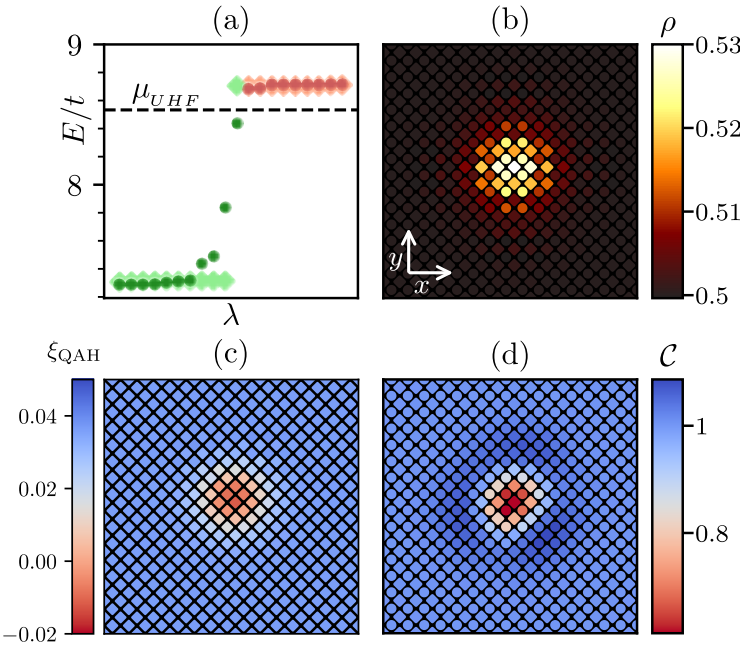

FIGURE 6.1: Self-trapped polaron for $\delta = 1$. (a) Energies of the eigenstates λ around the energy gap for the RHF (diamonds) and UHF (dots) ansatz. The dashed line indicates the chemical potential of the UHF solution, and green (red) colors are used for occupied (empty) states. (b)–(d) Real-space quantities in a region of 16×16 unit cells. (b) Density profile. (c) Local order parameter of the QAH phase ξ_{QAH}. (d) Local Chern number.

in the TMI there is also the possibility of lowering the energy by creating states inside the gap, which need to be localized in a finite region of the lattice, leading to a spontaneous breaking of translational symmetry. We study this possibility with the UHF ansatz, described in the preliminary Chapter 1, on a 24×24 unit-cell lattice. The results are shown in the same Fig. 6.1(a): the UHF bands are deformed in order to accommodate the extra particle, with the appearance of states inside the insulating gap, and a decrease of the energy $\Delta E_{\text{UHF}} \equiv \langle H \rangle_{\text{UHF}} - \langle H \rangle_{\text{RHF}} = -0.12t$. These midgap states are localized in a finite region of the lattice, leading to the density cloud shown in Fig. 6.1(b). We denote such state as the self-trapped polaron solution, as the added particle is confined due to its interaction with the topological background. Notice that this notion of a self-trapped polaron differs from the concept of a mobile polaron quasiparticle in a topological background [331]. Indeed, in this thesis we focus only on static properties, as it is not warranted that a study of

the polaron mobility can be made within a coherent quasiparticle picture due to the interaction-induced localization.

The appearance of self-trapped polarons and other localized excitations has been extensively studied using the UHF method [135, 327, 328] for nontopological phases. We here show that the topological character of the material leads to very interesting physics. On the one hand, Fig. 6.1(c) shows that, in the polaron region, there is a large reduction of the order parameter ξ_{QAH}, accompanied by a change of the SSB sector in the inner region. Notice that this behavior is similar to the one exhibited by the self-trapped antiferromagnetic polaron observed in the 2D Fermi-Hubbard model [327], and can be understood as a collapsed domain wall. On the other hand, as mentioned above, despite the lack of translational invariance one can characterize the topology of the system, by means of the local Chern number $\mathcal{C}$ [329, 330, 332]. As shown in Fig. 6.1(d), this quantity is not quantized at all inside the polaron; however, it stabilizes to $\mathcal{C} = +1$ further away from the latter. We emphasize that, as in the half-filling case, the sign of $\mathcal{C}$ depends on the ground-state SSB sector. Notice also that these local fluctuations of $\mathcal{C}$, which are caused by a spontaneous breaking of translational symmetry, are reminiscent of those induced by quenched disorder in a gauge-induced Chern insulator [333].

6.2.1 Configuration interaction analysis

We use the configuration interaction method [134–137], introduced in Chapter 1, to analyze the stability of the polaron localization within the UHF ansatz. That is, for different initial conditions on the UHF parameters, we get degenerate polarons centered at different sites, which corresponds to a flat polaron band in reciprocal space. It is important to check that such localization is not an artifact of the method. In a nutshell, in the configuration interaction method, one lowers the UHF energy by hybridizing several UHF solutions to restore some of the lattice symmetries spontaneously broken in each UHF solution. In our case, we restore the translational invariance of the polaron solution in smaller checkerboard lattices with up to $2 \times 9 \times 9$ sites, as shown in Fig. 6.2. Our analysis yields a polaron band supporting our UHF treatment: the minimum energy of the band is similar to the UHF energy (with a reduction of $\simeq 0.1\%$), and this energy corresponds to a plateau of degenerate states in a region of the band of size $|\Delta\mathbf{k}|$. The latter is compatible with a polaron extended over a finite region with radius $\ell_p \simeq 1/|\Delta\mathbf{k}|$, as observed in the UHF solution.

6.2.2 Two polarons

For two extra particles ($\delta = 2$) we find two types of self-consistent solutions. The lowest energy solution is a composite state of two polarons [see Fig. 6.3(a)]. The inner region of this bipolaron, slightly larger than the one corresponding to the single polaron, also exhibits a change in the SSB sector (not shown). The other type of solutions corresponds to two spatially nonoverlapping polarons [see Fig. 6.3(b)]. The latter are metastable solutions with a higher energy than the composite state, which indicates that there is an attractive interaction between polarons. However, for large initial separations, individual polarons are likely to be detectable. In order to characterize the formation of these metastable solutions, we choose for the initial UHF values those of a spatial superposition of two single polarons, and vary their initial separation. Figure 6.3(c) shows the final distance between them d_{p-p} as a function of their initial separation d^0_{p-p}. Considering the self-consistent UHF algorithm as some virtual dynamics for the HF parameters, we observe a collapse radius $d^0_{p-p} \simeq 12$ in

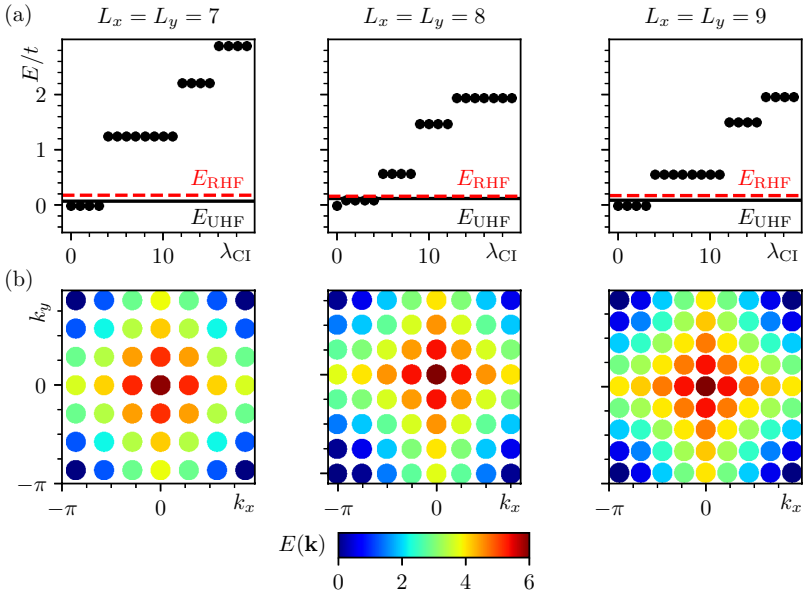

FIGURE 6.2: Results of the configuration-interaction method applied to the extended polaron obtained in the UHF ansatz ($\delta = 1$). (a) Configuration-interaction spectrum for three different lattice sizes. The UHF (RHF) energies are indicated as solid black (dashed red) lines. For each lattice size, the zero of energy is set as the CI ground state energy. (b) Configuration-interaction band structure.

the initial separation, below which the two polarons interact until the stabilization of the lowest energy composite solution with $d_{p-p} \simeq 9$ is achieved. At larger initial separations, the system stabilizes the nonoverlapping solution, with a forbidden range $d_{p-p} \in (12, 25]$, showing that metastable solutions avoid residual overlaps.

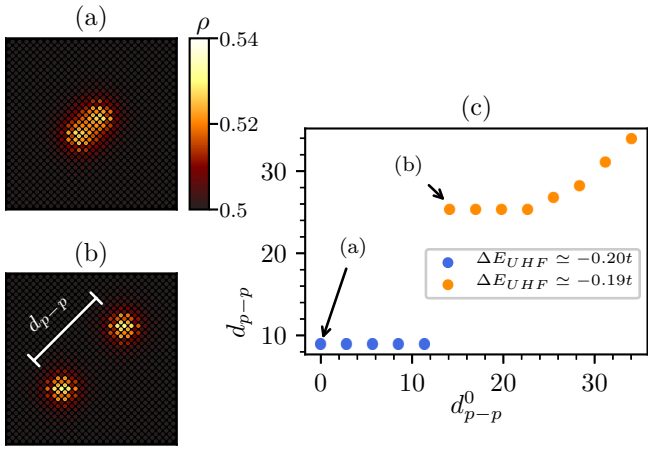

FIGURE 6.3: Two polarons for $\delta = 2$. (a),(b) Density profile of the composite and nonoverlapping solutions. (c) Final distance between the two polarons, taken as the separation between the two sites with largest density, as a function of the separation in the initial ansatz for the UHF values. Blue (orange) circles correspond to composite (nonoverlapping) solutions.

6.3 Topological defects

Even at higher particle doping, we find that the system retains its bulk insulating character: it is energetically favorable to create several midgap localized states, as can be seen in Fig. 6.4(a) for $\delta = 8$. Taking as a reference the polaron solutions, the attractive interaction between them leads to a ground state whose inner region is in the other SSB sector. For a sufficiently large value of δ, this eventually leads to the formation of a domain wall between two extended half-filling regions that are in the QAH phase, as can be seen in Fig. 6.4(b). Interestingly, the inversion of the time-reversal SSB order parameter across the domain wall leads to the two opposite values of the local Chern number $\mathcal{C} = \pm 1$ depicted in Fig. 6.4(b). Notice here the role of interactions, leading to a SSB: the coexistence of topologically opposite phases would not occur if the Chern insulator was induced by a homogeneous external gauge field, that would define the global topology sector of the system. Furthermore, the change of the local Chern number $|\Delta\mathcal{C}| = 2$ between the two regions gives rise to topologically protected edge states with a fixed chirality in the ring. This is exactly what we observe in the ground-state currents $\mathcal{J}_{x(y)} \equiv 2J^{A/B}_{x(y)}\mathrm{Im}\langle \hat{c}^{\dagger}_{i+x(y)}\hat{c}_i\rangle$ shown in Figs. 6.4(c) and 6.4(d), which are carried by midgap states. We also verified that the solution with $\mathcal{C} = -1$ in the inner part of the rig and $\mathcal{C} = 1$ in the outer part has the same energy and presents edge states with opposite chirality.

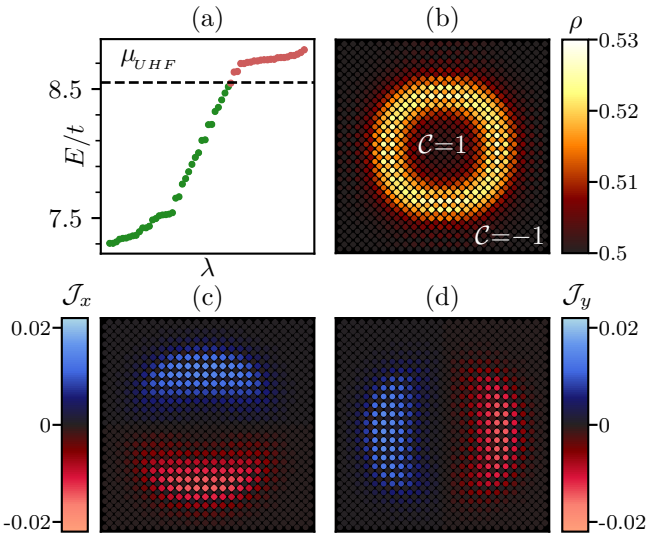

FIGURE 6.4: Domain wall for $\delta = 8$. This UHF solution lowers the RHF energy by $\Delta E_{\mathrm{UHF}} \simeq -0.67t$. (a) Single-particle energies in the gap region. (b) Density profile. Here we indicate the approximately constant value of $\mathcal{C}$ in the inner and outer regions of the ring. (c),(d) Ground-state currents $\mathcal{J}_x$ and $\mathcal{J}_y$.

For $\delta = 8$, we also find a metastable self-consistent solution, in which the system develops two domain walls (see Fig. 6.5). The extra density is deposited in these linear structures, as depicted in Fig. 6.5(b). As in the previous case, the domain walls separate two regions with a reversed time-reversal SSB order parameter, leading to two opposite values of the local Chern number, as can be seen in Fig. 6.5(c). The main difference, however, is that here the change in the local Chern number $|\Delta\mathcal{C}| = 2$ occurs in each of the two disconnected domain walls, leading to pairs of degenerate chiral edge states (one at each domain wall) with opposite chiralities, as shown in Figs. 6.5(a)-6.5(d).

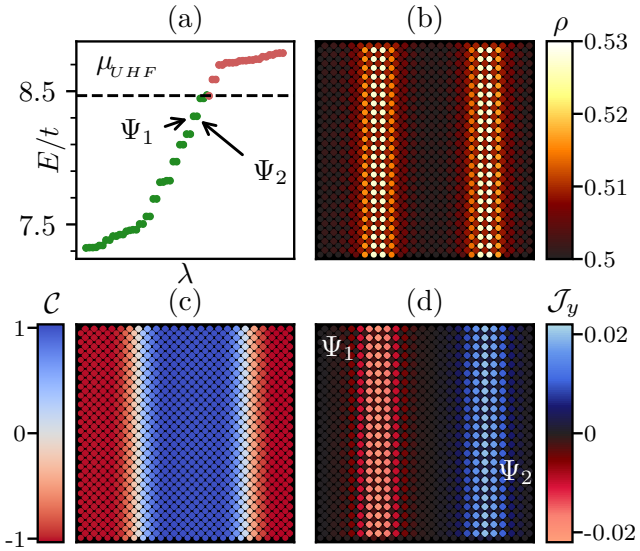

FIGURE 6.5: Linear domain walls for $\delta = 8$. This metastable UHF solution lowers the RHF energy by $\Delta E_{\text{UHF}} \simeq -0.65t$. (a) Energies in the gap region, with two degenerate edge states Ψ_1 and Ψ_2. (b) Density profile. (c) Local Chern number. (d) Current $\mathcal{J}_y$ flowing in opposite directions at each boundary, and carried by midgap states such as Ψ_1 and Ψ_2.

6.4 Fate of defects in Rydberg-dressed atoms

In this section we analyze the stability of the nonhomogeneous solutions presented above in the presence of the realistic Rydberg interactions described in Section 5.3. As the location of the QAH phase in the phase diagram is shifted when including the Rydberg-dressed potential up to fourth-order neighbors, here we use the values of interactions $V_1 = 4t$, and $V_2 = 2.5t$, which correspond to a point deep in the QAH phase (see Fig. 5.4).

Figure 6.6 shows that at finite doping one encounters the same type of localized solutions obtained with the simplified $V_1 - V_2$ model. In the case $\delta = 1$, Fig. 6.6(a) shows that the added particle does not populate the conducting band but instead occupies a midgap localized state induced by interactions, a self-trapped polaron. In this solution, the local current loop order ξ_{QAH} changes its sign inside the polaron region, which can be understood as a collapsed domain wall. As δ increases, the number of mid-gap states and the polaron size also increase [see Fig. 6.6(b)]. Eventually, we observe the formation of a ring-shaped domain wall separating an inner and outer region with opposite current chiralities [see Fig. 6.6(c)] which correspond to opposite Chern numbers inside and outside the ring.

6.4.1 Finite temperature analysis

In Section 5.3.2 we saw that, at half filling, the critical temperature of the QAH phase at which the gap closes is roughly $k_{\text{B}}T_c \sim t$ for Rydberg-dressed atoms, within the HF ansatz. At incommensurate fillings, one expects a lower critical temperature for the defects, as they are related to mid-gap states. To provide with a quantitative example of this behavior, in Fig. 6.7 we show the finite temperature solutions for $\delta = 5$, which corresponds to a ring-shaped domain wall at zero temperature, as seen in Fig. 6.7(a). Fig. 6.7(b) shows the results for a first finite temperature $k_B T/t = 0.05$; while there is no appreciable difference of the order parameter in real space compared to the zero temperature case, the conducting band starts to be populated.

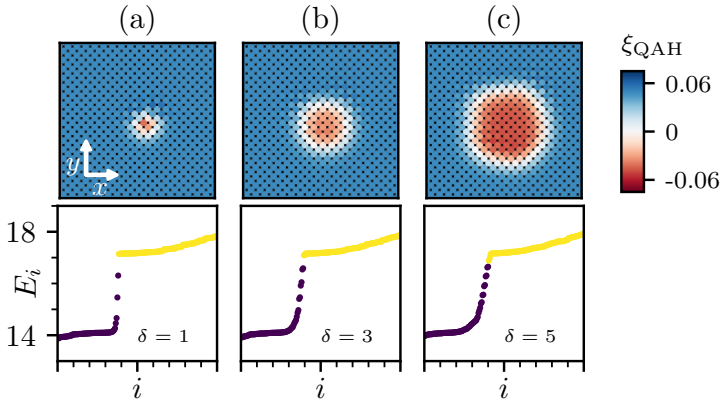

FIGURE 6.6: Incommensurate solutions at zero temperature in a 24×24 unit cells lattice. Here we choose the Rydberg potential such that $\tilde{V}_1 = 4t$, and $\tilde{V}_2 = 2.5t$, leading to $\tilde{V}_3 = 0.63t$, and $\tilde{V}_4 = 0.34t$. The number of added particles is $\delta = 1,\ 3,\ 5$ in (a),(b), and (c), respectively. (upper panels) Real-space profiles of ξ_{QAH}. (lower panels) Hartree-Fock single-particle spectra corresponding to the solutions shown in the upper panels. Yellow (dark purple) points represent empty (occupied) sites.

For an even higher temperature $k_B T/t = 0.2$, Fig. 6.7(c) shows that the spatially homogeneous QAH phase is recovered, but one sees that the excess particles are distributed in the upper band, destroying the gap insulating nature of the phase. Note, however, that at this temperature inhomogeneous solutions also appear as metastable states, and could be present as a consequence of a temperature annealing process from a high temperature disordered phase to the low temperature ordered QAH phase, or due to the crossing of a quantum phase transition [334–336].

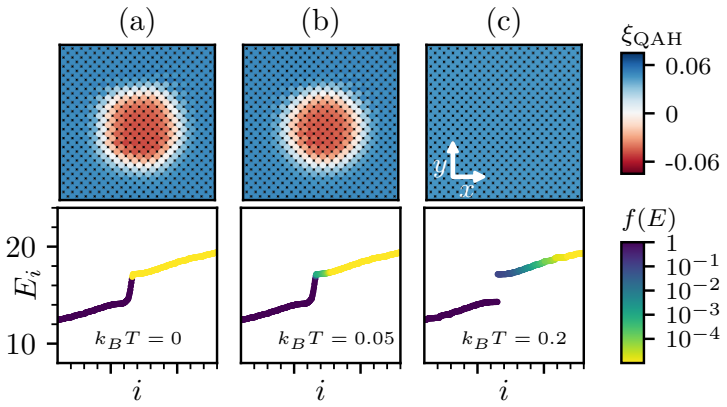

FIGURE 6.7: Temperature behavior of the ring solution obtained for $\delta = 5$. Here we consider the same lattice size and interactions used in Fig. 6.6. The temperature in (a),(b), and (c) panels is $k_B T/t = 0,\ 0.05,\ 0.2$, respectively. (upper panels) Real-space profile of ξ_{QAH} for different temperatures. (lower panels) HF single-particle spectrum corresponding to the upper panels. The color code indicates the Fermi occupation $f(E)$ of each state.

6.5 Summary

In this chapter, we have investigated the exotic consequences of the ground state degeneracy exhibited by the half-filled TMI state, introduced in Chapter 5. In particular, we have shown that, for finite particle dopings around the half filling insulating state, the ground state of the system exhibits rich spatial properties intertwined with

the topological nature of the system. The latter type of solutions take the form of self-trapped polarons at low particle dopings, or domain walls separating two TMI states with opposite Chern number, when larger particle dopings are considered. For our numerical analysis, we have employed an UHF method in real space, and a quasi-local definition of the topological invariant, the local Chern number. The latter have provided us with a route to describe the presence of more than one topological invariant in the bulk of the system, and the appearance of interaction-induced edge states in the bulk, located at the domain walls. Finally, in connection with the analysis of a quantum simulation scheme for the TMI with Rydberg-dressed atoms, introduced in Chapter 5, we have also confirmed the presence of self-trapped polarons and domain wall solutions for finite particle dopings when considering a Rydberg-dressed interaction potential, and for moderate finite temperatures.

Chapter 7

Topological Mott insulator in quasi two-dimensional geometries

In the past decades, the development of tensor network approaches, together with the increase in computer capabilities, has allowed us to improve our understanding of many two-dimensional physical systems that previously could only be treated approximately with, for instance, mean-field methods. In the case of the DMRG algorithm, while its application to two-dimensional systems is restricted to quasi two-dimensional geometries, such as cylinders or ladders with finite widths, it is still one of the most powerful methods available to describe two-dimensional strongly correlated phenomena [156]. A paradigmatic example is the case of the underdoped two-dimensional spinful Hubbard model: early HF studies [129, 337, 338] pointed towards the presence of a stripe order in this model, which has been recently confirmed in two-dimensional DMRG studies [158, 159].

In the case of the TMI, while in previous sections we limited ourselves to a mean-field HF treatment, the stability of the phase in the model under consideration is confirmed by DMRG studies [161, 162] at half filling and considering up to next-to-nearest neighbor interactions. In this chapter, we perform a thorough DMRG analysis of the system in a cylinder geometry, in order to capture quantum fluctuations beyond mean-field that typically lead to shifts of the phase boundaries. Apart from confirming the novel results obtained in the previous chapters with the HF approximation, we also generalize the DMRG computation of the Chern number for systems in which this topological invariant takes more than one quantized value in the bulk of the system. Furthermore, we also discuss experimental aspects concerning the state preparation and detection of the TMI phase that can be properly analyzed within the numerical accuracy of the DMRG method.

This chapter is organized as follows. In Sections 7.1 and 7.2, we outline the numerical lattice model and DMRG algorithm used to solve it. In Section 7.3, we present the DMRG results for the half-filling phase. After confirming the presence of a TMI in a wide region of parameters, including the case of Rydberg-dressed interactions, we review the computation of the Chern number in this interacting system by means of a periodic flux insertion. In Section 7.4, we confirm the appearance of inhomogeneous TMI states around half filling, by analyzing a DMRG solution for which a hole is doped into the half-filled state. We furthermore generalize the periodic flux insertion in order to analize the Chern number of such exotic states exhibiting a topological domain wall structure. In Section 7.5, we use an efficient method to draw local density snapshots of an MPS to simulate the experimental measurement of quantized transport of charges, useful to determine the Chern number in optical lattices. Finally, in Section 7.6, we focus on prospects to adiabatically prepare the TMI state. With this aim, we introduce a control parameter of the optical lattice and

use the DMRG method to show that there is a continuous phase transition to the TMI when this parameter is varied.

7.1 Hamiltonian model in a cylinder geometry

Concerning the Hamiltonian used in this chapter, we consider a slightly different version of the one introduced in Eq. (5.1) and used in Chapters 5 and 6. To avoid confusion, we use the prime notation for the Hamiltonian of this chapter $\hat{H}' = \hat{H}'_0 + \hat{H}'_{\text{int}}$. On the one hand, here we consider the free Hamiltonian

$$\begin{aligned}\hat{H}'_0 = &- t\sum_{\langle ij\rangle}(\hat{c}^\dagger_{i,A}\hat{c}_{j,B} + \text{H.c.}) + \\ &+ \sum_i \sum_{\substack{\alpha=A,B \\ \nu=x,y}} (J^\alpha_\nu \hat{c}^\dagger_{i,\alpha}\hat{c}_{i+2\nu,\alpha} + \text{H.c.}).\end{aligned} \tag{7.1}$$

Here t and J^α_ν take the same value as in Chapters 5 and 6: $t = 1$, and $J^A_x = J^B_y = +0.5$ and $J^A_y = J^B_x = -0.5$, which generates a π flux on each sublattice. Notice that in this chapter we work with an MPS representation of the ground state for which the particle number is a conserved quantum number during the DMRG algorithm, so we do not need to include a chemical potential term in the free Hamiltonian.

Regarding the interaction Hamiltonian, in this chapter we consider the form

$$\begin{aligned}\hat{H}'_{\text{int}} = V_1 \sum_{\langle ij\rangle}\left(\hat{n}_i - \frac{1}{2}\right)\left(\hat{n}_j - \frac{1}{2}\right) + V_2 \sum_{\langle ij\rangle_2}\left(\hat{n}_i - \frac{1}{2}\right)\left(\hat{n}_j - \frac{1}{2}\right) + \\ + V_3 \sum_{\langle ij\rangle_3}\left(\hat{n}_i - \frac{1}{2}\right)\left(\hat{n}_j - \frac{1}{2}\right) + V_4 \sum_{\langle ij\rangle_4}\left(\hat{n}_i - \frac{1}{2}\right)\left(\hat{n}_j - \frac{1}{2}\right),\end{aligned} \tag{7.2}$$

where the density-density interaction terms $\hat{n}_i\hat{n}_j$ of previous chapters are replaced by $(\hat{n}_i - 1/2)(\hat{n}_j - 1/2)$. On a torus (fully periodic boundary conditions) these two forms of interactions only differ by a global chemical potential term. However, for the cylinder under consideration, the sharp decay of interactions at the open borders in the case $\hat{n}_i\hat{n}_j$ leads to unwanted charge orders at the edges, which complicate the numerical analysis. On the contrary, such charge orders are considerably suppressed at or close to half filling when the H'_{int} of Eq. (7.2) is considered instead. Also notice that, even though V_3 and V_4 are not essential to obtain a QAH phase in the system, there are two reasons to include them. On the one hand, there is the physical motivation, as they are present in the Rydberg-dressed potential presented in the previous chapter. On the other hand, including finite values of such terms, especially of V_3, is convenient for numerically finding the QAH with DMRG. The reason is that they allow to work with smaller cylinder widths, as they prevent finite-size charge orders associated with the finite width of the cylinder and the breaking of inversion symmetry in the checkerboard lattice in such cylinder geometry.

7.2 Details of the tensor network algorithm

For the results of this section we apply the DMRG method [156] on a cylinder geometry [see Fig. 7.1(a)] of the checkerboard lattice introduced in Chapter 5. The lattice

has $L_y = 6$ two-site unit cells in the short direction, to which periodic boundary conditions are applied, and L_x in the long direction with open boundary conditions, giving a total of $L = 6L_x$ unit cells and $2L$ physical lattice sites. The one-dimensional folding of the cylinder sites into a chain is depicted in Fig. 7.1(b), and it allows to express the state of the system in the MPS representation. Furthermore, we start the DMRG with an MPS of bond dimension $\chi_{\text{min}} \simeq 1000$ (imposing $U(1)$ particle number conservation) and increase it progressively to bond dimensions up to $\chi_{\text{max}} = 4000$ in the last sweeps of the algorithm, leading to truncation errors of the MPS of 10^{-5} at most. The latter are in accordance with state-of-the art DMRG studies of similar TMI phases [161, 162, 274]. For the implementation of the algorithm we have used the TENPY [142] and ITENSOR [143] libraries. In terms of computational resources, it is worth to notice that the calculations presented in this chapter have been performed in a workstation with 256 GB of RAM memory, with an estimated time for a single run of the DMRG algorithm of more than 100 CPU hours. In some cases, when the RAM memory is not sufficient to perform the DMRG optimization, some of the tensors of the MPS can be written to disk, taking advantage of the implementation of this functionality in ITENSOR.

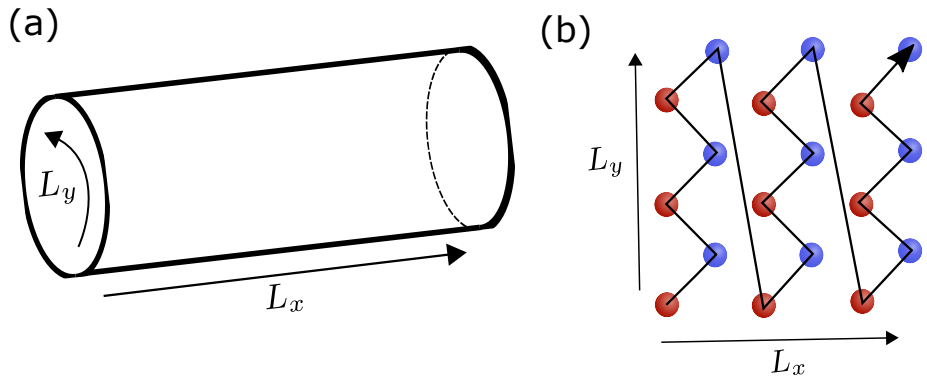

FIGURE 7.1: (a) Cylinder geometry used in the DMRG simulations. (b) Snake-like folding of the cylinder sites into a one-dimensional chain.

7.3 Half-filled topological Mott insulator in the cylinder geometry

Let us start by showing the appearance of the TMI with the DMRG method for $\hat{H}'$ in a concrete example at half filling, where we choose the values $V_1/t = 4$, $V_2/t = 2$, and $V_3/t = 0.5$. The finite DMRG method applied on a cylinder with $L_x = 32$ and $L_y = 6$ leads to the ground state of Fig. 7.2.

The current loop order between nearest-neighbors is shown in Fig. 7.2(a), and has a constant behavior in the bulk of the system. By evaluating Eq. (5.5) to a loop of nearest-neighbors, we obtain $\xi_{\text{QAH}} \simeq 0.063$ in the whole bulk. Such current loop order signals the SSB of the time-reversal symmetry in this ground state, characteristic of the QAH phase. In the DMRG, this symmetry is broken by introducing a small guiding field at the beginning of the algorithm, and turning it off after the initial sweeps. Figure 7.2(b) shows the density profile in the cylinder, which does not exhibit any appreciable charge order apart from a residual site-nematic edge order due to the open boundaries in the cylinder geometry.

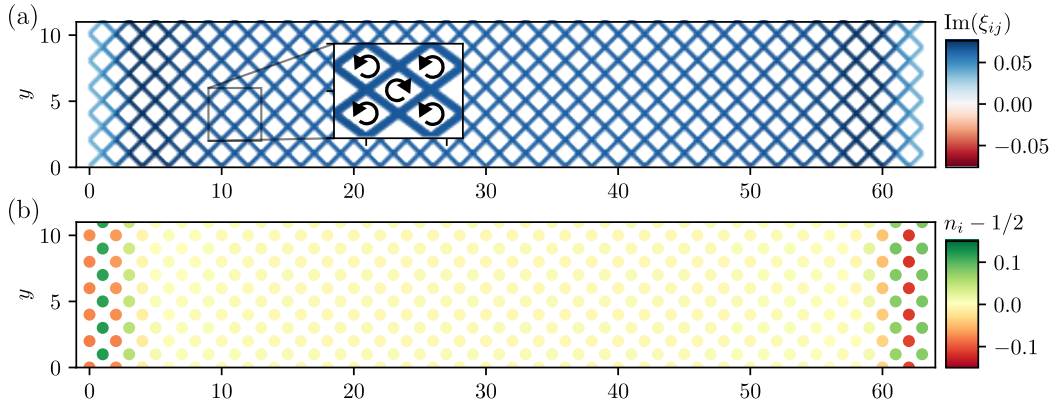

FIGURE 7.2: TMI at half filling obtained in a DMRG simulation. Here $V_1/t = 4$, $V_2/t = 2$, $V_3/t = 0.5$. (a) Current loop order between NN bonds. For positive values the current between two NN follows the arrow convention for a spatially homogeneous QAH state, as indicated in the inset. (b) Deviation of the local fermionic density with respect to half filling. One can observe small boundary effects due to the open boundary conditions, without a net charge accumulation in any of the edges.

Furthermore, as already observed with the HF method in Chapter 5, the QAH found with DMRG is neither restricted to fine tuned values of the interactions, and it is rather present in a wide region of parameters. To exemplify this, we parameterize the V_i interactions of the Hamiltonian (7.2) according to the Rydberg-dressed potential $\tilde{V}_i$ described in Eq. (5.14) of Chapter 5. We then study the evolution of the QAH order parameter ξ_{QAH} with the iDMRG method. The results are shown in Fig. 7.3. For a fixed $\tilde{V}_1/t = 4$ [Fig. 7.3(a)], the DMRG ground state leads to a site-nematic charge order at small values of V_2/t, as in the HF method. When increasing $\tilde{V}_2$, the DMRG calculation confirms the site-nematic to QAH phase transition. One observes a shift of the QAH boundary compared to the HF phase diagram of Fig. 5.4, which is expected since mean-field methods are known to be less accurate in the vicinity of a quantum phase transition. That is, with DMRG the QAH phase appears at $\tilde{V}_2/t \simeq 1.5$ and disappears for $\tilde{V}_2/t > 2.5$. In contrast, with a HF ansatz the QAH phase is not present until $\tilde{V}_2/t > 2$ and disappears for $\tilde{V}_2/t > 3.5$. We also establish

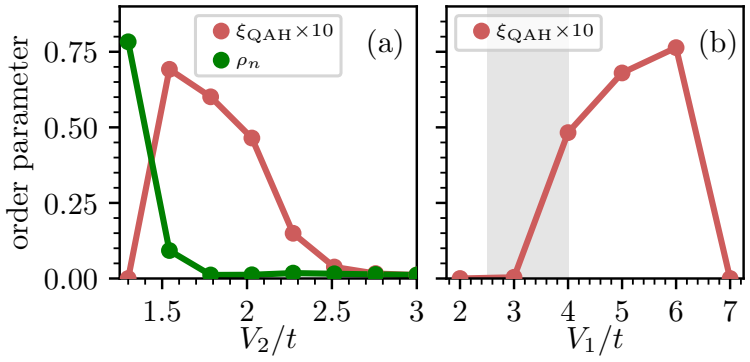

FIGURE 7.3: iDMRG study of the QAH phase considering the Rydberg potential. (a) QAH and site-nematic order parameters as a function of $\tilde{V}_2$ for a fixed $\tilde{V}_1/t = 4$. (b) QAH order parameter as a function of $\tilde{V}_1/t$ along the line $\tilde{V}_2 = \tilde{V}_1/2$

the existence of the QAH for a wide range of $\tilde{V}_1/t$ ratios, as shown in Fig. 7.3(b). As hinted by the previous HF calculations, the Rydberg potential stabilizes the phase

in a larger window of interaction strengths compared to the simplified V_1-V_2 model (shaded area extracted from Ref. [162]).

7.3.1 Topological pump

While the presence of a current loop order breaking time-reversal symmetry, together with the absence of charge orders, are clearly strong signatures for the presence of a QAH also with the DMRG method, the ultimate characteristic of this phase is that it is characterized by a quantized Chern number. Hence, here we show how we compute the quantized Chern number for ground states obtained in a DMRG simulation. Notice that the two-band formula of the Chern number in Eq. (5.10), or the local Chern number in Eq. (6.6), rely on a single-particle description of the interacting ground state, and thus cannot be used here, as the strongly correlated ground state is expressed in the MPS representation. Instead, we follow the flux insertion procedure, which was introduced by Laughlin as a gedanken experiment to interpret the quantization of the Hall conductance [339, 340]. According to Laughlin's argument, the Chern number is equal to the quantized $U(1)$ charge that is pumped from one edge of the cylinder to the other when inserting a $U(1)$ charge flux in the whole bulk.

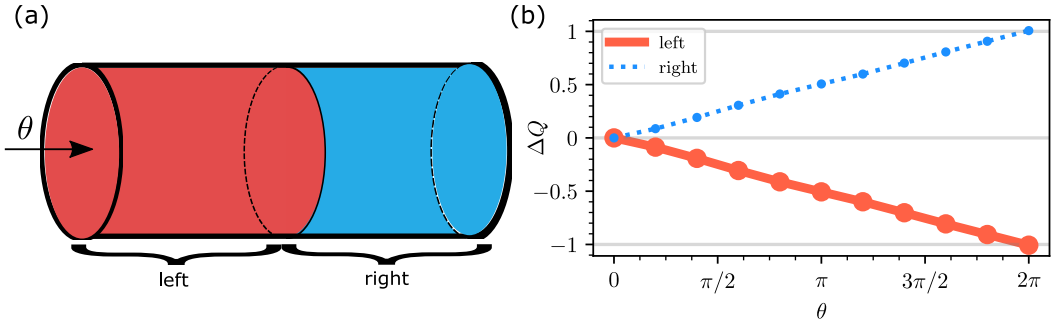

FIGURE 7.4: Pump protocol to determine the Chern number of the TMI state in the cylinder geometry. (a) A flux θ is inserted perpendicularly to the cylinder circumference, leading to a quantized charge transfer between the left and right regions. (b) Transfer of charge as a function of the inserted flux. One can observe a flow from the left to the right edge of the cylinder and a quantization of the total charge transferred at the end of the pumping protocol.

In DMRG, this procedure can be easily implemented as follows [341]. One defines the Hamiltonian $\hat{H}_0'(\theta)$, in which we modify the hopping terms crossing the y periodic boundary by $\hat{c}_i^\dagger \hat{c}_j \rightarrow e^{i\theta}\hat{c}_i^\dagger \hat{c}_j$, where $\theta \in [0, 2\pi]$. Starting from the DMRG solution of $\hat{H}_0'(0)$, the flux is inserted in small steps $\delta\theta$ until reaching $\hat{H}_0'(2\pi)$. The converged ground state at each θ is used as the initial state for the DMRG ground state at $\theta + \delta\theta$. At the end of the cycle, the charge transferred from one edge to the other is equal to the Chern number ν. To quantify this charge transfer, we define ΔQ for a given region $\mathcal{R}$ of the cylinder [see Fig. 7.4(a)], as the charge accumulation or depletion in this region with respect to the spatially homogeneous half filling distribution, i.e.,

$$\Delta Q_{\mathcal{R}} = \sum_{\mathcal{R}} (\bar{n}_i - 0.5). \tag{7.3}$$

Then, for a pumping protocol that transfers one unit of charge from the left to the right edge of the cylinder the Chern number takes the value:

$$\nu = \Delta Q_{\text{left}}(\theta = 2\pi) - \Delta Q_{\text{left}}(\theta = 0) = -\left[\Delta Q_{\text{right}}(\theta = 2\pi) - \Delta Q_{\text{right}}(\theta = 0)\right]. \quad (7.4)$$

Such a protocol has been used to characterize the spatially homogeneous TMI in several systems [161, 162, 274]. Here we also present this calculation, to provide with background for the more complicated topological pump in spatially inhomogeneous systems of the next section.

Figure 7.4 shows the results of this pumping protocol for the QAH ground state of Fig. 7.2. As θ increases the charge flows from the left to the right edge without a net accumulation in the bulk, and at the end of the cycle one unit of charge is transferred, leading to a measured $\nu = -1$ according to Eq. (7.4).

7.4 Topological defects

The main result of Chapter 6 is the appearance of spatially inhomogeneous TMI states around half filling. The use of the unrestricted HF method provides a simple way to obtain such exotic states, and analyze their properties within a simplified single-particle picture (e.g., by means of the local Chern number). However, it is of big importance to check the stability of such solutions against quantum fluctuations not captured by the HF ansatz. Here, we show the appearance of these solutions also with the DMRG method in a long cylinder.

Note that the spatially homogeneous TMI phase is already challenging with the DMRG, and finding TMI states which strongly break translational invariance increase the complexity of the DMRG algorithm. For instance, at incommensurate fillings close to half filling, and for a fix set of parameters, one has to compare the energies of converged solutions with different spatial patterns of the current loop order that are likely to arise spontaneously in the DMRG procedure. Moreover, the cylinder needs to be sufficiently long in the x direction to be able to accommodate such domain wall solutions. And lastly, the presence of boundaries might lead to the occupation of edge states keeping a unique (spatially homogeneous) TMI phase in the bulk even at incommensurate fillings.

Due to the above mentioned numerical complexity, here we present and analyze in depth a particular choice of parameters for which the lowest energy state of the cylinder is a domain wall separating two bulks with opposite Chern number. This is the case for a single hole doped to the half-filled state of Fig. 7.2. The results are shown in Fig. 7.5.

Figure 7.5(a) shows the inversion of the current loop order. One can observe that, for this DMRG solution, the time-reversal symmetry in the left half of the cylinder is broken in the same sector as in the solution of Fig. 7.2(a). However, there is a sector change across the domain wall located at the middle of the cylinder, which corresponds to a defect in the current loop order. Notice that this state is similar to the domain wall solutions obtained with the HF method in Chapter 6 and shown in Figs. 6.4-6.5.

In the present case, and due to the finite cylinder width, a single hole can act as a domain wall instead of forming a polaron state. The presence of the hole can be seen in the density plot shown in Figs. 7.5(b), where one can observe a weak site-nematic order pinned to the domain wall caused by the local deviation from the half-filled state, as well as the stronger charge orders at the edges that where also present in Fig 7.2. For a better visualization of the hole location, the charge integrated over the

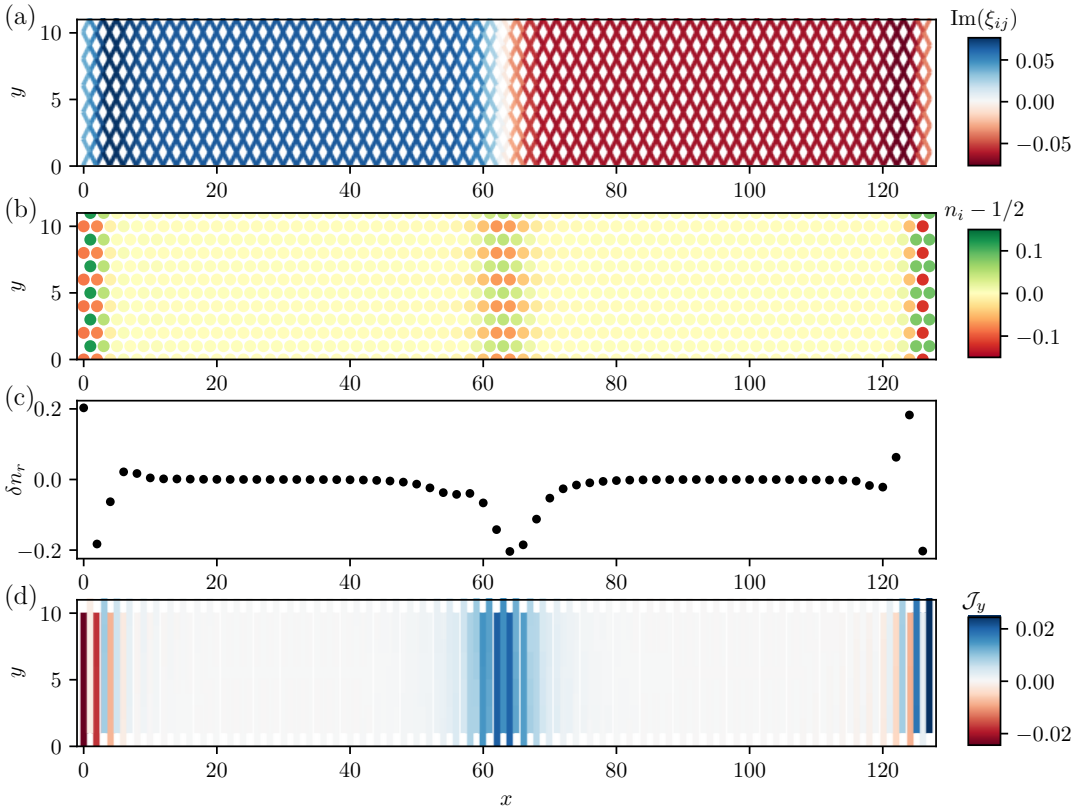

FIGURE 7.5: Domain wall solution separating two TMI states with opposite Chern numbers. Here we consider a long cylinder with $(L_x, L_y) = (48, 6)$, and the parameters $V_1/t = 4$, $V_2/t = 2$, $V_3/t = 0.5$ and $\delta = -1$, so that a hole is added to the homogeneous half-filled state. (a) Current loop order between nearest-neighbors bonds. The sign convention is the same as in Fig. 7.2(a), so that the change of sign across the domain wall indicates a flip of the current loop order. (b) Deviation of the local fermionic density with respect to half filling. One can observe small boundary effects due to the open boundary conditions, and the pinning of the hole at the domain wall location. (c) Deviation of the density from half filling integrated over a ring of two-site unit cells, defined as δn_r, for a better visualization of the charge depletion caused by the hole. (d) Vertical currents in the y direction computed as $\mathcal{J}_y = 2J_y^{\alpha}\mathrm{Im}\langle \hat{c}_{i+y}^{\dagger}\hat{c}_i\rangle$, where α indicates the sublattice (A or B) of the site i.

cylinder rings is shown in 7.5(c), where one can clearly observe that the hole leads to a net charge depletion at the domain wall.

Finally, the change in the topological invariant ν between the two halves of the cylinder, expected from the inversion of the current loop order across the domain wall, is also signalled by the appearance of localized chiral currents along the domain wall (in the y direction), as seen in Fig. 7.5(d). Notice that one can also observe similar currents at the open borders of the cylinder, where the Chern number changes from $\nu = \pm 1$ to a zero value.

7.4.1 Topological pump in inhomogeneous systems

The exotic nature of TMI states with domain wall patterns, as the one shown in Fig. 7.5, together with the impossibility to use the local Chern number of Eq. (6.6) in the MPS representation, requires an extension of the topological pump procedure to analyze the topological invariant of such spatially inhomogeneous solutions. We

thus generalize the pump protocol to compute the two values of the Chern number in the cylinder, expected from the change of the current loop order across the domain wall. To this aim, we divide the cylinder in three regions, as sketched in Fig. 7.6(a), such that we can trace quantized transfers of charges between them. We then proceed to insert the flux θ. As shown in Fig. 7.6(b), in a full cycle one quantized charge

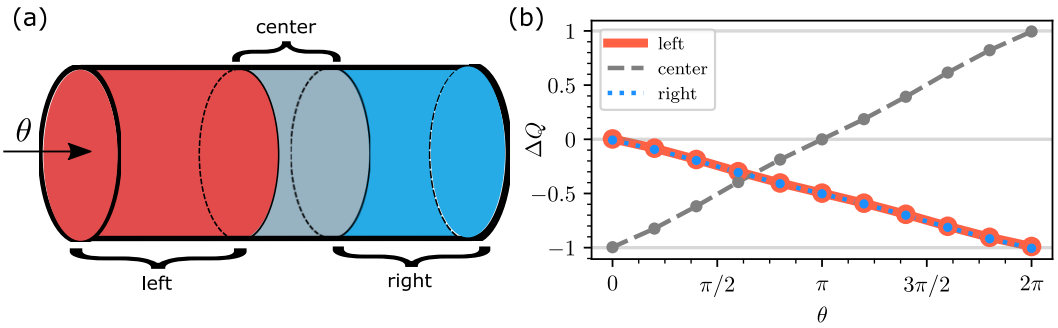

FIGURE 7.6: Pump protocol for the domain wall solution between two TMI states of Fig. 7.5. (a) Sketch of the cylinder used in the DMRG simulation, showing the left, right, and center regions. The latter has a smaller width, as it is chosen to include only the domain wall, while left and right regions are considered to be extended bulks. A flux θ is inserted in the long direction of the cylinder during the pump protocol $\theta = 0 \to 2\pi$. (b) Quantized charge transport during a pump cycle for each of the three regions in (a).

is transferred to the center from the left as well as from the right edge, giving an estimated value of the Chern number of $\nu_{\text{left}} = -0.993$ and $\nu_{\text{right}} = 0.999$. At the domain wall, this means that the initial hole is converted to a particle at the end of the pump.

7.5 Snapshot-based detection with matrix product states

The adiabatic flux insertion described above not only allows one to numerically determine the Chern number in DMRG simulations, but it is also closely related to transport experiments used to measure the Hall conductance in solid state systems. Interestingly, similar transport measurements have been also used to measure the Chern number in cold atom lattices [75, 207], and recently it has been proposed that they could be extended to interacting systems [342]. In these transport schemes, one applies a force to the lattice to generate time-dynamics analogous to the adiabatic evolution of the ground state under the flux insertion described above. The latter leads to a quantized transport of the atomic charge perpendicular to the direction of the applied force, which can be measured via standard local density probes.

In order to account for a realistic experimental measurement of the transported charge in the MPS obtained from our DMRG simulations, we perform snapshots of the local density in the initial and final MPS of the pumping protocol described in Fig. 7.6. To this aim, we follow the procedure introduced by Ferris and Vidal in Ref. [343], which allows to efficiently sample uncorrelated density snapshots from a given MPS [344]. For an MPS of L physical sites, one starts by simulating a local measurement of the density at site $i = 1$ according to the local occupation probability at that site. Then, one projects the MPS onto the local projector of site i corresponding to the outcome of the measurement. After normalizing the MPS, the same measurement procedure is applied to the site $i = 2$ and so on, until the measurement sweep reaches the site $i = L$. The results are shown in Fig. 7.7. Each individual snapshot

yields a binary density distribution of occupied and unoccupied sites, as exemplified in Fig. 7.7(a) for the initial state at $\theta = 0$ and in Fig. 7.7(c) for the final one at $\theta = 2\pi$. The actual density distribution can be inferred by averaging a sufficiently large number of snapshots, as seen in Figs. 7.7(b) and (d) for the initial and final state of the pump, respectively. While the latter are still noisy distributions for the number of snapshots considered here, the charge transfer between the initial and final states give a reasonable estimate of the left and right Chern numbers: $\nu_{\text{left}} \sim -0.89$, $\nu_{\text{right}} \sim 0.9$.

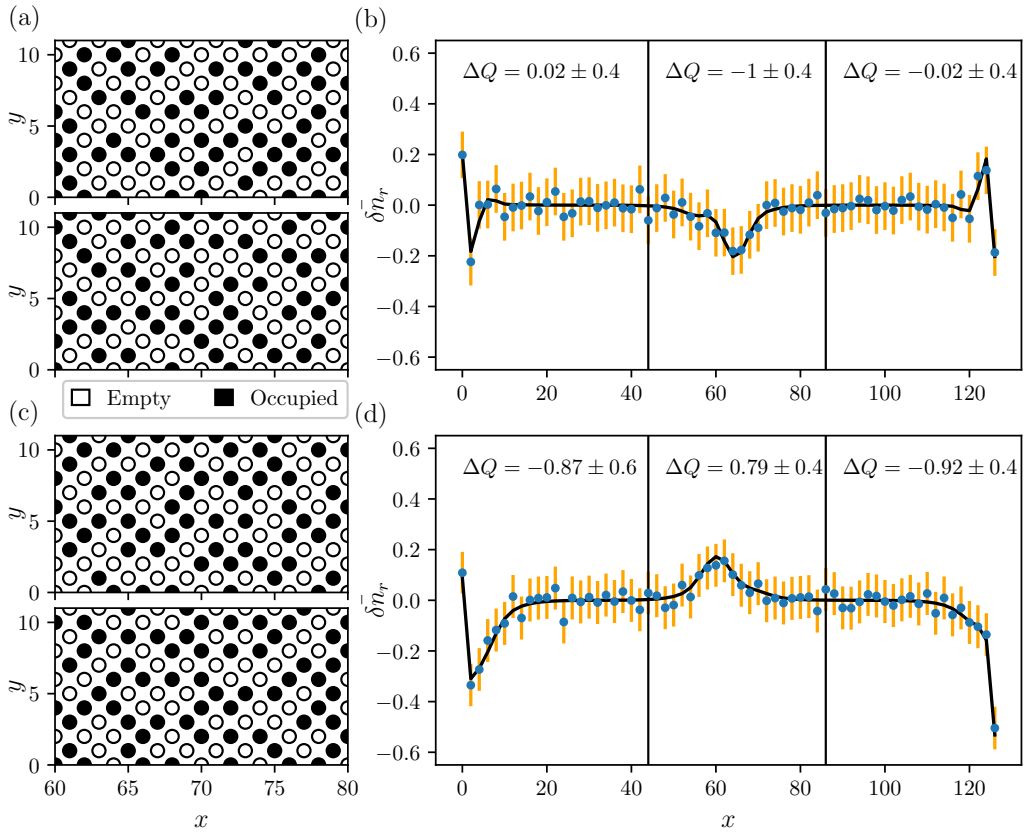

FIGURE 7.7: Snapshot-based measurement of the density distribution in the MPS. (a) Two instances of local density snapshots for the $\theta = 0$ ground state. Only the center region of the cylinder is shown. (b) Deviation of the charge from half filling at each of the rings of the cylinder averaged over 1000 snapshots for the $\theta = 0$ ground state. The solid line corresponds to the expectation value of the density in the MPS. (c)-(d) Same as in (a)-(b) for the state at the end of the pumping protocol ($\theta = 2\pi$).

7.6 Adiabatic state preparation through a continuous phase transition

The preparation of Chern insulators in optical lattices [75] can be achieved by a quasi adiabatic state preparation protocol [345, 346]. In this scheme, one starts from an initial set of lattice parameters corresponding to a Hamiltonian whose ground state exhibits a trivial band gap, and which can be easily prepared. Then, the lattice parameters are slowly changed to values for which the ground state of the modified Hamiltonian has a topological gap instead. During this quasi adiabatic evolution, the state of the system follows adiabatically the instantaneous ground state of the

Hamiltonian, so that for a sufficiently slow change of lattice parameters the final state is the desired topological ground state. For this protocol, it is highly desirable that the ground state transition crossed during the change of lattice parameters is continuous, as first order phase transitions are more likely to lead to metastable state resembling the initial trivial state [347, 348]. It is thus important to find a second order transition to the TMI state, in which the topological phase transition occurs via a SSB of the time-reversal symmetry driven by competing interactions. On the one hand, while there is a continuous phase transition from the noninteracting quadratic band touching system to the TMI [162], it is challenging to prepare a half-filled state in the semimetallic phase. One the other hand, the phase transitions between the TMI phase and its two surrounding trivial charge insulators, i.e., site-nematic insulator and diagonal stripe insulator shown in Fig. 5.1(c), are of first order [162], which can be understood as level crossings between different SSB states. Despite the lack of the desired second order phase transition in the phase diagram studied for our model, one can also add extra terms in the Hamiltonian that can be tuned to induce a continuous transition. As an example, in the experiment of Ref. [75], a staggered on-site potential was used to initialize the system in a trivial charge insulator. In that model, there is a continuous phase transition to a bosonic Chern insulator when decreasing the value of such staggered potential, which was used to successfully prepare the topological phase. Extensions of this protocol have been also proposed to adiabatically prepare fractional Chern insulators by varying extra staggered on-site potentials [349] or interchain hopping amplitudes [350].

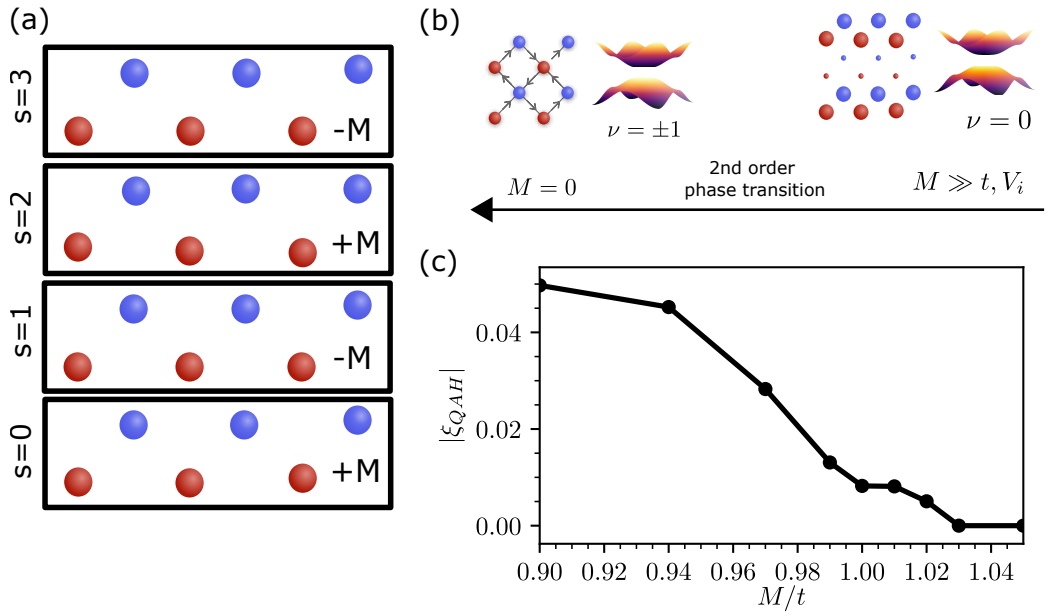

FIGURE 7.8: Second order phase transition to the TMI phase at half filling. (a) Spatial dependence of the on-site potential varied during the adiabatic protocol, leading to an energy penalty of $2M$ for stripes with even s. (b) Sketch of the phases encountered in the limiting values of M. For large M the system is a trivial insulator with a strong charge imbalance between horizontal stripes. When decreasing M, there is a second order phase transition to the TMI, characterized by a nonzero Chern number of the lower band and a current loop order. (c) Continuous evolution of the local current loop order as a function of M in iDMRG simulations, which shows the second order nature of the phase transition. Here the value of interactions are set to $V_1/t = 4$ and $V_2/t = 2$ such that the system is a TMI for $M = 0$.

In the same spirit, in order to induce a second order phase transition, we propose to modify the total Hamiltonian such that

$$\hat{H}' = \hat{H}'_0 + \hat{H}'_{\text{int}} + M\sum_s (-1)^s \hat{n}_i, \tag{7.5}$$

where the last term is an on-site potential which has alternating strength $\pm M$ along unit cells in the vertical direction, as shown in Fig. 7.8(a). This term is similar to the one considered in Refs. [75, 349], and as it externally induces a charge order incompatible with the site-nematic and stripe order driven by interactions, it is likely to lead to a continuous phase transition from the TMI state, as depicted in Fig. 7.8(b). For our numerical analysis of the phase transition, we set the values of the interactions to $V_1/t = 4$ and $V_2/t = 2$. For $M = 0$ this choice corresponds to the TMI phase with a topological gap at half filling ($\nu = \pm 1$) with the DMRG method. Alternatively, for dominant M the system is a charge insulator with alternating occupied and unoccupied horizontal stripes, and the gap is trivial ($\nu = 0$). Notice that as this charge insulator also has a two-band structure, it is convenient for preparing a half-filled insulator. To certify the nature of the phase transition to the QAH phase, the accuracy of the DMRG method is advantageous with respect to the HF ansatz. At the vicinity of the second order phase transition one needs to use a large bond dimension $\chi_{\text{max}} = 4000$ due to the small value of the insulating gap, as otherwise the DMRG solution without time-reversal symmetry breaking has lower energy than the QAH phase. The results are shown in Fig. 7.8(c) where we do no not observe a sudden jump in the current loop order at the transition, which would be characteristic of a first order transition to the TMI state. Instead, the continuous behavior of the local order parameter points to a smooth second order transition desirable for the adiabatic state preparation protocol discussed above. Notice that, to further confirm the continuous transition, it would be interesting to perform a finite-size scaling of Fig. 7.8(c) by considering larger cylinder widths $L_y \geq 8$ compared to the one considered here ($L_y = 6$). However, the latter would require the use of even larger bond dimensions close to the transition point.

A final remark is that the continuous transition to the TMI state differs from the ones in Refs. [75, 349, 350] in that here the topological phase is acquired through a SSB, in which the two degenerate ground states have opposite values of the topological Chern number $\nu = \pm 1$. Hence, there are still many open questions concerning the dynamics of the topological Mott transition. For instance, in the context of the quantum Kibble-Zurek mechanism [334, 336], it would be very interesting to study the interplay between topological protection and the creation of defects in a second order quantum phase transition with SSB.

7.7 Summary

In this chapter, we have studied the TMI in the checkerboard lattice, introduced in Chapter 5, considering a cylinder geometry, which has allowed us to treat the system very accurately with the two-dimensional DMRG algorithm. First, we have confirmed the prediction of the mean-field study in Chapter 5, and we have shown that the inclusion of long-range interactions up to fourth neighbors leads to an enlarged TMI in the phase diagram, compared to the more simple model with up to next-nearest-neighbors interactions. The latter is encouraging from a quantum simulation perspective, as this long-range nature of interactions is expected in our proposal with Rydberg-dressed atoms of Chapter 5. Second, inspired by the mean-field

results of Chapter 6, we have studied the appearance of spatially inhomogeneous TMI phases for particle numbers incommensurate with the number of unit cells in the system. Our numerically demanding DMRG study of this case has lead to a domain wall solution in the cylinder geometry under consideration, where each half of the cylinder exhibits an opposite value of the topological Chern number. The numerical determination of such topological invariants is of independent interest due to the strongly-correlated nature of our system, as the commonly used tools to study spatially varying Chern numbers are formulated in a single-particle picture. To this aim, we have generalized the topological pump procedure in DMRG, to successfully obtain quantized Chern numbers with opposite values at each side of the cylinder. Third, as the topological pump procedure is in general connected to the experimental determination of the Chern number in cold atoms through quantized displacements, we have performed a snapshot-based analysis of the density distribution at the first and last stages of this pump, to better connect our numerical results with an experimental detection scheme. Finally, we have shown that it is a priori possible to adiabatically prepare the TMI with cold atoms in an optical lattice, by preparing the system in a trivial insulator and inducing a second order phase transition via a controlled change of the on-site light potentials.

Part III

Microscopic explanation of collective effects in quantum materials

Chapter 8

Cuprate pseudogap phase in an exotic electron-phonon model

Superconductivity was discovered in 1911 by K.H. Onnes [89], who showed that the resistance of a mercury wire dropped to zero when cooled down to $T \sim 4.3$K with liquid Helium. This discovery represented a breakthrough, as materials with zero resistivity can lead to a huge improvement in the energetic development of our society due to their ability to transport large electric currents without losses. For this purpose, however, the need of liquid Helium to achieve the low temperatures at which the superconducting phase appears represents a major obstacle.

The microscopic explanation of normal superconductivity was found by Bardeen, Cooper and Schrieffer in terms of Cooper pairs created due to the interaction with virtual phonons (the so-called BCS theory) in 1957 [94], and in 1972 a theoretical bound to the highest transition temperature achievable within this mechanism was found to be $30K$ [351]. Nevertheless, it is possible to find other materials that are not captured by the BCS theory and are superconductors beyond this upper bound, the high-T_c superconductors.

The first experimental evidence of high-T_c superconductivity dates from 1986, when G. Bednorz and K.A. Müller [88] found that the layered material Barium doped compound of Lanthanum and Copper Oxide was superconducting at around 35 K. This system was a particular instance of a family of layered materials with CuO_2 planes called cuprates, which have been shown to be able to have critical temperatures higher than 100K [46]. Thus, these high-T_c superconductors can lead to a huge improvement in the energetic development, as they can transport large electric currents without losses and without requiring liquid Helium to cool the systems to extremely low temperatures.

The mechanism giving rise to high-T_c superconductivity is not fully understood and represents one of the most intriguing questions of contemporary physics [46, 47]. Nevertheless, many experimental studies of cuprates have led to a universal phase diagram for their electronic bands [46, 352], which is shown in Fig. 8.1(a). As a function of temperature and doping from half-filling, one can identify a long range ordered anti-ferromagnetic phase, the so-called superconducting dome, and the pseudogap phase, whose properties are described below.

From many theoretical studies, it is thought that the two-dimensional Fermi-Hubbard model, which describes electrons hopping in a lattice including strong correlations, can explain some of the features of the cuprates phase diagram [40]. This is quiet remarkable, since such two-dimensional model used to describe the CuO_2 planes represents a major simplification of the real multilayered material. However, even this apparently simple model is numerically difficult to solve on a classical computer, and the use of Fermi-Hubbard quantum simulators has emerged as

a promising route to understand the physics behind the high-T_c superconductivity. In the same spirit, the recent experiments in twisted bilayer graphene [99, 100] were able to observe a high-T_c superconducting phase in a much simpler material than cuprates.

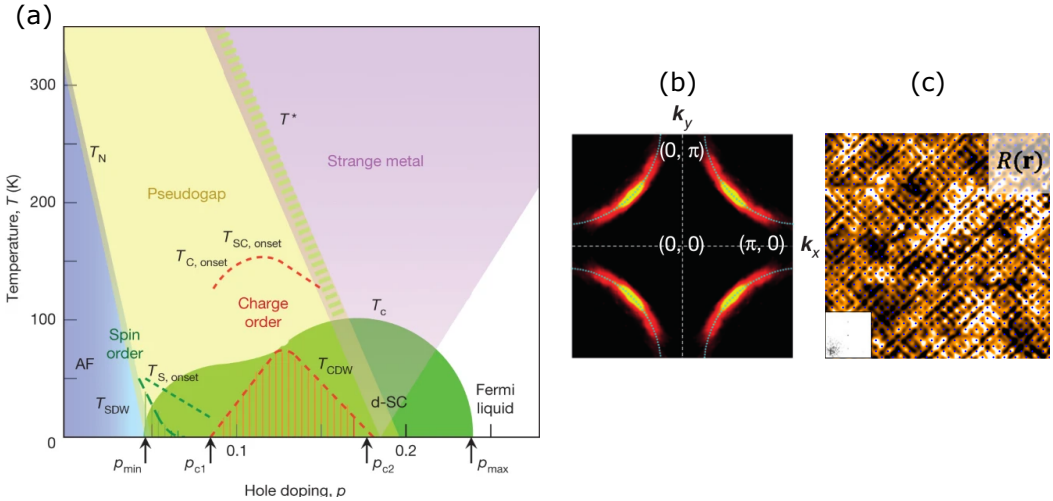

FIGURE 8.1: (a) Phase diagram of cuprate high-T_c superconductors. Reprinted from [46]. (b)-(c) Experimental data of the pseudogap phase. (b) Electronic density of states obtained from ARPES measurements. One can see that the Brillouin zone is disconnected, as it presents a gap at $(\pi, 0), (0, \pi)$. Reprinted from [46]. (c) Results from the STM measurements that show the electronic hopping amplitude in real space. One can observe that in this pseudogap phase there are local $C_4 \to C_2$ reductions of the lattice symmetry (stripes) and also that the electronic sample is not homogeneous (microphase separation). Reprinted from [353].

Note however that, while the main theoretical and experimental routes to model the CuO_2 planes have been undertaken by considering only electronic interactions, several effects suggest that the coupling to the lattice modes should not be neglected. These include the anomalous isotope effect [354], the universal oxygen vibration frequency shift in the superconducting phase [355–357], and more recently the identification of the inequivalence of oxygen electronic and vibrational states in the two lattice directions of the CuO_2 plane in the pseudogap phase [358, 359]. Furthermore, experiments which drive the Cu-O bond to large displacements with resonant femtosecond laser pulses have shown evidence that a light-induced superconducting phase can be achieved for high temperatures [95].

A development in this direction has been made through the modeling of fluctuating Cu-O-Cu bonds [360–362]: these works were able to reproduce the d-wave superconductivity and some characteristics of the pseudogap phase without electronic correlation effects.

In this chapter, based on Ref. [2], we focus on the pseudogap phase of such fluctuating bond model (FBM), as it is thought that the underlying mechanism giving rise to this phase is a key ingredient for the appearance of superconductivity. The pseudogap phase owes his name to the presence of Fermi arcs [Fig. 8.1(b)] in angle-resolved photoemission spectroscopy (ARPES) measurements i.e., the electronic Fermi surface shows gaps only around certain points in the Brillouin zone [363–365]. In real space, scanning tunnelling microscope (STM) measurements have shown the presence of nematic C_4 symmetry-breaking real-space orderings [Fig. 8.1(c)], often associated with a local charge modulation [366–368].

The Fermi-surface properties of the pseudogap phase [369–376] have been theoretically linked to various mechanisms: topological order and spin liquid physics [377], phase incoherent d-wave superconductivity [378–383], and the breaking of various electronic symmetries not necessarily related to superconductivity [384–392]. A number of electronic correlation-based approaches [393, 394] predict nematic C_4 symmetry-breaking real-space orderings, where the organization of such phases into nanoscale domains is usually considered to arise from glassiness, i.e., the disordering effect of impurities [395, 396].

Interestingly, the FBM predicts a *uniform* smectic/nematic oxygen bond order with C_2 spatial symmetry. The mechanism for its disintegration into the experimentally observed nanoscale domains remains, however, unclear. In this chapter, we revisit the FBM and show that some extensions of this model are crucial to find physically stable solutions with properties resembling the experimental findings in the pseudogap phase.

This chapter is organized as follows. In Section 8.1, we review the FBM and the mean-field decoupling needed to solve it numerically. We also provide a benchmark of such mean-field approach against exact diagonalization studies on a small lattice. Then, we revisit the pseudogap phase encountered in previous works and show that it is unstable towards macrophase separation. In Section 8.2, we present an extended FBM including on-site electron repulsion, and study it at the mean-field level as well as with an exact treatment of the electronic interactions in small lattices. The results of this section show that on-site interactions are key in preventing the phase separation of the original model, but also that the increased numerical complexity of the extended model prevents a precise characterization of any pseudogap features. In Section 8.3, we present a simplified effective model that incorporates the main effect of on-site interactions (i.e., prevention of macrophase separation) without increasing the numerical complexity of the original model. Remarkably, such model leads to a nanoscale phase separated pseudogap in real space with a local C_4 symmetry-breaking bond order and Fermi arcs in momentum space. Moreover, as reported in experiments, the pseudogap is enhanced (reduced) by adding magnetic (nonmagnetic) impurities to the system.

8.1 Fluctuating bond model

The FBM describes the interplay of the buckling of anharmonically oscillating Cu-O-Cu bonds and hopping of electrons via a nonlinear electron-phonon coupling. The Hamiltonian $\hat{H}_{\text{FBM}} = \hat{H}_{\text{el}} + \hat{H}_{\text{ph}} + \hat{H}_{\text{el-ph}}$ consists of the bare electron and phonon Hamiltonians, and the electron-phonon interaction. The bare electron Hamiltonian reads

$$\hat{H}_{\text{el}} = -t_0 \sum_{\langle i,j\rangle,\sigma} \hat{c}^{\dagger}_{i,\sigma}\hat{c}_{j,\sigma} + t' \sum_{\langle\langle i,j\rangle\rangle,\sigma} \hat{c}^{\dagger}_{i,\sigma}\hat{c}_{j,\sigma} - \mu \sum_{j,\sigma} \hat{n}_{j,\sigma}, \tag{8.1}$$

where $\hat{c}_{j,\sigma}$ ($\hat{n}_{j,\sigma}$) is the electron annihilation (occupation) operator of a spin-σ electron in the $3d_{x^2-y^2}$ orbital centered on site j of a square lattice, and t_0 and t' are the NN and NNN hopping amplitudes. The bare phonon Hamiltonian is written as the sum over the bond oscillators,

$$\hat{H}_{\text{ph}} = \sum_b \frac{\hat{p}_b^2}{2M} + \frac{\chi_0}{2}\hat{u}_b^2 + \frac{w}{16}\hat{u}_b^4, \tag{8.2}$$

where M is the O mass and $\hat{u}_b$ is its displacement operator, perpendicular to the Cu-O-Cu NN bond b. The oscillator potential has a double-well structure with $\chi_0 < 0$ and $w > 0$. A strong quartic potential for the Cu-O bond has been recently observed in coherent phonon experiments in Yttrium Barium Copper Oxide [397]. The electron-phonon interaction couples the anti-bonding electron orbital charge $\hat{Q}_b = \frac{1}{2}\sum_\sigma(\hat{n}_{i,\sigma} + \hat{n}_{j,\sigma} - \hat{c}^\dagger_{i,\sigma}\hat{c}_{j,\sigma} - \hat{c}^\dagger_{j,\sigma}\hat{c}_{i,\sigma})$ nonlinearly to the displacement $\hat{u}_b$,

$$\hat{H}_{\text{el-ph}} = -\frac{\nu}{2}\sum_b \hat{u}_b^2\hat{Q}_b, \tag{8.3}$$

where b is the bond connecting the sites i and j. In this chapter, we show that the effects due to the interplay of $\hat{H}_{\text{FBM}}$ and Coulomb interactions, which we consider as maximally screened, i.e., via an on-site term $U\sum_i \hat{n}_{i,\uparrow}\hat{n}_{i,\downarrow}$, are of defining importance. These interactions are distinct from the long-range interactions between charges in antibonding orbitals $\propto\hat{Q}_b\hat{Q}_{b'}$ at different bonds considered in earlier works on the FBM [361, 362].

8.1.1 Mean-field decoupling of the electron-phonon interaction

The large dimension of the Hilbert space of the Hamiltonian $\hat{H}_{\text{FBM}}$ makes it impossible to treat with exact numerical methods: In addition to the square lattice of fermions, the motion of each O atom represents an additional continuum quantum degree of freedom at each lattice bond. Hence, one needs to perform a series of approximations in order to extract the physics of the model.

Due to the large difference in electron and O masses, the motion of the latter on each bond can be treated as an oscillation around the quartic potential minima, which allows for a mean-field decoupling. One defines the mean-field FBM Hamiltonian $\hat{H}^{\text{MF}}_{\text{FBM}}$, which only differs from $\hat{H}_{\text{FBM}}$ in the electron-phonon interaction term

$$\begin{aligned}\hat{H}^{\text{MF}}_{\text{el-ph}} = &-\frac{\nu}{4}\sum_{b,\sigma}\langle\hat{u}_b^2\rangle(\hat{n}_{i,\sigma} + \hat{n}_{j,\sigma} - \hat{c}^\dagger_{i,\sigma}\hat{c}_{j,\sigma} - \hat{c}^\dagger_{j,\sigma}\hat{c}_{i,\sigma})\\ &-\frac{\nu}{4}\sum_{b,\sigma}\hat{u}_b^2\langle\hat{n}_{i,\sigma} + \hat{n}_{j,\sigma} - \hat{c}^\dagger_{i,\sigma}\hat{c}_{j,\sigma} - \hat{c}^\dagger_{j,\sigma}\hat{c}_{i,\sigma}\rangle\\ &+\frac{\nu}{4}\sum_{b,\sigma}\langle\hat{u}_b^2\rangle\langle\hat{n}_{i,\sigma} + \hat{n}_{j,\sigma} - \hat{c}^\dagger_{i,\sigma}\hat{c}_{j,\sigma} - \hat{c}^\dagger_{j,\sigma}\hat{c}_{i,\sigma}\rangle.\end{aligned} \tag{8.4}$$

Notice that the mean-field Hamiltonian consists of a quadratic electron Hamiltonian with renormalized bond-dependent hopping amplitudes $t_b = t_0 - \nu\langle\hat{u}_b^2\rangle/4$, and a set of isolated phonon oscillators with renormalized bond-dependent $\chi_b = \chi_0 + \nu\langle\hat{Q}_b\rangle/2$, and chemical potential $\mu_{i,\sigma} = \mu + \frac{\nu}{4}\sum_{b\in i}\langle\hat{u}_b^2\rangle$.

The mean-field parameters $\langle\hat{u}_b^2\rangle$, $\langle\hat{Q}_b\rangle$, and $\langle\hat{n}_{i,\sigma}\rangle$ are found with a self-consistent iterative loop, similar to the one described in Section 1.1 for the Hartree-Fock decoupling. Before starting the iterative algorithm, we have fitted the value of $\langle\hat{u}_b^2\rangle$ as a function of $\langle\hat{Q}_b\rangle$ at a given temperature T. For this purpose, we have used a local phononic basis of 800 states to find the eigenstates of $\hat{\tilde{H}}_{\text{ph}}$ for 200 values of $\langle\hat{Q}_b\rangle$ in the interval $[0, 2]$. These eigenstates are then used to compute the thermal expectation value of $\langle\hat{u}_b^2\rangle$ according to the Boltzmann distribution. After that, a simple fitting routine is used to extract $\langle\hat{u}_b^2\rangle$ as a function of $\langle\hat{Q}_b\rangle$ from the 200 values obtained.

Finally, in order to benchmark the accuracy of the mean-field decoupling of the electron-phonon term, we have exactly solved a simplified system of a four-site lattice with periodic boundary conditions, and compared the results of the two approaches. The results of Table 8.1 show that the mean-field energy is higher than the one obtained through exact diagonalization, but close to it, and that the effective hopping t_b is also similar in the two approaches.

TABLE 8.1: Comparison of the homogeneous ground-state properties using exact diagonalization (left columns) and a mean-field decoupling of the electron-phonon interaction (right columns) for different sizes of the local phononic basis. Here we work at zero T, half-filling, $t_0 = 0.0083$, $t' = 0$, $\nu = 0.03$, $w = 0.17$, $\chi_0 = -0.0025$, and $U = 0$, where we use atomic units (energy $E_0 = 27.2$ eV and length $a_0 = 0.53$ Å). For both methods the set of coherent states is used as a variational ansatz of the bond phonons to find the ground state around one of the minima of the quartic potential. The different parameters appearing in the table are the number of local phononic states taken into account (basis), the effective hopping of the electrons $t_\mathrm{b} \equiv t_0 - \nu\langle x^2\rangle/4$, the ground-state energy (E), and the expected value of the local phonon operator ($\langle \hat{N}_\mathrm{ph}\rangle$).

Basis	t_b/t_0		E/t_0		$\langle \hat{N}_{ph}\rangle$	
1	0.742	0.742	−5.795	−5.795	0	0
5	0.786	0.799	−5.855	−5.819	0.099	0.084
10	0.792	0.805	−5.855	−5.819	0.186	0.140
15	0.796	0.808	−5.855	−5.831	0.303	0.226
100	–	0.819	–	−5.831	–	5.594

8.1.2 Instability of the pseudogap phase

The authors of Refs. [360–362] found the SSB C_4 to C_2 $\langle \hat{u}_x^2\rangle \neq \langle \hat{u}_y^2\rangle$ within a translationally invariant mean-field ansatz. From the electronic viewpoint, this is a bond ordered state with different hopping strengths $t_x \neq t_y$. The resulting disconnected Fermi surface for each of the two symmetry-breaking solutions is shown in Fig. 8.2(a)-(b). We notice that the corresponding Fermi surface does not present Fermi arcs, which exhibit a C_4 symmetry. Instead, the system only has a suppression of the spectral weight at $\mathbf{k}_{t_x>t_y} = (\pi, 0)$ or $\mathbf{k}_{t_y>t_x} = (0, \pi)$, as can bee seen in Fig. 8.2(a)-(b). The authors of Ref. [360] suggested that impurities would form, in real space, domains of the two sectors of the symmetry breaking, leading to a restoration of the Fermi arcs, as shown in Fig. 8.2(c).

The pseudogap phase of the model is then characterized by the order parameter $\Omega_\mathrm{PG} \propto |t_x - t_y|$. Notice that the pseudogap phase owes his name to the fact that while for $\Omega_\mathrm{PG} = 0$ there is a Van Hove singularity at the Fermi level corresponding to a connected (metallic) Fermi surface with a pronounced peak in the density of states, for $\Omega_\mathrm{PG} > 0$ the peak splits in two peaks, and there is a strong reduction of the density of states between them, leading to the Fermi arc structure.

Figure 8.3 shows the order parameter Ω_PG with respect to hole doping $\delta = 1 - n$ (n is the electron density) at different temperatures (solid lines). A more careful analysis nevertheless shows that this homogeneous pseudogap solution is intrinsically unstable. The inset of Fig. 8.3 shows that the compressibility $\partial\mu/\partial n = -\partial\mu/\partial\delta$ is negative in the pseudogap phase. We find this feature not to be specific to the choice of FBM parameters but rather to persist for $\langle \hat{u}_x^2\rangle \neq \langle \hat{u}_y^2\rangle$ solutions. The effects of this instability can be visualized in real-space calculations using an unrestricted mean-field approach, in which the self-consistent averages $\langle \hat{u}_b^2\rangle$ and $\langle \hat{Q}_b\rangle$ are allowed to be independent for each bond. One then obtains macroscopic phase separation with

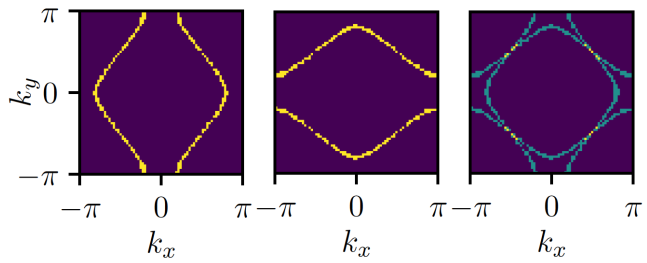

FIGURE 8.2: DOS at the Fermi level for a square lattice of electrons with anisotropic hopping $t_x > t_y$ ($t_x < t_y$) for the left (center) plot. The right plot shows the addition of the two previous Fermi surfaces, which would correspond to the real situation in which microphase separation creates domains with different choice of the SSB parameter. In this situation, one can observe the Fermi arcs (the four bright regions) resulting for the addition of the two other Fermi surfaces. For simplicity, all the plots have been obtained at half filling and at zero temperature.

distinct uniform regions of low and high electron density, without any bond order (see Fig. 8.4 for $U = 0$).

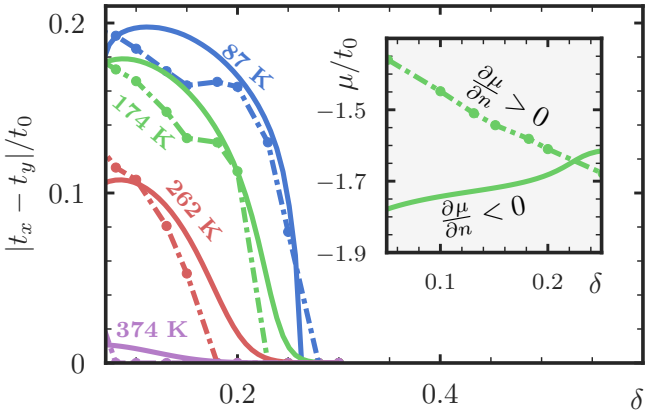

FIGURE 8.3: Pseudogap phase as a function of hole doping and for different temperatures. The Figure shows the homogeneous mean-field parameter $|t_x - t_y|$ of the $\hat{H}_{\text{FBM}}$ Hamiltonian on an 80×80-site lattice (solid lines) and the spatial average $|t_x - t_y|$ of the RI model on a 30×30-site lattice (dashed lines). The inset depicts the chemical potential as a function of the hole doping at 174 K. We observe a negative compressibility $\partial\mu/\partial n < 0$ in the homogeneous pseudogap phase of $\hat{H}_{\text{FBM}}$, which indicates the instability of this phase. On the contrary, the pseudogap phase of $\hat{H}_{\text{RI}}$ has a positive compressibility. The parameters of both Hamiltonians are fixed to $t_0 = 0.0083$, $t' = 0.0011$, $\nu = 0.03$, $w = 0.17$, $\chi_0 = -0.0025$, and $U = 0$, where we use atomic units (energy $E_0 = 27.2$ eV and length $a_0 = 0.53$ Å).

8.2 Fluctuating bond model with on-site interactions

An important conclusion of Section 8.1.2 is that Coulomb interactions are intrinsically needed to suppress the large charge imbalance of the FBM, and are therefore not only interesting from the point of view of competing phases (e.g., the charge density wave). A minimal extension of the FBM including Coulomb interactions leads to the Fermi-Hubbard model with bond phonons

$$\hat{H}_{\text{FBM}+U} = \hat{H}_{\text{e}} + \hat{H}_{\text{ph}} + \hat{H}_{\text{el-ph}} + U \sum_i \hat{n}_{i,\uparrow}\hat{n}_{i,\downarrow}. \tag{8.5}$$

A rigorous analysis of the FBM+U Hamiltonian, for U values typical for cuprate superconductors, constitutes a great challenge due to the strong electron correlations brought by the Hubbard term. In the following, we first discuss the numerical results obtained under different approximations. We then present an effective model that can be numerically studied in large clusters and leads to a stable pseudogap phase.

8.2.1 Mean-field approach

We first study the effect of a large Hubbard repulsive U on the phase separation with the unrestricted mean-field decoupling

$$\left(\hat{n}_{i,\uparrow}\hat{n}_{i,\downarrow}\right)^{MF} = \left\langle \hat{n}_{i,\uparrow}\right\rangle \hat{n}_{i,\downarrow} + \hat{n}_{i,\uparrow}\left\langle \hat{n}_{i,\downarrow}\right\rangle - \left\langle \hat{n}_{i,\uparrow}\right\rangle \left\langle \hat{n}_{i,\downarrow}\right\rangle , \tag{8.6}$$

where we do not impose the translational invariance ansatz of Section 8.1.2. Each unrestricted solution has been obtained after $\sim 3 \times 10^4$ iterations, starting from noisy homogeneous distributions of $\langle u_b^2 \rangle$ and $\langle \hat{n}_{i,\sigma} \rangle$. The update parameter η (see Section 1.1) has been initialized at $\eta = 0.03$ and progressively increased until reaching the value $\eta = 1$ for the last $\sim 3 \times 10^3$ iteration steps. The variation in the free energy in the last steps of the iteration algorithm is around $\Delta F \sim 10^{-8} t_0$. The solutions

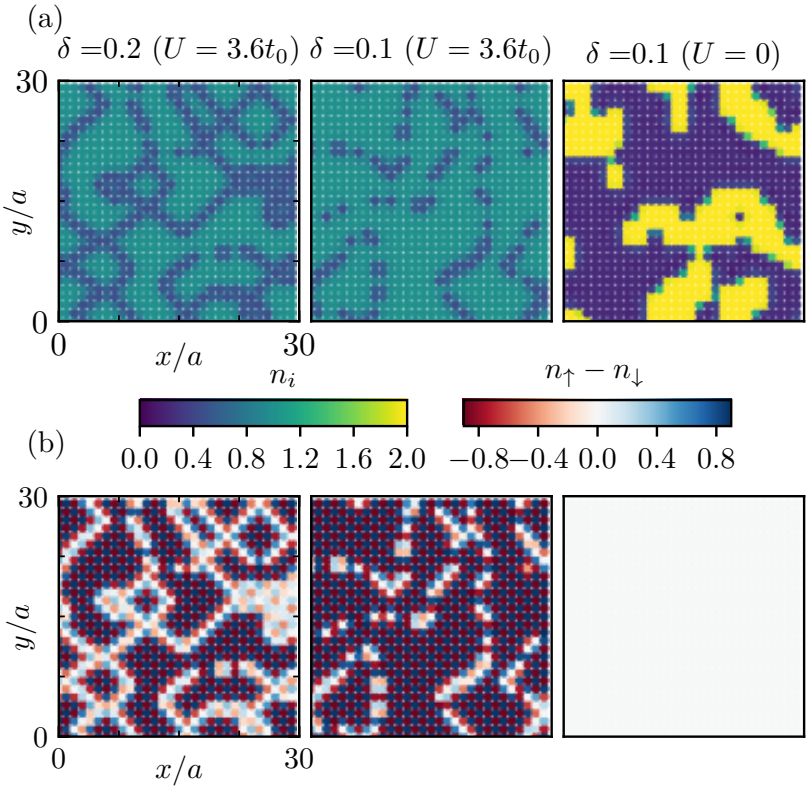

FIGURE 8.4: Real-space features of $\hat{H}_{\text{FBM}+U}$ at $K_B T = t_0/15$ for different dopings on a 30x30-site lattice. Parameters are set as in Fig. 8.3, except for the Hubbard, which is specified on each column. (a) Density plots showing microphase separation with small density amplitude (left and center) and macrophase separation with huge density amplitude (right). (b) Local spin polarization showing strongly polarized antiferromagnetic phase in the cases with finite U (left and center).

of the self-consistent equations are shown in Fig. 8.4. A first observation is that in general the mean-field parameters evolve towards nonhomogeneous patterns, reflecting the meta-stability of the homogeneous ansatz. For $U = 0$, we observe the

macrophase separation in agreement with by the prediction of the previous section. On the contrary, we observe that for a sufficiently large $U \gtrsim 3t_0$, the on-site interaction cures the macrophase separation generated by the electron-phonon interaction: the system exhibits smaller disconnected charge domains with lower density fluctuations. However, we do not observe any local C_4 symmetry breaking. This is due to the well-known overestimation of the magnetic correlations from the mean-field decoupling (see, e.g., Ref. [398]). In particular, the system has here a true gap with antiferromagnetic order at the relevant dopings and temperatures, as shown in Fig. 8.4(b), which masks any pseudogap features.

8.2.2 Exact diagonalization approach

We now characterize more rigorously the pseudogap close to half filling and in the presence of Hubbard interactions. To this end, we study the FBM+U model for a 3×3 cluster with periodic boundary conditions. We treat the Hubbard interactions exactly and the electron-phonon interactions with an unrestricted mean-field decoupling. In Fig. 8.5, for the unpolarized subspace of eight electrons (density $n = 0.89$), we observe macrophase separation at $U = 0$ with large density fluctuations through the lattice. For a moderately large interaction $U = 3.6t_0$, these fluctuations are strongly suppressed. Importantly, the C_4 symmetry breaking of the bonds is manifest and survives the formation of local magnetic moments.

We emphasize that the exact treatment of the FBM+U model for larger system sizes is numerically challenging due to the large values of U typical of the cuprates. Nevertheless, we are here interested in the phonon bond order mechanism of the pseudogap state and the associated generation of microphase separation, and the previous numerical results point to a scenario where electronic correlations do not generate the pseudogap phase but are essential to stabilize it.

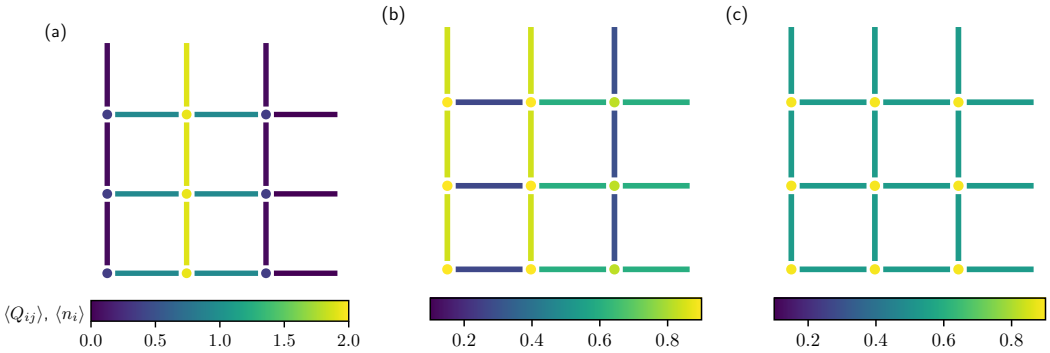

FIGURE 8.5: Exact diagonalization results for $K_B T = t_0/15$. (a) $U = 0$. (b) $U = 3.6t_0$. (c) $U = 3.6t_0$, $\nu = 0$. We show the relevant local observables on a 3×3 lattice at electron filling $8/9$. The site colors encode the on-site occupation while the bond colors encode the values of the bond charge $\hat{Q}_b$. The color scales are shown in the lower panel.

8.3 Residual interactions model

We propose to discard the spatial fluctuations of the local density in the electron-phonon interaction as it would allow one to better treat larger systems without having the exaggerated effects of magnetic correlations at low hole doping. This effective model preserves the main effect of the repulsive interaction, which is to prevent

macrophase separation. One then obtains a model with at most a residual small U that now does not lead to magnetic order at temperatures relevant for the pseudogap phase. We will see that this approximation reproduces qualitatively the exact diagonalization results of the FBM+U model, preventing the macrophase separation while allowing for a C_4 symmetry breaking.

The resulting model, which we call the residual interactions (RI) model, differs from the FBM in the electron-phonon term, which is obtained by replacing the number operators $\hat{n}_{i,\sigma}$ by the average density per spin species $\langle \hat{n}_\sigma \rangle$ in the $\hat{Q}_b$ of Eq. (8.3). The latter gives rise to an effective

$$\tilde{Q}_b = -\frac{1}{2}\sum_\sigma (\hat{c}^\dagger_{i,\sigma}\hat{c}_{j,\sigma} + \text{H.c.}), \tag{8.7}$$

and a (total) density dependent renormalization of the quadratic part of the oscillator potential,

$$\tilde{\chi}_0 = \chi_0 - \nu/2\langle n \rangle. \tag{8.8}$$

The total RI Hamiltonian in mean-field approximation thus reads

$$\begin{aligned}\hat{H}_{\text{RI}} = \hat{H}_{\text{el}} + \hat{H}_{\text{ph}}\left[\tilde{\chi}_0(\langle n \rangle)\right] + \frac{\nu}{4}\sum_{b,\sigma}\Big[&\langle \hat{u}_b^2\rangle(\hat{c}^\dagger_{i,\sigma}\hat{c}_{j,\sigma} + \hat{c}^\dagger_{j,\sigma}\hat{c}_{i,\sigma}) + \hat{u}_b^2\langle + \hat{c}^\dagger_{i,\sigma}\hat{c}_{j,\sigma} + \hat{c}^\dagger_{j,\sigma}\hat{c}_{i,\sigma}\rangle \\ &- \langle \hat{u}_b^2\rangle\langle \hat{c}^\dagger_{i,\sigma}\hat{c}_{j,\sigma} + \hat{c}^\dagger_{j,\sigma}\hat{c}_{i,\sigma}\rangle\Big] + U\sum_i \left(\langle \hat{n}_{i,\uparrow}\rangle \hat{n}_{i,\downarrow} + \hat{n}_{i,\uparrow}\langle \hat{n}_{i,\downarrow}\rangle - \langle \hat{n}_{i,\uparrow}\rangle\langle \hat{n}_{i,\downarrow}\rangle\right)\end{aligned} \tag{8.9}$$

8.3.1 Pseudogap phase features

In this section we analyze in depth the pseudogap phase of the RI model with no translational invariance.

Fermi arcs and nanoscale domains Figure 8.3 shows the pseudogap parameters obtained for the unrestricted mean field of the RI model for $U = 0$ at different temperatures (dashed lines). These results are qualitatively similar to the ones obtained for the homogeneous solution of the FBM, but with a positive compressibility. We now characterize more in depth the pseudogap phase of the RI model. Figure 8.6 shows the pseudogap dependence with respect to hole doping for a fixed temperature. Figure 8.6(a) shows the real-space distribution of the bond order parameter: for large doping, i.e., $\delta = 0.2$, we observe a homogeneous C_4 symmetry breaking. Then, for smaller dopings, the system adopts a microphase separation with nanoscale domains, restoring on average the C_4 symmetry. We also study the Fermi surface $\mathcal{D}(\mathbf{k})$ given by

$$\mathcal{D}(\mathbf{k}) = \sum_{j\in\mathcal{F}} |\langle \mathbf{k}|\phi_j\rangle|^2, \tag{8.10}$$

where $|\mathbf{k}\rangle$ are the periodic Bloch states of the square lattice, $|\phi_j\rangle$ are the fermionic single-particle states of the unrestricted mean-field solution, and $\mathcal{F}$ is the subset of these states whose energy lies inside a window of width $t_0/10$ around the Fermi energy. The results are shown in Fig. 8.6(b). For $\delta = 0.2$, close to the C_4 symmetry-breaking transition, the system is homogeneous and the Fermi surface is simply connected. The quasiparticle energies at the nodal points $\mathbf{k} = (\pm\pi/2, \pm\pi/2)$ are not affected by bond orderings, whereas at antinodal points, the dependence on

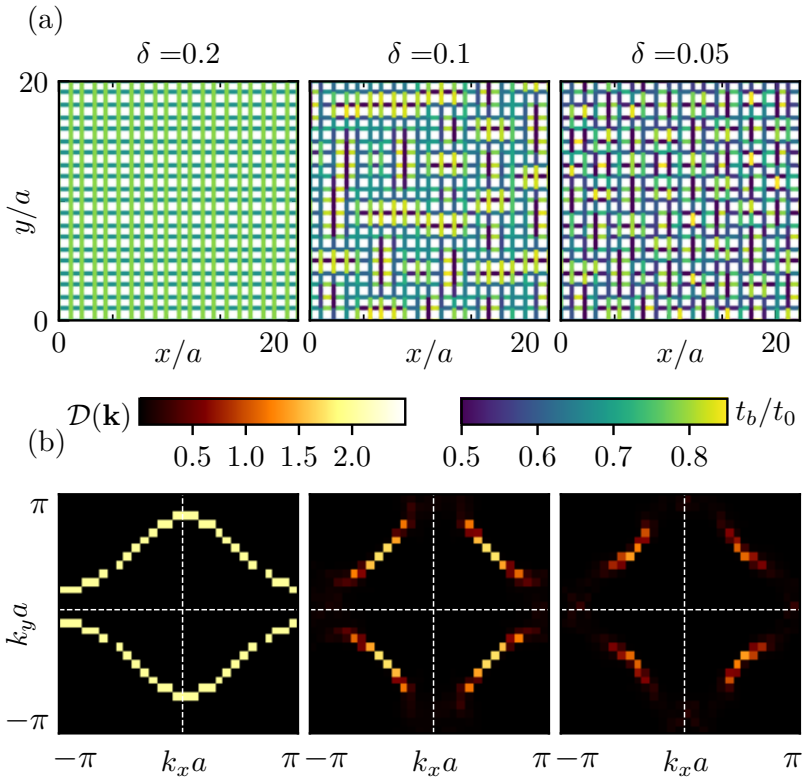

FIGURE 8.6: Pseudogap dependence on hole doping for a fixed temperature $T = 174$ K on a 30×30-site lattice for the RI model with the parameters of Fig. 8.3. (a) Real-space plots of the effective electron hopping at each bond t_b. For $\delta = 0.2$, the system presents an homogeneous C_4 symmetry breaking. For smaller dopings, we observe the formation of nanoscale domains with ladder structures. (b) Fermi surface $\mathcal{D}(\mathbf{k})$ in the Brillouin zone. We observe the appearance of Fermi arcs when increasing the hole doping.

bond orderings is stronger. Therefore, for small dopings where microphase separation occurs, the system presents nodal "cold regions" [399], forming characteristic anisotropic Fermi arcs, and strongly scattered "hot regions" at anti-nodal points, resulting in a disconnected Fermi surface. This picture bears some similarity to the nematic glass theory [390, 396], which however depends on external disorder. The Fermi arcs' length increases with hole doping and leads to reconstruction of a simply connected Fermi surface close to the C_4-C_2 transition. The latter is in qualitative agreement with experimental observations [46, 400].

Figure 8.7 depicts the dependence of the pseudogap with respect to temperature for a fixed doping. For increasing temperature, a progressive closing of the Fermi arcs towards a metallic Fermi surface is observed. In real space, the local amplitudes of the inhomogeneous C_4 symmetry breaking then become strongly suppressed.

8.3.2 Role of impurities

The previous section shows that the nanoscale domains appear without the need of any type of quenched disorder. We now address the effect of non-doping impurities on the pseudogap phase. These are often used as (destructive) probes of superconducting and pseudogap properties of high-T_c materials. In particular, disorder is expected to destabilize nematic phases. However, two different behaviors

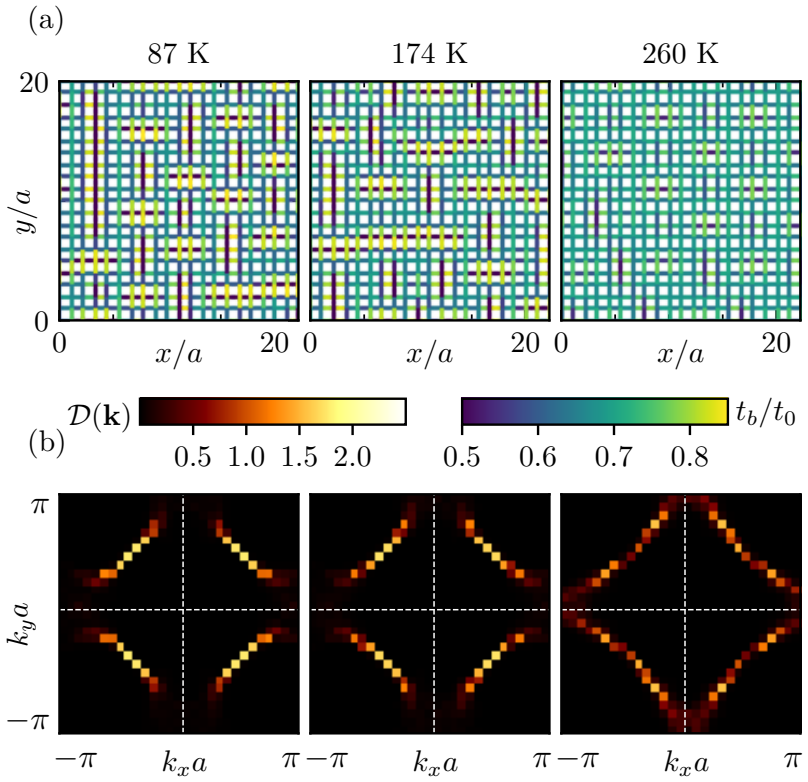

FIGURE 8.7: Pseudogap dependence on temperature for a fixed hole doping of $\delta = 0.1$ on a 30×30-site lattice for the RI model with the parameters of Fig. 8.3 (a) Real-space plots of the effective electron hopping at each bond t_b. The nanoscale domains are smeared out for increasing temperatures. (b) Fermi surface in the Brillouin zone. As the temperature is increased, the Fermi arcs evolve towards a closed metallic surface.

are observed in experiments [401]: while substituting Cu for nonmagnetic Zn suppresses the pseudogap, substitution by magnetic Ni, remarkably, seems to have an enhancing effect on the pseudogap energy scale. Here, we show that the results obtained from the RI model are in qualitative agreement with this impurity related phenomenology. For Ni impurities, we use the Hamiltonian proposed in Ref. [402]

$$\begin{aligned}\hat{H} = &- t_0 \sum_{\langle i,j\rangle,\sigma} \tilde{c}^{\dagger}_{i,\sigma}\tilde{c}_{j,\sigma} + J \sum_{\langle i,j\rangle} \left(\mathbf{S}_i \cdot \mathbf{S}_j - \frac{1}{4}\hat{n}_i\hat{n}_j \right) \\ &+ E_{\mathrm{Ni}} \sum_{\alpha} \hat{n}_{\alpha} - 4K \sum_{\alpha} \mathbf{S}'_{\alpha} \cdot \mathbf{S}_{\alpha},\end{aligned} \tag{8.11}$$

where $\tilde{c}^{\dagger}_{i,\sigma} = \hat{c}^{\dagger}_{i,\sigma}(1 - \hat{n}_{i,-\sigma})$ are the electron creation operators in the $3d_{x^2-y^2}$ orbitals projected to avoid double occupancy in $\hat{n}_i = \sum_{\sigma} c^{\dagger}_{i,\sigma}\hat{c}_{i,\sigma}$, and $\mathbf{S}_i$ are the spin operators of the d orbital. The Ni impurity sites are denoted as α and host additional $3d_{3z^2-r^2}$ orbitals. These orbitals carry a magnetic spin $\mathbf{S}'_{\alpha}$. The last term in Eq. (8.11) describes ferromagnetic Ni on-site interaction between d orbitals. Considering an initial antiferromagnetic state polarized in the z direction and in mean-field approximation, only the S^z components survive,

$$\mathbf{S}_{\alpha} \cdot \mathbf{S}'_{\alpha} \approx \langle S^z_{\alpha}\rangle S'^z_{\alpha} + S^z_{\alpha}\langle S'^z_{\alpha}\rangle - \langle S^z_{\alpha}\rangle\langle S'^z_{\alpha}\rangle. \tag{8.12}$$

Since the $3d_{3z^2-r^2}$ orbitals are not affected by hopping, their spin within such approximation is classical. Nevertheless, the effect of these classical spins $\mathbf{S}'_\alpha$ cannot be considered as quenched disorder, as their equilibrium magnetization is determined self-consistently with the other spins $\mathbf{S}_\alpha$: at each step of the self-consistent loop, the requirement for $\langle S'^z_\alpha \rangle = 1/2\ \mathrm{sgn}(S^z_\alpha)$ aligns it to the local $3d_{x^2-y^2}$ orbital magnetization S_α lowering the energy by

$$-4K' S^z_\alpha \langle S'^z_\alpha \rangle \approx -4K' (S^z_\alpha)^2. \tag{8.13}$$

The latter follows from that $\mathrm{sgn}(4S^z_\alpha) \approx 4S^z_\alpha$. As a consequence, we can consider the following effective Hamiltonian for Ni impurities: for the doped sites α we neglect the shift in the chemical potential proportional to E_{Ni} and consider that the Hamiltonian is modified by the addition of the on-site term

$$\begin{aligned} \hat{H}_{\alpha,Ni} &= -4KS^2_{z,\alpha} = -K(\hat{n}_{\alpha,\uparrow} - \hat{n}_{\alpha,\downarrow})^2 \\ &= -K(\hat{n}_{\alpha,\uparrow} + \hat{n}_{\alpha,\downarrow}) + 2K\hat{n}_{\alpha,\uparrow}\hat{n}_{\alpha,\downarrow}, \end{aligned} \tag{8.14}$$

which leads to a modified on-site chemical potential $\mu_i \to \mu_i + K$ and Hubbard strength $U_i \to U_i + 2K$. K is set to $3/4t_0$. On the other hand, we denote the Zn-doped sites as λ, and we set $\mu_\lambda = \infty$ to effectively remove the doped site from the lattice [403]. In order to keep the hole concentration constant in the remaining available sites, we increase this quantity by $\tilde{\delta} = \delta + n_{\mathrm{Zn}}$, being n_{Zn} the concentration of Zn impurities.

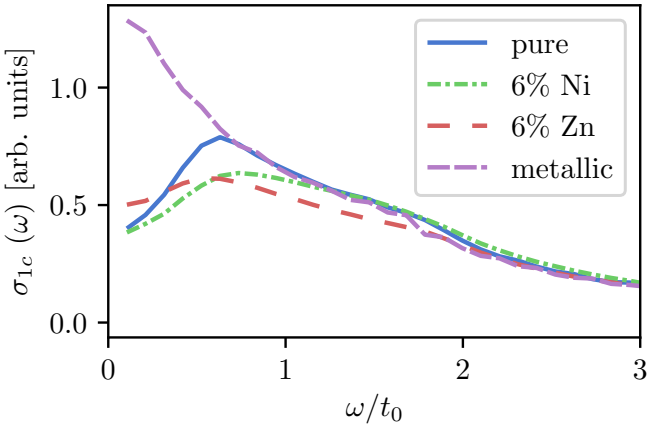

FIGURE 8.8: Effect of impurities on the real part of the c-axis conductivity spectra in the RI model for hole density $\delta = 0.1$, $T = 174$ K, and $U/t_0 = 1.6$ on a 30×30 lattice. The metallic solution (violet, dashed curve) is compared to the pseudogap phase with and without impurities. The pseudogap without impurities presents a characteristic peak. The latter is shifted to the left (right) for Zn (Ni) impurities.

To quantify the effect of the above-mentioned impurities in the pseudogap unrestricted solutions we use the frequency-dependent transverse conductivity $\sigma_{1c}(\omega)$. The transverse conductivity is in general some combination of two parts, a momentum-conserving and a momentum-nonconserving part (see discussion in [404]). The hole doping in cuprates results in disorder in interlayer coupling since dopants can reside between the Copper Oxide layers. In this paper we focus therefore on the nonconserving part of the c-axis conductivity assuming that interlayer tunnelings are in principle randomized both with and without Zn/Ni substitution, as in Ref. [402].

This c-axis conductivity contribution is given by

$$\sigma_{1c}(\omega) \sim \frac{1}{\omega} \int d\omega' \, \left[f(\omega' - \mu) - f(\omega' + \omega - \mu) \right] \times \mathcal{N}(\omega') \mathcal{N}(\omega' + \omega) \,, \tag{8.15}$$

where $\mathcal{N}(\omega)$ is the density of states, and $f(\omega)$ is the Fermi-Dirac distribution.

The c-axis conductivity results are shown in Fig. 8.8 for both types of impurities, together for the pure case and a metallic solution, obtained as the self-consistent homogeneous mean-field solution with C_4 symmetry ($\hat{n}_{i,\sigma} = n/2$ and $t_b = t$). The pseudogap solutions show a characteristic low-energy suppression in the real c-axis conductivity spectrum as well as a peak. The pseudogap energy scale Ω_{PG} is often taken to be the peak position. It indeed behaves as advertised above. Furthermore, the depth of the suppression of the pure and Ni cases are similar, while the Zn pseudogap is more filled in.

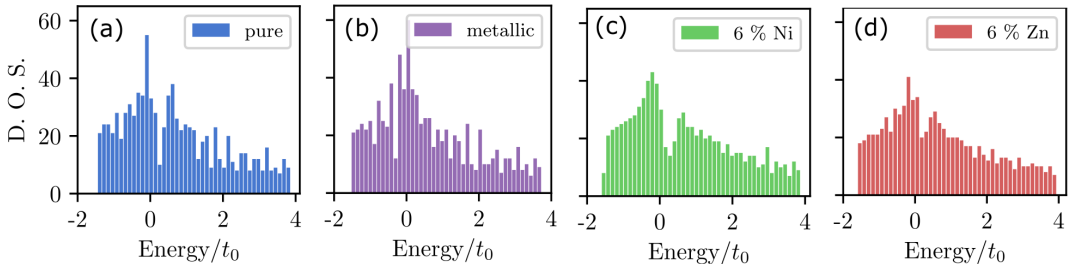

FIGURE 8.9: Density of states $\mathcal{N}(\omega)$ histograms for the cases considered in Fig. 8.8. The number of bins is set to 45. For the RI model, we set the bare hole density $\delta = 0.1$, $T = 174$ K, and $U/t_0 = 1.6$ on a 30×30 lattice.

For completeness, in Fig. 8.9 we show the density of states $\mathcal{N}(\omega)$ corresponding to the cases plotted in Fig. 8.8.

8.4 Summary

In this chapter, we have shown that including anharmonic Cu-O-Cu bond oscillations in Hubbard-type models leads to a number of key features of the pseudogap phase including an inherent mechanism for nanoscale phase separation, Fermi arcs, and appropriate response to defects. This points towards the fact that phonons play a key role in dictating the properties of high-T_c cuprates, and are not simply secondary corrections to electronic correlation effects. Fundamentally, we therefore believe that our results will fuel deeper investigations into the FBM+U model, in particular via the treatment of electronic correlation effects more exactly beyond the mean-field approximation. Furthermore, it would be interesting to study the interplay of the electron-phonon interaction and the Coulomb interaction on the properties of the high-T_c superconductivity, within a non-transitionally invariant ansatz. Finally, the FBM+U model could also serve as a natural basis to investigate how nonthermal and dynamical phonon distributions can be used to enhance and control phase competition in the cuprates. This would provide insights into the origins of light-induced nonequilibrium superconductivity and potentially lead to improved nonequilibrium control of the cuprates phase diagram.

Chapter 9

Bound on the collective power of quantum batteries

In the past decades quantum thermodynamics has emerged as a very active research field, whose main goal is to extend core concepts of classical thermodynamics (e.g., heat, work, entropy) to physical regimes where quantum effects such as entanglement become relevant. A review on the recent progress can be found in [102].

On the experimental side, one of the motivations for developing a quantum theory of thermodynamics has been the observation of equilibration effects in cold atom experiments [113]. Moreover, impressive steps have been achieved towards the miniaturization of classical thermodynamic machines, such as the realization of a single-ion quantum heat engine [52].

In this work we focus on the study of yet another quantum version of a classical machine: a quantum battery. In analogy to a cell-based classical battery, a quantum battery was introduced in the seminal work by Alicki and Fannes [405] as a system composed of N identical quantum systems (quantum cells) whose goal is to store and deliver energy at the microscopic scale. In this early work, it was proposed that the presence of quantum entanglement during a discharging process could boost the amount of extractable energy from the battery. However, later it was shown that the same amount of extractable work could be accessed only via classical correlations [406].

The situation is different for the power of a quantum battery, i.e., the rate at which energy is stored, for which the use of quantum effects can lead to a genuine enhancement. In the seminal work [126], Binder et al. introduced the notion of a quantum speedup in the charging of a quantum battery when the cells become entangled during the time evolution. Such speedup was related to the fact that when the battery evolves through an entangled subspace it follows a geodesic in Hilbert space, i.e., the path with minimal length. The latter leads to a quantum speedup when one constraints the norm of the Hamiltonian governing the time evolution, which is related to the speed of evolution in Hilbert space.

After this seminal work, several groups have studied the relation between entanglement and power of a quantum battery in concrete models that could be experimentally realized [407, 408]. In a more fundamental approach, Campaioli et al. [409] bounded the quantum speedup in power in terms of the interaction order and participation number of the Hamiltonian driving a unitary charging evolution.

In this chapter, we introduce a new bound on the instantaneous power of a quantum battery that depends on two terms. The first term is a measure of the speed in energy space, which allows to explicitly quantify the impact of this factor in the power of a quantum battery, without the need of imposing any normalization constraint that may or may not correspond to the experimental implementation. The

second term corresponds to the variance of the battery Hamiltonian, which witnesses the presence of entanglement between the cells and it can even quantify it for the case of spin-based batteries. Therefore, our bound provides, for the first time, a general framework to analyze and quantify the impact of entanglement and normalization constraints in the charging power of a general quantum battery.

This chapter, mostly based on Ref. [1], is organized as follows. In Section 9.1, we review the definition of a cell-based quantum battery and the relevant physical quantities associated to such systems. Section 9.2 contains the main result, that is, a derivation of a bound in the power of a quantum battery, together with a discussion on the role of entanglement in power in the framework of this bond. In Section 9.3, we analyze the charging power of trivial paradigmatic models of quantum batteries by means of our derived bound, highlighting the impact of both entanglement and normalization constraints. Finally, in Section 9.4, we show the usefulness of the bound by analyzing more complex models that had been already discussed in the literature, and some new ones.

9.1 Quantum batteries and their figures of merit

To account for the cell structure of the quantum battery, the battery Hamiltonian describing the stored energy is modelled as the sum of independent Hamiltonians

$$\hat{H}_B = \sum_{i=1}^{N} \hat{h}_B^i, \tag{9.1}$$

where $\hat{h}_B^i$ is the Hamiltonian describing the energy stored in the i-th quantum cell.

At any time t, a quantum battery is described as a quantum state $\hat{\rho}_B(t)$. In a charging (discharging) process, the latter changes under the effect of a general quantum evolution,

$$\hat{\rho}(t) = \Gamma_t(\hat{\rho}(t_0)) \tag{9.2}$$

which in the unitary evolution case is fully specified by a charging Hamiltonian $\hat{H}_C$,

$$\hat{\rho}(t) = e^{i\hat{H}_C t}\hat{\rho}(t_0)e^{-i\hat{H}_C t}. \tag{9.3}$$

The first figure of merit is the stored energy in the battery with respect to the one of the initial state $\hat{\rho}(0)$, that is

$$E(t) \coloneqq \mathrm{Tr}\big(\hat{\rho}(t)\hat{H}_B\big) - \mathrm{Tr}\big(\hat{\rho}(0)\hat{H}_B\big). \tag{9.4}$$

In general, a good quantum battery is expected to be able to store as maximum energy as possible. Notice, however, that $E(t)$ is in general an upper bound to the stored thermodynamic work, and the two quantities only coincides in the case of a unitary time evolution.

Even in the case of a unitary evolution, the final work stored in the energy can exhibit huge quantum fluctuations, which can be quantified through the variance in the battery energy

$$\Delta\hat{H}_B(t)^2 = \mathrm{Tr}\big(\hat{\rho}(t)\hat{H}_B^2\big) - \mathrm{Tr}\big(\hat{\rho}(0)\hat{H}_B\big)^2. \tag{9.5}$$

Even though such fluctuations can be useful during the charging process, as will be described below, one would like a final charged state with minimal fluctuations.

Finally, the central quantity of interest here is the charging power of the quantum battery, defined as the rate of change of the stored energy:

$$P(t) \coloneqq \frac{\mathrm{d}}{\mathrm{d}t} E\left(\rho(t)\right) . \tag{9.6}$$

9.2 Derivation of the bound on power

In this section, we derive the bound on power, following geometric approaches towards quantum speed and trajectories. Although our discussion is focused on the problem of energy storage, our bound can also be applied to any other observable O, when the main goal is to increase its expectation value $\langle O(t)\rangle$ as fast as possible.

9.2.1 Speed of evolution in state space and energy eigenspace

We start by introducing a notion of distance between states in Hilbert space. At this point we deem appropriate to mention that many of the concepts that will appear in this section appear naturally in the framework of quantum speed limits (for a review, see Ref. [410]). However, here we will use them in the form crafted for the study of energy storage. Let us consider the *Bures angular distance* [411], between two quantum states ρ and σ, defined as

$$D_Q(\hat{\rho},\hat{\sigma}) = \arccos\left[F(\hat{\rho},\hat{\sigma})\right] , \tag{9.7}$$

where $F(\hat{\rho},\hat{\sigma}) = \mathrm{tr}\left(\sqrt{\sqrt{\hat{\rho}}\hat{\sigma}\sqrt{\hat{\rho}}}\right)$ is the Uhlmann's fidelity [18]. Now, for an evolution of a system $\hat{\rho}(t) \to \hat{\rho}(t+dt)$, the instantaneous speed in state space is defined as

$$v(t) \coloneqq \lim_{\delta t\to 0} \frac{D(\hat{\rho}(t+\delta t),\hat{\rho}(t))}{\delta t} . \tag{9.8}$$

After a straightforward calculation (see, for example, Ref. [410]), it can be rewritten as

$$v(t) = \frac{1}{2}\sqrt{I_Q(\hat{\rho}(t))}, \tag{9.9}$$

where $\mathcal{I}_Q(\rho(t))$ is the *quantum Fisher information*. For any quantum state $\hat{\rho}(t) = \sum_i p_i|i\rangle\langle i|$, which is undergoing a unitary evolution driven by a Hamiltonian $\hat{H}(t)$, the quantum Fisher information is given by

$$I_Q(\hat{\rho}(t)) = \sum_{i\neq j} \frac{(p_i-p_j)^2}{p_i+p_j} |\left\langle i|\hat{H}(t)|j\right\rangle|^2. \tag{9.10}$$

The quantum Fisher information, in information theory, has the interpretation of an information measure [412]. In fact, the $I_Q(\hat{\rho}(t))dt^2$ quantifies the distance between states $\hat{\rho}(t)$ and $\hat{\rho}(t+dt)$ that are separated by an infinitesimal time dt and driven by the Hamiltonian $\hat{H}(t)$. In the context of quantum metrology, a higher value of the quantum Fisher information indicates a potential to result in a higher precision estimation of a parameter. For instance, $\mathcal{I}_Q(\hat{\rho}(\theta)) = 0$ implies that no information about the parameter θ can be extracted, whereas divergent $\mathcal{I}_Q(\hat{\rho}(\theta)) \to \infty$ means that one can estimate the parameter θ with infinite precision. We refer to the Refs.

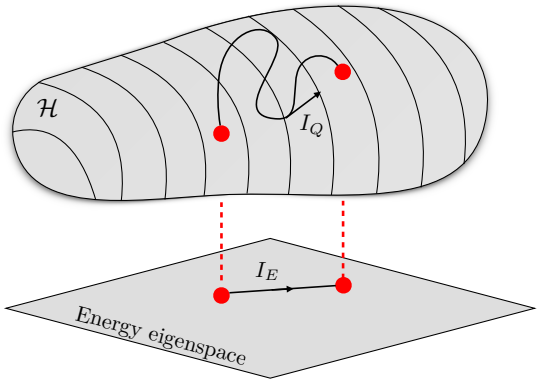

FIGURE 9.1: A schematic representation of speed of quantum evolution in Hilbert space (I_Q) and the speed of evolution in the energy eigenspace of the battery Hamiltonian (I_E). Notice that, in general, $I_Q \geqslant I_E$.

[413] and [414] for a review in the context of quantum Information and quantum optics, respectively.

For the case of pure states, the Bures distance reduces to the Fubini-Study distance, which is given by

$$D(\psi, \phi) \coloneqq \arccos |\langle \phi | \psi \rangle| \,. \tag{9.11}$$

Then, the corresponding speed, for the case of a unitary time evolution driven by a Hamiltonian $\hat{H}_C(t)$, becomes

$$v(t) = \sqrt{\langle \psi(t)| \hat{H}_C(t)^2 |\psi(t)\rangle - \langle \psi(t)| \hat{H}_C(t) |\psi(t)\rangle^2} =: \Delta \hat{H}_C(t) \,. \tag{9.12}$$

Hence, for pure states, the speed of the system in the Hilbert space is given by the instantaneous energy variance measured by the charging Hamiltonian $\hat{H}_C(t)$ that drives the evolution of the system. Note that, in the case of a time-independent charging Hamiltonian, the energy variance does not change during the entire evolution. Once we have a notion of speed, the length of the trajectory followed for a time t_F is given by

$$L[\hat{\rho}(t), t_F] = \int_0^{t_F} \mathrm{d}t \; v(t) \,. \tag{9.13}$$

When considering the Bures angle as a measure of distance, we are looking at the physical distinguishability of the system. However, when looking at systems as quantum batteries, i.e., energy storage devices, we are not interested in how fast the state changes, but in how fast its energy distribution evolves. In other words, there are orthogonal states (perfectly distinguishable) that have identical energy distributions. Thereby, although the system can be moving very fast in the state space, its change in the energy content can be negligible. From this perspective, it is useful to introduce a measure of distance between quantum states not based on their statistical distinguishability, but in their energetic distinguishability (see Fig. 9.1). To do so, let us write the battery Hamiltonian in its spectral representation

$$\hat{H}_B = \sum_k E_k \hat{P}_k \,, \tag{9.14}$$

where $\hat{P}_k$ is the projector onto the eigenspace associated to the eigenvalue E_k. The energy distribution of a state $\hat{\rho}$ is given by the populations

$$p_k \coloneqq \mathrm{Tr}\left(\hat{P}_k\,\hat{\rho}\right)\,. \tag{9.15}$$

The speed in the energy space can then be defined as the relative entropy distance between the energy distributions in two consecutive moments of time

$$v_E(t) \coloneqq \lim_{\delta t\to 0}\frac{D_{KL}(\vec{p}(t+\delta t)\|\vec{p}(t))^{1/2}}{\delta t}\,, \tag{9.16}$$

where $D_{KL}(\vec{p},\vec{q})$ is the relative entropy or Kullback-Leibler divergence [411] between two discrete probability distributions $\vec{p}$ and $\vec{q}$. It is defined by

$$D_{KL}(\vec{p}\|\vec{q}) \coloneqq \sum_k p_k \log_2\frac{p_k}{q_k}\,. \tag{9.17}$$

After a straightforward calculation, one gets

$$D_{KL}\left(\vec{p}(t+\delta t)\|\vec{p}(t)\right) = \sum_k \frac{\dot{p}_k^2}{p_k}\delta t^2 + O(\delta t^3)\,, \tag{9.18}$$

where the first order contribution vanishes due to $\sum_k \dot{p}_k = 0$. This means that the right distance to define a speed is the square root of the relative entropy, which can be written in terms of the *Fisher information in the energy eigenspace* as

$$I_E(t) \coloneqq 2v_E(t)^2 = \sum_k \left(\frac{\mathrm{d}}{\mathrm{d}t}\log_2 p_k(t)\right)^2 p_k(t)\,. \tag{9.19}$$

It is interesting to point out that the same conclusion is reached when, instead of using the Kullback-Leibler distance, one employs the angular distance $D(p,q) \coloneqq \arccos F_{\mathrm{cl}}(p,q)$, with $F_{\mathrm{cl}}(p,q) = \sum_k \sqrt{p_k q_k}$ being the classical fidelity. As the quantum fidelity reduces to the classical one in the case where the states are diagonal in the same eigenbasis, the speed in energy space can be understood as the speed in the state space of the dephased states in the energy basis

$$v_E(t) = \lim_{\delta t\to 0}\frac{D\left(\overline{\hat{\rho}(t+\delta t)},\overline{\hat{\rho}(t)}\right)}{\delta t} \leqslant v(t)\,, \tag{9.20}$$

where $\bar{\hat{\rho}} \coloneqq \sum_k \hat{P}_k\hat{\rho}\hat{P}_k$ represents the dephased state in the energy eigenbasis. We refer to the Fig. 9.1 for a schematic representation. The last inequality is a consequence of the Bures distance being monotonically decreasing under quantum operations.

Note that both the I_Q and the I_E of uncorrelated and independent systems are additive. Thus, for a system composed on N identical subsystems in which each subsystem goes through the same independent evolution, the speed at which the system runs along a trajectory scales as $\sqrt{N}$. This scaling for independent subsystems will be relevant in the later discussion.

9.2.2 The bound on power

Equipped with this geometric framework, let us introduce the following result. That is an upper bound on the rate at which any dynamical process can change the mean

value of a given moment of an observable.

Theorem 1. *Given an observable $\hat{O}$, that is time-independent in the Schrödinger picture, the following inequality is satisfied*

$$\left(\frac{d}{dt}\langle\hat{O}^m\rangle\right)^2 \leq \Delta\left(\hat{O}^m\right)^2 I_O(t), \tag{9.21}$$

where $\Delta\left(\hat{O}^m\right)^2$ is the variance of the m-th moment of the observable that captures how non-local the evolution process is, and $I_O(t)$ is the Fisher information, which corresponds to the speed of the process in the observable ($\hat{O}$) eigenspace.

Proof. We first write the m-th power of the operator $\hat{O}$ in its spectral decomposition:

$$\hat{O}^m = \sum_k \hat{O}_k^m \hat{\Pi}_k, \tag{9.22}$$

where O_k are the eigenvalues of $\hat{O}$ and $\hat{\Pi}_k$ the projectors onto the corresponding subspaces. Using this decomposition, we can write the expected value of $\hat{O}^m$ as

$$\langle\hat{O}^m\rangle = \sum_k O_k^m \pi_k(t), \tag{9.23}$$

where $\pi_k(t) \coloneqq \mathrm{tr}\left\{(\hat{\rho}(t)\hat{\Pi}_k)\right\}$. Taking the time-derivative of the last equation we get

$$\frac{\mathrm{d}}{\mathrm{dt}}\langle\hat{O}^m\rangle = \sum_k O_k^m \dot{\pi}_k(t) = \sum_k \sqrt{\pi_k(t)}\left(O_k^m - C(t)\right)\frac{\dot{\pi}_k(t)}{\sqrt{\pi_k(t)}}, \tag{9.24}$$

where in the last step we have used $\sum_k \dot{\pi}_k(t) = 0$. Finally, using the Cauchy-Schwarz inequality, we get

$$\left(\frac{\mathrm{d}}{\mathrm{dt}}\langle\hat{O}^m\rangle\right)^2 \leq \left[\sum_k \pi_k(t)\left(O_k^m - C(t)\right)^2\right]\left[\sum_l \frac{\dot{\pi}_l(t)^2}{\pi_l(t)}\right]. \tag{9.25}$$

We can now identify the second factor on the right-hand side as the *Fisher information* I_O, representing the speed of evolution in the observable $(\hat{O})$ eigenspace. Furthermore, as Eq. (9.25) is valid for any $C(t)$, a minimization over C yields

$$C = \langle\hat{O}^m\rangle, \tag{9.26}$$

which leads us to identify the first factor on the right-hand side as $\Delta\left(\hat{O}^m\right)^2$, and completes the proof.

Corollary 2 (Power)**.** *Given a process for charging (or discharging) a battery, with Hamiltonian $\hat{H}_B$, its instantaneous power fulfills*

$$P(t)^2 \leqslant \Delta\hat{H}_B(t)^2 I_E(t), \tag{9.27}$$

where $\Delta\hat{H}_B(t)^2$ is the variance of the battery Hamiltonian that captures how nonlocal in energy the charging process is, and $I_E(t)$ is the Fisher information, which corresponds to the speed of the charging process in the energy eigenspace.

The corollary above can be seen as a special case of the theorem 1, where the observable is the battery Hamiltonian, $O = \hat{H}_B$, and $m = 1$. We can parametrize the

tightness of the bound for power via an angle θ_P that satisfies

$$\cos\theta_P \coloneqq \frac{P}{\sqrt{\Delta\hat{H}_B^2 I_E^2}}. \tag{9.28}$$

This angle may be used to quantify how efficient a charging process is in terms of power, if one considers $\Delta\hat{H}_B^2$ and I_E as resources that can give maximum power when $\cos(\theta_P) = 1$. Furthermore, in some cases, it could be useful to consider a time-averaged version of the bound (9.27) to eliminate the time-dependence. One possibility would be to consider the bound

$$\frac{\Delta E}{\Delta t} \leq \sqrt{\langle \Delta\hat{H}_B^2 \rangle_{\Delta t} \langle I_E \rangle_{\Delta t}}, \tag{9.29}$$

where ΔE is the change in the battery energy during the interval Δt, and

$$\langle X \rangle_{\Delta t} \coloneqq 1/\Delta t \int_{t_0}^{t_0+\Delta t} X \, dt. \tag{9.30}$$

To show that the speed of evolution in energy eigenspace I_E is more informative than the one in Hilbert space when studying power, let us consider that the charging process is driven by a Hamiltonian evolution given by $\hat{H}_C(t)$. We can derive the following inequality from Heisenberg's uncertainty principle:

$$\left(\frac{\mathrm{d}}{\mathrm{dt}} \langle \hat{H}_B \rangle\right)^2 = |\langle [\hat{H}_B, \hat{H}_C(t)] \rangle|^2 \leq 4\Delta\hat{H}_B^2 \Delta\hat{H}_C(t)^2, \tag{9.31}$$

showing that our bound (9.27) is lower than the one obtained using Heisenberg's principle, as $I_E \leq 4\Delta\hat{H}_C^2$. Note that this improvement is due to the fact that we are lowering the factor $4\Delta\hat{H}_C^2$, which is the speed of evolution in Hilbert space by replacing it with I_E that specifically quantifies the speed in energy space.

We also remark that, by using I_E instead of $\Delta\hat{H}_C^2$, the quantities appearing in the bound (9.27) only depend on the battery Hamiltonian $\hat{H}_B$ and the battery state $\hat{\rho}(t)$. Thus, the bound is not restricted to the case of Hamiltonian evolution, but it can be used for any dynamical map. However, one should be careful with the connection between stored energy and stored work in the presence of an environment.

9.2.3 Quantum advantage in power

Once again, let us consider a battery that is made up of N identical quantum cells, each with a Hamiltonian $\hat{h}_j$, such that the total battery Hamiltonian reads $\hat{H}_B = \sum_{j=0}^{N-1} \hat{h}_j$. Now, given two charging processes, how can we meaningfully state that one of the two has a better performance in terms of power than the other? In the literature, this comparison is made in reference to the *parallel charging* case [126, 407, 409]. For a battery composed of N identical quantum cells, a parallel charging process is a unitary evolution driven by a charging Hamiltonian of the form

$$\hat{H}_C^{||} = \sum_{j=0}^{N-1} \hat{h}_c^j, \tag{9.32}$$

where the Hamiltonian $\hat{h}_c^j$ locally drives the charging process of the j-th quantum cell in the battery.

Now, to compare with any other unitary charging process, driven by a general charging Hamiltonian $\hat{H}_C$, different quantities are chosen and normalized such that they give rise to the same scaling with the number of cells as in the parallel case. These normalization procedures impose an extensive scaling (linear in N) of the norm of the Hamiltonian $\left\|\hat{H}_C\right\|$, its variance $\Delta\hat{H}_C^2$, or their time-averages in the case of time-dependent Hamiltonians, equal to the case with $\hat{H}_C^{||}$. Under this constraint, unnormalized and normalized Hamiltonians are related by a rescaling $\hat{H}_C \to x(N)\hat{H}_C$. The rescaling ensures that the total energy available to drive the charging process is always the same at order N. In the context of these normalization criteria, speedups in power compared to parallel charging have been theoretically explored in Refs. [126, 409]. In these works, entangled states or entangling operations are considered to be closely related with such speedups.

There are two main issues with the aforementioned approach to compare among batteries. First, the presented normalization criteria may not correspond with the real experimental limitations. It could very well be that the experimentalist is limited by the strength of the local interactions but not by its amount. Hence, a fair comparison will mainly depend on the experimental capabilities. A solution to this limitation can be given by our approach, in terms of the bound in (9.27), as it is derived irrespective of any normalization. There, the bound is given in terms of I_E, which may scale faster than N.

Once the speed of evolution in energy eigenspace has been properly taken into account, we focus on the second term in the bound (9.27), i.e., the energy variance $\Delta(\hat{H}_B)^2_{\hat{\rho}}$, and we analyze it from the geometrical point view. In particular, this term encodes the information about how quantum properties, such as quantum entanglement, plays an important role in enhancing the power of the battery. Below, we study its relation with quantum entanglement, and relate it with the charging power.

9.2.4 Relation of power with entanglement

Consider a battery that is made up of N identical quantum cells, with the battery Hamiltonian $\hat{H}_B = \sum_{i=0}^{N} \hat{h}_i$. The variance of $\hat{H}_B$ for an arbitrary state $\hat{\rho}$ reads

$$\begin{aligned}\Delta(\hat{H}_B)^2_{\hat{\rho}} = &\sum_i \left(\mathrm{tr}\left(\hat{h}_i^2\hat{\rho}\right) - \mathrm{tr}\left(\hat{h}_i\hat{\rho}\right)^2\right) + \\ &+ \sum_{i\neq j}\left(\mathrm{tr}\left(\hat{h}_i\hat{h}_j\hat{\rho}\right) - \mathrm{tr}\left(\hat{h}_i\hat{\rho}\right)\mathrm{tr}\left(\hat{h}_j\hat{\rho}\right)\right) .\end{aligned} \tag{9.33}$$

Let us discuss the relation of entanglement with (9.33) for the case of pure states of the battery. The first sum corresponds to the single-cell energy variance, which we denote as $\Delta^{Loc}(\hat{H}_B)^2_{\hat{\rho}} = \sum_i \left(\mathrm{tr}\left(\hat{h}_i^2\hat{\rho}\right) - \mathrm{tr}\left(\hat{h}_i\hat{\rho}\right)^2\right)$. This quantity scales linearly with the number of cells N and coincides with $\Delta(\hat{H}_B)^2_{\hat{\rho}}$ in the case of separable states ($\hat{\rho} = \bigotimes \hat{\rho}_i$). As a consequence, the only way for the variance to scale faster than N is that the battery state is non-separable, and thus entangled.

Indeed, in some cases one can even bound the energy variance $\Delta(\hat{H}_B)^2_{\hat{\rho}}$ with the multipartite entanglement properties of the battery state [415, 416]. For example, let us consider linear qubit Hamiltonians, typically used as models of a quantum battery [126, 407, 408], and that will be studied in Sections 9.3 and 9.4, which have

the form

$$\hat{H}_B = \frac{1}{2}\sum_{j=0}^{N-1}\hat{\sigma}_z^j, \tag{9.34}$$

where $\hat{\sigma}_z^j$ is the z Pauli matrix corresponding to the j-th site of the qubit chain, and we have defined the single-cell energy spacing as the unit of energy. To characterize the multipartite entanglement of this system consisting on N qubits, one introduces the notion of a k-producible state [417, 418]: a pure state is k-producible if it can be writen as the tensor product

$$\left|\Psi_{k-\text{prod}}\right\rangle = \otimes_l \left|\Psi_l\right\rangle \tag{9.35}$$

where $|\Psi_l\rangle$ is a state of at most k qubits of the chain. A mixed state is k-producible if it is a mixture of pure k-producible states

$$\hat{\rho}_{k-\text{prod}} = \sum_\alpha p_\alpha \left|\Psi^\alpha_{k-\text{prod}}\right\rangle\left\langle\Psi^\alpha_{k-\text{prod}}\right|, \qquad \left(\sum_\alpha p_\alpha = 1\right). \tag{9.36}$$

Based on this classification of states, a state is k-qubit entangled if it is k-producible but not $(k-1)$-producible. For our purposes, a useful inequality for N-qubit k-producible states is [415, 416]

$$4\Delta(\hat{H}_B)^2_\rho \leqslant rk^2 + (N-rk)^2, \tag{9.37}$$

where r is the integer part of N/k. Any state (pure or mixed) that violates the bound of Eq. (9.37) thus contains $(k+1)$-qubit entanglement. Using the above inequality, we recast the bound on power and arrive to the corollary (3).

Corollary 3 (Power and entanglement)**.** *Given a process for charging (or discharging) a quantum battery composed of N-qubits, with a battery Hamiltonian of the form of Eq. (9.34), if at time t the battery is at most k-qubit entangled, its instantaneous power fulfills*

$$P(t)^2 \leqslant \Delta\hat{H}_B(t)^2 I_E(t) \leqslant \underbrace{\frac{1}{4}\left[rk^2 + (N-rk)^2\right]}_{k\text{-producibility}} \underbrace{I_E(t)}_{\substack{\text{disting. in}\\ \text{energy eig.}}}, \tag{9.38}$$

where r is the integer part of N/k. In the cases where r is an exact integer, the inequality reduces to

$$P(t)^2 \leqslant \frac{kN}{4} I_E(t). \tag{9.39}$$

Notice that the bound of Eq. (9.38) sets the limitations imposed in power by the multipartite entanglement properties of the battery state and its distinguishability in the energy eigenspace, both for pure and mixed states. Thus, this bound leads to a deeper understanding of the relation between entanglement and power in qubit-based quantum batteries. For instance, the inequality (9.37) is saturated only by a battery state which is a product of r Greenberger-Horne-Zeilinger (GHZ) states of k qubits $|\text{GHZ}_k\rangle$, and another set of GHZ states of $N-rk$ qubits $|\text{GHZ}_{N-rk}\rangle$[416], with

$$|\text{GHZ}_k\rangle = \frac{1}{\sqrt{2}}\left(|0\rangle^{\otimes k} + |1\rangle^{\otimes k}\right). \tag{9.40}$$

An example of such a GHZ state was indeed introduced (with $k = N$) in the seminal paper [126], introducing the potential entanglement boost in quantum batteries.

Another important insight is that many-body charging Hamiltonians with a large participation number and low order of interactions will generically lead to battery states that strongly differ from the optimal GHZ ones. In that sense, we would also like to note that it is interesting to compare our bound of Eq. (9.38) with the ones derived in the work [409], where the relation of the quantum advantage in Power with the interaction order and participation number has been considered.

9.3 Paradigmatic examples

One example that has become paradigmatic in the field [126, 407, 408] is the charging of a battery composed of noninteracting cells by a time-independent Hamiltonian evolution. Once again, let us consider the battery Hamiltonian of N two-level systems with the Hamiltonian $\hat{H}_B = \frac{1}{2}\sum_{j=0}^{N-1}\hat{\sigma}_z^j$, which has the same form as Eq. (9.34). Initially, at $t = 0$, the battery is in its ground state $|\psi_0\rangle = |0\rangle^{\otimes N}$. Notice that the ground state has a negative energy and, as we are interested in the energy difference, hereafter we will define the stored energy at a given time as

$$E(t) := \mathrm{Tr}\big(|\psi(t)\rangle\langle\psi(t)|\hat{H}_B\big) - \mathrm{Tr}\big(|\psi_0\rangle\langle\psi_0|\hat{H}_B\big). \tag{9.41}$$

In order to charge the battery, one can use different charging Hamiltonians $\hat{H}_C$. In particular, illustrative examples are the cases of a *parallel*, *global* and *hybrid* Hamiltonians, represented by $\hat{H}_C^{||}$, $\hat{H}_C^{\#}$, and $\hat{H}_C^{h}$, respectively. These Hamiltonians are given by

$$\begin{aligned}
\hat{H}_C^{||} &= \lambda \sum_{j=0}^{N-1} \hat{\sigma}_x^j, \\
\hat{H}_C^{\#} &= \lambda \otimes_{j=0}^{N-1} \hat{\sigma}_x^j, \\
\hat{H}_C^{h} &= \lambda \sum_{j=0}^{q-1} \otimes_{i=1}^{r} \hat{\sigma}_x^{qj+i},
\end{aligned} \tag{9.42}$$

where $\hat{\sigma}_x^j$ is the x Pauli matrix operator acting on the jth cell, and in the *hybrid* case $N = qr$. Regarding time-units, here λ represents a charging frequency, where we use the convention $\hbar = 1$. The main features of these three charging processes are outlined in the Table 9.1 below.

It is easy to see that all these Hamiltonians evolve the initial ground state to the highest energy state $|1\rangle^{\otimes N}$. Therefore, the system achieves the maximum stored energy possible at time $\lambda t_f = \pi/2$. The power is the same for all the cases, and the bound (9.27) is always saturated. Furthermore, for these cases, the evolution speed in state space and energy eigenspace coincide, as $I_E = 4\Delta\hat{H}_C^2$ (see Table 9.1). As can be seen in Fig. 9.2, without any normalization constraints, I_E scales linearly with N in the *parallel* case, as there are many energy levels involved in the evolution. The situation is drastically different in the *global* case, where only the ground state and maximally excited energy levels participate, leading to an N-independent scaling of I_E. The *hybrid* case presents an intermediate behavior.

The quantum enhancement in power in these paradigmatic examples was understood [126, 409] with the help of certain normalization criteria, as explained in Section 9.2.3. The approach in Ref. [409], for instance, imposes a linear scaling of $\Delta\hat{H}_C^2$ with N, and one should perform the normalization $\hat{H}_C^{\#} \to \sqrt{N}\hat{H}_C^{\#}$. With this

TABLE 9.1: Comparison between three different charging Hamiltonians of a battery composed of N qubit cells: the *parallel* charging, the fully interactive *global* Hamiltonian (optimal) and an *hybrid* construction where m blocks of q qubits are in parallel charged in a fully interactive way. See also Fig. 9.2.

	Parallel	**Global**	**Hybrid**
$\hat{H}_C$	$\lambda \sum_j \hat{\sigma}_x^j$	$\lambda \otimes_j \hat{\sigma}_x^j$	$\lambda \sum_{j=0}^{q-1} \otimes_{i=1}^{r} \hat{\sigma}_x^{qj+i}$
$\left\|\hat{H}_C\right\|$	$N\lambda$	λ	$q\lambda$
λt_F	$\pi/2$	$\pi/2$	$\pi/2$
$\Delta\hat{H}_C^2$	$N\lambda^2$	λ^2	$q\lambda^2$
I_E	$4N\lambda^2$	$4\lambda^2$	$4q\lambda^2$
$E(t)$	Np	Np	Np
$\Delta\hat{H}_B(t)^2$	$Np(1-p)$	$N^2p(1-p)$	$Nrp(1-p)$
k-qubit ent.	1	N	r
$\Delta^{Ent}\hat{H}_B(t)^2$	0	$Np(N-1)(1-p)$	$Np(r-1)(1-p)$
$P(t)$	$\sqrt{\Delta^2\hat{H}_B I_E}$	$\sqrt{\Delta^2\hat{H}_B I_E}$	$\sqrt{\Delta^2\hat{H}_B I_E}$

*$p = \sin^2(\lambda t)$. **Note, at t_0 and t_f the state of the system is always a product state regardless of the form of $\hat{H}_C$.

criterion, the global charging is $\sqrt{N}$ times faster than the parallel one. On the other hand, under the constraint of $\left\|\hat{H}_C\right\|$ scaling as N, imposed in Ref. [126], one should perform the normalization $\hat{H}_C^{\#} \to N\hat{H}_C^{\#}$. Within such norm rescaling, the global charging performs N times faster than the parallel one.

Instead, the approach presented in the previous sections allows us to discuss the role of the entanglement between the cells in the power of these models, without the need of relying on a normalization constraint, and in a quantitative manner. It is easy to see that the *global* (*r-hyrbid*) Hamiltonians leads to a battery state that will have $N(r)$-qubit entanglement:

$$\begin{aligned} |\Psi\rangle_{global} &= \sqrt{1-p}\,|0\rangle^{\otimes N} + \sqrt{p}\,|1\rangle^{\otimes N}, \\ |\Psi\rangle_{hybrid} &= \otimes_{j=0}^{q-1} |\Psi(t)\rangle_j, \\ |\Psi\rangle_j &= \sqrt{1-p}\otimes_{i=1}^{r}|0\rangle_{qj+i} + \sqrt{p}\otimes_{i=1}^{r}|1\rangle_{qj+i}. \end{aligned} \tag{9.43}$$

Notice (compare rows 7 and 8 of Table 9.1) that this amount of k-qubit entanglement impacts the super-linear scaling factor of $\Delta^2\hat{H}_B$, and thus also the one of power. In the middle of the evolution, for $t = \pi/4$ the states are exactly in the GHZ form, and the bound of Eq. (9.38) is saturated.

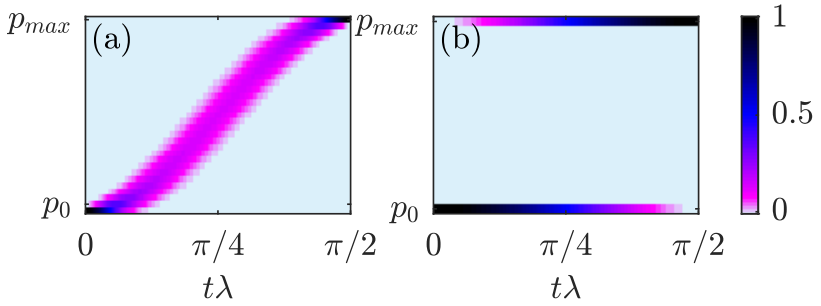

FIGURE 9.2: Dynamics of energy levels p_k, according to their definition (9.15), during a parallel (a) and a global (b) charging process. Here one can see the contribution of each energy level (y-axis) to the total energy, as a function of time. One can see absolute nonlocality in energy space for the global case, where there is a coexistence in time of the highest and lowest energy level, and locality of the parallel one, where at a given time only levels that are close contribute to the total energy.

9.4 Specific spin models

In this section, we study our previously derived bounds in specific spin-$\frac{1}{2}$ models, effectively described in terms of qubits. The models, which can in principle be realized experimentally (see, for instance, Ref. [40]), are (i) integrable spin models in one dimension with ultracold fermionic atoms, (ii) the Lipkin-Meshkov-Glick (LMG) model with ultracold atoms or atoms near nanostructures, and (iii) Dicke model with ultracold ions, Bose-Einstein condensates in an optical cavity, or cavity circuit quantum electrodynamics. While it is true that some of these spin models have already been presented in the literature [126, 407, 408] as candidates for an experimentally realizable quantum battery, we use our formalism to systematically analyze them. More specifically, for each model we discuss the impact of both the evolution speed, quantified by I_E, and the smartness of the path undergone in the power of the battery, related to $\Delta\hat{H}_B^2$ and k-qubit(spin) entanglement, hence clarifying the origin of possible speedups. Furthermore, we also study the amount and quality of stored energy in the final battery state.

In all the cases we consider that the quantum battery is a chain of N spin-$\frac{1}{2}$ cells. We work in the local basis of Pauli matrices for each spin, i.e., any local operator acting on j-th spin can be expressed in terms of $\{\hat{\sigma}_x^j, \hat{\sigma}_y^j, \hat{\sigma}_z^j, \mathbb{1}\}$, and define our battery Hamiltonian as

$$\hat{H}_B = \frac{1}{2}\sum_{j=0}^{N-1} \hat{\sigma}_z^j. \tag{9.44}$$

We consider that the spin system is initially in the ground state of the battery Hamiltonian $\hat{H}_B$. We now look at different charging models.

9.4.1 Integrable spin models

Here we consider a general class of charging Hamiltonians in one dimension of the form

$$\begin{aligned}\hat{H}_{JW} = \hat{H}_B + \frac{1}{2}\sum_{\substack{j=0\\m=1}}^{N-1} \Big[&(\lambda_m + \gamma_m)\sigma_x^j(\otimes_{l=j+1}^{j+m-1}\hat{\sigma}_z^l)\hat{\sigma}_x^{j+m} + \\ &+ (\lambda_m - \gamma_m)\hat{\sigma}_y^j(\otimes_{l=j+1}^{j+m-1}\hat{\sigma}_z^l)\hat{\sigma}_y^{j+m}\Big],\end{aligned} \tag{9.45}$$

that can be diagonalized exploiting the Jordan-Wigner transformation. Above, we have implicitly assumed translational invariance and periodic boundary conditions. The above family of Hamiltonians includes the one-dimensional transverse field Ising model and XY model with a transverse field if we limit the interaction range to nearest-neighbors only. The dynamics of these spin systems, parametrized by (λ_m, γ_m), can be easily solved by a mapping through the aforementioned Jordan-Wigner transformation to a fermionic chain, followed by a Fourier transformation of the fermionic operators exploiting the translational invariance, and a final Bogoliubov transformation of the Fourier transformed fermionic operators. That is, after a standard Jordan-Wigner transformation, the Hamiltonian is the one of a fermionic chain with the battery and charging Hamiltonians in quadratic forms, i.e.,

$$\begin{aligned} \hat{H}_B &= \sum_j \hat{f}_j^\dagger \hat{f}_j, \\ \hat{H}_{JW} &= \hat{H}_B + \sum_{j=0,m=1}^{N-1} \left[\lambda_m (\hat{f}_j \hat{f}_{j+m}^\dagger - \hat{f}_j^\dagger \hat{f}_{j+m}) + \gamma_m (\hat{f}_j \hat{f}_{j+m} - \hat{f}_j^\dagger \hat{f}_{j+m}^\dagger) \right], \end{aligned} \tag{9.46}$$

where $\hat{f}_j$ ($\hat{f}_j^\dagger$) are the annihilation (creation) fermionic operation at the j-th site of the chain, and we have dropped an irrelevant constant from $\hat{H}_B$. Notice that, in the fermionic picture, the battery Hamiltonian is the particle number operator, and therefore a charging process occurs through the creation of particles driven by $\hat{H}_{JW}$, from the initial vacuum state. It is useful to perform a Fourier transformation of the fermionic operators to bring the battery and charging Hamiltonian into the following form:

$$\hat{H}_B = \sum_{k \in \#\mathrm{BZ}} (\hat{f}_k^\dagger \hat{f}_k + \hat{f}_{-k}^\dagger \hat{f}_{-k}), \quad \hat{H}_{JW} = \sum_{k \in \#\mathrm{BZ}} \Psi_k^\dagger M_k \Psi_k, \tag{9.47}$$

with the definitions

$$\Psi_k = (\hat{f}_k, \hat{f}_{-k}^\dagger)^T, \quad \hat{f}_k = \frac{1}{\sqrt{N}} \sum_j e^{-\mathrm{i}kj} \hat{f}_j, \tag{9.48}$$

Notice that $\#BZ$ stands for the reduced Brillouin zone, that is, the subset of positive k's from the set $k = -\pi + \frac{2\pi}{n} m$, with $m \in [0, N-1]$. M_k is a 2×2 matrix, which form depends on the parameters of the model and reads

$$M_k = \omega_k \begin{pmatrix} \cos\theta_k & \sin\theta_k e^{-i\pi/2} \\ \sin\theta_k e^{i\pi/2} & -\cos\theta_k \end{pmatrix} \tag{9.49}$$

where θ_k and ω_k are defined as

$$\begin{aligned} \omega_k &= 2 \sqrt{\left[\frac{1}{2} - \sum_m \lambda_m \cos(km) \right]^2 + \left[\sum_m \gamma_m \sin(km) \right]^2}, \\ \sin\theta_k &= \frac{2 \sum_m \gamma_m \sin(km)}{\omega_k}. \end{aligned} \tag{9.50}$$

The dynamics can now be solved by performing a simple Bogoliubov transformation. To do so, we define the Bogoliubov fermionic modes as $\Phi_k = U_k \Psi_k$, where U_k is a 2×2 unitary matrix. The matrix U_k is chosen such that the Hamiltonian $\hat{H}_{JW}$ in Eqs. (9.47) becomes diagonal, when rewritten in terms of the newly defined Φ_k

operators (i.e., the matrix $U_k M_k U_k^\dagger$ is a diagonal matrix for all k). This matrix reads

$$U_k = \begin{pmatrix} e^{-i\pi/4}\cos(\theta_k/2) & e^{-i\pi/4}\sin(\theta_k/2) \\ -e^{+i\pi/4}\sin(\theta_k/2) & e^{+i\pi/4}\cos(\theta_k/2) \end{pmatrix}, \tag{9.51}$$

and the charging Hamiltonian takes the form

$$\hat{H}_{JW} = \sum_{k\in\#\mathrm{BZ}} \omega_k \Phi_k^\dagger \begin{pmatrix} 1 & 0 \\ 0 & -1 \end{pmatrix} \Phi_k. \tag{9.52}$$

From the last expression, it is easy to see that, in the Heisenberg picture, the dynamics generated by $\hat{H}_{JW}$ will lead to

$$\Phi_k(t) = \begin{pmatrix} e^{-i\omega_k} & 0 \\ 0 & e^{+i\omega_k} \end{pmatrix} \Phi_k(0). \tag{9.53}$$

Finally, one can then transform back to the Fourier transformed fermionic modes,

$$\Psi_k(t) = U_k^\dagger \Phi_k(t), \tag{9.54}$$

and compute all the relevant dynamical quantities of the problem.

What is important in our discussion of these systems, acting as quantum batteries, is that in the fermionic picture they present a local structure in momentum space due to their translational invariance. This means that the Hilbert space structure of the problem can be expressed as

$$\mathcal{H} = \bigotimes \mathcal{H}_{k,-k}, \tag{9.55}$$

where k labels the quasimomentum, and thus these models are very similar to an *hybrid* model with $r = 2$ (see Table 9.1), which is close to the *parallel* case, as there is only two-particle entanglement between $(k, -k)$ modes. We see this fact in that we are able to write all the relevant dynamical quantities as a sum of independent contributions from each $(k, -k)$ subspace. For instance,

$$\begin{aligned} E(t) &= \sum_{k\in\#\mathrm{BZ}} \varepsilon_k(t), \\ P(t) &= \sum_{k\in\#\mathrm{BZ}} \dot{\varepsilon}_k(t), \\ \Delta\hat{H}_B(t)^2 &= \sum_{k\in\#\mathrm{BZ}} \varepsilon_k(t)(2-\varepsilon_k(t)), \\ \Delta\hat{H}_{JW}^2 &= \sum_{k\in\#\mathrm{BZ}} \sin^2(\theta_k)\omega_k^2, \end{aligned} \tag{9.56}$$

where ε_k, θ_k, and ω_k depend on the parameters of the model and $\#BZ$ refers to the reduced Brillouin zone of the fermionic chain. Notice that, as the size of the reduced Brillouin zone is proportional to N, the quantities appearing in Eqs. (9.56) have a natural linear scaling with N.

Comparing the *parallel* and *hybrid* rows of Table 9.1, we observe that these integrables models can present a quantum advantage by at most a factor of 2, under the criteria that the speed factor I_E is kept at a constant value. This result is in agreement

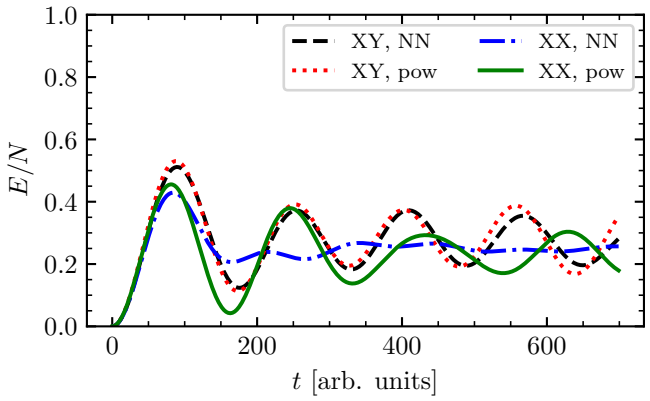

FIGURE 9.3: Dynamics of the stored energy for different spin integrable models described by the Hamiltonian Eq. (9.45). The legend indicates to which model corresponds each line. We have studied the XY (XX) model that corresponds to $\lambda_m = 0$ ($\lambda_m = \gamma_m$). For each of these models we have studied the nearest-neighbor (NN) case, where $\gamma_1 = 1$ and $\gamma_{m\neq 1} = 0$, and also the power law (pow) case, where $\gamma_m = m^{-2}$. We have fixed the system size to $N = 20$ spins and normalized the stored energy (Y-axis) accordingly, such that it is bounded to 1. We observe that for all the models the maximum stored energy is about 50% of the total due to the desynchronization between the different modes that contribute to this quantity.

with the one in Ref. [409], showing that, for a fixed $\Delta\hat{H}_{JW}^2$, the maximum quantum advantage is given by the order of interaction of $\hat{H}_{JW}$.

The only collective effect we are left with is the synchronization between independent modes [two producible states of $(k, -k)$ particles]. This phenomenon has a direct consequence: it limits the stored energy and its quality, as in general the set of energies $\varepsilon_k(t)$ will not be maximized simultaneously. This feature is discussed in Fig. 9.3 for particular choices of (λ_m, γ_m). It is also important to notice that, in general, the system will not be in an energy eigenstate when it reaches maximum stored energy. However, the energy uncertainty associated with the final state will be negligible in the thermodynamical limit, as $\Delta\hat{H}_B(t_f)/E(t_f) \sim 1/\sqrt{N}$.

Moreover, one can compute the Fisher information in energy eigenspace for these models to see how tight our bound is for different choices of parameters and as a function of N, a result which is shown in Fig. 9.4.

To compute the Fisher information, we first notice that in the fermionic picture the coefficient $p_l(t)$ that appears in the definition of the Fisher information of Eq. (9.19) is the probability of having l particles at a time t. We also notice that $p_l(t)$ will only have a nonzero value for even l, as particles need to be created in pairs $(k, -k)$ to conserve momentum. Finally, the local structure of the problem in k-space allows us to compute separately for every $(k, -k)$ subspace the probability of being in the vacuum state or in the pair state at a given instant of time. It is easy to see that

$$p_{k,-k}(t) = \frac{\varepsilon_k(t)}{2}. \tag{9.57}$$

To compute the Fisher information we use these local probabilities to determine the probability that the hole state contains l particles:

$$p_l(t) = \sum_{\{\sigma\}_l} p(\sigma_1) \dots p(\sigma_N) \tag{9.58}$$

where the sum runs over the configurations $\{\sigma\}_l$, which are binary strings, each bit

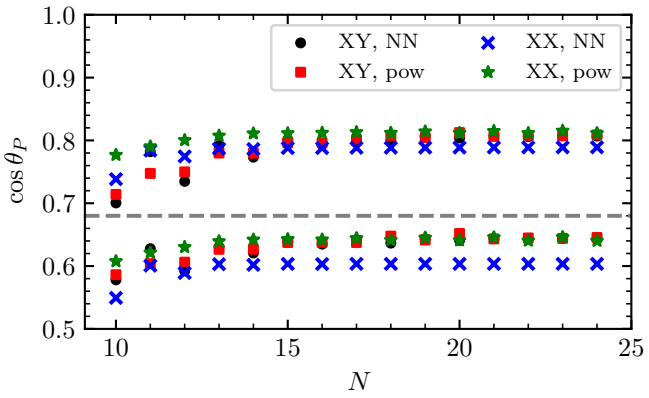

FIGURE 9.4: Over the grey dashed line, we plot the value of $\cos\theta_P := P/\sqrt{\langle\Delta\hat{H}_B^2\rangle_{\Delta t}\langle I_E\rangle_{\Delta t}}$ as a function of the number of spins N for the models presented in Fig. 9.3. We observe a fast saturation to an approximate 0.8 value. Below the grey dashed line, we plot the same quantity but substituting $\langle I_E\rangle_{\Delta t} \to 4\Delta^2\hat{H}_{JW}$, and it saturates to an approximate 0.6 value. This shows how lower is our bound obtained using the Fisher information in energy eigenspace instead of the speed in Hilbert space for these particular models.

representing the state of a $(k, -k)$ subspace, with 0's (1's) representing the vacuum (pair) state. These configurations are constrained to contain $l/2$ pairs (1's) and

$$p(\sigma_k) = \begin{cases} \varepsilon_k/2 & \text{if } \sigma_k = 1, \\ 1 - \varepsilon_k/2 & \text{if } \sigma_k = 0. \end{cases} \tag{9.59}$$

And the time derivative of the above probability reads

$$\dot{p}_l(t) = \sum_{\{\sigma\}_l} \sum_{\sigma_k} \frac{\dot{\varepsilon}_k}{2} (-1)^{1+\sigma_k} \prod_{\sigma_{j\neq k}} p(\sigma_j). \tag{9.60}$$

9.4.2 Lipkin-Meshkov-Glick model

Another class of charging Hamiltonians that we consider is based on the LMG model [419], which allows for two-body spin interactions with an infinite range. Namely, the charging Hamiltonian is given by

$$\hat{H}_{LMG} = \frac{\lambda}{N} \sum_{i<j} (\hat{\sigma}_x^i \hat{\sigma}_x^j + \gamma \hat{\sigma}_y^i \hat{\sigma}_y^j) + \frac{1}{2} \sum_{j=0}^{N-1} \hat{\sigma}_z^j, \tag{9.61}$$

where λ is the coupling strength, γ the anisotropy parameter, and the factor $\frac{1}{N}$ is included in the model in order to have a finite interaction energy per spin in the thermodynamic limit. For the infinite range Ising model ($\gamma = 0$), $\hat{H}_{LMG}$ is analog to the so-called twist-and-turn Hamiltonian [420]. There λ mimics the twisting parameter, and the linear term coming from $\hat{H}_B$ is a rotation around the z-axis. Using the components of the total spin operator $\boldsymbol{J} := (\hat{J}_x, \hat{J}_y, \hat{J}_z)$, with

$$\hat{J}_\alpha = \sum_{j=0}^{N-1} \frac{\hat{\sigma}_\alpha^j}{2}, \quad (\alpha = x, y, z), \tag{9.62}$$

the LMG Hamiltonian of Eq. (9.61) can be rewritten as

$$\hat{H}_{LMG} = \frac{\lambda}{2N}\Big[(1+\gamma)\Big(\hat{J}_+\hat{J}_- + \hat{J}_-\hat{J}_+ - N\Big) + (1-\gamma)\Big(\hat{J}_+^2 + \hat{J}_-^2\Big)\Big] + \hat{J}_z, \tag{9.63}$$

where we have introduced the ladder operators $\hat{J}_+$ and $\hat{J}_-$, that are related to the total spin operators by $\hat{J}_x{=}\frac{1}{2}(\hat{J}_+{+}\hat{J}_-)$, and $\hat{J}_y{=}\frac{1}{2i}(\hat{J}_+{-}\hat{J}_-)$. Notice that, in the total spin notation, the battery Hamiltonian reads $\hat{H}_B = \hat{J}_z$. Note also that $\boldsymbol{J}$ is a constant of motion, i.e., $[\mathbf{J}, \hat{H}_{LMG}] = 0$, and that the initial state lies in the maximum spin sector. These properties effectively reduce the size of the Hilbert space of the problem, that scales only linearly with N, instead of the exponential 2^N scaling of the total Hilbert space described by local Pauli matrices.

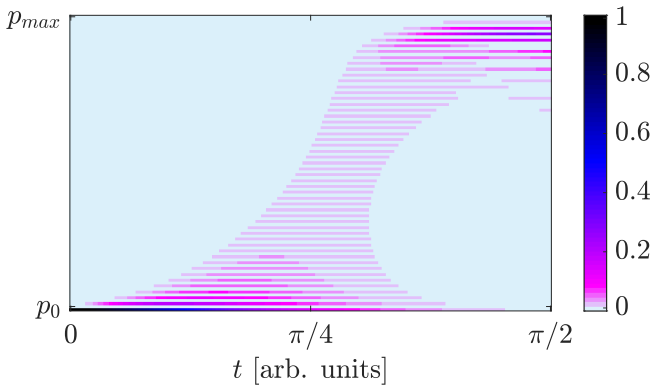

FIGURE 9.5: Dynamics of the energy levels during the charging process based on the LMG model for $\lambda = 5$. Due to the structure of $\hat{H}_{LMG}$, only every second energy level starting from the initial state is occupied during the evolution.

Let us first discuss some general properties of the Hamiltonian (9.63) that mainly affect the storage properties of the LMG model. First, note that deposition of energy into the battery only occurs if $\gamma \neq 1$, and the maximum stored energy is achieved for $\gamma = -1$ [see Figs. 9.7(c) and 9.7(d)]. This comes from the fact that the mixed terms in the Hamiltonian (i.e. $\hat{J}_+\hat{J}_-$ and $\hat{J}_-\hat{J}_+$) are diagonal operators in the energy eigenbasis, and hence they only contribute to the free evolution and not to the charging process.

Second, there are two regimes depending on the value of the parameter λ. The strong-coupling regime is defined by $\lambda \geq 1$, whereas in the weak-coupling regime $\lambda < 1$. In the latter, the LMG model leads to very poor charging properties, as the maximum stored energy tends to zero in the thermodynamic limit. This is due to the fact that the ground state of the battery Hamiltonian $\hat{H}_B$ (i.e., the initial state) is also an eigenstate of $\hat{H}_{LMG}$, when $N \to \infty$ [421]. Therefore, for our discussion, we will focus on the strong coupling regime.

In studying the power for the LMG model, a first quantity of interest is the variance of the charging Hamiltonian

$$\Delta\hat{H}^2_{LMG} = \frac{\lambda^2}{2}(1-\gamma)^2 + O\Big(\frac{1}{N}\Big). \tag{9.64}$$

We see that this variance does not scale with N, implying that I_E cannot scale with N neither, as $I_E \leq 4\Delta\hat{H}^2_{LMG}$. Hence, our bound (9.27) tells us that any scaling of the power with N can only be associated with $\Delta\hat{H}^2_B$. Note, the correlations are expected to be enhanced in this model due to the long-range nature of the interactions between spins, and also because it does not have any "hidden" local structure in the

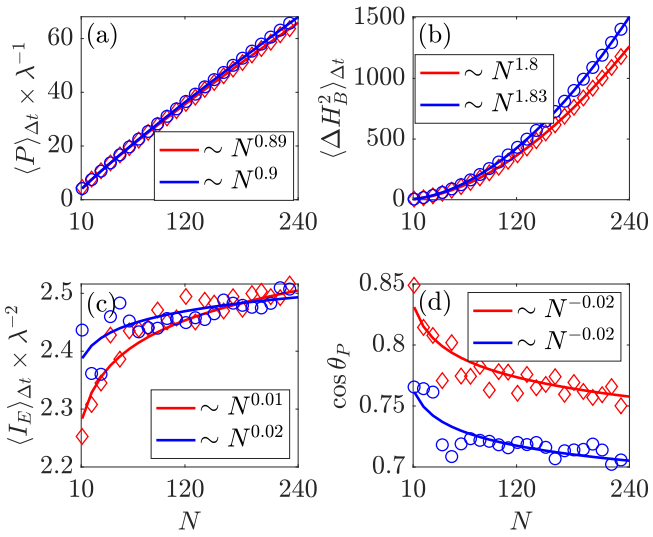

FIGURE 9.6: The figures consider time-averaged quantities of the LMG model, which are relevant in the study of power, as a function of the number of spins N. The final time has been chosen as the one for which the stored energy is maximized. Blue color is used for $\lambda = 20$, whereas red color is used for $\lambda = 5$. Quantities that carry units of time (i.e., power and Fisher information) have been renormalized with the coupling strength λ. The legends indicate the scaling with N of the different curves.

energy eigenspace, unlike the previous case of integrable spin models. Nevertheless, they are bounded to scale as N^2 at most. As a consequence, power can scale at maximum linearly with N for the LMG charging Hamiltonian, and no N-dependent speedup is possible.

To make a quantitative analysis of the scaling of such correlations with the number of spins N, and also study the tightness of our bound on power, we have solved its dynamics for two values of the coupling strength in the strong-coupling regime ($\lambda = 5,\ 20$), and a fixed value of $\gamma = -1$.

First, we would like to draw attention to Fig. 9.5, where one can visualize the evolution of the LMG battery in the eigenspace of $\hat{H}_B$. If one compares this evolution with the ones of the paradigmatic cases (see Fig. 9.2), one observes that the LMG battery has some common properties with the global charging case, as there appears entanglement between the states that are far away in energy during evolution. This enhances the battery variance $\Delta\hat{H}_B^2$, as explained below. However, in the LMG battery, there are many energy levels involved in the charging process, contrary to what happened in the global charging case, where only the lowest and highest energy states participate.

In Fig. 9.6(b), one can see the enhancement of the time-averaged energy variance $\Delta\hat{H}_B^2$ in the LMG battery. Even though this variance does not saturate the bound of N^2 scaling, it definitely scales super-extensively, as $\sim N^{1.8}$. As per Eq. (9.37), this scaling means that the battery is in a highly k-qubit entangled state during the charging process. In Fig. 9.6(c) one observes that the Fisher information I_E does not vary with the system size, a result that is in agreement with the analytical formula of Eq. (9.64). Finally, we note that, for the LMG battery in the strong-coupling regime, the bound (9.27) is tight at order N (see Fig. 9.6d), and power scales approximately linearly with N [see Fig. 9.6(a)], inheriting the scaling of $\Delta\hat{H}_B$. We also remark that increasing the driving parameter λ decreases the tightness of the bound.

At this point, it is interesting to compare the conclusions obtained for the LMG

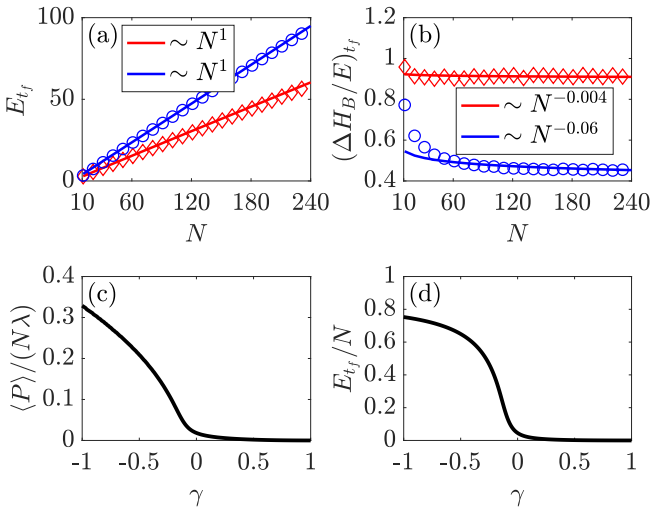

FIGURE 9.7: Stored energy properties of the LMG battery. In Figures (a) and (b) one can see the expected scaling of the stored energy and the final relative energy variance as a function of the system size. The blue color is used for $\lambda = 20$, whereas red color is used for $\lambda = 5$, and the legends indicate the scaling law. In Figures (c) and (d) we plot the dependence with the anisotropy parameter γ of both the stored energy and the power. For this plot, we consider a system of 50 spins and set $\lambda = 5$.

model within the scope of the bound (9.27) and the analysis on speedups under certain normalization criteria. In Ref. [409], it was predicted that, under a fixed linear scaling with N of $\Delta\hat{H}_C^2$, power could scale super-extensively in batteries with a large participation number, e.g. the present LMG model. In Section 9.2.3, we showed that if one imposes a linear scaling with N of the Fisher information I_E (and thus of $\Delta\hat{H}_C^2$), speedups in power are directly related to the enhancement of the battery variance $\Delta\hat{H}_B^2$. We have seen that, in the LMG battery, such variance is indeed highly enhanced and it translates into power, as the bound (9.27) is tight for this model. However, this enhancement in power does not come from the speed of evolution, as the Fisher information I_E remains invariant with the system size. Thus the normalization criterion under which such enhancement in power was predicted does not apply.

Hence, the example of the LMG model shows the importance of both $\Delta\hat{H}_B^2$ and I_E, and it stresses the twofold origin of quantum advantage in power.

To conclude with the LMG model, let us now briefly discuss the maximum stored energy and its variance, quantitatively. In Fig. 9.7(a), we see that in the strong-coupling regime the energy stored scales linearly with the number of cells N, as expected. However, in Fig. 9.7(b) we see that there is no decay of the relative variance of the final stored energy in the large N limit. This presents an important problem for a deterministic extraction of the stored energy, and it means that the super extensive energy variance $\Delta\hat{H}_B^2$, which takes place during the charging process to enhance power, does not disappear in the final state.

9.4.3 Dicke model

A quantum battery can also be constructed by placing an array of spins inside an optical cavity [422]. This particular model has been studied in Ref. [407], where a collection of N spins interact with a cavity field mode. In this section, we reconsider this battery model and study it in the light of our bounds presented before. The paradigm assumed here is qualitatively different from the previous ones, as the

system that provides the energy to the battery (i.e., the charging agent) is explicitly considered. The battery Hamiltonian is still given by $\hat{H}_B = \hat{J}_z$. The charging Hamiltonian includes the free evolution of both the spins and the cavity and a linear interaction between them. It reads

$$\hat{H}_{DK} = \hat{J}_z + \hat{a}^\dagger \hat{a} + \frac{2\lambda}{\sqrt{N}} J_x (\hat{a}^\dagger + \hat{a}), \tag{9.65}$$

where $\hat{a}^\dagger(\hat{a})$ are the usual creation (annihilation) operators of cavity photons, satisfying $[\hat{a}, \hat{a}^\dagger] = \mathbb{I}$, and the macro-spin notation is adopted as previously. In contrast to the convention used in [407], here we include the factor $\frac{1}{\sqrt{N}}$ in the coupling in order to have a well defined thermodynamical limit [5], for $N \to \infty$. We consider that in the initial state the spins (i.e., the battery) are in the ground state of $\hat{H}_B$, and the cavity is in the eigenstate of the photon number that contains N photons.

A first observation is that one can analytically compute

$$\Delta \hat{H}^2_{DK} = 2\lambda^2 (2N+1)\,, \tag{9.66}$$

and therefore one sees that I_E is bounded to scale linearly with N (parallel case scaling) at most. One is then left with $\Delta \hat{H}^2_B$ as the only quantity appearing in our bound (9.27) that could scale super-extensively in order to enhance the power scaling. Notice that this is only possible if a normalized coupling $\lambda/\sqrt{N}$ is introduced. The non-normalized case, considered in Ref. [407], can be experimentally engineered [423] if one considers that N ranges from 1 to some large but finite value. In such scenario, we have $\Delta \hat{H}^2_{DK} = 2N\lambda^2(2N+1)$. Then, the power can scale super-extensively without the need of a super-extensive scaling in of $\Delta \hat{H}^2_B$, i.e., the spins do not need to explore highly correlated subspaces.

In order to be able to make stronger statements about this system, we have numerically solved the dynamics for $\lambda = 0.01$ ($\lambda = 0.5$), which are representative examples of the weak (strong) coupling regime of the Dicke model. The qualitative difference between these two regimes can be pictorially seen in Fig. 9.8, where we observe that the dynamics of energy levels are very local (and thus similar to the parallel charging case) in the weak-coupling regime, whereas in the strong coupling regime they exhibit highly nonlocal properties, with levels well separated in energy get entangled during evolution.

Let us now turn to the quantitative discussion of these two regimes. A first result [see Fig. 9.9(c)] is that, when including the normalization $\frac{1}{\sqrt{N}}$ in the coupling, the super-extensive behavior of power presented in Ref. [407] disappears, and linear scaling in N (as in the parallel case) is approximately recovered, both in the weak and the strong-coupling regime. In contrast, when analyzed in terms of the quantities appearing in our bound, the strong-coupling regime shows relevant differences with respect to a parallel charging scenario.

In Fig. 9.9(b), we see that in both the weak and strong-coupling regime, the time-averaged Fisher information I_E scales approximately linearly with N, in agreement with the linear bound set by $\Delta \hat{H}^2_{DK}$. The differences appear when looking at the

[5] The thermodynamical limit is considered on the cavity-spin system as a whole. This implies that if one adds spins the cavity length L should also increase to allocate them, keeping the density N/L constant, or in other words $N \propto L$. On the other hand, the coupling term in the Hamiltonian (9.65) has its origin in the electric-dipole interaction $\sum E_j \cdot d_j$, where d_j is the dipole of each spin, and E_j the electric field at the spin position. Of course, the individual dipole operators d_j do not carry any scaling with N, but the electric field quantized inside a cavity of length L carries a normalization factor $1/\sqrt{L}$. Thus L and N need to be proportional.

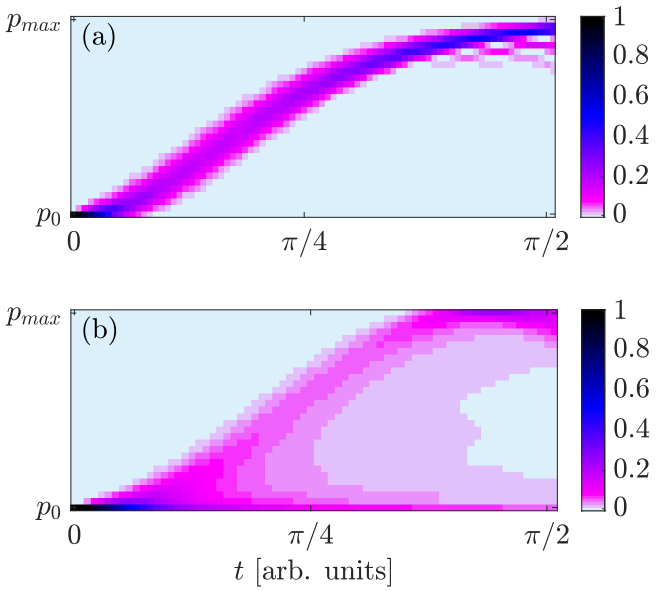

FIGURE 9.8: Dynamics of the energy levels p_k during the charging process based on Dicke model for λ=0.01 (a) and λ=0.5 (b). In (a) we see that for the weak-coupling regime the behavior is similar to the parallel charging case. On the other hand, (b) shows an intermediate behavior between parallel and global charging.

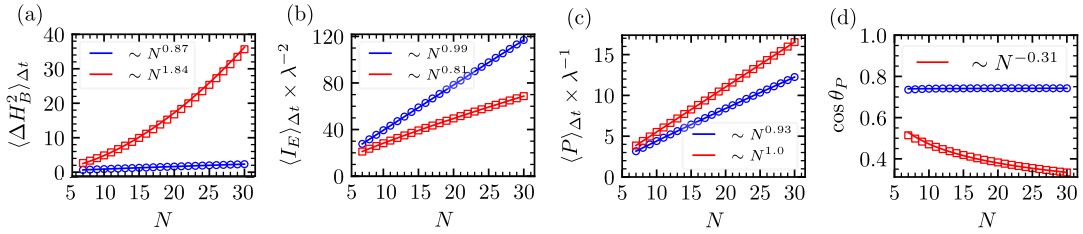

FIGURE 9.9: The figures consider time-averaged quantities of the Dicke model, which are relevant in the study of power, as a function of the number of spins N inside the cavity. The final time has been chosen as the one for which the stored energy is maximized. The blue color (circles) is used for the weak-coupling regime ($\lambda = 0.01$), whereas the red color (squares) is used for the strong-coupling regime ($\lambda = 0.5$). Quantities that carry units of time (i.e., power and Fisher information) have been renormalized with the coupling strength λ. The legends indicate the scaling with N of the different curves.

time averaged $\Delta\hat{H}_B^2$ [see Fig. 9.9(a)]. While in the weak-coupling regime it scales linearly with N, in the strong-coupling regime this quantity is enhanced and close to the N^2 scaling. This superlinear scaling is clearly associated to the large value of the coupling λ, that allows for cavity-mediated interactions between the spins, that explore highly correlated subspaces. In fact, as Eq. (9.37) is also valid for mixed states, this super-linear scaling means that the spins (i.e., the battery) are in a mixture of k-qubit entangled pure states, with $k \gg 1$.

Nevertheless, the enhancement of $\Delta\hat{H}_B^2$ in the strong-coupling regime is not reflected in the scaling of power, as one can see in Fig. 9.9(d) that the bound (9.27) is far from being saturated in this regime, i.e., $\langle P \rangle_{\Delta t} \ll \sqrt{\langle \Delta\hat{H}_B^2 \rangle_{\Delta t} \langle I_E \rangle_{\Delta t}}$, leading to power scaling only linearly with N. Remarkably, our bound is tight at order N in the weak-coupling regime.

Let us finally discuss the Dicke model in terms of storage. We observe in Fig. 9.10 that, while in the weak coupling regime the maximum stored energy properties are

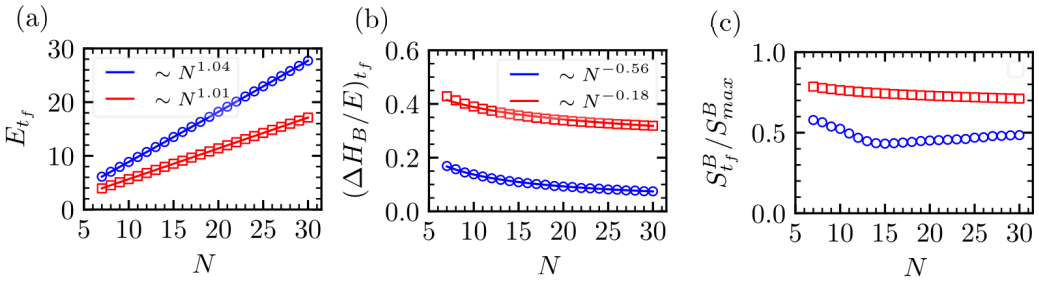

FIGURE 9.10: The figures show the relevant quantities for the stored energy of the Dicke model evaluated at the final time t_f, as a function of the number of spins N inside the cavity. Blue color (circles) is used for the weak-coupling regime ($\lambda = 0.01$), whereas red color (squares) is used for the strong-coupling regime ($\lambda = 0.5$). In (c) we plot the entanglement entropy $S^B := -\mathrm{Tr}(\hat{\rho}_B \log_2 \hat{\rho}_B)$ of the battery reduced density matrix, defined as $\hat{\rho}_B = \mathrm{Tr}_c(\hat{\rho})$, where the trace is performed over the cavity degree of freedom. We normalize this quantity by its maximum value $S^B_{max} = \log_2(N+1)$.

similar than those of a parallel charging, in the strong coupling regime there is a worsening in the quality of the stored energy. This is because the super-extensive energy variance generated during the charging process does not disappear completely in the final state [see Fig. 9.10(b)], as they decay much slower than $1/\sqrt{N}$. In Fig. 9.10(c) we also show the significant presence of entanglement between the final state of the battery and the source (i.e., the cavity) in this strong-coupling regime.

9.5 Summary

In this chapter, we have introduced a novel bound on the power of a quantum battery by means of a geometrical approach in the energy eigenspace of the battery. According to this bound, the power of a quantum battery is bounded by the product of two quantities: the Fisher information in energy eigenspace and the variance of the battery Hamiltonian. While both of these quantities are influenced by the appearance of entanglement during a charging process, the former signifies how fast the process takes place in the energy eigenspace and the latter encodes how smart (in terms of path length) the trajectory of evolution is. This approach enables us to characterize quantum advantages arising from two different sources, and analyze the role of entanglement in charging processes without relying on any normalization constraint for the time evolution. To exemplify the usefulness of our bound, we have proved that for spin-based quantum batteries it leads to an inequality that shows the maximum charging power that a battery can exhibit when it has at most k-qubit entanglement, thus establishing a novel interrelation between entanglement and power. The fact that the k-producibility is related with the violation of Bell inequalities [424, 425] could also lead to further studies, in which the relation of power with nonlocality [426] is explored. Furthermore, we have used our bound to systematically analyze several models that have become popular in the literature of quantum batteries. We have first discussed a set of paradigmatic models that saturate the bound, which have also served us to illustrate the typical scalings with the number of cells of the relevant quantities. We have also studied a few physically realizable models, for which we have seen that a superlinear scaling in power cannot be attributed to the exploration of a smart entangled path during the charging process, but rather to an enhanced speed of evolution (Fisher information). As a final remark, the bound presented in this chapter has been already used in Ref. [427] to certify the

quantum advantage in power in a charging scheme based on the Sachdev-Ye-Kitaev model [428–430].

Conclusions and outlook

In this thesis, we explored a variety of interacting phenomena in many-body quantum systems, with a combination of numerical and analytical techniques.

In part II, we studied interaction-induced topological insulators, with the motivation to propose novel effects in models that could be realized in cold atom quantum simulators. In the case of one-dimensional fermionic chains (Chapter 4), we showed that the bond order wave, a dimerized phase induced by frustrated fermionic interactions, is a symmetry-protected topological phase. Moreover, we discussed a possible experimental implementation of the model with magnetic dipolar gases. Compared to previous quantum simulations or proposals of similar topological phases, here the bond order wave occurs via the intrinsic fermionic interactions. In the case of two-dimensional systems (Chapters 5-7), we investigated the topological Mott insulator, an interaction-induced Chern insulator. The mean-field results of Chapter 5 suggest that this phase could be realized with cold Rydberg-dressed atoms in optical lattices, by taking advantage of very recent technical advances in this field. Then, in Chapter 6, we showed, also in mean-field approximation, that the ground state degeneracy of the topological Mott insulator can lead to novel many-body states, exhibiting both topological properties and spatial inhomogeneities. The latter includes localized polaron solutions, or spatial domains with changes of the topological invariant across them, leading to topological edge currents at the domain boundaries. In Chapter 7, we performed a quasi-exact treatment of the topological Mott insulator and its domain solutions by means of a tensor network approach in a cylinder geometry. To analyze the experimental detection of the topological invariant in quantized transport experiments, we generalized the topological pump numerical procedure to the spatially inhomogeneous case. Finally, we addressed the state preparation of the phase, showing that by tuning an external lattice parameter one can induce a second-order transition to a trivial phase, that could be used in a quasi-adiabatic state-preparation preparation protocol. The results of part II thus provide prospects for the quantum simulation of exotic interaction-induced topological insulators. The use of a quantum simulator would shed light into interesting fundamental questions beyond the ones considered in this thesis. For instance, while here we have limited ourselves to ground states, the phase transition dynamics, or the mobility properties of defects, such as solitons or domain walls, deserve further attention.

In part III, we analyzed complex many-body phenomena from a microscopic perspective. On the one hand, in Chapter 8, we considered a microscopic model to describe the cuprate high-T_c superconductors. One of the main ingredients of such model is a coupling term between electrons and bond phonons, which is believed to explain the pseudogap phase of these materials. Our numerical studies showed that not only the electron-phonon term is important, but also the proper inclusion of electron-electron interactions, to obtain a stable pseudogap phase in the model. In the latter case, we showed the appearance of Fermi arcs in momentum space, and domains with spontaneously broken full rotational symmetry, the two main features of the pseudogap. As a further work, it would also be interesting to model the

coupling between the bond phonons and external light in a dynamical framework, which could be used to explain some of the properties of recent experiments focusing on light-induced transient behaviors on similar materials.

On the other hand, in Chapter 9, we examined the microscopic origin of collective enhancements in the charging power of quantum batteries, which in the last years have been claimed to appear in several models. We introduced a bound in the power of cell-based quantum batteries, which relates the collective enhancements in power to the presence of quantum entanglement between the cells. One of the consequences of this bound is that extensive enhancements in power can only be achieved when the instantaneous quantum state is in a macroscopic superposition of ground and excited states. This imposes severe constraints to the observation of collective speed-ups in physically realizable models. The bound introduced in this thesis also provides a physical framework that can be used to benchmark the performance of quantum battery prototypes, as we already did for some integrable or interacting models.

Bibliography

[1] S. Julià-Farré, T. Salamon, A. Riera, M. N. Bera, and M. Lewenstein, "Bounds on the capacity and power of quantum batteries", Phys. Rev. Research **2**, 023113 (2020).

[2] S. Julià-Farré, A. Dauphin, R. W. Chhajlany, P. T. Grochowski, S. Wall, M. Lewenstein, and P. R. Grzybowski, "Nanoscale phase separation and pseudogap in the hole-doped cuprates from fluctuating Cu-O-Cu bonds", Phys. Rev. B **101**, 125107 (2020).

[3] S. Julià-Farré, M. Müller, M. Lewenstein, and A. Dauphin, "Self-Trapped Polarons and Topological Defects in a Topological Mott Insulator", Phys. Rev. Lett. **125**, 240601 (2020).

[4] S. Julià-Farré, D. González-Cuadra, A. Patscheider, M. J. Mark, F. Ferlaino, M. Lewenstein, L. Barbiero, and A. Dauphin, *Revealing the topological nature of the bond order wave in a strongly correlated quantum system*, arXiv:2112.08785 [cond-mat.quant-gas] (2021).

[5] L. Cardarelli, S. Julià-Farré, M. Lewenstein, A. Dauphin, and M. Müller, *Accessing the topological Mott insulator in cold atom quantum simulators with realistic Rydberg dressing*, arXiv:2203.14818 [cond-mat.quant-gas] (2022).

[6] M. L. Bera, S. Julià-Farré, M. Lewenstein, and M. N. Bera, "Quantum heat engines with Carnot efficiency at maximum power", Phys. Rev. Research **4**, 013157 (2022).

[7] S. Julià-Farré, A. Dauphin, and L. Cardarelli, *Hartree-Fock toolbox for the Topological Mott Insulator*, GitHub repository at: https://sergijulia94.github.io/topological_mott_insulator (2022).

[8] M. Planck, "On the Theory of the Energy Distribution Law of the Normal Spectrum", Verhandl. Dtsch. phys. Ges. **2**, 237 (1900).

[9] A. Einstein, "Über einen die Erzeugung und Verwandlung des Lichtes betreffenden heuristischen Gesichttspunkt", Annalen der Physik **4** (1905).

[10] A. L. Schawlow and C. H. Townes, "Infrared and Optical Masers", Phys. Rev. **112**, 1940 (1958).

[11] T. H. Maiman, "Stimulated Optical Radiation in Ruby", Nature **187**, 493 (1960).

[12] A. Javan, W. R. Bennett, and D. R. Herriott, "Population Inversion and Continuous Optical Maser Oscillation in a Gas Discharge Containing a He-Ne Mixture", Phys. Rev. Lett. **6**, 106 (1961).

[13] A. G. J. MacFarlane, J. P. Dowling, and G. J. Milburn, "Quantum technology: the second quantum revolution", Philos. Trans. R. Soc. A **361**, 1655 (2003).

[14] V. Giovannetti, S. Lloyd, and L. Maccone, "Advances in quantum metrology", Nat. Photonics **5**, 222 (2011).

[15] C. L. Degen, F. Reinhard, and P. Cappellaro, "Quantum sensing", Rev. Mod. Phys. **89**, 035002 (2017).

[16] A. Trabesinger, "Quantum simulation", Nat. Phys. **8**, 263 (2012).

[17] I. M. Georgescu, S. Ashhab, and F. Nori, "Quantum simulation", Rev. Mod. Phys. **86**, 153 (2014).

[18] M. L. Nielsen and I. L. Chuang, *Quantum Computation and Quantum Information* (Cambridge University Press, Cambridge, 2000).

[19] N. Gisin and R. Thew, "Quantum communication", Nat. Photonics **1**, 165 (2007).

[20] A. K. Geim, "Graphene: Status and Prospects", Science **324**, 1530 (2009).

[21] J. W. McIver, B. Schulte, F. .-. Stein, T. Matsuyama, G. Jotzu, G. Meier, and A. Cavalleri, "Light-induced anomalous Hall effect in graphene", Nat. Phys. **16**, 38 (2020).

[22] D. Fausti, R. I. Tobey, N. Dean, S. Kaiser, A. Dienst, M. C. Hoffmann, S. Pyon, T. Takayama, H. Takagi, and A. Cavalleri, "Light-Induced Superconductivity in a Stripe-Ordered Cuprate", Science **331**, 189 (2011).

[23] W. D. Phillips, "Nobel Lecture: Laser cooling and trapping of neutral atoms", Rev. Mod. Phys. **70**, 721 (1998).

[24] H. J. Metcalf and P. van der Straten, "Laser Cooling and Trapping of Neutral Atoms", in *The Optics Encyclopedia* (John Wiley & Sons, Ltd, 2007).

[25] A. E. Leanhardt, T. A. Pasquini, M. Saba, A. Schirotzek, Y. Shin, D. Kielpinski, D. E. Pritchard, and W. Ketterle, "Cooling Bose-Einstein Condensates Below 500 Picokelvin", Science **301**, 1513 (2003).

[26] P. Medley, D. M. Weld, H. Miyake, D. E. Pritchard, and W. Ketterle, "Spin Gradient Demagnetization Cooling of Ultracold Atoms", Phys. Rev. Lett. **106**, 195301 (2011).

[27] C. N. Cohen-Tannoudji, "Nobel Lecture: Manipulating atoms with photons", Rev. Mod. Phys. **70**, 707 (1998).

[28] J. M. Raimond, M. Brune, and S. Haroche, "Manipulating quantum entanglement with atoms and photons in a cavity", Rev. Mod. Phys. **73**, 565 (2001).

[29] D. Leibfried, R. Blatt, C. Monroe, and D. Wineland, "Quantum dynamics of single trapped ions", Rev. Mod. Phys. **75**, 281 (2003).

[30] D. Jaksch, C. Bruder, J. I. Cirac, C. W. Gardiner, and P. Zoller, "Cold Bosonic Atoms in Optical Lattices", Phys. Rev. Lett. **81**, 3108 (1998).

[31] D. Jaksch and P. Zoller, "The cold atom Hubbard toolbox", Ann. Phys. **315**, Special Issue, 52 (2005).

[32] J. I. Cirac and P. Zoller, "Quantum Computations with Cold Trapped Ions", Phys. Rev. Lett. **74**, 4091 (1995).

[33] I. Bloch, J. Dalibard, and W. Zwerger, "Many-body physics with ultracold gases", Rev. Mod. Phys. **80**, 885 (2008).

[34] Bose, S.N., "Plancks Gesetz und Lichtquantenhypothese", Zeitschrift fur Physik **26**, 178 (1924).

[35] Einstein, A., "Quantentheorie des einatomigen idealen Gases", Sitzungsberichte der Preussichen Akademie der Wissenschaften Physikalisch-Mathematische Klasse **261** (1924).

[36] Einstein, A., "Quantentheorie des einatomigen idealen Gases", Sitzungsberichte der Preussichen Akademie der Wissenschaften Physikalisch-Mathematische Klasse **3** (1925).

[37] M. H. Anderson, J. R. Ensher, M. R. Matthews, C. E. Wieman, and E. A. Cornell, "Observation of Bose-Einstein Condensation in a Dilute Atomic Vapor", Science **269**, 198 (1995).

[38] K. B. Davis, M. .-. Mewes, M. R. Andrews, N. J. van Druten, D. S. Durfee, D. M. Kurn, and W. Ketterle, "Bose-Einstein Condensation in a Gas of Sodium Atoms", Phys. Rev. Lett. **75**, 3969 (1995).

[39] R. P. Feynman, "Simulating physics with computers", Int. J. Theor. Phys. **21**, 467 (1982).

[40] M. Lewenstein, A. Sanpera, and V. Ahufinger, *Ultracold Atoms in Optical Lattices: Simulating Quantum many-body systems*, Vol. 54 (Oxford University Press, Oxford, 2012).

[41] R. Blatt and C. F. Roos, "Quantum simulations with trapped ions", Nat. Phys. **8**, 277 (2012).

[42] I. Bloch, J. Dalibard, and S. Nascimbène, "Quantum simulations with ultracold quantum gases", Nat. Phys. **8**, 267 (2012).

[43] B. P. Lanyon, C. Hempel, D. Nigg, M. Müller, R. Gerritsma, F. Zähringer, P. Schindler, J. T. Barreiro, M. Rambach, G. Kirchmair, M. Hennrich, P. Zoller, R. Blatt, and C. F. Roos, "Universal Digital Quantum Simulation with Trapped Ions", Science **334**, 57 (2011).

[44] A. Mazurenko, C. S. Chiu, G. Ji, M. F. Parsons, M. Kanász-Nagy, R. Schmidt, F. Grusdt, E. Demler, D. Greif, and M. Greiner, "A cold-atom Fermi–Hubbard antiferromagnet", Nature **545**, 462 (2017).

[45] R. Jördens, N. Strohmaier, K. Günter, H. Moritz, and T. Esslinger, "A Mott insulator of fermionic atoms in an optical lattice", Nature **455**, 204 (2008).

[46] B. Keimer, S. A. Kivelson, M. R. Norman, S. Uchida, and J. Zaanen, "From quantum matter to high-temperature superconductivity in copper oxides.", Nature **518**, 179 (2015).

[47] X. Zhou, W.-S. Lee, M. Imada, N. Trivedi, P. Phillips, H.-Y. Kee, P. Törmä, and M. Eremets, "High-temperature superconductivity", Nat. Rev. Phys. **3**, 462 (2021).

[48] C. Schweizer, F. Grusdt, M. Berngruber, L. Barbiero, E. Demler, N. Goldman, I. Bloch, and M. Aidelsburger, "Floquet approach to $\mathbb{Z}_2$ lattice gauge theories with ultracold atoms in optical lattices", Nat. Phys. **15**, 1168 (2019).

[49] M. Aidelsburger, L. Barbiero, A. Bermudez, T. Chanda, A. Dauphin, D. González-Cuadra, P. R. Grzybowski, S. Hands, F. Jendrzejewski, J. Jünemann, G. Juzeliūnas, V. Kasper, A. Piga, S.-J. Ran, M. Rizzi, G. Sierra, L. Tagliacozzo, E. Tirrito, T. V. Zache, J. Zakrzewski, E. Zohar, and M. Lewenstein, "Cold atoms meet lattice gauge theory", Philos. Trans. R. Soc. A **380**, 20210064 (2022).

[50] N. R. Cooper, J. Dalibard, and I. B. Spielman, "Topological bands for ultracold atoms", Rev. Mod. Phys. **91**, 015005 (2019).

[51] M. Z. Hasan and C. L. Kane, "Colloquium: Topological insulators", Rev. Mod. Phys. **82**, 3045 (2010).

[52] J. Roßnagel, S. T. Dawkins, K. N. Tolazzi, O. Abah, E. Lutz, F. Schmidt-Kaler, and K. Singer, "A single-atom heat engine", Science **352**, 325 (2016).

[53] C.-K. Chiu, J. C. Y. Teo, A. P. Schnyder, and S. Ryu, "Classification of topological quantum matter with symmetries", Rev. Mod. Phys. **88**, 035005 (2016).

[54] K. v. Klitzing, G. Dorda, and M. Pepper, "New Method for High-Accuracy Determination of the Fine-Structure Constant Based on Quantized Hall Resistance", Phys. Rev. Lett. **45**, 494 (1980).

[55] D. J. Thouless, M. Kohmoto, M. P. Nightingale, and M. den Nijs, "Quantized Hall Conductance in a Two-Dimensional Periodic Potential", Phys. Rev. Lett. **49**, 405 (1982).

[56] L. D. Landau, E. M. Lifshitz, and M. Pitaevskii, *Statistical Physics* (Butterworth-Heinemann, New York, 1999).

[57] K. G. Wilson and J. Kogut, "The renormalization group and the ϵ expansion", Phys. Rep. **12**, 75 (1974).

[58] K. von Klitzing, "Metrology in 2019", Nat. Phys. **13**, 198 (2017).

[59] C. L. Kane and E. J. Mele, "Z_2 Topological Order and the Quantum Spin Hall Effect", Phys. Rev. Lett. **95**, 146802 (2005).

[60] M. König, S. Wiedmann, C. Brüne, A. Roth, H. Buhmann, L. W. Molenkamp, X.-L. Qi, and S.-C. Zhang, "Quantum Spin Hall Insulator State in HgTe Quantum Wells", Science **318**, 766 (2007).

[61] B. A. Bernevig, T. L. Hughes, and S.-C. Zhang, "Quantum Spin Hall Effect and Topological Phase Transition in HgTe Quantum Wells", Science **314**, 1757 (2006).

[62] A. Kitaev, "Periodic table for topological insulators and superconductors", AIP Conf. Proc. **1134**, 22 (2009).

[63] S. Ryu, A. P. Schnyder, A. Furusaki, and A. W. W. Ludwig, "Topological insulators and superconductors: tenfold way and dimensional hierarchy", New J. Phys. **12**, 065010 (2010).

[64] X.-L. Qi and S.-C. Zhang, "Topological insulators and superconductors", Rev. Mod. Phys. **83**, 1057 (2011).

[65] B. Yan and C. Felser, "Topological Materials: Weyl Semimetals", Annu. Rev. Condens. Matter Phys. **8**, 337 (2017).

[66] Z. K. Liu, B. Zhou, Y. Zhang, Z. J. Wang, H. M. Weng, D. Prabhakaran, S.-K. Mo, Z. X. Shen, Z. Fang, X. Dai, Z. Hussain, and Y. L. Chen, "Discovery of a Three-Dimensional Topological Dirac Semimetal, Na_3Bi", Science **343**, 864 (2014).

[67] S.-Y. Xu, I. Belopolski, D. S. Sanchez, C. Zhang, G. Chang, C. Guo, G. Bian, Z. Yuan, H. Lu, T.-R. Chang, P. P. Shibayev, M. L. Prokopovych, N. Alidoust, H. Zheng, C.-C. Lee, S.-M. Huang, R. Sankar, F. Chou, C.-H. Hsu, H.-T. Jeng, A. Bansil, T. Neupert, V. N. Strocov, H. Lin, S. Jia, and M. Z. Hasan, "Experimental discovery of a topological Weyl semimetal state in TaP", Sci. Adv. **1**, e1501092 (2015).

[68] T. Oka and H. Aoki, "Photovoltaic Hall effect in graphene", Phys. Rev. B **79**, 081406 (2009).

[69] T. Kitagawa, E. Berg, M. Rudner, and E. Demler, "Topological characterization of periodically driven quantum systems", Phys. Rev. B **82**, 235114 (2010).

[70] N. Goldman, J. C. Budich, and P. Zoller, "Topological quantum matter with ultracold gases in optical lattices", Nat. Phys. **12**, 639 (2016).

[71] W. P. Su, J. R. Schrieffer, and A. J. Heeger, "Solitons in Polyacetylene", Phys. Rev. Lett. **42**, 1698 (1979).

[72] M. Atala, M. Aidelsburger, J. T. Barreiro, D. Abanin, T. Kitagawa, E. Demler, and I. Bloch, "Direct measurement of the Zak phase in topological Bloch bands", Nat. Phys. **9**, 795 (2013).

[73] P. G. Harper, "Single Band Motion of Conduction Electrons in a Uniform Magnetic Field", Proc. Phys. Soc. A **68**, 874 (1955).

[74] D. R. Hofstadter, "Energy levels and wave functions of Bloch electrons in rational and irrational magnetic fields", Phys. Rev. B **14**, 2239 (1976).

[75] M. Aidelsburger, M. Lohse, C. Schweizer, M. Atala, J. T. Barreiro, S. Nascimbène, N. R. Cooper, I. Bloch, and N. Goldman, "Measuring the Chern number of Hofstadter bands with ultracold bosonic atoms", Nat. Phys. **11**, 162 (2015).

[76] H. Miyake, G. A. Siviloglou, C. J. Kennedy, W. C. Burton, and W. Ketterle, "Realizing the Harper Hamiltonian with Laser-Assisted Tunneling in Optical Lattices", Phys. Rev. Lett. **111**, 185302 (2013).

[77] B. K. Stuhl, H. I. Lu, L. M. Aycock, D. Genkina, and I. B. Spielman, "Visualizing edge states with an atomic Bose gas in the quantum Hall regime", Science **349**, 1514 (2015).

[78] F. D. M. Haldane, "Model for a Quantum Hall Effect without Landau Levels: Condensed-Matter Realization of the "Parity Anomaly"", Phys. Rev. Lett. **61**, 2015 (1988).

[79] G. Jotzu, M. Messer, R. Desbuquois, M. Lebrat, T. Uehlinger, D. Greif, and T. Esslinger, "Experimental realization of the topological Haldane model with ultracold fermions", Nature **515**, 237 (2014).

[80] M. Mancini, G. Pagano, G. Cappellini, L. Livi, M. Rider, J. Catani, C. Sias, P. Zoller, M. Inguscio, M. Dalmonte, and L. Fallani, "Observation of chiral edge states with neutral fermions in synthetic Hall ribbons", Science **349**, 1510 (2015).

[81] D. Jaksch and P. Zoller, "Creation of effective magnetic fields in optical lattices: the Hofstadter butterfly for cold neutral atoms", New J. Phys. **5**, 56 (2003).

[82] N. Goldman, G. Juzeliūnas, P. Öhberg, and I. B. Spielman, "Light-induced gauge fields for ultracold atoms", Rep. Prog. Phys. **77**, 126401 (2014).

[83] A. Celi, P. Massignan, J. Ruseckas, N. Goldman, I. B. Spielman, G. Juzeli ūnas, and M. Lewenstein, "Synthetic Gauge Fields in Synthetic Dimensions", Phys. Rev. Lett. **112**, 043001 (2014).

[84] J. Cayssol, B. Dóra, F. Simon, and R. Moessner, "Floquet topological insulators", Phys. Status Solidi RRL **7**, 101 (2013).

[85] M. C. Rechtsman, J. M. Zeuner, Y. Plotnik, Y. Lumer, D. Podolsky, F. Dreisow, S. Nolte, M. Segev, and A. Szameit, "Photonic Floquet topological insulators", Nature **496**, 196 (2013).

[86] A. D'Errico, F. Cardano, M. Maffei, A. Dauphin, R. Barboza, C. Esposito, B. Piccirillo, M. Lewenstein, P. Massignan, and L. Marrucci, "Two-dimensional topological quantum walks in the momentum space of structured light", Optica **7**, 108 (2020).

[87] S. Rachel, "Interacting topological insulators: a review", Rep. Prog. Phys. **81**, 116501 (2018).

[88] J. G. Bednorz and K. A. Müller, "Possible highTc superconductivity in the Ba-La-Cu-O system", Zeitschrift für Physik B Condensed Matter **64**, 189 (1986).

[89] H. Onnes, "The Superconductivity of Mercury", Comm. Phys. Lab. Univ., Leiden **12**, 122 (1911).

[90] A. P. Drozdov, M. I. Eremets, I. A. Troyan, V. Ksenofontov, and S. I. Shylin, "Conventional superconductivity at 203 kelvin at high pressures in the sulfur hydride system", Nature **525**, 73 (2015).

[91] I. Troyan, A. Gavriliuk, R. Rüffer, A. Chumakov, A. Mironovich, I. Lyubutin, D. Perekalin, A. P. Drozdov, and M. I. Eremets, "Observation of superconductivity in hydrogen sulfide from nuclear resonant scattering", Science **351**, 1303 (2016).

[92] H. Liu, I. I. Naumov, R. Hoffmann, N. W. Ashcroft, and R. J. Hemley, "Potential high-T_c superconducting lanthanum and yttrium hydrides at high pressure", Proc. Natl. Acad. Sci. U.S.A. **114**, 6990 (2017).

[93] M. Somayazulu, M. Ahart, A. K. Mishra, Z. M. Geballe, M. Baldini, Y. Meng, V. V. Struzhkin, and R. J. Hemley, "Evidence for Superconductivity above 260 K in Lanthanum Superhydride at Megabar Pressures", Phys. Rev. Lett. **122**, 027001 (2019).

[94] J. Bardeen, L. N. Cooper, and J. R. Schrieffer, "Microscopic Theory of Superconductivity", Phys. Rev. **106**, 162 (1957).

[95] S. Kaiser, C. R. Hunt, D. Nicoletti, W. Hu, I. Gierz, H. Y. Liu, M. Le Tacon, T. Loew, D. Haug, B. Keimer, and A. Cavalleri, "Optically induced coherent transport far above T_c in underdoped $YBa_2Cu_3O_{6+\delta}$", Phys. Rev. B **89**, 184516 (2014).

[96] B. Liu, M. Först, M. Fechner, D. Nicoletti, J. Porras, T. Loew, B. Keimer, and A. Cavalleri, "Pump Frequency Resonances for Light-Induced Incipient Superconductivity in $YBa_2Cu_3O_{6.5}$", Phys. Rev. X **10**, 011053 (2020).

[97] D. M. Kennes, E. Y. Wilner, D. R. Reichman, and A. J. Millis, "Transient superconductivity from electronic squeezing of optically pumped phonons", Nat. Phys. **13**, 479 (2017).

[98] D. M. Kennes, E. Y. Wilner, D. R. Reichman, and A. J. Millis, "Nonequilibrium optical conductivity: General theory and application to transient phases", Phys. Rev. B **96**, 054506 (2017).

[99] Y. Cao, V. Fatemi, S. Fang, K. Watanabe, T. Taniguchi, E. Kaxiras, and P. Jarillo-Herrero, "Unconventional superconductivity in magic-angle graphene superlattices", Nature **556**, 43 (2018).

[100] Y. Cao, V. Fatemi, A. Demir, S. Fang, S. L. Tomarken, J. Y. Luo, J. D. Sanchez-Yamagishi, K. Watanabe, T. Taniguchi, E. Kaxiras, R. C. Ashoori, and P. Jarillo-Herrero, "Correlated insulator behaviour at half-filling in magic-angle graphene superlattices", Nature **556**, 80 (2018).

[101] L. Tarruell and L. Sanchez-Palencia, "Quantum simulation of the Hubbard model with ultracold fermions in optical lattices", C. R. Phys. **19**, 365 (2018).

[102] F. Binder, L. A. Correa, C. G. J. Anders, and G. Adesso, *Thermodynamics in the Quantum Regime* (Springer, Cham, 2018).

[103] F. G. S. L. Brandao, M. Horodecki, N. Ng, J. Oppenheim, and S. Wehner, "The second laws of quantum thermodynamics", Proc. Natl. Acad. Sci. **112**, 3275 (2015).

[104] L. Masanes and J. Oppenheim, "A general derivation and quantification of the third law of thermodynamics", Nat. Commun. **8**, 14538 (2017).

[105] C. Jarzynski, "Nonequilibrium Equality for Free Energy Differences", Phys. Rev. Lett. **78**, 2690 (1997).

[106] G. E. Crooks, "Entropy production fluctuation theorem and the nonequilibrium work relation for free energy differences", Phys. Rev. E **60**, 2721 (1999).

[107] M. Campisi, P. Hänggi, and P. Talkner, "Colloquium: Quantum fluctuation relations: Foundations and applications", Rev. Mod. Phys. **83**, 771 (2011).

[108] Á. M. Alhambra, L. Masanes, J. Oppenheim, and C. Perry, "Fluctuating Work: From Quantum Thermodynamical Identities to a Second Law Equality", Phys. Rev. X **6**, 041017 (2016).

[109] J. Åberg, "Fully Quantum Fluctuation Theorems", Phys. Rev. X **8**, 011019 (2018).

[110] J. Goold, M. Huber, A. Riera, L. del Rio, and P. Skrzypczyk, "The role of quantum information in thermodynamics—a topical review", J. Phys. A: Math. Theor. **49**, 143001 (2016).

[111] M. N. Bera, A. Riera, M. Lewenstein, Z. B. Khanian, and A. Winter, "Thermodynamics as a Consequence of Information Conservation", Quantum **3**, 121 (2019).

[112] C. Gogolin and J. Eisert, "Equilibration, thermalisation, and the emergence of statistical mechanics in closed quantum systems", Rep. Prog. Phys. **79**, 056001 (2016).

[113] S. Trotzky, Y.-A. Chen, A. Flesch, I. P. McCulloch, U. Schollwöck, J. Eisert, and I. Bloch, "Probing the relaxation towards equilibrium in an isolated strongly correlated one-dimensional Bose gas", Nat. Phys. **8**, 325 (2012).

[114] M. Gring, M. Kuhnert, T. Langen, T. Kitagawa, B. Rauer, M. Schreitl, I. Mazets, D. A. Smith, E. Demler, and J. Schmiedmayer, "Relaxation and Prethermalization in an Isolated Quantum System", Science **337**, 1318 (2012).

[115] T. Langen, S. Erne, R. Geiger, B. Rauer, T. Schweigler, M. Kuhnert, W. Rohringer, I. E. Mazets, T. Gasenzer, and J. Schmiedmayer, "Experimental observation of a generalized Gibbs ensemble", Science **348**, 207 (2015).

[116] A. M. Kaufman, M. E. Tai, A. Lukin, M. Rispoli, R. Schittko, P. M. Preiss, and M. Greiner, "Quantum thermalization through entanglement in an isolated many-body system", Science **353**, 794 (2016).

[117] H. E. D. Scovil and E. O. Schulz-DuBois, "Three-Level Masers as Heat Engines", Phys. Rev. Lett. **2**, 262 (1959).

[118] J. E. Geusic, E. O. Schulz-DuBios, and H. E. D. Scovil, "Quantum Equivalent of the Carnot Cycle", Phys. Rev. **156**, 343 (1967).

[119] J. Jaramillo, M. Beau, and A. del Campo, "Quantum supremacy of many-particle thermal machines", New J. Phys. **18**, 075019 (2016).

[120] J. Bengtsson, M. N. Tengstrand, A. Wacker, P. Samuelsson, M. Ueda, H. Linke, and S. M. Reimann, "Quantum Szilard Engine with Attractively Interacting Bosons", Phys. Rev. Lett. **120**, 100601 (2018).

[121] S. W. Kim, T. Sagawa, S. De Liberato, and M. Ueda, "Quantum Szilard Engine", Phys. Rev. Lett. **106**, 070401 (2011).

[122] A. Ü. C. Hardal, M. Paternostro, and Ö. E. Müstecapl ıo ğlu, "Phase-space interference in extensive and nonextensive quantum heat engines", Phys. Rev. E **97**, 042127 (2018).

[123] R. Uzdin, "Coherence-Induced Reversibility and Collective Operation of Quantum Heat Machines via Coherence Recycling", Phys. Rev. Applied **6**, 024004 (2016).

[124] Y. Zheng and D. Poletti, "Quantum statistics and the performance of engine cycles", Phys. Rev. E **92**, 012110 (2015).

[125] G. Watanabe, B. P. Venkatesh, P. Talkner, M.-J. Hwang, and A. del Campo, "Quantum Statistical Enhancement of the Collective Performance of Multiple Bosonic Engines", Phys. Rev. Lett. **124**, 210603 (2020).

[126] F. C. Binder, S. Vinjanampathy, K. Modi, and J. Goold, "Quantacell: powerful charging of quantum batteries", New J. Phys. **17**, 075015 (2015).

[127] C. Lanczos, "An iteration method for the solution of the eigenvalue problem of linear differential and integral operators", J. Res. Natl. Inst. Stand. Technol. **45**, 255 (1950).

[128] J. Surace and L. Tagliacozzo, *Fermionic Gaussian states: an introduction to numerical approaches*, arXiv:2111.08343 [quant-ph] (2021).

[129] D. Poilblanc and T. M. Rice, "Charged solitons in the Hartree-Fock approximation to the large-U Hubbard model", Phys. Rev. B **39**, 9749 (1989).

[130] R. M. Martin, *Electronic Structure: Basic Theory and Practical Methods*, 2nd ed. (Cambridge University Press, 2020).

[131] G. W. Pratt, "Unrestricted Hartree-Fock Method", Phys. Rev. **102**, 1303 (1956).

[132] H. Fukutome, "Unrestricted Hartree–Fock theory and its applications to molecules and chemical reactions", Int. J. Quantum Chem. **20**, 955 (1981).

[133] I. Shavitt, "The Method of Configuration Interaction", in *Methods of Electronic Structure Theory* (Springer US, Boston, MA, 1977), pp. 189–275.

[134] E. Louis, F. Guinea, M. P. López Sancho, and J. A. Vergés, "Configuration-interaction approach to hole pairing in the two-dimensional Hubbard model", Phys. Rev. B **59**, 14005 (1999).

[135] A. Rüegg and G. A. Fiete, "Fractionally charged topological point defects on the kagome lattice", Phys. Rev. B **83**, 165118 (2011).

[136] K. Ferhat and A. Ralko, "Phase diagram of the $\frac{1}{3}$-filled extended Hubbard model on the kagome lattice", Phys. Rev. B **89**, 155141 (2014).

[137] F. Plasser, M. Ruckenbauer, S. Mai, M. Oppel, P. Marquetand, and L. González, "Efficient and Flexible Computation of Many-Electron Wave Function Overlaps", J. Chem. Theory Comput. **12**, 1207 (2016).

[138] R. Orús, "Tensor networks for complex quantum systems", Nat. Rev. Phys. **1**, 538 (2019).

[139] S. R. White, "Density matrix formulation for quantum renormalization groups", Phys. Rev. Lett. **69**, 2863 (1992).

[140] R. Orus, "A practical introduction to tensor networks: Matrix product states and projected entangled pair states", Ann. Phys. **349**, 117 (2014).

[141] U. Schollwöck, "The density-matrix renormalization group in the age of matrix product states", Ann. Phys. **326**, 96 (2011).

[142] J. Hauschild and F. Pollmann, "Efficient numerical simulations with Tensor Networks: Tensor Network Python (TeNPy)", SciPost Phys. Lect. Notes, 5 (2018).

[143] M. Fishman, S. R. White, and E. M. Stoudenmire, *The ITensor Software Library for Tensor Network Calculations*, arXiv:2007.14822 [quant-ph] (2020).

[144] M. Fannes, B. Nachtergaele, and R. F. Werner, "Finitely correlated states on quantum spin chains", Commun. Math. Phys. **144**, 443 (1992).

[145] J. Eisert, M. Cramer, and M. B. Plenio, "Colloquium: Area laws for the entanglement entropy", Rev. Mod. Phys. **82**, 277 (2010).

[146] D. N. Page, "Average entropy of a subsystem", Phys. Rev. Lett. **71**, 1291 (1993).

[147] M. B. Hastings, "An area law for one-dimensional quantum systems", J. Stat. Mech. **2007**, 08024 (2007).

[148] F. Verstraete, V. Murg, and J. Cirac, "Matrix product states, projected entangled pair states, and variational renormalization group methods for quantum spin systems", Adv. Phys. **57**, 143 (2008).

[149] S. Singh, R. N. C. Pfeifer, and G. Vidal, "Tensor network decompositions in the presence of a global symmetry", Phys. Rev. A **82**, 050301 (2010).

[150] S. Singh, R. N. C. Pfeifer, and G. Vidal, "Tensor network states and algorithms in the presence of a global U(1) symmetry", Phys. Rev. B **83**, 115125 (2011).

[151] S. Singh and G. Vidal, "Tensor network states and algorithms in the presence of a global SU(2) symmetry", Phys. Rev. B **86**, 195114 (2012).

[152] A. Weichselbaum, "Non-abelian symmetries in tensor networks: A quantum symmetry space approach", Ann. Phys. **327**, 2972 (2012).

[153] P. Scholl, M. Schuler, H. J. Williams, A. A. Eberharter, D. Barredo, K.-N. Schymik, V. Lienhard, L.-P. Henry, T. C. Lang, T. Lahaye, A. M. Läuchli, and A. Browaeys, "Quantum simulation of 2D antiferromagnets with hundreds of Rydberg atoms", Nature **595**, 233 (2021).

[154] P. Jordan and E. Wigner, "Über das Paulische Äquivalenzverbot", Zeitschrift für Physik **47**, 631 (1928).

[155] T. D. Schultz, D. C. Mattis, and E. H. Lieb, "Two-Dimensional Ising Model as a Soluble Problem of Many Fermions", Rev. Mod. Phys. **36**, 856 (1964).

[156] E. Stoudenmire and S. R. White, "Studying Two-Dimensional Systems with the Density Matrix Renormalization Group", Annu. Rev. Condens. Matter Phys. **3**, 111 (2012).

[157] G. Semeghini, H. Levine, A. Keesling, S. Ebadi, T. T. Wang, D. Bluvstein, R. Verresen, H. Pichler, M. Kalinowski, R. Samajdar, A. Omran, S. Sachdev, A. Vishwanath, M. Greiner, V. Vuletić, and M. D. Lukin, "Probing topological spin liquids on a programmable quantum simulator", Science **374**, 1242 (2021).

[158] B.-X. Zheng, C.-M. Chung, P. Corboz, G. Ehlers, M.-P. Qin, R. M. Noack, H. Shi, S. R. White, S. Zhang, and G. K.-L. Chan, "Stripe order in the underdoped region of the two-dimensional Hubbard model", Science **358**, 1155 (2017).

[159] E. W. Huang, C. B. Mendl, S. Liu, S. Johnston, H.-C. Jiang, B. Moritz, and T. P. Devereaux, "Numerical evidence of fluctuating stripes in the normal state of high-Tc cuprate superconductors", Science **358**, 1161 (2017).

[160] A. Szasz, J. Motruk, M. P. Zaletel, and J. E. Moore, "Chiral Spin Liquid Phase of the Triangular Lattice Hubbard Model: A Density Matrix Renormalization Group Study", Phys. Rev. X **10**, 021042 (2020).

[161] T.-S. Zeng, W. Zhu, and D. Sheng, "Tuning topological phase and quantum anomalous Hall effect by interaction in quadratic band touching systems", npj Quant. Mater. **3**, 1 (2018).

[162] S. Sur, S.-S. Gong, K. Yang, and O. Vafek, "Quantum anomalous Hall insulator stabilized by competing interactions", Phys. Rev. B **98**, 125144 (2018).

[163] H.-Q. Wu, Y.-Y. He, C. Fang, Z. Y. Meng, and Z.-Y. Lu, "Diagnosis of Interaction-driven Topological Phase via Exact Diagonalization", Phys. Rev. Lett. **117**, 066403 (2016).

[164] W. Lenz, "Beiträge zum Verständnis der magnetischen Eigenschaften in festen Kzörper", Physikalische Zeitschrif **21**, 613 (1920).

[165] E. Ising, "Beitrag zur Theorie des Ferromagnetismusr", Zeitschrift für Physik A **31**, 253 (1925).

[166] H. A. Kramers and G. H. Wannier, "Statistics of the Two-Dimensional Ferromagnet. Part I", Phys. Rev. **60**, 252 (1941).

[167] H. A. Kramers and G. H. Wannier, "Statistics of the Two-Dimensional Ferromagnet. Part II", Phys. Rev. **60**, 263 (1941).

[168] L. Onsager, "Crystal Statistics. I. A Two-Dimensional Model with an Order-Disorder Transition", Phys. Rev. **65**, 117 (1944).

[169] C. N. Yang, "The Spontaneous Magnetization of a Two-Dimensional Ising Model", Phys. Rev. **85**, 808 (1952).

[170] E. A. Cornell and C. E. Wieman, "Nobel Lecture: Bose-Einstein condensation in a dilute gas, the first 70 years and some recent experiments", Rev. Mod. Phys. **74**, 875 (2002).

[171] W. Ketterle, "Nobel lecture: When atoms behave as waves: Bose-Einstein condensation and the atom laser", Rev. Mod. Phys. **74**, 1131 (2002).

[172] Y. Hatsugai, "Chern number and edge states in the integer quantum Hall effect", Phys. Rev. Lett. **71**, 3697 (1993).

[173] L. Fu, "Topological Crystalline Insulators", Phys. Rev. Lett. **106**, 106802 (2011).

[174] L. Fidkowski and A. Kitaev, "Effects of interactions on the topological classification of free fermion systems", Phys. Rev. B **81**, 134509 (2010).

[175] Z.-C. Gu and X.-G. Wen, "Tensor-entanglement-filtering renormalization approach and symmetry-protected topological order", Phys. Rev. B **80**, 155131 (2009).

[176] F. Pollmann, A. M. Turner, E. Berg, and M. Oshikawa, "Entanglement spectrum of a topological phase in one dimension", Phys. Rev. B **81**, 064439 (2010).

[177] A. M. Turner, F. Pollmann, and E. Berg, "Topological phases of one-dimensional fermions: An entanglement point of view", Phys. Rev. B **83**, 075102 (2011).

[178] R. Peierls, *Quantum Theory of Solids*, International series of monographs on physics (Clarendon Press, Oxford, 1955).

[179] J. Zak, "Berry's phase for energy bands in solids", Phys. Rev. Lett. **62**, 2747 (1989).

[180] T. Fukui, Y. Hatsugai, and H. Suzuki, "Chern Numbers in Discretized Brillouin Zone: Efficient Method of Computing (Spin) Hall Conductances", J. Phys. Soc. Japan **74**, 1674 (2005).

[181] Y. Hatsugai, "Quantized Berry Phases as a Local Order Parameter of a Quantum Liquid", J. Phys. Soc. Japan **75**, 123601 (2006).

[182] M. Greiner, O. Mandel, T. Esslinger, T. W. Hänsch, and I. Bloch, "Quantum phase transition from a superfluid to a Mott insulator in a gas of ultracold atoms", Nature **415**, 39 (2002).

[183] C. Gross and I. Bloch, "Quantum simulations with ultracold atoms in optical lattices", Science **357**, 995 (2017).

[184] F. Schäfer, T. Fukuhara, S. Sugawa, Y. Takasu, and Y. Takahashi, "Tools for quantum simulation with ultracold atoms in optical lattices", Nat. Rev. Phys. **2**, 411 (2020).

[185] B. DeMarco and D. S. Jin, "Onset of Fermi Degeneracy in a Trapped Atomic Gas", Science **285**, 1703 (1999).

[186] W. S. Bakr, A. Peng, M. E. Tai, R. Ma, J. Simon, J. I. Gillen, S. Fölling, L. Pollet, and M. Greiner, "Probing the Superfluid-to-Mott Insulator Transition at the Single-Atom Level", Science **329**, 547 (2010).

[187] T. Fukuhara, A. Kantian, M. Endres, M. Cheneau, P. Schauß, S. Hild, D. Bellem, U. Schollwöck, T. Giamarchi, C. Gross, I. Bloch, and S. Kuhr, "Quantum dynamics of a mobile spin impurity", Nat. Phys. **9**, 235 (2013).

[188] M. Aidelsburger, M. Atala, M. Lohse, J. T. Barreiro, B. Paredes, and I. Bloch, "Realization of the Hofstadter Hamiltonian with Ultracold Atoms in Optical Lattices", Phys. Rev. Lett. **111**, 185301 (2013).

[189] H. Feshbach, "Unified theory of nuclear reactions", Ann. Phys. **5**, 357 (1958).

[190] U. Fano, "Effects of Configuration Interaction on Intensities and Phase Shifts", Phys. Rev. **124**, 1866 (1961).

[191] M. Greiner, O. Mandel, T. Esslinger, T. W. Hänsch, and I. Bloch, "Quantum phase transition from a superfluid to a Mott insulator in a gas of ultracold atoms", Nature **415**, 39 (2002).

[192] M. Greiner, I. Bloch, O. Mandel, T. W. Hänsch, and T. Esslinger, "Exploring Phase Coherence in a 2D Lattice of Bose-Einstein Condensates", Phys. Rev. Lett. **87**, 160405 (2001).

[193] W. S. Bakr, J. I. Gillen, A. Peng, S. Fölling, and M. Greiner, "A quantum gas microscope for detecting single atoms in a Hubbard-regime optical lattice", Nature **462**, 74 (2009).

[194] C. Weitenberg, M. Endres, J. F. Sherson, M. Cheneau, P. Schauß, T. Fukuhara, I. Bloch, and S. Kuhr, "Single-spin addressing in an atomic Mott insulator", Nature **471**, 319 (2011).

[195] J. F. Sherson, C. Weitenberg, M. Endres, M. Cheneau, I. Bloch, and S. Kuhr, "Single-atom-resolved fluorescence imaging of an atomic Mott insulator", Nature **467**, 68 (2010).

[196] L. W. Cheuk, M. A. Nichols, K. R. Lawrence, M. Okan, H. Zhang, and M. W. Zwierlein, "Observation of 2D Fermionic Mott Insulators of ^{40}K with Single-Site Resolution", Phys. Rev. Lett. **116**, 235301 (2016).

[197] D. Greif, M. F. Parsons, A. Mazurenko, C. S. Chiu, S. Blatt, F. Huber, G. Ji, and M. Greiner, "Site-resolved imaging of a fermionic Mott insulator", Science **351**, 953 (2016).

[198] M. Endres, M. Cheneau, T. Fukuhara, C. Weitenberg, P. Schauß, C. Gross, L. Mazza, M. C. Bañuls, L. Pollet, I. Bloch, and S. Kuhr, "Observation of Correlated Particle-Hole Pairs and String Order in Low-Dimensional Mott Insulators", Science **334**, 200 (2011).

[199] M. Boll, T. A. Hilker, G. Salomon, A. Omran, J. Nespolo, L. Pollet, I. Bloch, and C. Gross, "Spin- and density-resolved microscopy of antiferromagnetic correlations in Fermi-Hubbard chains", Science **353**, 1257 (2016).

[200] M. F. Parsons, A. Mazurenko, C. S. Chiu, G. Ji, D. Greif, and M. Greiner, "Site-resolved measurement of the spin-correlation function in the Fermi-Hubbard model", Science **353**, 1253 (2016).

[201] L. W. Cheuk, M. A. Nichols, K. R. Lawrence, M. Okan, H. Zhang, E. Khatami, N. Trivedi, T. Paiva, M. Rigol, and M. W. Zwierlein, "Observation of spatial charge and spin correlations in the 2D Fermi-Hubbard model", Science **353**, 1260 (2016).

[202] T. A. Hilker, G. Salomon, F. Grusdt, A. Omran, M. Boll, E. Demler, I. Bloch, and C. Gross, "Revealing hidden antiferromagnetic correlations in doped Hubbard chains via string correlators", Science **357**, 484 (2017).

[203] T. Fukuhara, S. Hild, J. Zeiher, P. Schauß, I. Bloch, M. Endres, and C. Gross, "Spatially Resolved Detection of a Spin-Entanglement Wave in a Bose-Hubbard Chain", Phys. Rev. Lett. **115**, 035302 (2015).

[204] P. M. Preiss, R. Ma, M. E. Tai, J. Simon, and M. Greiner, "Quantum gas microscopy with spin, atom-number, and multilayer readout", Phys. Rev. A **91**, 041602 (2015).

[205] L. Asteria, H. P. Zahn, M. N. Kosch, K. Sengstock, and C. Weitenberg, "Quantum gas magnifier for sub-lattice-resolved imaging of 3D quantum systems", Nature **599**, 571 (2021).

[206] H. M. Price and N. R. Cooper, "Mapping the Berry curvature from semiclassical dynamics in optical lattices", Phys. Rev. A **85**, 033620 (2012).

[207] A. Dauphin and N. Goldman, "Extracting the Chern Number from the Dynamics of a Fermi Gas: Implementing a Quantum Hall Bar for Cold Atoms", Phys. Rev. Lett. **111**, 135302 (2013).

[208] D. T. Tran, A. Dauphin, A. G. Grushin, P. Zoller, and N. Goldman, "Probing topology by "heating": Quantized circular dichroism in ultracold atoms", Sci. Adv. **3**, e1701207 (2017).

[209] L. Asteria, D. T. Tran, T. Ozawa, M. Tarnowski, B. S. Rem, N. Fläschner, K. Sengstock, N. Goldman, and C. Weitenberg, "Measuring quantized circular dichroism in ultracold topological matter", Nat. Phys. **15**, 449 (2019).

[210] C. Wang, P. Zhang, X. Chen, J. Yu, and H. Zhai, "Scheme to Measure the Topological Number of a Chern Insulator from Quench Dynamics", Phys. Rev. Lett. **118**, 185701 (2017).

[211] M. Tarnowski, F. N. Ünal, N. Fläschner, B. S. Rem, A. Eckardt, K. Sengstock, and C. Weitenberg, "Measuring topology from dynamics by obtaining the Chern number from a linking number", Nat. Commun. **10**, 1728 (2019).

[212] E. J. Meier, F. A. An, and B. Gadway, "Observation of the topological soliton state in the Su–Schrieffer–Heeger model", Nat. Commun. **7**, 13986 (2016).

[213] E. J. Meier, F. A. An, A. Dauphin, M. Maffei, P. Massignan, T. L. Hughes, and B. Gadway, "Observation of the topological Anderson insulator in disordered atomic wires", Science **362**, 929 (2018).

[214] I. Affleck, T. Kennedy, E. H. Lieb, and H. Tasaki, "Rigorous results on valence-bond ground states in antiferromagnets", Phys. Rev. Lett. **59**, 799 (1987).

[215] P. Sompet, S. Hirthe, D. Bourgund, T. Chalopin, J. Bibo, J. Koepsell, P. Bojović, R. Verresen, F. Pollmann, G. Salomon, C. Gross, T. A. Hilker, and I. Bloch, *Realising the Symmetry-Protected Haldane Phase in Fermi-Hubbard Ladders*, arXiv:2103.10421 [cond-mat.quant-gas] (2021).

[216] S. R. Manmana, A. M. Essin, R. M. Noack, and V. Gurarie, "Topological invariants and interacting one-dimensional fermionic systems", Phys. Rev. B **86**, 205119 (2012).

[217] V. Gurarie, "Single-particle Green's functions and interacting topological insulators", Phys. Rev. B **83**, 085426 (2011).

[218] T. Yoshida, R. Peters, S. Fujimoto, and N. Kawakami, "Characterization of a Topological Mott Insulator in One Dimension", Phys. Rev. Lett. **112**, 196404 (2014).

[219] B. Sbierski and C. Karrasch, "Topological invariants for the Haldane phase of interacting Su-Schrieffer-Heeger chains: Functional renormalization-group approach", Phys. Rev. B **98**, 165101 (2018).

[220] L. Barbiero, L. Santos, and N. Goldman, "Quenched dynamics and spin-charge separation in an interacting topological lattice", Phys. Rev. B **97**, 201115 (2018).

[221] S. de Léséleuc, V. Lienhard, P. Scholl, D. Barredo, S. Weber, N. Lang, H. P. Büchler, T. Lahaye, and A. Browaeys, "Observation of a symmetry-protected topological phase of interacting bosons with Rydberg atoms", Science **365**, 775 (2019).

[222] D. González-Cuadra, P. R. Grzybowski, A. Dauphin, and M. Lewenstein, "Strongly Correlated Bosons on a Dynamical Lattice", Phys. Rev. Lett. **121**, 090402 (2018).

[223] D. González-Cuadra, A. Dauphin, P. R. Grzybowski, P. Wójcik, M. Lewenstein, and A. Bermudez, "Symmetry-breaking topological insulators in the $\mathbb{Z}_2$ Bose-Hubbard model", Phys. Rev. B **99**, 045139 (2019).

[224] D. González-Cuadra, A. Bermudez, P. R. Grzybowski, M. Lewenstein, and A. Dauphin, "Intertwined topological phases induced by emergent symmetry protection", Nat. Commun. **10**, 2694 (2019).

[225] F. Mivehvar, H. Ritsch, and F. Piazza, "Superradiant Topological Peierls Insulator inside an Optical Cavity", Phys. Rev. Lett. **118**, 073602 (2017).

[226] T. Chanda, R. Kraus, G. Morigi, and J. Zakrzewski, "Self-organized topological insulator due to cavity-mediated correlated tunneling", Quantum **5**, 501 (2021).

[227] K. Hallberg, E. Gagliano, and C. Balseiro, "Finite-size study of a spin-1/2 Heisenberg chain with competing interactions: Phase diagram and critical behavior", Phys. Rev. B **41**, 9474 (1990).

[228] P. Schmitteckert and R. Werner, "Charge-density-wave instabilities driven by multiple umklapp scattering", Phys. Rev. B **69**, 195115 (2004).

[229] T. Mishra, J. Carrasquilla, and M. Rigol, "Phase diagram of the half-filled one-dimensional t-V-V' model", Phys. Rev. B **84**, 115135 (2011).

[230] M. Nakamura, "Mechanism of CDW-SDW Transition in One Dimension", J. Phys. Soc. Japan **68**, 3123 (1999).

[231] M. Nakamura, "Tricritical behavior in the extended Hubbard chains", Phys. Rev. B **61**, 16377 (2000).

[232] E. Jeckelmann, "Ground-State Phase Diagram of a Half-Filled One-Dimensional Extended Hubbard Model", Phys. Rev. Lett. **89**, 236401 (2002).

[233] P. Sengupta, A. W. Sandvik, and D. K. Campbell, "Bond-order-wave phase and quantum phase transitions in the one-dimensional extended Hubbard model", Phys. Rev. B **65**, 155113 (2002).

[234] A. W. Sandvik, L. Balents, and D. K. Campbell, "Ground State Phases of the Half-Filled One-Dimensional Extended Hubbard Model", Phys. Rev. Lett. **92**, 236401 (2004).

[235] Y. Z. Zhang, "Dimerization in a Half-Filled One-Dimensional Extended Hubbard Model", Phys. Rev. Lett. **92**, 246404 (2004).

[236] K.-M. Tam, S.-W. Tsai, and D. K. Campbell, "Functional Renormalization Group Analysis of the Half-Filled One-Dimensional Extended Hubbard Model", Phys. Rev. Lett. **96**, 036408 (2006).

[237] S. Glocke, A. Klümper, and J. Sirker, "Half-filled one-dimensional extended Hubbard model: Phase diagram and thermodynamics", Phys. Rev. B **76**, 155121 (2007).

[238] S. Ejima and S. Nishimoto, "Phase Diagram of the One-Dimensional Half-Filled Extended Hubbard Model", Phys. Rev. Lett. **99**, 216403 (2007).

[239] M. Di Dio, L. Barbiero, A. Recati, and M. Dalmonte, "Spontaneous Peierls dimerization and emergent bond order in one-dimensional dipolar gases", Phys. Rev. A **90**, 063608 (2014).

[240] M. P. Zaletel, R. S. K. Mong, and F. Pollmann, "Flux insertion, entanglement, and quantized responses", J. Stat. Mech. Theory Exp. **2014**, P10007 (2014).

[241] D. Wang, S. Xu, Y. Wang, and C. Wu, "Detecting edge degeneracy in interacting topological insulators through entanglement entropy", Phys. Rev. B **91**, 115118 (2015).

[242] M. den Nijs and K. Rommelse, "Preroughening transitions in crystal surfaces and valence-bond phases in quantum spin chains", Phys. Rev. B **40**, 4709 (1989).

[243] L. Barbiero, A. Montorsi, and M. Roncaglia, "How hidden orders generate gaps in one-dimensional fermionic systems", Phys. Rev. B **88**, 035109 (2013).

[244] A. Montorsi, F. Dolcini, R. C. Iotti, and F. Rossi, "Symmetry-protected topological phases of one-dimensional interacting fermions with spin-charge separation", Phys. Rev. B **95**, 245108 (2017).

[245] E. Haller, J. Hudson, A. Kelly, D. A. Cotta, B. Peaudecerf, G. D. Bruce, and S. Kuhr, "Single-atom imaging of fermions in a quantum-gas microscope", Nat. Phys. **11**, 738 (2015).

[246] F. Anfuso and A. Rosch, "String order and adiabatic continuity of Haldane chains and band insulators", Phys. Rev. B **75**, 144420 (2007).

[247] H. T. Wang, B. Li, and S. Y. Cho, "Topological quantum phase transition in bond-alternating spin-$\frac{1}{2}$ Heisenberg chains", Phys. Rev. B **87**, 054402 (2013).

[248] J. Fraxanet, D. González-Cuadra, T. Pfau, M. Lewenstein, T. Langen, and L. Barbiero, "Topological Quantum Critical Points in the Extended Bose-Hubbard Model", Phys. Rev. Lett. **128**, 043402 (2022).

[249] M. Dalmonte, J. Carrasquilla, L. Taddia, E. Ercolessi, and M. Rigol, "Gap scaling at Berezinskii-Kosterlitz-Thouless quantum critical points in one-dimensional Hubbard and Heisenberg models", Phys. Rev. B **91**, 165136 (2015).

[250] B.-T. Ye, L.-Z. Mu, and H. Fan, "Entanglement spectrum of Su-Schrieffer-Heeger-Hubbard model", Phys. Rev. B **94**, 165167 (2016).

[251] N. H. Le, A. J. Fisher, N. J. Curson, and E. Ginossar, "Topological phases of a dimerized Fermi–Hubbard model for semiconductor nano-lattices", npj Quantum Inf. **6**, 24 (2020).

[252] D. González-Cuadra, A. Dauphin, P. R. Grzybowski, M. Lewenstein, and A. Bermudez, "Dynamical Solitons and Boson Fractionalization in Cold-Atom Topological Insulators", Phys. Rev. Lett. **125**, 265301 (2020).

[253] D. González-Cuadra, A. Dauphin, P. R. Grzybowski, M. Lewenstein, and A. Bermudez, "$\mathbb{Z}_n$ solitons in intertwined topological phases", Phys. Rev. B **102**, 245137 (2020).

[254] A. Patscheider, B. Zhu, L. Chomaz, D. Petter, S. Baier, A.-M. Rey, F. Ferlaino, and M. J. Mark, "Controlling dipolar exchange interactions in a dense three-dimensional array of large-spin fermions", Phys. Rev. Research **2**, 023050 (2020).

[255] C. Gross and W. S. Bakr, "Quantum gas microscopy for single atom and spin detection", Nat. Phys. **17**, 1316 (2021).

[256] M. A. Norcia and F. Ferlaino, "Developments in atomic control using ultracold magnetic lanthanides", Nat. Phys. **17**, 1349 (2021).

[257] N. Petersen, M. Trümper, and P. Windpassinger, "Spectroscopy of the 1001-nm transition in atomic dysprosium", Phys. Rev. A **101**, 042502 (2020).

[258] A. Patscheider, B. Yang, G. Natale, D. Petter, L. Chomaz, M. J. Mark, G. Hovhannesyan, M. Lepers, and F. Ferlaino, "Observation of a narrow inner-shell orbital transition in atomic erbium at 1299 nm", Phys. Rev. Research **3**, 033256 (2021).

[259] O. Jürgensen, F. Meinert, M. J. Mark, H.-C. Nägerl, and D.-S. Lühmann, "Observation of Density-Induced Tunneling", Phys. Rev. Lett. **113**, 193003 (2014).

[260] C. N. Varney, K. Sun, M. Rigol, and V. Galitski, "Interaction effects and quantum phase transitions in topological insulators", Phys. Rev. B **82**, 115125 (2010).

[261] T. Neupert, L. Santos, C. Chamon, and C. Mudry, "Fractional Quantum Hall States at Zero Magnetic Field", Phys. Rev. Lett. **106**, 236804 (2011).

[262] H. L. Stormer, "Nobel Lecture: The fractional quantum Hall effect", Rev. Mod. Phys. **71**, 875 (1999).

[263] S. Raghu, X.-L. Qi, C. Honerkamp, and S.-C. Zhang, "Topological Mott Insulators", Phys. Rev. Lett. **100**, 156401 (2008).

[264] B.-B. Chen, Y. D. Liao, Z. Chen, O. Vafek, J. Kang, W. Li, and Z. Y. Meng, "Realization of topological Mott insulator in a twisted bilayer graphene lattice model", Nat. Commun. **12**, 5480 (2021).

[265] A. Dauphin, M. Müller, and M. A. Martin-Delgado, "Rydberg-atom quantum simulation and Chern-number characterization of a topological Mott insulator", Phys. Rev. A **86**, 053618 (2012).

[266] N. A. García-Martínez, A. G. Grushin, T. Neupert, B. Valenzuela, and E. V. Castro, "Interaction-driven phases in the half-filled spinless honeycomb lattice from exact diagonalization", Phys. Rev. B **88**, 245123 (2013).

[267] Y. Jia, H. Guo, Z. Chen, S.-Q. Shen, and S. Feng, "Effect of interactions on two-dimensional Dirac fermions", Phys. Rev. B **88**, 075101 (2013).

[268] M. Daghofer and M. Hohenadler, "Phases of correlated spinless fermions on the honeycomb lattice", Phys. Rev. B **89**, 035103 (2014).

[269] H. Guo and Y. Jia, "Interaction-driven phases in a Dirac semimetal: exact diagonalization results", J. Phys. Condens. Matter **26**, 475601 (2014).

[270] J. Motruk, A. G. Grushin, F. de Juan, and F. Pollmann, "Interaction-driven phases in the half-filled honeycomb lattice: An infinite density matrix renormalization group study", Phys. Rev. B **92**, 085147 (2015).

[271] S. Capponi and A. M. Läuchli, "Phase diagram of interacting spinless fermions on the honeycomb lattice: A comprehensive exact diagonalization study", Phys. Rev. B **92**, 085146 (2015).

[272] D. D. Scherer, M. M. Scherer, and C. Honerkamp, "Correlated spinless fermions on the honeycomb lattice revisited", Phys. Rev. B **92**, 155137 (2015).

[273] K. Sun, H. Yao, E. Fradkin, and S. A. Kivelson, "Topological Insulators and Nematic Phases from Spontaneous Symmetry Breaking in 2D Fermi Systems with a Quadratic Band Crossing", Phys. Rev. Lett. **103**, 046811 (2009).

[274] W. Zhu, S.-S. Gong, T.-S. Zeng, L. Fu, and D. N. Sheng, "Interaction-Driven Spontaneous Quantum Hall Effect on a Kagome Lattice", Phys. Rev. Lett. **117**, 096402 (2016).

[275] M. Saffman, T. G. Walker, and K. Mølmer, "Quantum information with Rydberg atoms", Rev. Mod. Phys. **82**, 2313 (2010).

[276] R. Heidemann, U. Raitzsch, V. Bendkowsky, B. Butscher, R. Löw, L. Santos, and T. Pfau, "Evidence for Coherent Collective Rydberg Excitation in the Strong Blockade Regime", Phys. Rev. Lett. **99**, 163601 (2007).

[277] A. Browaeys and T. Lahaye, "Many-body physics with individually controlled Rydberg atoms", Nat. Phys. **16**, 132 (2020).

[278] L. Isenhower, E. Urban, X. L. Zhang, A. T. Gill, T. Henage, T. A. Johnson, T. G. Walker, and M. Saffman, "Demonstration of a Neutral Atom Controlled-NOT Quantum Gate", Phys. Rev. Lett. **104**, 010503 (2010).

[279] T. Wilk, A. Gaëtan, C. Evellin, J. Wolters, Y. Miroshnychenko, P. Grangier, and A. Browaeys, "Entanglement of Two Individual Neutral Atoms Using Rydberg Blockade", Phys. Rev. Lett. **104**, 010502 (2010).

[280] H. Levine, A. Keesling, A. Omran, H. Bernien, S. Schwartz, A. S. Zibrov, M. Endres, M. Greiner, V. Vuletić, and M. D. Lukin, "High-Fidelity Control and Entanglement of Rydberg-Atom Qubits", Phys. Rev. Lett. **121**, 123603 (2018).

[281] A. Omran, H. Levine, A. Keesling, G. Semeghini, T. T. Wang, S. Ebadi, H. Bernien, A. S. Zibrov, H. Pichler, S. Choi, J. Cui, M. Rossignolo, P. Rembold, S. Montangero, T. Calarco, M. Endres, M. Greiner, V. Vuletić, and M. D. Lukin, "Generation and manipulation of Schrödinger cat states in Rydberg atom arrays", Science **365**, 570 (2019).

[282] L. Henriet, L. Beguin, A. Signoles, T. Lahaye, A. Browaeys, G.-O. Reymond, and C. Jurczak, "Quantum computing with neutral atoms", Quantum **4**, 327 (2020).

[283] I. Cong, S.-T. Wang, H. Levine, A. Keesling, and M. D. Lukin, *Hardware-Efficient, Fault-Tolerant Quantum Computation with Rydberg Atoms*, arXiv:2105.13501 [quant-ph] (2021).

[284] M. Endres, H. Bernien, A. Keesling, H. Levine, E. R. Anschuetz, A. Krajenbrink, C. Senko, V. Vuletic, M. Greiner, and M. D. Lukin, "Atom-by-atom assembly of defect-free one-dimensional cold atom arrays", Science **354**, 1024 (2016).

[285] H. Bernien, S. Schwartz, A. Keesling, H. Levine, A. Omran, H. Pichler, S. Choi, A. S. Zibrov, M. Endres, M. Greiner, V. Vuletić, and M. D. Lukin, "Probing many-body dynamics on a 51-atom quantum simulator", Nature **551**, 579 (2017).

[286] A. Keesling, A. Omran, H. Levine, H. Bernien, H. Pichler, S. Choi, R. Samajdar, S. Schwartz, P. Silvi, S. Sachdev, P. Zoller, M. Endres, M. Greiner, V. Vuletić, and M. D. Lukin, "Quantum Kibble–Zurek mechanism and critical dynamics on a programmable Rydberg simulator", Nature **568**, 207 (2019).

[287] H. Labuhn, D. Barredo, S. Ravets, S. de Léséleuc, T. Macrì, T. Lahaye, and A. Browaeys, "Tunable two-dimensional arrays of single Rydberg atoms for realizing quantum Ising models", Nature **534**, 667 (2016).

[288] S. Ebadi, T. T. Wang, H. Levine, A. Keesling, G. Semeghini, A. Omran, D. Bluvstein, R. Samajdar, H. Pichler, W. W. Ho, S. Choi, S. Sachdev, M. Greiner, V. Vuletić, and M. D. Lukin, "Quantum phases of matter on a 256-atom programmable quantum simulator", Nature **595**, 227 (2021).

[289] L. Chomaz, S. Baier, D. Petter, M. J. Mark, F. Wächtler, L. Santos, and F. Ferlaino, "Quantum-Fluctuation-Driven Crossover from a Dilute Bose-Einstein Condensate to a Macrodroplet in a Dipolar Quantum Fluid", Phys. Rev. X **6**, 041039 (2016).

[290] M. Schmitt, M. Wenzel, F. Böttcher, I. Ferrier-Barbut, and T. Pfau, "Self-bound droplets of a dilute magnetic quantum liquid", Nature **539**, 259 (2016).

[291] F. Böttcher, J.-N. Schmidt, M. Wenzel, J. Hertkorn, M. Guo, T. Langen, and T. Pfau, "Transient Supersolid Properties in an Array of Dipolar Quantum Droplets", Phys. Rev. X **9**, 011051 (2019).

[292] L. Tanzi, E. Lucioni, F. Famà, J. Catani, A. Fioretti, C. Gabbanini, R. N. Bisset, L. Santos, and G. Modugno, "Observation of a Dipolar Quantum Gas with Metastable Supersolid Properties", Phys. Rev. Lett. **122**, 130405 (2019).

[293] L. Chomaz, D. Petter, P. Ilzhöfer, G. Natale, A. Trautmann, C. Politi, G. Durastante, R. M. W. van Bijnen, A. Patscheider, M. Sohmen, M. J. Mark, and F. Ferlaino, "Long-Lived and Transient Supersolid Behaviors in Dipolar Quantum Gases", Phys. Rev. X **9**, 021012 (2019).

[294] M. A. Norcia, C. Politi, L. Klaus, E. Poli, M. Sohmen, M. J. Mark, R. N. Bisset, L. Santos, and F. Ferlaino, "Two-dimensional supersolidity in a dipolar quantum gas", Nature **596**, 357 (2021).

[295] L. D. Marco, G. Valtolina, K. Matsuda, W. G. Tobias, J. P. Covey, and J. Ye, "A degenerate Fermi gas of polar molecules", Science **363**, 853 (2019).

[296] J. L. Bohn, A. M. Rey, and J. Ye, "Cold molecules: Progress in quantum engineering of chemistry and quantum matter", Science **357**, 1002 (2017).

[297] C. Trefzger, C. Menotti, B. Capogrosso-Sansone, and M. Lewenstein, "Ultracold dipolar gases in optical lattices", J. Phys. B **44**, 193001 (2011).

[298] A. de Paz, A. Sharma, A. Chotia, E. Maréchal, J. H. Huckans, P. Pedri, L. Santos, O. Gorceix, L. Vernac, and B. Laburthe-Tolra, "Nonequilibrium Quantum Magnetism in a Dipolar Lattice Gas", Phys. Rev. Lett. **111**, 185305 (2013).

[299] O. Dutta, M. Gajda, P. Hauke, M. Lewenstein, D.-S. Lühmann, B. A. Malomed, T. Sowiński, and J. Zakrzewski, "Non-standard Hubbard models in optical lattices: a review", Rep. Prog. Phys. **78**, 066001 (2015).

[300] S. Baier, M. J. Mark, D. Petter, K. Aikawa, L. Chomaz, Z. Cai, M. Baranov, P. Zoller, and F. Ferlaino, "Extended Bose-Hubbard models with ultracold magnetic atoms", Science **352**, 201 (2016).

[301] S. Lepoutre, J. Schachenmayer, L. Gabardos, B. Zhu, B. Naylor, E. Maréchal, O. Gorceix, A. M. Rey, L. Vernac, and B. Laburthe-Tolra, "Out-of-equilibrium quantum magnetism and thermalization in a spin-3 many-body dipolar lattice system", Nat. Commun. **10**, 1714 (2019).

[302] L. Santos, G. V. Shlyapnikov, P. Zoller, and M. Lewenstein, "Bose-Einstein Condensation in Trapped Dipolar Gases", Phys. Rev. Lett. **85**, 1791 (2000).

[303] G. Pupillo, A. Micheli, M. Boninsegni, I. Lesanovsky, and P. Zoller, "Strongly Correlated Gases of Rydberg-Dressed Atoms: Quantum and Classical Dynamics", Phys. Rev. Lett. **104**, 223002 (2010).

[304] N. Henkel, R. Nath, and T. Pohl, "Three-Dimensional Roton Excitations and Supersolid Formation in Rydberg-Excited Bose-Einstein Condensates", Phys. Rev. Lett. **104**, 195302 (2010).

[305] J. E. Johnson and S. L. Rolston, "Interactions between Rydberg-dressed atoms", Phys. Rev. A **82**, 033412 (2010).

[306] Y. .-. Jau, A. M. Hankin, T. Keating, I. H. Deutsch, and G. W. Biedermann, "Entangling atomic spins with a Rydberg-dressed spin-flip blockade", Nat. Phys. **12**, 71 (2016).

[307] J. Zeiher, R. van Bijnen, P. Schauß, S. Hild, J.-y. Choi, T. Pohl, I. Bloch, and C. Gross, "Many-body interferometry of a Rydberg-dressed spin lattice", Nat. Phys. **12**, 1095 (2016).

[308] J. Zeiher, J.-y. Choi, A. Rubio-Abadal, T. Pohl, R. van Bijnen, I. Bloch, and C. Gross, "Coherent Many-Body Spin Dynamics in a Long-Range Interacting Ising Chain", Phys. Rev. X **7**, 041063 (2017).

[309] V. Borish, O. Markovi ć, J. A. Hines, S. V. Rajagopal, and M. Schleier-Smith, "Transverse-Field Ising Dynamics in a Rydberg-Dressed Atomic Gas", Phys. Rev. Lett. **124**, 063601 (2020).

[310] S. Hollerith, K. Srakaew, D. Wei, A. Rubio-Abadal, D. Adler, P. Weckesser, A. Kruckenhauser, V. Walther, R. van Bijnen, J. Rui, C. Gross, I. Bloch, and J. Zeiher, "Realizing Distance-Selective Interactions in a Rydberg-Dressed Atom Array", Phys. Rev. Lett. **128**, 113602 (2022).

[311] E. Guardado-Sanchez, B. M. Spar, P. Schauss, R. Belyansky, J. T. Young, P. Bienias, A. V. Gorshkov, T. Iadecola, and W. S. Bakr, "Quench Dynamics of a Fermi Gas with Strong Nonlocal Interactions", Phys. Rev. X **11**, 021036 (2021).

[312] D.-S. Lühmann, O. Jürgensen, M. Weinberg, J. Simonet, P. Soltan-Panahi, and K. Sengstock, "Quantum phases in tunable state-dependent hexagonal optical lattices", Phys. Rev. A **90**, 013614 (2014).

[313] L. Tarruell, D. Greif, T. Uehlinger, G. Jotzu, and T. Esslinger, "Creating, moving and merging Dirac points with a Fermi gas in a tunable honeycomb lattice", Nature **483**, 302 (2012).

[314] A. Eckardt, C. Weiss, and M. Holthaus, "Superfluid-Insulator Transition in a Periodically Driven Optical Lattice", Phys. Rev. Lett. **95**, 260404 (2005).

[315] H. Lignier, C. Sias, D. Ciampini, Y. Singh, A. Zenesini, O. Morsch, and E. Arimondo, "Dynamical Control of Matter-Wave Tunneling in Periodic Potentials", Phys. Rev. Lett. **99**, 220403 (2007).

[316] R. Ma, M. E. Tai, P. M. Preiss, W. S. Bakr, J. Simon, and M. Greiner, "Photon-Assisted Tunneling in a Biased Strongly Correlated Bose Gas", Phys. Rev. Lett. **107**, 095301 (2011).

[317] T. F. Gallagher, *Rydberg Atoms* (Cambridge University Press, 1994).

[318] N. Sibalic, *Rydberg Physics* (IOP Publishing, 2018).

[319] C. S. Adams, J. D. Pritchard, and J. P. Shaffer, "Rydberg atom quantum technologies", J. Phys. B **53**, 012002 (2019).

[320] E. Urban, T. A. Johnson, T. Henage, L. Isenhower, D. D. Yavuz, T. G. Walker, and M. Saffman, "Observation of Rydberg blockade between two atoms", Nat. Phys. **5**, 110 (2009).

[321] A. Gaëtan, Y. Miroshnychenko, T. Wilk, A. Chotia, M. Viteau, D. Comparat, P. Pillet, A. Browaeys, and P. Grangier, "Observation of collective excitation of two individual atoms in the Rydberg blockade regime", Nat. Phys. **5**, 115 (2009).

[322] W. Xu, A. V. Venkatramani, S. H. Cantú, T. Šumarac, V. Klüsener, M. D. Lukin, and V. Vuleti ć, "Fast Preparation and Detection of a Rydberg Qubit Using Atomic Ensembles", Phys. Rev. Lett. **127**, 050501 (2021).

[323] I. Shavitt and L. T. Redmon, "Quasidegenerate perturbation theories. A canonical van Vleck formalism and its relationship to other approaches", J. Chem. Phys. **73**, 5711 (1980).

[324] A. Rivas, O. Viyuela, and M. A. Martin-Delgado, "Density-matrix Chern insulators: Finite-temperature generalization of topological insulators", Phys. Rev. B **88**, 155141 (2013).

[325] S. Weber, C. Tresp, H. Menke, A. Urvoy, O. Firstenberg, H. P. Büchler, and S. Hofferberth, "Tutorial: Calculation of Rydberg interaction potentials", J. Phys. B: At. Mol. Opt. Phys. **50**, 133001 (2017).

[326] I. I. Beterov, I. I. Ryabtsev, D. B. Tretyakov, and V. M. Entin, "Quasiclassical calculations of blackbody-radiation-induced depopulation rates and effective lifetimes of Rydberg nS, nP, and nD alkali-metal atoms with $n \leq 80$", Phys. Rev. A **79**, 052504 (2009).

[327] J. A. Vergés, E. Louis, P. S. Lomdahl, F. Guinea, and A. R. Bishop, "Holes and magnetic textures in the two-dimensional Hubbard model", Phys. Rev. B **43**, 6099 (1991).

[328] J. A. Vergés, F. Guinea, and E. Louis, "Unrestricted Hartree-Fock study of the two-band Hamiltonian in doped CuO_2 planes", Phys. Rev. B **46**, 3562 (1992).

[329] R. Bianco, "Chern invariant and orbital magnetization as local quantities", PhD thesis (Università degli studi di Trieste, 2014).

[330] R. Bianco and R. Resta, "Mapping topological order in coordinate space", Phys. Rev. B **84**, 241106(R) (2011).

[331] A. Camacho-Guardian, N. Goldman, P. Massignan, and G. M. Bruun, "Dropping an impurity into a Chern insulator: A polaron view on topological matter", Phys. Rev. B **99**, 081105 (2019).

[332] D.-T. Tran, A. Dauphin, N. Goldman, and P. Gaspard, "Topological Hofstadter insulators in a two-dimensional quasicrystal", Phys. Rev. B **91**, 085125 (2015).

[333] L. Ul čakar, J. Mravlje, and T. ž. Rejec, "Kibble-Zurek Behavior in Disordered Chern Insulators", Phys. Rev. Lett. **125**, 216601 (2020).

[334] W. H. Zurek, U. Dorner, and P. Zoller, "Dynamics of a Quantum Phase Transition", Phys. Rev. Lett. **95**, 105701 (2005).

[335] A. del Campo and W. H. Zurek, "Universality of phase transition dynamics: Topological defects from symmetry breaking", Int. J. Mod. Phys. A **29**, 1430018 (2014).

[336] A. Keesling, A. Omran, H. Levine, H. Bernien, H. Pichler, S. Choi, R. Samajdar, S. Schwartz, P. Silvi, S. Sachdev, P. Zoller, M. Endres, M. Greiner, V. Vuletić, and M. D. Lukin, "Quantum Kibble–Zurek mechanism and critical dynamics on a programmable Rydberg simulator", Nature **568**, 207 (2019).

[337] K. Machida, "Magnetism in La2CuO4 based compounds", Physica (Amsterdam) **158C**, 192 (1989).

[338] H. Schulz, "Domain walls in a doped antiferromagnet", J. Phys. (Paris) **50**, 2833 (1989).

[339] R. B. Laughlin, "Quantized Hall conductivity in two dimensions", Phys. Rev. B **23**, 5632 (1981).

[340] D. N. Sheng, X. Wan, E. H. Rezayi, K. Yang, R. N. Bhatt, and F. D. M. Haldane, "Disorder-Driven Collapse of the Mobility Gap and Transition to an Insulator in the Fractional Quantum Hall Effect", Phys. Rev. Lett. **90**, 256802 (2003).

[341] S.-S. Gong, W. Zhu, and D. N. Sheng, "Emergent Chiral Spin Liquid: Fractional Quantum Hall Effect in a Kagome Heisenberg Model", Sci. Rep. **4**, 6317 (2014).

[342] J. Motruk and I. Na, "Detecting Fractional Chern Insulators in Optical Lattices through Quantized Displacement", Phys. Rev. Lett. **125**, 236401 (2020).

[343] A. J. Ferris and G. Vidal, "Perfect sampling with unitary tensor networks", Phys. Rev. B **85**, 165146 (2012).

[344] M. Buser, U. Schollwöck, and F. Grusdt, "Snapshot-based characterization of particle currents and the Hall response in synthetic flux lattices", Phys. Rev. A **105**, 033303 (2022).

[345] M. Popp, B. Paredes, and J. I. Cirac, "Adiabatic path to fractional quantum Hall states of a few bosonic atoms", Phys. Rev. A **70**, 053612 (2004).

[346] A. S. Sørensen, E. Altman, M. Gullans, J. V. Porto, M. D. Lukin, and E. Demler, "Adiabatic preparation of many-body states in optical lattices", Phys. Rev. A **81**, 061603 (2010).

[347] R. Schützhold and G. Schaller, "Adiabatic quantum algorithms as quantum phase transitions: First versus second order", Phys. Rev. A **74**, 060304 (2006).

[348] M. Barkeshli, N. Y. Yao, and C. R. Laumann, "Continuous Preparation of a Fractional Chern Insulator", Phys. Rev. Lett. **115**, 026802 (2015).

[349] J. Motruk and F. Pollmann, "Phase transitions and adiabatic preparation of a fractional Chern insulator in a boson cold-atom model", Phys. Rev. B **96**, 165107 (2017).

[350] Y.-C. He, F. Grusdt, A. Kaufman, M. Greiner, and A. Vishwanath, "Realizing and adiabatically preparing bosonic integer and fractional quantum Hall states in optical lattices", Phys. Rev. B **96**, 201103 (2017).

[351] M. L. Cohen and P. W. Anderson, "Comments on the Maximum Superconducting Transition Temperature", AIP Conference Proceedings **4**, 17 (1972).

[352] P. A. Lee, "From high temperature superconductivity to quantum spin liquid: progress in strong correlation physics", Rep. Prog. Phys. **71**, 012501 (2008).

[353] A. R. Schmidt, K. Fujita, E.-A. Kim, M. J. Lawler, H. Eisaki, S. Uchida, D.-H. Lee, and J. C. Davis, "Electronic structure of the cuprate superconducting and pseudogap phases from spectroscopic imaging STM", New J. Phys. **13**, 065014 (2011).

[354] P. S. Häfliger, A. Podlesnyak, K. Conder, E. Pomjakushina, and A. Furrer, "Pseudogap of the high-temperature superconductor $La_{1.96-x}Sr_xHo_{0.04}CuO_4$ as observed by neutron crystal-field spectroscopy", Phys. Rev. B **74**, 184520 (2006).

[355] D. Reznik, B. Keimer, F. Dogan, and I. A. Aksay, "q Dependence of Self-Energy Effects of the Plane Oxygen Vibration in $YBa_2Cu_3O_7$", Phys. Rev. Lett. **75**, 2396 (1995).

[356] K. C. Hewitt, X. K. Chen, C. Roch, J. Chrzanowski, J. C. Irwin, E. H. Altendorf, R. Liang, D. Bonn, and W. N. Hardy, "Hole concentration and phonon renormalization of the $340 - \mathrm{cm}^{-1}$ B_{1g} mode in 2% Ca-doped $YBa_2Cu_3O_y$ $(6.76 \lesssim y \lesssim 7.00)$", Phys. Rev. B **69**, 064514 (2004).

[357] L. Pintschovius, "Electron-phonon coupling effects explored by inelastic neutron scattering", Phys. Status Solidi B **242**, 30 (2005).

[358] V. Hinkov, D. Haug, B. Fauqué, P. Bourges, Y. Sidis, A. Ivanov, C. Bernhard, C. T. Lin, and B. Keimer, "Electronic Liquid Crystal State in the High-Temperature Superconductor YBa2Cu3O6.45", Science **319**, 597 (2008).

[359] R. Daou, J. Chang, D. LeBoeuf, O. Cyr-Choinière, F. Laliberté, N. Doiron-Leyraud, B. J. Ramshaw, R. Liang, D. A. Bonn, W. N. Hardy, and L. Taillefer, "Broken rotational symmetry in the pseudogap phase of a high-Tc superconductor", Nature **463**, 519 (2010).

[360] D. M. Newns and C. C. Tsuei, "Fluctuating Cu–O–Cu bond model of high-temperature superconductivity", Nat. Phys. **3**, 184 (2007).

[361] R. A. Nistor, G. J. Martyna, D. M. Newns, C. C. Tsuei, and M. H. Müser, "Ab initio theory of the pseudogap in cuprate superconductors driven by $C4$ symmetry breaking", Phys. Rev. B **83**, 144503 (2011).

[362] J. Hsiao, G. J. Martyna, and D. M. Newns, "Phase Diagram of Cuprate High-Temperature Superconductors Described by a Field Theory Based on Anharmonic Oxygen Degrees of Freedom", Phys. Rev. Lett. **114**, 107001 (2015).

[363] D. S. Marshall, D. S. Dessau, A. G. Loeser, C.-H. Park, A. Y. Matsuura, J. N. Eckstein, I. Bozovic, P. Fournier, A. Kapitulnik, W. E. Spicer, and Z.-X. Shen, "Unconventional Electronic Structure Evolution with Hole Doping in $Bi_2Sr_2CaCu_2O_{8+\delta}$: Angle-Resolved Photoemission Results", Phys. Rev. Lett. **76**, 4841 (1996).

[364] A. Damascelli, Z. Hussain, and Z.-X. Shen, "Angle-resolved photoemission studies of the cuprate superconductors", Rev. Mod. Phys. **75**, 473 (2003).

[365] I. M. Vishik, "Photoemission perspective on pseudogap, superconducting fluctuations, and charge order in cuprates: a review of recent progress", Rep. Prog. Phys. **81**, 062501 (2018).

[366] Y. Kohsaka, C. Taylor, K. Fujita, A. Schmidt, C. Lupien, T. Hanaguri, M. Azuma, M. Takano, H. Eisaki, H. Takagi, S. Uchida, and J. C. Davis, "An Intrinsic Bond-Centered Electronic Glass with Unidirectional Domains in Underdoped Cuprates", Science **315**, 1380 (2007).

[367] Y. Kohsaka, T. Hanaguri, M. Azuma, M. Takano, J. C. Davis, and H. Takagi, "Visualization of the emergence of the pseudogap state and the evolution to superconductivity in a lightly hole-doped Mott insulator", Nat. Phys. **8**, 534 (2012).

[368] K. Fujita, M. H. Hamidian, S. D. Edkins, C. K. Kim, Y. Kohsaka, M. Azuma, M. Takano, H. Takagi, H. Eisaki, S.-i. Uchida, A. Allais, M. J. Lawler, E.-A. Kim, S. Sachdev, and J. C. S. Davis, "Direct phase-sensitive identification of a d-form factor density wave in underdoped cuprates", Proc. Natl. Acad. Sci. U.S.A. **111**, E3026 (2014).

[369] A.-M. S. Tremblay, B. Kyung, and D. Sénéchal, "Pseudogap and high-temperature superconductivity from weak to strong coupling. Towards a quantitative theory (Review Article)", Low Temp. Phys. **32**, 424 (2006).

[370] M. Civelli, M. Capone, S. S. Kancharla, O. Parcollet, and G. Kotliar, "Dynamical Breakup of the Fermi Surface in a Doped Mott Insulator", Phys. Rev. Lett. **95**, 106402 (2005).

[371] M. Ferrero, P. S. Cornaglia, L. De Leo, O. Parcollet, G. Kotliar, and A. Georges, "Pseudogap opening and formation of Fermi arcs as an orbital-selective Mott transition in momentum space", Phys. Rev. B **80**, 064501 (2009).

[372] G. Sordi, P. Sémon, K. Haule, and A.-M. S. Tremblay, "Strong Coupling Superconductivity, Pseudogap, and Mott Transition", Phys. Rev. Lett. **108**, 216401 (2012).

[373] O. Gunnarsson, T. Schäfer, J. P. F. LeBlanc, E. Gull, J. Merino, G. Sangiovanni, G. Rohringer, and A. Toschi, "Fluctuation Diagnostics of the Electron Self-Energy: Origin of the Pseudogap Physics", Phys. Rev. Lett. **114**, 236402 (2015).

[374] T. A. Maier, T. Pruschke, and M. Jarrell, "Angle-resolved photoemission spectra of the Hubbard model", Phys. Rev. B **66**, 075102 (2002).

[375] E. Gull, O. Parcollet, and A. J. Millis, "Superconductivity and the Pseudogap in the Two-Dimensional Hubbard Model", Phys. Rev. Lett. **110**, 216405 (2013).

[376] W. Wu, M. S. Scheurer, S. Chatterjee, S. Sachdev, A. Georges, and M. Ferrero, "Pseudogap and Fermi-Surface Topology in the Two-Dimensional Hubbard Model", Phys. Rev. X **8**, 021048 (2018).

[377] P. A. Lee, N. Nagaosa, and X.-G. Wen, "Doping a Mott insulator: Physics of high-temperature superconductivity", Rev. Mod. Phys. **78**, 17 (2006).

[378] R. Micnas, J. Ranninger, and S. Robaszkiewicz, "Superconductivity in narrow-band systems with local nonretarded attractive interactions", Rev. Mod. Phys. **62**, 113 (1990).

[379] M. Randeria, N. Trivedi, A. Moreo, and R. T. Scalettar, "Pairing and spin gap in the normal state of short coherence length superconductors", Phys. Rev. Lett. **69**, 2001 (1992).

[380] V. J. Emery and S. A. Kivelson, "Importance of phase fluctuations in superconductors with small superfluid density", Nature **374**, 434 (1995).

[381] A. S. Alexandrov, V. V. Kabanov, and N. F. Mott, "Coherent *ab* and *c* Transport Theory of High- T_c Cuprates", Phys. Rev. Lett. **77**, 4796 (1996).

[382] M. Franz and A. J. Millis, "Phase fluctuations and spectral properties of underdoped cuprates", Phys. Rev. B **58**, 14572 (1998).

[383] E. Berg and E. Altman, "Evolution of the Fermi Surface of *d*-Wave Superconductors in the Presence of Thermal Phase Fluctuations", Phys. Rev. Lett. **99**, 247001 (2007).

[384] C. M. Varma, "Theory of the pseudogap state of the cuprates", Phys. Rev. B **73**, 155113 (2006).

[385] S. Chakravarty, R. B. Laughlin, D. K. Morr, and C. Nayak, "Hidden order in the cuprates", Phys. Rev. B **63**, 094503 (2001).

[386] C. Honerkamp, H. C. Fu, and D.-H. Lee, "Phonons and *d*-wave pairing in the two-dimensional Hubbard model", Phys. Rev. B **75**, 014503 (2007).

[387] J. Zaanen and O. Gunnarsson, "Charged magnetic domain lines and the magnetism of high-T_c oxides", Phys. Rev. B **40**, 7391 (1989).

[388] V. J. Emery, S. A. Kivelson, and J. M. Tranquada, "Stripe phases in high-temperature superconductors", Proc. Natl. Acad. Sci. U.S.A. **96**, 8814 (1999).

[389] S. Sachdev, "Colloquium: Order and quantum phase transitions in the cuprate superconductors", Rev. Mod. Phys. **75**, 913 (2003).

[390] E.-A. Kim, M. J. Lawler, P. Oreto, S. Sachdev, E. Fradkin, and S. A. Kivelson, "Theory of the nodal nematic quantum phase transition in superconductors", Phys. Rev. B **77**, 184514 (2008).

[391] A. V. Chubukov and J. Schmalian, "Temperature variation of the pseudogap in underdoped cuprates", Phys. Rev. B **57**, R11085 (1998).

[392] S. A. Kivelson, E. Fradkin, and V. J. Emery, "Electronic liquid-crystal phases of a doped Mott insulator", Nature **393**, 550 (1998).

[393] M. Vojta, "Lattice symmetry breaking in cuprate superconductors: Stripes, nematics, and superconductivity", Adv. Phys. **58**, 699 (2009).

[394] E. Fradkin, S. A. Kivelson, M. J. Lawler, J. P. Eisenstein, and A. P. Mackenzie, "Nematic Fermi Fluids in Condensed Matter Physics", Annu. Rev. Condens. Matter Phys. **1**, 153 (2010).

[395] L. Nie, G. Tarjus, and S. A. Kivelson, "Quenched disorder and vestigial nematicity in the pseudogap regime of the cuprates", Proc. Natl. Acad. Sci. U.S.A. **111**, 7980 (2014).

[396] K. Lee, S. A. Kivelson, and E.-A. Kim, "Cold-spots and glassy nematicity in underdoped cuprates", Phys. Rev. B **94**, 014204 (2016).

[397] A. Ramos-Alvarez, N. Fleischmann, L. Vidas, A. Fernandez-Rodriguez, A. Palau, and S. Wall, "Probing the lattice anharmonicity of superconducting $YBa_2Cu_3O_{7-\delta}$ via phonon harmonics", Phys. Rev. B **100**, 184302 (2019).

[398] P. Fulde, *Electron Correlations in Molecules and Solids*, third, Vol. 100, Springer Series in Solid-State Sciences (Springer-Verlag, Berlin, 1995).

[399] L. B. Ioffe and A. J. Millis, "Zone-diagonal-dominated transport in high-T_c cuprates", Phys. Rev. B **58**, 11631 (1998).

[400] K. Fujita, C. K. Kim, I. Lee, J. Lee, M. H. Hamidian, I. A. Firmo, S. Mukhopadhyay, H. Eisaki, S. Uchida, M. J. Lawler, E.-A. Kim, and J. C. Davis, "Simultaneous Transitions in Cuprate Momentum-Space Topology and Electronic Symmetry Breaking", Science **344**, 612 (2014).

[401] A. V. Pimenov, A. V. Boris, L. Yu, V. Hinkov, T. Wolf, J. L. Tallon, B. Keimer, and C. Bernhard, "Nickel Impurity-Induced Enhancement of the Pseudogap of Cuprate High-T_c Superconductors", Phys. Rev. Lett. **94**, 227003 (2005).

[402] J. ř. Va šátko and D. Munzar, "Exact diagonalization study of the effects of Zn and Ni impurities on the pseudogap of underdoped cuprate high-T_c superconductors", Phys. Rev. B **93**, 094512 (2016).

[403] D. Poilblanc, D. J. Scalapino, and W. Hanke, "Resonant impurity scattering in a strongly correlated electron model", Phys. Rev. Lett. **72**, 884 (1994).

[404] P. Prelovšek, A. Ramšak, and I. Sega, "C-axis conductivity in the normal state of cuprate superconductors", Phys. Rev. Lett. **81**, 3745 (1998).

[405] R. Alicki and M. Fannes, "Entanglement boost for extractable work from ensembles of quantum batteries", Phys. Rev. E **87**, 042123 (2013).

[406] M. Perarnau-Llobet, K. V. Hovhannisyan, M. Huber, P. Skrzypczyk, N. Brunner, and A. Acín, "Extractable Work from Correlations", Phys. Rev. X **5**, 041011 (2015).

[407] D. Ferraro, M. Campisi, G. M. Andolina, V. Pellegrini, and M. Polini, "High-Power Collective Charging of a Solid-State Quantum Battery", Phys. Rev. Lett. **120**, 117702 (2018).

[408] T. P. Le, J. Levinsen, K. Modi, M. M. Parish, and F. A. Pollock, "Spin-chain model of a many-body quantum battery", Phys. Rev. A **97**, 022106 (2018).

[409] F. Campaioli, F. A. Pollock, F. C. Binder, L. Céleri, J. Goold, S. Vinjanampathy, and K. Modi, "Enhancing the Charging Power of Quantum Batteries", Phys. Rev. Lett. **118**, 150601 (2017).

[410] S. Deffner and S. Campbell, "Quantum speed limits: from Heisenberg's uncertainty principle to optimal quantum control", J. Phys. A: Math. Theor. **50**, 453001 (2017).

[411] I. Bengtsson and K. Zyczkowski, *Geometry of Quantum States: An Introduction to Quantum Entanglement*, 2nd ed. (Cambridge University Press, Cambridge, 2017).

[412] S. L. Braunstein and C. M. Caves, "Statistical distance and the geometry of quantum states", Phys. Rev. Lett. **72**, 3439 (1994).

[413] G. Tóth and I. Apellaniz, "Quantum metrology from a quantum information science perspective", J. Phys. A: Math. Theor. **47**, 424006 (2014).

[414] R. Demkowicz-Dobrzański, M. Jarzyna, and J. Kołodyński, "Quantum Limits in Optical Interferometry", Prog. Opt. **60**, 345 (2015).

[415] G. Tóth, "Multipartite entanglement and high-precision metrology", Phys. Rev. A **85**, 022322 (2012).

[416] P. Hyllus, W. Laskowski, R. Krischek, C. Schwemmer, W. Wieczorek, H. Weinfurter, L. Pezzé, and A. Smerzi, "Fisher information and multiparticle entanglement", Phys. Rev. A **85**, 022321 (2012).

[417] Z. Chen, "Wigner-Yanase skew information as tests for quantum entanglement", Phys. Rev. A **71**, 052302 (2005).

[418] O. Gühne, G. Tóth, and H. J. Briegel, "Multipartite entanglement in spin chains", New J. Phys. **7**, 229 (2005).

[419] H. J. Lipkin, N. Meshkov, and A. J. Glick, "Validity of many-body approximation methods for a solvable model. (I). Exact solutions and perturbation theory", Nucl. Phys. A **62**, 188 (1965).

[420] W. Muessel, H. Strobel, D. Linnemann, T. Zibold, B. Juliá-Díaz, and M. K. Oberthaler, "Twist-and-turn spin squeezing in Bose-Einstein condensates", Phys. Rev. A **92**, 023603 (2015).

[421] J. Vidal, G. Palacios, and R. Mosseri, "Entanglement in a second-order quantum phase transition", Phys. Rev. A **69**, 022107 (2004).

[422] R. H. Dicke, "Coherence in Spontaneous Radiation Processes", Phys. Rev. **93**, 99 (1954).

[423] J. M. Fink, R. Bianchetti, M. Baur, M. Göppl, L. Steffen, S. Filipp, P. J. Leek, A. Blais, and A. Wallraff, "Dressed Collective Qubit States and the Tavis-Cummings Model in Circuit QED", Phys. Rev. Lett. **103**, 083601 (2009).

[424] A. Aloy, J. Tura, F. Baccari, A. Acín, M. Lewenstein, and R. Augusiak, "Device-Independent Witnesses of Entanglement Depth from Two-Body Correlators", Phys. Rev. Lett. **123**, 100507 (2019).

[425] J. Tura, A. Aloy, F. Baccari, A. Acín, M. Lewenstein, and R. Augusiak, "Optimization of device-independent witnesses of entanglement depth from two-body correlators", Phys. Rev. A **100**, 032307 (2019).

[426] J. S. Bell, "On the Einstein Podolsky Rosen paradox", Phys. Phys. Fiz. **1**, 195 (1964).

[427] D. Rossini, G. M. Andolina, D. Rosa, M. Carrega, and M. Polini, "Quantum Advantage in the Charging Process of Sachdev-Ye-Kitaev Batteries", Phys. Rev. Lett. **125**, 236402 (2020).

[428] S. Sachdev and J. Ye, "Gapless spin-fluid ground state in a random quantum Heisenberg magnet", Phys. Rev. Lett. **70**, 3339 (1993).

[429] Y. Gu, A. Kitaev, S. Sachdev, and G. Tarnopolsky, "Notes on the complex Sachdev-Ye-Kitaev model", J. High Energy Phys. **2020**, 157 (2020).

[430] V. Rosenhaus, "An introduction to the SYK model", J. Phys. A: Math. Theor. **52**, 323001 (2019).